

HU ISSN 1586–2070

JOURNAL OF COMPUTATIONAL AND APPLIED MECHANICS

A Publication of the University of Miskolc

VOLUME 5, NUMBER 1 (2004)



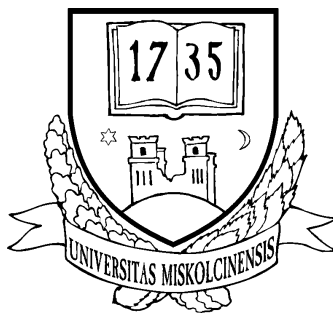
MISKOLC UNIVERSITY PRESS

HU ISSN 1586–2070

JOURNAL OF COMPUTATIONAL AND APPLIED MECHANICS

A Publication of the University of Miskolc

VOLUME 5, NUMBER 1 (2004)



MISKOLC UNIVERSITY PRESS

EDITORIAL BOARD

- István PÁCZELT, Editor in Chief, Department of Mechanics, University of Miskolc, 3515 MISKOLC, Hungary, mechpacz@gold.uni-miskolc.hu
- Vladimir KOMPIŠ, Department of Mechanics, Faculty of Mechanical Engineering, University of Žilina, ŽILINA, Slovakia, kompis@fstroj.utc.sk
- László BARANYI, Department of Fluid and Heat Engineering, University of Miskolc, 3515 MISKOLC, Hungary, arambl@gold.uni-miskolc.hu
- Imre KOZÁK, Department of Mechanics, University of Miskolc, 3515 MISKOLC, Hungary, mechkoz@gold.uni-miskolc.hu
- Edgár BERTÓTI, Department of Mechanics, University of Miskolc, 3515 MISKOLC, Hungary, mechber@gold.uni-miskolc.hu
- Márta KURUTZ, Department of Structural Mechanics, Budapest University of Technology and Economics, Műegyetem rkp. 3, 1111 BUDAPEST, Hungary, kurutzm@eik.bme.hu
- Tibor CZIBERE, Department of Fluid and Heat Engineering, University of Miskolc, 3515 MISKOLC, Hungary, aramct@gold.uni-miskolc.hu
- R. Ivan LEWIS, Room 2-16 Bruce Building, Newcastle University, NEWCASTLE UPON TYNE, NE1 7RU, UK, R.I.Lewis@NCL.AC.UK
- Wolfram FRANK, Institut für Fluid- und Thermodynamik, Universität Siegen, Paul-Bonatz-Strasse 9-11, 57076 SIEGEN, Germany, frank@ift.mb.uni-siegen.de
- Gennadij LVOV, Department of Mechanics, Kharkov Polytechnical Institute, 2 Frunze Str., 310002 KHARKOV, Ukraine, lvovgi@kpi.kharkov.ua
- Ulrich GABBERT, Institut für Mechanik, Otto-von-Guericke-Universität Magdeburg, Universitätsplatz 2, 39106 MAGDEBURG, Germany, ulrich.gabbert@mb.uni-magdeburg.de
- Herbert MANG, Institute for Strength of Materials, University of Technology, Karlsplatz 13, 1040 VIENNA, Austria, Herbert.Mang@tuwien.ac.at
- Zsolt GÁSPÁR, Department of Structural Mechanics, Budapest University of Technology and Economics, Műegyetem rkp. 3, 1111 BUDAPEST, Hungary, gaspar@ep-mech.me.bme.hu
- Zenon MROZ, Polish Academy of Sciences, Institute of Fundamental Technological Research, Swietokrzyska 21, WARSAW, Poland, zmroz@ippt.gov.pl
- Robert HABER, Department of Theoretical and Applied Mechanics, University of Illinois at Urbana-Champaign, 216 Talbot Lab., 104 S. Wright Str., URBANA, IL 61801, USA, r-haber@uiuc.edu
- Tibor NAGY, Department of Physics, University of Miskolc, 3515 MISKOLC, Hungary, fiznagy@uni-miskolc.hu
- Gyula PATKÓ, Department of Machine Tools, University of Miskolc, 3515 MISKOLC, Hungary, mechpgy@uni-miskolc.hu
- Gábor HALÁSZ, Department of Hydraulic Machines, Budapest University of Technology and Economics, Műegyetem rkp. 3, 1111 BUDAPEST, Hungary, HALASZ@vizgep.bme.hu
- Jan SLADEK, Ústav stavbenictva a architektúry, Slovenskej akadémie vied, Dubróvska cesta 9, 842 20 BRATISLAVA, Slovakia, usarslad@savba.sk
- Ji Huan HE, Department of Mathematics, College of Basic Science, Shanghai Donghua University, No. 1882 Yan'anxilu Road, 200051 Shanghai, China, jhhe@dhu.edu.cn
- Gábor STÉPÁN, Department of Mechanics, Budapest University of Technology and Economics, Műegyetem rkp. 3, 1111 BUDAPEST, Hungary, stepan@mm.bme.hu
- Károly JÁRMAI, Department of Materials Handling and Logistics, University of Miskolc, 3515 MISKOLC, Hungary, altjar@gold.uni-miskolc.hu
- Barna SZABÓ, Center for Computational Mechanics, Washington University, Campus Box 1129, St. LOUIS, MO63130, USA, szabo@ccm.wustl.edu
- László KOLLÁR, Department of Strength of Materials and Structures, Budapest University of Technology and Economics, Műegyetem rkp. 1-3. K.II.42., 1521 BUDAPEST, Hungary, lkollar@goliat.eik.bme.hu
- Szilárd SZABÓ, Department of Fluid and Heat Engineering, University of Miskolc, 3515 MISKOLC, Hungary, aram2xs@uni-miskolc.hu
- György SZEIDL, Department of Mechanics, University of Miskolc, 3515 MISKOLC, Hungary, Gyorgy.SZEIDL@uni-miskolc.hu

LOCAL EDITORIAL COUNCIL

T. CZIBERE, I. KOZÁK, I. PÁCZELT, G. PATKÓ, G. SZEIDL

PREFACE

A Professional Life Dedicated to Structural Optimization Professor József Farkas Is 75 Years Old

On the occasion of his 75th birthday, his friends, colleagues and former students, dedicate a part of this special issue of the Journal of Computational and Applied Mechanics to József Farkas, Professor emeritus at the University of Miskolc. Professor Farkas graduated as a civil engineer from the Technical University of Budapest in 1950. He has been teaching at the University of Miskolc since 1950. Between 1950-59 he taught at the Department of Mechanics and from 1959 at the Department of Materials Handling, now Department of Materials Handling and Logistics.



In the past five decades he has developed courses on *Metal Structures*, *Welded Structures* and achieved an international reputation. The international novelty of these courses is that they are devoted to the design of structural components of machines and load-carrying structures. They take into account dynamic effects, stiffness and vibration damping. These features made them suitable for the modular academic system of the Faculty of Mechanical Engineering. The most important features of these courses consist in the application of mathematics, mechanics, optimization methods and applicability in the engineering practice. Optimum design provides a wide horizon, which is necessary for engineers. On the basis of Professor Farkas's work, the students of the faculty can obtain a comprehensive overview of the design of metal and welded structures.

Professor Farkas was one of the first to realize the importance of the application of computers in structural optimization. It must be pointed out that economic aspects are also considered in optimization by means of self-developed cost functions.

The theoretical calculations are complemented in most cases by experimental measurements carried out in laboratories, or in the field.

His complex approach resulting from the structural synthesis has had a great effect not only on his students, but also on his colleagues at the university and the engineers practising in the industry.

In 1996 he retired and since 1998 he has been working as Professor emeritus continuing his previous work unrelentingly. He gives lectures week by week, offers the students advice on their design assignments and guidance on writing the theses. Related to his tutorial activity he published a university textbook entitled *Metal structures* in 1974. The second and revised edition came out in 1983.

As regards his teaching activity he has been involved in the programs of welding engineers as well as in those offered to foreign students in English since the beginnings. He joined the PhD training at the beginning and has been the scientific advisor of several PhD students.

His scientific activity has been continuous and undiminished for decades. He obtained his Ph.D. degree in 1966. His thesis was devoted to the design of stiffened plates. He obtained the title doctor of the Hungarian Academy of Sciences, i.e., the DSc degree, which is equivalent to the German habilitation, for a thesis on the optimum design of metal structures in 1978. After being revised and supplemented his DSc thesis was published under the title *Optimum design of metal structures* by Ellis Horwood, Chichester, UK and the Hungarian Publishing House Akadémiai Kiadó, Budapest in 1984. The book won an academic award.

His third and fourth books *Analysis and optimum design of metal structures*, and *Economic design of metal structures*, were published by Balkema, and Millpress Science Publishes in Rotterdam, in 1997 and 2003, respectively. His coauthor was one of his former students Károly Jármai. Beside the books he has published about 250 papers and studies. Half of them were written in a foreign language, mainly in English.

His expertise has been utilized by the industry as well. His main research areas are as follows: optimum design of metal structures, residual welding distortions and stresses, tubular structures, stiffened plates, sandwich structures, vibration damping and stability problems of steel structures.

His five decade long activity in the field of structural optimization should be especially highlighted. His optimum design methods can be used in other disciplines as well. He holds lectures also in English, German and Slovak languages. He covered the application of design methods for the following materials handling machines and equipment: cranes, crane runways, silos, bunkers, conveyor galleries, frames, cellular plates, tubular structures. In the field of machine tools he also worked out a course for welded structures, mainly press frames.

His main external activities are in the Welding Division of the Scientific Society of Mechanical Engineers (GTE), the International Institute of Welding (IIW), the International Society for Structural and Multidisciplinary Optimization (ISSMO). The Scientific Society of Mechanical Engineers awarded him the Pattantyús Medal. He was also awarded the Apáczai Csere János Award and the Memorial Medal of the 45 years old Technical University of Kosice. He became Dr. Honoris Causa of the University of Miskolc in 2002.

He has attended the Annual Assemblies of IIW and the symposia on Tubular Structures, organized by the Subcommission IIW XV-E for several years.

His international co-operation ranges from Japan to Canada. He has established connections with professors from all over the world as it is illustrated by the list of participants of the International Conference on Metal Structures (ICMS'2003).

His role in the Department of Materials Handling and Logistics has been crucial. He has been the head of the Division of Metal Structures. He has been the scientific supervisor of several specialists in engineering optimization: Dr. Habil. Imre Tímár, Prof. Károly Jármái, Ferenc Orbán, Sándor Rácz, László Szabó, Ferenc Szabó. He gave the first initiative for the research work of some professors including the member of the Hungarian Academy of Sciences István Páczelt, Dr. Habil. Mátyás Matolcsy and József Cselényi.

He is an excellent lecturer. He has the gift to present highly complicated ideas, relationships, lines of thoughts in an elegant and simple manner and to make his audience understand what at first seems to be difficult.

His personal hobby is listening to and playing classical music. He plays baroque and classical music on the electrophonic organ.

The range of topics covered by the various contributions to this issue reflects the scientific interests of József Farkas. In the present issue of the journal the authors V. Chukin, Gy. Kovács, K. Jármái, I. Ecsedi and K. Dluhi, S. Jendo, Y. Savula, B. Kovács, I. Tímár, M. Vorel and Z. Virág have dedicated their papers to Professor Farkas. With this volume, all his former and present colleagues, students and co-workers wish him good health and many more active years at the University of Miskolc.

Miskolc, December 22, 2003

Károly Jármái

VARIATIONAL THEORY FOR 2-DIMENSIONAL FREE SURFACE FLOW: WHY ARE G.L. LIU'S VARIATIONAL PRINCIPLES INCORRECT?

JI HUAN HE

College of Science, Shanghai Donghua University
P.O. Box 471, Shanghai 20051, People's Republic of China
jhhe@dhu.edu.cn

[Received: February 28, 2003]

Abstract. Interests in variational theory of the problem discussed have grown rapidly in recent years, various variational formulae have appeared in literature. But some of the variational principles are wrong. The paper illustrates how to establish variational principles by the semi-inverse method step by step. Comparison with Liu's results reveals that the present technique is much more convenient and reliable. Liu's variational formulation is based on technical, theoretical and conceptual errors, including misrepresentations of the semi-inverse method.

Mathematical Subject Classification: 78M30

Keywords: variational theory, free boundary problem, semi-inverse method

1. Introduction

The basic equations governing 2-D incompressible inviscid rotational flow under gravity can be written in the form

$$\frac{\partial u}{\partial x} + \frac{\partial v}{\partial y} = 0, \quad (1.1)$$

$$u \frac{\partial v}{\partial x} + v \frac{\partial v}{\partial y} = -g - \frac{1}{\rho} \frac{\partial P}{\partial y}, \quad (1.2)$$

$$\frac{1}{2}(u^2 + v^2) + gy + \frac{P}{\rho} = B(\Psi), \quad (1.3)$$

where B is the Bernoulli constant, which does not change along the stream line, the stream function Ψ is also constant, u and v are velocity components in the x - and y -directions respectively, g is gravitational acceleration, P is pressure.

Difficulty arises when we apply the finite element method to free surface problems. In order to overcome the difficulty, an imaginary plane is introduced [1, Liu, 1995] [2, He, 1998] since the value of the stream function Ψ on the free surface should be given

according to the inlet condition. Therefore it will be convenient for us to introduce an imaginary plane $\xi - \Psi$ defined as

$$\xi = x, \quad (1.4)$$

$$\psi = \psi(x, y), \quad (1.5)$$

where the stream function ψ takes the form

$$\frac{\partial \psi}{\partial x} = -v, \quad \frac{\partial \psi}{\partial y} = u. \quad (1.6)$$

It is easy to find that

$$\frac{\partial}{\partial x} = \frac{\partial}{\partial \xi} \frac{\partial \xi}{\partial x} + \frac{\partial}{\partial \psi} \frac{\partial \Psi}{\partial x} = \frac{\partial}{\partial \xi} - v \frac{\partial}{\partial \psi}$$

and

$$\frac{\partial}{\partial y} = \frac{\partial}{\partial \xi} \frac{\partial \xi}{\partial y} + \frac{\partial}{\partial \psi} \frac{\partial \Psi}{\partial y} = u \frac{\partial}{\partial \psi}.$$

Consequently we have the following basic equations in the imaginary plane:

$$\frac{\partial}{\partial \xi} \left(\frac{1}{u} \right) - \frac{\partial}{\partial \psi} \left(\frac{v}{u} \right) = 0, \quad (1.7)$$

$$\frac{\partial v}{\partial \xi} + \frac{\partial}{\partial \psi} (\Pi) = 0, \quad (1.8)$$

$$\Pi + \frac{1}{2}(u^2 + v^2) = B, \quad (1.9)$$

where $\Pi = gy + P/\rho$.

Making use of equation (1.8) a general function Ω can be introduced [1, Liu, 1995]

$$\frac{\partial \Omega}{\partial \xi} = \Pi, \quad \frac{\partial \Omega}{\partial \psi} = -v. \quad (1.10)$$

Luke [3, 1967] first studied the variational principle for fluids with free surface in a physical plane, and Liu [1, 1995] was the first to deduce variational principles in the imaginary plane. Recently Liu [5, 2001] re-studied the problem by Liu's systematic method [6, 2000], but, unfortunately, the variational principles obtained are proved to be wrong. We re-write two formulae for evaluation. Consider first the variational formulations obtained by Liu:

$$\begin{aligned} J_{Liu1}(\Omega, v, \Pi, u) = & \iint \frac{1}{\sqrt{2(B - \Pi) - v^2}} \left\{ v \frac{\partial \Omega}{\partial \Psi} - \frac{\partial \Omega}{\partial \xi} + 2B - \Pi \right\} dA \\ & - \iint \left\{ au^{n-2}(u^2 + v^2 + 2\Pi - 2B) - \frac{2a}{n}u^n \right\} dA, \quad (1.11) \end{aligned}$$

$$\begin{aligned} J_{Liu2}(\Omega, u, v, \Pi) = & \iint \left\{ \frac{v}{u} \frac{\partial \Omega}{\partial \Psi} - \frac{1}{u} \frac{\partial \Omega}{\partial \xi} + \frac{u^2 + v^2}{u} + \frac{B}{u} \right\} dA \\ & - \iint \left\{ a\Pi^{n-1}(u^2 + v^2 + 2\Pi - 2B) - \frac{2a}{n}\Pi^n \right\} dA. \quad (1.12) \end{aligned}$$

It is easy to prove that the above two functionals are wrong. As is pointed out by He [7, 2000], Liu's systematic method [6, 2000] contains a contradiction [8, 2000] leading to very limited validity of this approach [9, He, 2000]. Liu's method might result in incorrect functionals, for example, the variational functional obtained by Liu et al. in (Liu and Wang, [10, 1996]) is incorrect, which is corrected by He's semi-inverse method [11, 2000], [12, 1997].

2. Inverse problem of calculus of variations

In recent years the inverse problem of calculus of variations has brought about a renewed interest in continuum mechanics. It emanates from the powerful applications of the finite element methods (Zienkiewicz and Taylor [13], Liu [14]) and the meshfree particle methods (He [15, 1999]).

In 1997, the present author proposed a powerful tool called the semi-inverse method (He [12, 1997]) to search for various variational principles directly from the field equations and boundary conditions. Applications of the semi-inverse method can be found in the author's previous publications (He [16], [17], [18]).

In 2000, Liu [6] proposed a systematic approach to the derivation of variational principles from partial differential equations. Liu's method consists of two major lines. There are a number of books devoted to the issue of variational principles, e.g. the classical monographs by Chien [19, 1983] and Hildebrand [20, 1965]. The first line of Liu's approach is also discussed by Chien [19, 1983] and Hildebrand [20, 1965] in great detail. The question of determining whether a set of field equations can be derived from a functional may be systematically elucidated by recourse to Veinberg's theorem, which also provides a formula for the computation of the corresponding functional. Therefore the first line of Liu's approach offers nothing new. The application of this line can also be found in the literature (e.g. Meylan 2001). The key contribution of Liu's method lies in the second line, which provides a method for searching for a generalized variational principle directly from field equations. But the application of Liu's method might lead to incorrect results.

Consider the equation system

$$\frac{\partial u}{\partial x} + \frac{\partial v}{\partial y} = 0, \quad (2.1)$$

$$\frac{\partial v}{\partial x} - \frac{\partial u}{\partial y} = 0. \quad (2.2)$$

By Liu's approach one obtains the following functional [6, 2000a]

$$J(u, v) = \iint \left\{ v \left(\frac{\partial u}{\partial x} + \frac{\partial v}{\partial y} \right) + u \left(\frac{\partial v}{\partial x} - \frac{\partial u}{\partial y} \right) \right\} dx dy. \quad (2.3)$$

We cannot obtain any Euler equation from the above functional. Consequently, Liu's method has been proved to be incorrect for the above equations.

In view of the semi-inverse method [12, 1997], we can suppose that there exists an unknown functional [7, 2001]

$$J = \iint F dx dy \quad (2.4)$$

under the constraint (2.2). By the Lagrange multiplier method, we have

$$J(u, v, \Psi) = \iint \left\{ F + \Psi \left(\frac{\partial v}{\partial x} - \frac{\partial u}{\partial y} \right) \right\} dx dy, \quad (2.5)$$

where Ψ is a Lagrange multiplier. The stationary conditions for the above functional are as follows

$$\frac{\partial v}{\partial x} - \frac{\partial u}{\partial y} = 0, \quad (2.6)$$

$$\frac{\delta F}{\delta u} + \frac{\partial \Psi}{\partial y} = 0, \quad (2.7)$$

$$\frac{\delta F}{\delta v} - \frac{\partial \Psi}{\partial x} = 0. \quad (2.8)$$

Here $\delta F / \delta u$ is called variational derivative of F with respect to u , and is defined as

$$\frac{\delta F}{\delta u} = \frac{\partial F}{\partial u} - \frac{\partial}{\partial x} \left(\frac{\partial F}{\partial u_x} \right) - \frac{\partial}{\partial y} \left(\frac{\partial F}{\partial u_y} \right).$$

From equations (2.7) and (2.8), we have

$$\frac{\partial}{\partial x} \left(\frac{\delta F}{\delta u} \right) + \frac{\partial}{\partial y} \left(\frac{\delta F}{\delta v} \right) = 0, \quad (2.9)$$

which should be the field equation $u_x + v_y = 0$. Hence we set

$$\frac{\delta F}{\delta u} = u,$$

and

$$\frac{\delta F}{\delta v} = v, \quad (2.10)$$

from which we identify the unknown F as follows

$$F = \frac{1}{2}(u^2 + v^2). \quad (2.11)$$

Therefore we obtain the following variational principle

$$J = \iint \frac{1}{2}(u^2 + v^2) dx dy \quad (2.12)$$

and the following generalized variational principle

$$J(u, v, \Psi) = \iint \left\{ \frac{1}{2}(u^2 + v^2) + \Psi \left(\frac{\partial v}{\partial x} - \frac{\partial u}{\partial y} \right) \right\} dx dy. \quad (2.13)$$

The Lagrange multiplier now has a physical meaning, i.e., the stream function. To search for a generalized variational principle, we always begin with an energy-like

trial functional with an unknown function F . For example, we can construct a trial functional in the form

$$J(u, v, \Phi) = \iint \left\{ u \frac{\partial \Phi}{\partial x} + v \frac{\partial \Phi}{\partial y} + F \right\} dx dy, \quad (2.14)$$

where Φ is the potential function for which

$$\frac{\partial \Phi}{\partial x} = u, \quad \frac{\partial \Phi}{\partial y} = v$$

while F is an unknown function of u , v , and their derivatives.

It is obvious that the stationary condition of the functional (2.14) with respect to Φ results in (2.9). Calculating variation of functional (2.14) with respect to u and v , we have

$$\frac{\partial \Phi}{\partial x} + \frac{\delta F}{\delta u} = 0, \quad (2.15)$$

$$\frac{\partial \Phi}{\partial y} + \frac{\delta F}{\delta v} = 0. \quad (2.16)$$

We search for such an F that the above two equations should become

$$\frac{\partial \Phi}{\partial x} = u$$

and

$$\frac{\partial \Phi}{\partial y} = v,$$

respectively, so that we can immediately identify F as $F = -(u^2 + v^2)/2$.

There exist many alternative approaches to the construction of the trial functionals. Illustrative examples can be found in the author's previous publications.

3. Semi-inverse method and variational principles

We will apply the semi-inverse method (He [12, 1997]) to search for a variational principle for the problem discussed above. The basic idea of the semi-inverse method is to construct a trial functional with an unknown function.

If we want to establish a generalized variational principle with 4 independent variables (u , v , Ω and Π), we can construct a trialfunctional in the form

$$J(u, v, \Omega, \Pi) = \iint \left\{ \frac{1}{u} \frac{\partial \Omega}{\partial \xi} - \frac{v}{u} \frac{\partial \Omega}{\partial \psi} + F \right\} d\xi d\psi, \quad (3.1)$$

where F is the unknown function to be determined. We call the functional

$$L(u, v, \Omega, \Pi) = \frac{1}{u} \frac{\partial \Omega}{\partial \xi} - \frac{v}{u} \frac{\partial \Omega}{\partial \psi} + F \quad (3.2)$$

trial-Lagrangian.

The advantage of the above trial functional is that the Euler equation with respect to Ω is equation (1.7). Now calculating the variation of equation (3.1) with respect to u , we obtain the following trial-Euler equation

$$\delta u : \quad -\frac{1}{u^2} \frac{\partial \Omega}{\partial \xi} + \frac{v}{u^2} \frac{\partial \Omega}{\partial \psi} + \frac{\partial F}{\partial u} = 0. \quad (3.3)$$

In a view of equations (1.10), we have

$$\frac{\partial F}{\partial u} = \frac{1}{u^2} \frac{\partial \Omega}{\partial \xi} - \frac{v}{u^2} \frac{\partial \Omega}{\partial \psi} = \frac{1}{u^2} (\Pi + v^2). \quad (3.4)$$

From equation (3.4), the unknown F can be identified as follows

$$F = -\frac{1}{u} (\Pi + v^2) + F_1, \quad (3.5)$$

where F_1 is a newly introduced unknown function, which should be free of the variables u and Ω . Inserting equation (3.5) into equation (3.2), we obtain a renewed trial-Lagrangian, which reads

$$L(u, v, \Omega, \Pi) = \frac{1}{u} \frac{\partial \Omega}{\partial \xi} - \frac{v}{u} \frac{\partial \Omega}{\partial \psi} - \frac{1}{u} (\Pi + v^2) + F_1. \quad (3.6)$$

Now the trial-Euler equations for δv and $\delta \Pi$ can be easily obtained

$$\delta v : \quad -\frac{1}{u} \frac{\partial \Omega}{\partial \psi} - \frac{2v}{u} + \frac{\partial F_1}{\partial v} = 0, \quad (3.7)$$

$$\delta \Pi : \quad -\frac{1}{u} + \frac{\partial F_1}{\partial \Pi} = 0. \quad (3.8)$$

By means of the field equations (1.10) and (1.9), we have

$$\frac{\partial F_1}{\partial v} = \frac{1}{u} \frac{\partial \Omega}{\partial \psi} + \frac{2v}{u} = \frac{v}{u} = \frac{v}{\sqrt{2B - v^2 - \Pi}}, \quad (3.9)$$

$$\frac{\partial F_1}{\partial \Pi} = \frac{1}{u} = \frac{1}{\sqrt{2B - v^2 - \Pi}}. \quad (3.10)$$

From the above relations (3.9) and (3.10), we can immediately identify the unknown F_1 , which reads

$$F_1 = -\sqrt{2B - v^2 - \Pi}. \quad (3.11)$$

Finally we obtain the following Lagrangian

$$L(u, v, \Omega, \Pi) = \frac{1}{u} \frac{\partial \Omega}{\partial \xi} - \frac{v}{u} \frac{\partial \Omega}{\partial \psi} - \frac{1}{u} (\Pi + v^2) - \sqrt{2B - v^2 - \Pi}. \quad (3.12)$$

Liu (1995) obtained a similar Lagrangian, which reads

$$L_{Liu}(u, v, \Omega, \Pi) = \frac{1}{u} \frac{\partial \Omega}{\partial \xi} - \frac{v}{u} \frac{\partial \Omega}{\partial \psi} - \frac{u}{2} - \frac{v [2(B - \Pi) - u^2 + v^2]}{u \sqrt{2(B - \Pi) - u^2}}. \quad (3.13)$$

Supplementing the Lagrangian (3.12) or (3.13) by the field equation (1.9) as a side condition, we obtain a constrained functional

$$\tilde{J}_{Liu1}(\Omega, v, \Pi) = \iint \frac{1}{\sqrt{2(B - \Pi) - v^2}} \left\{ v \frac{\partial \Omega}{\partial \Psi} - \frac{\partial \Omega}{\partial \xi} + 2B - \Pi \right\} dA \quad (3.14)$$

and

$$\tilde{J}_{Liu2}(\Omega, u, v) = \iint \left\{ \frac{v}{u} \frac{\partial \Omega}{\partial \Psi} - \frac{1}{u} \frac{\partial \Omega}{\partial \xi} + \frac{u^2 + v^2}{u} + \frac{B}{u} \right\} dA. \quad (3.15)$$

The above two functionals are under the constrain of equation (1.9). Liu obtained functionals (1.11) and (1.12), respectively, from the above functional (3.14) and (3.15)

by eliminating the constraint of equation (1.9) through the so-called Liu's systematic method, which leads to incorrect results hereby. Our approach seems to be much more straightforward and reliable. We can also readily obtain a variational principle with three independent variables. For example, if we want to establish a sub-generalized variational principle with 3 independent variables (u, v , and Ω), a trial-Lagrangian can be constructed as follows

$$L_1(u, v, \Omega) = \frac{1}{u} \frac{\partial \Omega}{\partial \xi} - \frac{v}{u} \frac{\partial \Omega}{\partial \psi} + F, \quad (3.16)$$

which is assumed to be under the constraint of equation (1.9).

The trial-Lagrangian (3.16) is similar to equation (3.2). The difference is that the variable Π in equation (3.2) is an independent variable, while it is not involved in equation (3.16). The variation of Π depends upon equation (1.9), i.e.,

$$\delta \Pi = -u \delta u - v \delta v.$$

The stationary conditions can be readily obtained:

$$\delta u : \quad -\frac{1}{u^2} \frac{\partial \Omega}{\partial \xi} + \frac{v}{u^2} \frac{\partial \Omega}{\partial \psi} + \frac{\partial F}{\partial u} = 0, \quad (3.17)$$

$$\delta v : \quad \frac{1}{u} \frac{\partial \Omega}{\partial \psi} + \frac{\partial F}{\partial v} = 0. \quad (3.18)$$

In view of the field equations, we have

$$\frac{\partial F}{\partial u} = \frac{1}{u^2} \frac{\partial \Omega}{\partial \xi} - \frac{v}{u^2} \frac{\partial \Omega}{\partial \psi} = \frac{1}{u^2} (\Pi + v^2) = \frac{1}{u^2} (B - \frac{1}{2}u^2 + \frac{1}{2}v^2), \quad (3.19)$$

$$\frac{\partial F}{\partial v} = -\frac{v}{u}. \quad (3.20)$$

Hence the unknown function F can be identified as follows

$$F = -\frac{B}{u} - \frac{1}{2}u - \frac{v^2}{2u}. \quad (3.21)$$

Substituting equation (3.21) into equation (3.16), we obtain the following Lagrangian:

$$L_1(u, v, \Omega) = \frac{1}{u} \frac{\partial \Omega}{\partial \xi} - \frac{v}{u} \frac{\partial \Omega}{\partial \psi} - \frac{B}{u} - \frac{1}{2}u - \frac{v^2}{2u} = \frac{1}{u} \left[\frac{\partial \Omega}{\partial \xi} - v \frac{\partial \Omega}{\partial \psi} - B - \frac{1}{2}(u^2 + v^2) \right]. \quad (3.22)$$

Constraining the Lagrangian (3.22) by equations (1.10), we obtain

$$L_2(\Omega) = u = \sqrt{2(B - \frac{\partial \Omega}{\partial \xi}) - (\frac{\partial \Omega}{\partial \psi})^2}, \quad (3.23)$$

which is valid under the constraints formed by equations (1.10) and (1.9).

4. Lagrange multiplier method and variational crises

Liu tried his best to remove the constraint of the functionals (3.14) and (3.15) by Liu's systematic method, but in vain. In this section we discuss the Lagrange multiplier and its crises [19, 1, 21, 22, 23].

Now eliminating the constraints of equations (1.10) in equation (3.23), we obtain

$$\tilde{L}_2(\Omega, u, v, \lambda_1, \lambda_2) = u + \lambda_1 \left(\frac{\partial \Omega}{\partial \xi} - \Pi \right) + \lambda_2 \left(\frac{\partial \Omega}{\partial \psi} + v \right), \quad (4.1)$$

where λ_1 and λ_2 are multipliers to be further determined, and the variation of Π depends upon equation (1.9), i.e., it follows that

$$\delta \Pi = -u \delta u - v \delta v.$$

According to the Lagrange multiplier method, the multipliers are considered as independent variables. Thus we obtain the following Euler equations:

$$\delta \lambda_1 : \quad \frac{\partial \Omega}{\partial \xi} = \Pi, \quad (4.2)$$

$$\delta \lambda_2 : \quad \frac{\partial \Omega}{\partial \psi} = -v \quad (4.3)$$

$$\delta \Omega : \quad -\frac{\partial \lambda_1}{\partial \xi} - \frac{\partial \lambda_2}{\partial \psi} = 0, \quad (4.4)$$

$$\delta u : \quad 1 + \lambda_1 u = 0, \quad (4.5)$$

$$\delta v : \quad \lambda_1 v + \lambda_2 = 0. \quad (4.6)$$

Consequently, the multipliers can be determined as

$$\lambda_1 = -\frac{1}{u}, \quad \lambda_2 = \frac{v}{u}. \quad (4.7)$$

Substituting the identified Lagrange multipliers into equation (4.1) results in

$$\tilde{L}_2(\Omega, u, v) = u - \frac{1}{u} \left(\frac{\partial \Omega}{\partial \xi} - \Pi \right) + \frac{v}{u} \left(\frac{\partial \Omega}{\partial \psi} + v \right), \quad (4.8)$$

which is under the constraint of equation (1.9). Further eliminating the constraint (1.9), we obtain

$$\tilde{\tilde{L}}_2(\Omega, u, v, \Pi, \lambda_3) = u - \frac{1}{u} \left(\frac{\partial \Omega}{\partial \xi} - \Pi \right) + \frac{v}{u} \left(\frac{\partial \Omega}{\partial \psi} + v \right) + \lambda_3 \left[\Pi + \frac{1}{2}(u^2 + v^2) - B \right]. \quad (4.9)$$

Calculating variation with respect to Π , we can easily identify the multiplier, which reads

$$\lambda_3 = -1/u. \quad (4.10)$$

Thus we have

$$\tilde{\tilde{\tilde{L}}}_2(\Omega, u, v, \Pi) = u - \frac{1}{u} \left[\frac{\partial \Omega}{\partial \xi} - B + \frac{1}{2}(u^2 + v^2) \right] + \frac{v}{u} \left(\frac{\partial \Omega}{\partial \psi} + v \right). \quad (4.11)$$

According to the Lagrange multiplier method, the above Lagrangian contains four independent variables (Ω, u, v, Π). But by a careful inspection, we find the constraint, equation (1.9), is still kept as a non-variational constraint. So the Lagrange multiplier method is not valid in this case, and it is called by He the second variational crisis [21, 22, 23].

Now we apply the Lagrange multiplier method to eliminate the constraint (1.9) of equation (3.22):

$$\begin{aligned} \tilde{L}_1(u, v, \Omega, \Pi, \lambda_3) = \\ \frac{1}{u} \left[\frac{\partial \Omega}{\partial \xi} - v \frac{\partial \Omega}{\partial \psi} - B - \frac{1}{2}(u^2 + v^2) \right] + \lambda_3 \left[\Pi + \frac{1}{2}(u^2 + v^2) - B \right]. \end{aligned} \quad (4.12)$$

The stationary condition with respect to Π is

$$\lambda_3 = 0. \quad (4.13)$$

Consequently the constraint cannot be eliminated by the multiplier either. This phenomenon is called the first variational crisis [19]. The same phenomenon will appear if we use a multiplier to eliminate the constraint of equation (1.9) or of the functionals (3.22) and (3.23).

As it was pointed out by He [12, 21, 16] the Lagrange multiplier can finally be expressed in the form

$$\lambda = \lambda(u, v, \Omega, \Phi). \quad (4.14)$$

Thus we can introduce an unknown function F :

$$F = \lambda(u^2 + v^2 + 2\Pi - 2B). \quad (4.15)$$

The augmented functional (4.12), therefore, can be rewritten in the form

$$\begin{aligned} J_{He1}(\Omega, v, \Pi, u) = \iint \frac{1}{\sqrt{2(B - \Pi) - v^2}} \left\{ v \frac{\partial \Omega}{\partial \Psi} - \frac{\partial \Omega}{\partial \xi} + 2B - \Pi \right\} dA + \\ \iint F(u, v, \Phi, \Pi) dA, \end{aligned} \quad (4.16)$$

where F is the function of the variables u, v, Φ , and Π .

To eliminate the constraint of the functional (3.22), a similar augmented functional can be constructed as follows

$$J_{He2}(\Omega, u, v, \Pi) = \iint \left\{ \frac{v}{u} \frac{\partial \Omega}{\partial \Psi} - \frac{1}{u} \frac{\partial \Omega}{\partial \xi} + \frac{u^2 + v^2}{u} + \frac{B}{u} \right\} dA + \iint F(u, v, \Phi, \Pi) dA. \quad (4.17)$$

The unknown F can be identified by the same procedure as illustrated before. The Euler equations of the functional (4.17) are

$$-\frac{\partial}{\partial \Psi} \left(\frac{v}{u} \right) + \frac{\partial}{\partial \xi} \left(\frac{1}{u} \right) + \frac{\delta F}{\delta \Omega} = 0, \quad (4.18)$$

$$-\frac{v}{u^2} \frac{\partial \Omega}{\partial \Psi} + \frac{1}{u^2} \frac{\partial \Omega}{\partial \xi} + \frac{u^2 - v^2 - 2B}{2u^2} + \frac{\delta F}{\delta u} = 0, \quad (4.19)$$

$$\frac{1}{u} \frac{\partial \Omega}{\partial \Psi} + \frac{v}{u} + \frac{\delta F}{\delta v} = 0, \quad (4.20)$$

$$\frac{\delta F}{\delta \Pi} = 0. \quad (4.21)$$

We search an F such that the above 4 equations turn out to be the 4 field equations, i.e., equations (1.7), (1.9) and (1.10). To this end, we set

$$\frac{\delta F}{\delta \Pi} = aH^n = a \left[\frac{1}{2}(u^2 + v^2) + \Pi - B(\Psi) \right]^n, \quad (4.22)$$

where a is a nonzero constant, and $n > 0$. So the unknown F can be identified as

$$F = \frac{a}{n+1} \left[\frac{1}{2}(u^2 + v^2) + \Pi - B(\Psi) \right]^{n+1} + F_1(u, v, \Phi), \quad (4.23)$$

where F_1 is an unknown function of u, v , and Φ . Substituting F into (4.18)–(4.20) we search for an F_1 that the left equations (4.18)–(4.20) satisfy the left field equations (1.7) and (1.10). It is clear that $F_1 = 0$. Therefore we obtain the following generalized variational principle:

$$J_{HE2}(\Omega, u, v, \Pi) = \iint \left\{ \frac{v}{u} \frac{\partial \Omega}{\partial \Psi} - \frac{1}{u} \frac{\partial \Omega}{\partial \xi} + \frac{u^2 + v^2}{u} + \frac{B}{u} + \frac{a}{n+1} \left[\frac{1}{2}(u^2 + v^2) + \Pi - B(\Psi) \right]^{n+1} \right\} dA. \quad (4.24)$$

Similarly the unknown F in (4.16) can be easily determined, and the following functional is arrived at:

$$J_{HE1}(\Omega, v, \Pi, u) = \iint \left\{ \frac{1}{\sqrt{2(B - \Pi) - v^2}} \left[v \frac{\partial \Omega}{\partial \Psi} - \frac{\partial \Omega}{\partial \xi} + 2B - \Pi \right] + \frac{a}{n+1} \left[\frac{1}{2}(u^2 + v^2) + \Pi - B(\Psi) \right]^{n+1} \right\} dA. \quad (a \neq 0, n > 1) \quad (4.25)$$

In view of equation (1.3), functional (4.17) can be re-written in the form

$$J_{HE3}(\Omega, v, \Pi, u) = \iint \left\{ \frac{1}{u} \left(v \frac{\partial \Omega}{\partial \Psi} - \frac{\partial \Omega}{\partial \xi} + 2B - \Pi \right) + F \right\} dA. \quad (4.26)$$

The corresponding Euler equations are of the form

$$-\frac{\partial}{\partial \Psi} \left(\frac{v}{u} \right) + \frac{\partial}{\partial \xi} \left(\frac{1}{u} \right) + \frac{\delta F}{\delta \Omega} = 0, \quad (4.27)$$

$$-\frac{1}{u^2} \left(v \frac{\partial \Omega}{\partial \Psi} - \frac{\partial \Omega}{\partial \xi} + 2B - \Pi \right) + \frac{\delta F}{\delta u} = 0, \quad (4.28)$$

$$\frac{1}{u} \frac{\partial \Omega}{\partial \Psi} + \frac{\delta F}{\delta v} = 0, \quad (4.29)$$

$$-\frac{1}{u} + \frac{\delta F}{\delta \Pi} = 0. \quad (4.30)$$

Since the above equations should satisfy the field equations, we set

$$\frac{\delta F}{\delta \Omega} = \frac{\partial}{\partial \Psi} \left(\frac{v}{u} \right) - \frac{\partial}{\partial \xi} \left(\frac{1}{u} \right) = 0, \quad (4.31)$$

$$\frac{\delta F}{\delta u} = \frac{1}{u^2} \left(v \frac{\partial \Omega}{\partial \Psi} - \frac{\partial \Omega}{\partial \xi} + 2B - \Pi \right) = \frac{1}{u^2} (-v^2 + 2B - 2\Pi) = 1, \quad (4.32)$$

$$\frac{\delta F}{\delta v} = -\frac{1}{u} \frac{\partial \Omega}{\partial \Psi} = \frac{v}{u} = \frac{v}{\sqrt{2(B - \Pi) - v^2}}, \quad (4.33)$$

$$\frac{\delta F}{\delta \Pi} = \frac{1}{u} = \frac{1}{\sqrt{2(B - \Pi) - v^2}}. \quad (4.34)$$

From the above relations, we have

$$F = u - \frac{1}{2} \sqrt{2(B - \Pi) - v^2}. \quad (4.35)$$

We obtain another variational principle in the form:

$$J_{HE3}(\Omega, v, \Pi, u) = \iint \left\{ \frac{1}{u} \left(v \frac{\partial \Omega}{\partial \Psi} - \frac{\partial \Omega}{\partial \xi} + 2B - \Pi \right) + u - \frac{1}{2} \sqrt{2(B - \Pi) - v^2} \right\} dA. \quad (4.36)$$

5. A modified Lagrange multiplier method

In the procedure of variation, the multipliers are also considered to be independent variables. The present modification (He [21, 8]) considers the multipliers to be dependent functions. The problem of the independent Lagrange multipliers as well as the validity of the method are discussed in the paper [8] by He.

To overcome the problem the multipliers should be considered to be dependent functions during the identification of the multipliers.

Now re-consider equation (4.9), where λ_3 is not an independent variable. Thus the Euler equations can be expressed as follows

$$1 + \frac{1}{u^2} \left[\frac{\partial \Omega}{\partial \xi} - \Pi \right] - \frac{v}{u^2} \left(\frac{\partial \Omega}{\partial \psi} + v \right) + \frac{\partial \lambda_3}{\partial u} \left[\Pi + \frac{1}{2}(u^2 + v^2) - B \right] + \lambda_3 u = 0, \quad (5.1)$$

$$\frac{1}{u} \left(\frac{\partial \Omega}{\partial \psi} + v \right) + \frac{v}{u} + \frac{\partial \lambda_3}{\partial v} \left[\Pi + \frac{1}{2}(u^2 + v^2) - B \right] + \lambda_3 v = 0, \quad (5.2)$$

$$\frac{\partial}{\partial \xi} \left(\frac{1}{u} \right) - \frac{\partial \Omega}{\partial \psi} \left(\frac{v}{u} \right) + \frac{\partial \lambda_3}{\partial \Omega} \left[\Pi + \frac{1}{2}(u^2 + v^2) - B \right] = 0, \quad (5.3)$$

$$\frac{1}{u} + \frac{\partial \lambda_3}{\partial \Pi} \left[\Pi + \frac{1}{2}(u^2 + v^2) - B \right] + \lambda_3 = 0. \quad (5.4)$$

It is obvious that equation (5.4) vanishes completely if the multiplier is identified as $\lambda_3 = -1/u$ (See equation (4.10)). In order to recover equation (1.9) from equation (5.4), we can identify the multiplier in the following form

$$\lambda_3 = -\frac{1}{u} + C \left[\Pi + \frac{1}{2}(u^2 + v^2) - B \right]. \quad (5.5)$$

where C is a nonzero constant. In this way we obtain the following modified Lagrangian

$$\begin{aligned} \tilde{L}_2(\Omega, u, v, \Pi) = u - \frac{1}{u} \left(\frac{\partial \Omega}{\partial \xi} - \Pi \right) + \frac{v}{u} \left(\frac{\partial \Omega}{\partial \psi} + v \right) - \frac{1}{u} \left[\Pi + \frac{1}{2}(u^2 + v^2) - B \right] + \\ + C \left[\Pi + \frac{1}{2}(u^2 + v^2) - B \right]^2. \end{aligned} \quad (5.6)$$

The multiplier in equations (4.12) and (4.13) can be identified in a similar way. The variational crisis can also be eliminated by the semi-inverse method, for example, we can re-write equation (4.9) in the form

$$\tilde{\tilde{L}}_2(\Omega, u, v, \Pi) = u - \frac{1}{u} \left(\frac{\partial \Omega}{\partial \xi} - \Pi \right) + \frac{v}{u} \left(\frac{\partial \Omega}{\partial \psi} + v \right) + F. \quad (5.7)$$

where F is an unknown function to be determined.

6. Conclusion

We illustrate the effectiveness and convenience of the semi-inverse method in searching for variational principles for a physical problem, and also point out a difficulty in Liu's theory which leads to incorrect results. A modified Lagrange multiplier method is suggested, i.e., the multipliers cannot be considered to be independent variables during the procedure of their identification.

References

1. LIU, G.L.: *On variational crisis and generalized variational principles for inverse and hybrid problems of free surface flow*, The sixth Asian Congress of Fluid Mechanics, May 22-26, 1995, Singapore, 745-748.
2. HE, J.H.: A variational theory for 1-D unsteady compressible flow An imagine plane approach. *Applied Mathematical Modelling*, **22**(6), (1998), 395-403.
3. LUKE, J.C.: A variational principle for a fluid with a free surface. *J. Fluid Mech.*, **27**(2), (1967), 395-397.
4. MEYLAN, H.M.: A variational equation for the wave forcing of floating thin plates. *Applied Ocean Research*, **23**, (2001), 195-206.
5. LIU, G.L.: *Generalized variational principles in fluids and a simple approach to eliminating the variational crisis*, in Zhou, L. D. et al ed.: The 5th Chinese National Conference on Hydrodynamics, Haiyang Publishing, Beijing, 2001, 1-4.
6. LIU, G.L.: Derivation and transformation of variational principles with emphasis on inverse and hybrid problems in fluid mechanics: a systematic approach. *Acta Mechanica*, **140**, (2000), 73-89.
7. HE, J.H.: Comments on "Derivation and transformation of variational principles with emphasis on inverse and hybrid problems in fluid mechanics: a systematic approach", *Acta Mechanica*, **149**(1-4), (2001), 247-249.
8. HE, J.H.: A remark on the Lagrange multiplier method (I), *International Journal of Nonlinear Sciences and Numerical Simulation*, **2**(2), (2001), 161-164.

9. HE, J.H.: Validity of Liu's Systematic Method on Variational Principles, *Facta Universitatis, Series Mechanics, Automatic Control & Robotics*, **3**(12), (2002), 383-392.
10. LIU, G.L. and WANG, H. G.: A new pseudo-potential function for rotational turbo-flow: (I) Variational formulation and finite element solution for transonic blade-to-blade flow. *Int. J. Turbo & Jet-Engines*, **13**, (1996), 263-275.
11. HE, J.H.: A variational model for compressible rotational blade-to-blade flow using Liu-type potential function. *Int. J. Turbo & Jet-Engines*, **17**, (2000), 143-152.
12. HE, J.H.: Semi-inverse method of establishing generalized variational principles for fluid mechanics with emphasis on turbomachinery aerodynamics. *Int. J. Turbo & Jet-Engines*, **14**(1), (1997), 23-28.
13. ZIENKIEWICZ, O.C., and TAYLOR, R.L.: *The Finite Element Method*, 4th ed., Vol.1, McGraw-Hill, London, 1989.
14. LIU, G. L.: A new finite element with self-adapting built-in discontinuity for shock-capturing in transonic flow. *International Journal of Nonlinear Science and Numerical Simulation*, **1**(1), (2000), 25-30.
15. HE, J.H.: Treatment of shocks in transonic aerodynamics in meshless method. *Int. J. Turbo & Jet-Engines*, **16**(1), (1999), 19-26.
16. HE, J.H.: Generalized Hellinger-Reissner principle, *J. Appl. Mech.*, **67**, (2000), 326-331.
17. HE, J.H.: A classical variational model for micropolar elastodynamics, *International Journal of Nonlinear Sciences and Numerical Simulation*, **1**(2), (2000), 133-138
18. HE, J.H.: Coupled variational principles of piezoelectricity. *Int. J. Engineering Sciences*, **39**(3), (2001), 323-341.
19. CHIEN, W.Z.: Method of higher-order Lagrange multiplier and generalized variational principles of elasticity with more general forms. *Applied Math. Mech.*, **4**(2), (1983), 143-157.
20. HILDEBRAND, F.B.: *Methods of Applied Mathematics*, 2nd Ed., Englewood Cliffs, NJ, Prentice-Hill, 1965.
21. HE, J.H.: Modified Lagrange multiplier method and generalized variational principles in fluid mechanics. *Journal of the Shanghai University* (English edition), **1**(2), (1997), 117-122.
22. HE, J.H.: A Variational Crisis in Elasticity and its Removal. *Shanghai Journal of Mechanics*, **18**(4), (1997), 305-310. (in Chinese)
23. HE, J.H.: On a variational crises and a generalized variational principle in elasticity. *Journal of the University of Shanghai for Science & Technology*, **21**(2), (1999), 127-130. (in Chinese)

EFFECTS OF CHEMICAL REACTION, HEAT AND MASS TRANSFER ON NON-LINEAR LAMINAR BOUNDARY-LAYER FLOW OVER A WEDGE WITH SUCTION OR INJECTION

R. KANDASAMY

Department of Mathematics, Institute of Road and Transport Technology
Erode-638 316, India
kandan_kkk@yahoo.co.in

S. P. ANJALI DEVI

Bharathiar University
Coimbatore-641046, India.

[Received: February 22, 2003]

Abstract. An approximate numerical solution for the steady laminar boundary-layer flow over a wall of the wedge with suction or injection in the presence of species concentration and mass diffusion has been obtained by solving the governing equations using R.K. Gill method. The fluid is assumed to be a viscous and incompressible fluid. Numerical calculations up to third level of truncation are carried out for different values of dimensionless parameters and an analysis of the results obtained shows that the flow field is influenced appreciably by the chemical reaction (consumption and generation reactant) and suction or injection at the wall of the wedge.

Keywords: chemical reaction (consumption and generation reactant), suction or injection at the wall of the wedge, Boussinesq's approximation, steady laminar boundary-layer flow and mass diffusive

1. Introduction

Combined heat and mass transfer problems with chemical reaction are of importance in many processes and have, therefore, received a considerable amount of attention in recent years. In processes such as drying, evaporation at the surface of a water body, energy transfer in a wet cooling tower and the flow in a desert cooler, heat and mass transfer occur simultaneously. Natural convection processes involving the combined mechanisms are also encountered in many natural processes, such as evaporation, condensation and agricultural drying, and in many industrial applications, such as the curing of plastics, cleaning and chemical processing of materials relevant to the manufacture of printed circuitry, manufacture of pulp-insulated cables, etc.

Many practical diffusive operations involve the molecular diffusion of a species in the presence of chemical reaction within or at the boundary. There are two types of reactions. A homogeneous reaction is one that occurs uniformly throughout a given phase. The species generation in a homogeneous reaction is analogous to internal source of heat generation. In contrast, a heterogeneous reaction takes place in a restricted region or within the boundary of a phase. It can therefore be treated as a boundary condition similar to the constant heat flux condition in heat transfer. The study of heat and mass transfer with chemical reaction is of great practical importance to engineers and scientists because of its almost universal occurrence in many branches of science and engineering. The flow of a fluid past a wedge is of fundamental importance since this type of flow constitutes a general and wide class of flows in which the free stream velocity is proportional to a power of the length coordinate measured from the stagnation point.

All industrial chemical processes are designed to transform cheaper raw materials to high value products (usually via chemical reaction). A 'reactor', in which such chemical transformations take place, has to carry out several functions like bringing reactants into intimate contact, providing an appropriate environment (temperature and concentration fields) for adequate time and allowing for removal of products. Fluid dynamics plays a pivotal role in establishing relationship between reactor hardware and reactor performance. For a specific chemistry catalyst, the reactor performance is a complex function of the underlying transport processes. The first step in any reaction engineering analysis is formulating a mathematical framework to describe the rate (and mechanisms) by which one chemical species is converted into another in the absence of any transport limitations (chemical kinetics). Once the intrinsic kinetics is available, the production rate and composition of the products can be related, in principle, to reactor volume, reactor configuration and mode of operation by solving mass, momentum and energy balances over the reactor. This is the central task of a reaction and reactor engineering activity. Analysis of the transport processes and their interaction with chemical reactions can be quite difficult and is intimately connected to the underlying fluid dynamics. Such a combined analysis of chemical and physical processes constitutes the core of chemical reaction engineering. Recent advances in understanding the physics of flows and computational flow modelling (CFM) can make tremendous contributions in chemical engineering.

In these types of problems, the well-known Falkner-Skan transformation is used to reduce boundary-layer equations into ordinary differential equations for similar flows [1]. It can also be used for non-similar flows for convenience in numerical work because it reduces, even if it does not eliminate, dependence on the x -coordinate. The solutions of the Falkner-Skan equations are sometimes referred to as wedge flow solutions with only two of the wedge flows being common in practice [2]. The dimensionless parameter, m plays an important role in such type of problems because it denotes the shape factor of the velocity profiles. It has been shown [3] that when $m < 0$ (increasing pressure), the velocity profiles have a point of inflexion whereas when $m > 0$ (decreasing pressure), there is no point of inflexion. This fact is of great importance in the analysis of the stability of laminar flows with a pressure gradient. Yih [4]

presented an analysis of the forced convection boundary-layer flow over a wedge with uniform suction and blowing, whereas Watanabe [5] investigated the behavior of the boundary-layer over a wedge with suction and injection in forced flow. Recently, laminar boundary layer flow over a wedge with suction/injection has been discussed by Kafoussias and Nanousis [6] and Anjali Devi and Kandasamy [7] analyzed the effects of thermal stratification on laminar boundary layer flow over a wedge with suction and injection.

Since no attempt has been made to analyze non-linear boundary-layer flow with chemical reaction, heat and mass transfer over a wedge with suction or injection at the wall in the presence of a uniform transverse magnetic field, we have investigated it in this article. The similarity transformation has been utilized to convert the governing partial differential equations into ordinary differential equations and then the numerical solution of the problem is drawn using R.K.Gill method. Numerical calculations up to third level of truncation were carried out for different values of dimensionless parameters of the problem under consideration for the purpose of illustrating the results graphically. Examination of such flow models reveal the influence of chemical reaction on velocity, temperature and concentration profiles. The analysis of the results obtained shows that the flow field is influenced appreciably by the presence of chemical reaction (generation and consumption reactant) and suction or injection at the wall of the wedge.

2. Mathematical analysis

Two-dimensional laminar boundary-layer flow of a viscous and Boussinesq fluid over a wall of the wedge with suction or injection is analysed. As shown in Figure 1, the x-axis is parallel to the wedge and the y-axis is taken normal to it. The fluid properties are assumed to be constant in a limited temperature range. The concentration of diffusing species is very small in comparison to other chemical species, the concentration of

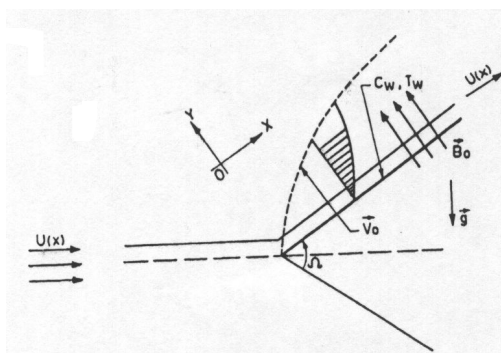


Figure 1. Flow analysis along the wall of the wedge

species far from the wall, $C_\alpha = 0$ is infinitesimally very small [8] and hence the Soret and Dufour effects are neglected. The chemical reactions take place in the flow and

the physical properties μ , D , ρ and the rate of chemical reaction, k_1 are constant throughout the fluid. Under these conditions, the governing boundary layer equations of momentum, energy and diffusion for free convection flow under Boussinesq's approximation are:

$$\frac{\partial u}{\partial x} + \frac{\partial v}{\partial y} = 0, \quad (1)$$

$$u \frac{\partial u}{\partial x} + v \frac{\partial v}{\partial y} = \nu \frac{\partial^2 u}{\partial x^2} + U \frac{\partial U}{\partial X} + g\beta(T - T_\infty) \sin \frac{\Omega}{2} + g\beta^*(C - C_\infty) \sin \frac{\Omega}{2}, \quad (2)$$

$$u \frac{\partial T}{\partial x} + v \frac{\partial T}{\partial y} = \alpha \frac{\partial^2 T}{\partial y^2}, \quad (3)$$

$$u \frac{\partial C}{\partial x} + v \frac{\partial C}{\partial y} = D \frac{\partial^2 C}{\partial y^2} - k_1 C. \quad (4)$$

The boundary conditions are

$$\begin{aligned} u = 0, \quad v = v_o, \quad C = C_w, \quad T = T_w & \quad \text{at } y = 0 \\ u = U(x), \quad C = C_\alpha, \quad T = T_\alpha, & \quad \text{at } y > \alpha \text{ by } y \rightarrow \alpha. \end{aligned} \quad (5)$$

As in [6], we introduce the following change of variables

$$\Psi(x, y) = \left(\frac{2U\nu x}{1+m} \right)^{1/2} f(x, \eta), \quad (6)$$

$$\eta(x, y) = y \left[\frac{(1+m)U}{2\nu x} \right]^{1/2}. \quad (7)$$

Under this consideration, the potential flow velocity can be written [6] as

$$U(x) = cx^m, \quad \beta_1 = \frac{2m}{1+m}, \quad (8)$$

where c is a constant and β_1 is the Hartree pressure gradient parameter that corresponds to $\beta_1 = \Omega/\Pi$ for a total angle Ω of the wedge.

The velocity components are given by

$$u = \frac{\partial \Psi}{\partial y}, \quad v = -\frac{\partial \Psi}{\partial x} \quad (9)$$

It can be easily verified that the continuity equation (1) is identically satisfied. If we introduce the non-dimensional form of temperature and the concentration as

$$\theta = \frac{T - T_\alpha}{T_w - T_\alpha}, \quad (10)$$

$$\phi = \frac{C - C_\alpha}{C_w - C_\alpha}, \quad (11)$$

$$Re_x = \frac{x}{\nu} \quad (\text{Reynolds number}), \quad (12)$$

$$Gr = \nu g \beta \frac{T_w - T_\alpha}{U^3} \quad (\text{Grashof number}), \quad (13)$$

$$G_c = \nu g \beta^* \frac{C_w - C_\alpha}{U^3} \quad (\text{Modified Grashof number}), \quad (14)$$

$$Pr = \mu \frac{c_p}{k} \quad (\text{Prandtl number}), \quad (15)$$

$$Sc = \frac{\nu}{D} \quad (\text{Schmidt number}), \quad (16)$$

$$S = -v_0 \left(\frac{(1+m)x}{2\nu U} \right)^{1/2} \quad (\text{suction or injection parameter}), \quad (17)$$

$$\gamma = \nu \frac{k_1}{U^2} \quad (\text{chemical reaction parameter}). \quad (18)$$

Now equations (2) to (4) become

$$\begin{aligned} \frac{\partial^3 f}{\partial \eta^3} + f \frac{\partial^2 f}{\partial \eta^2} + \frac{2m}{1+m} \left[1 - \left(\frac{\partial^2 f}{\partial \eta^2} \right)^2 \right] + \frac{2m}{1+m} (G_c Re_x \phi + G_r Re_x \theta) \sin(\Omega/2) = \\ = \frac{2x}{1+m} \left(\frac{\partial f}{\partial \eta} \frac{\partial^2 f}{\partial x \partial \eta} - \frac{\partial f}{\partial x} \frac{\partial^2 f}{\partial \eta^2} \right), \quad (19) \end{aligned}$$

$$\frac{\partial^2 \theta}{\partial \eta^2} + Pr f \frac{\partial \theta}{\partial \eta} = \frac{2Pr}{1+m} \theta \frac{\partial f}{\partial \eta} + Pr \frac{2x}{1+m} \left(\frac{\partial f}{\partial \eta} \frac{\partial \theta}{\partial x} - \frac{\partial f}{\partial x} \frac{\partial \theta}{\partial \eta} \right), \quad (20)$$

$$\begin{aligned} \frac{\partial^2 \phi}{\partial \eta^2} + Sc f \frac{\partial \phi}{\partial \eta} - \frac{2Sc}{1+m} Re_x \gamma \phi = \frac{2Sc}{1+m} \phi \frac{\partial f}{\partial \eta} + \\ + 2x \frac{Sc}{1+m} \left(\frac{\partial f}{\partial \eta} \frac{\partial \phi}{\partial x} - \frac{\partial \phi}{\partial \eta} \frac{\partial f}{\partial x} \right). \quad (21) \end{aligned}$$

The boundary condition (5) can be written as

$$\begin{aligned} \eta = 0, \quad \frac{\partial f}{\partial \eta} = 0, \quad \frac{f}{2} \left(1 + \frac{x}{U} \frac{dU}{dx} \right) + x \frac{\partial f}{\partial \xi} = -v_0 \left(\frac{(1+m)x}{2\nu U} \right)^{1/2}, \quad \theta = 1, \quad \phi = 1 \\ \eta > \alpha, \quad \frac{\partial f}{\partial \eta} = 1, \quad \theta = 0, \quad \phi = 0. \quad (22) \end{aligned}$$

Equations (19) to (21) and the boundary condition (22) can be written as

$$\begin{aligned} \frac{\partial^3 f}{\partial \eta^3} + \left(f + \frac{1-m}{1+m} \xi \frac{\partial f}{\partial \xi} \right) \frac{\partial^2 f}{\partial \eta^2} - \frac{1-m}{1+m} \xi \frac{\partial^2 f}{\partial \xi \partial \eta} + \\ + \frac{2m}{1+m} \left(1 - \frac{\partial^2 f}{\partial \eta^2} \right) + \frac{2}{1+m} (G_c Re_x \phi + G_r Re_x \theta) \sin(\Omega/2) = 0, \quad (23) \end{aligned}$$

$$\frac{\partial^2 \theta}{\partial \eta^2} + Pr \left(f + \frac{1-m}{1+m} \xi \frac{\partial f}{\partial \xi} \right) \frac{\partial \theta}{\partial \eta} - \left(\frac{2Pr}{1+m} \theta \frac{\partial f}{\partial \eta} - \frac{1-m}{1+m} \xi \frac{\partial \theta}{\partial \xi} \right) \frac{\partial f}{\partial \eta} = 0, \quad (24)$$

$$\frac{\partial^2 \phi}{\partial \eta^2} + S_c f \frac{\partial \phi}{\partial \eta} - \frac{2Sc}{1+m} R_{e_x} \gamma \Phi + S_c \frac{1-m}{1+m} \left(\frac{\partial \phi}{\partial \eta} \xi \frac{\partial f}{\partial \xi} - \frac{\partial f}{\partial \eta} \xi \frac{\partial \phi}{\partial \xi} \right) - \frac{2S_c}{1+m} \xi \frac{\partial f}{\partial \xi} = 0, \quad (25)$$

$$\frac{\partial f}{\partial \eta} = 0, \quad (1+m) \frac{f}{2} + \frac{1-m}{2} \xi \frac{\partial f}{\partial \xi} = S, \quad \theta = 1, \quad \phi = 1 \quad \text{at } \eta = 0$$

$$\frac{\partial f}{\partial \eta} = 1, \quad \theta = 0, \quad \phi = 0, \quad \text{at } y > \alpha \text{ by } y \rightarrow \alpha, \quad (26)$$

where S is the suction if $S > 0$ and injection if $S < 0$ and $\xi = kx^{(1-m)/2}$ is the dimensionless distance along the wedge ($\xi > 0$). In this system of equations $f(\xi, \eta)$ is the dimensionless stream function; $\theta(\xi, \eta)$ is the dimensionless temperature; $\Phi(\xi, \eta)$ is the dimensionless concentration; P_r is Prandtl number, R_{e_x} is Reynolds number etc. which are defined by equations (9) to (18). The parameter ξ indicates the dimensionless distance along the wedge ($\xi > 0$). It is obvious that to retain the x -derivative terms, it is necessary to employ a numerical scheme suitable for partial differential equations for the solution. In addition, owing to the coupling between adjacent stream-wise location through the ξ -derivatives, a locally autonomous solution, at any given stream-wise location cannot be obtained. In such a case, an implicit marching numerical solution scheme is usually applied proceeding the solution in the ξ -direction, i.e., calculating unknown profiles at ξ_{i+1} when the same profiles at ξ_i are known. The process starts at $\xi_i = 0$ and the solution proceeds from ξ_i to ξ_{i+1} but such a procedure is time-consuming. However, when the terms involving $\partial f / \partial \xi$, $\partial \theta / \partial \xi$ and $\partial \phi / \partial \xi$ and their η derivatives are deleted, the resulting system of equations resembles, in effect, a system of ordinary differential equations for the functions f , θ and ϕ with ξ as a parameter and the computational task is simplified. Furthermore a locally autonomous solution for any given ξ can be obtained because the stream-wise coupling is severed. So, following the lines of [6], a recent numerical solution scheme is utilized for obtaining the solution of the problem. Now, due to the above factors, equations (23) to (25) are changed to

$$f'''' + ff'' + \frac{2m}{1+m} [1 - (f')^2] + \frac{2}{1+m} (G_c R_{e_x} \phi + G_r R_{e_x} \theta) \sin(\Omega/2) = 0, \quad (27)$$

$$\theta'' + P_r f \theta' - \frac{2P_r}{1+m} f' \theta = 0, \quad (28)$$

$$\phi'' + S_c f \phi' - \frac{2S_c}{1+m} f' \phi - \frac{2S_c}{1+m} R_{e_x} \gamma \phi = 0 \quad (29)$$

with boundary conditions

$$f(0) = \frac{2}{1+m} S, \quad f'(0) = 0, \quad \theta(0) = 1, \quad \phi(0) = 1 \quad \text{at } \eta = 0$$

$$f'(\alpha) = 1, \quad \theta(\alpha) = 0, \quad \phi(\alpha) = 0, \quad \text{at } y > \alpha \text{ by } y \rightarrow \alpha. \quad (30)$$

Equations (27) to (29) with boundary conditions (30) are integrated using R.K Gill method. Chemical reaction, heat and mass transfer are studied for different values of suction/injection at the wall of the wedge and the strength of the applied magnetic field. In the following section, we discuss the results in detail.

3. Results and discussion

In order to get a clear insight of the physical problem, numerical results are displayed with the help of graphical illustrations.

In the absence of mass transfer and magnetic effects, the results have been compared with that of the previous work [6] and it is found that they are in good agreement. The numerical results obtained are illustrated by means of Figures 2–7.

Effects due to the suction or injection with uniform chemical reaction at the wall of the wedge over the velocity, temperature and concentration are shown through Figures 2, 3 and 4.

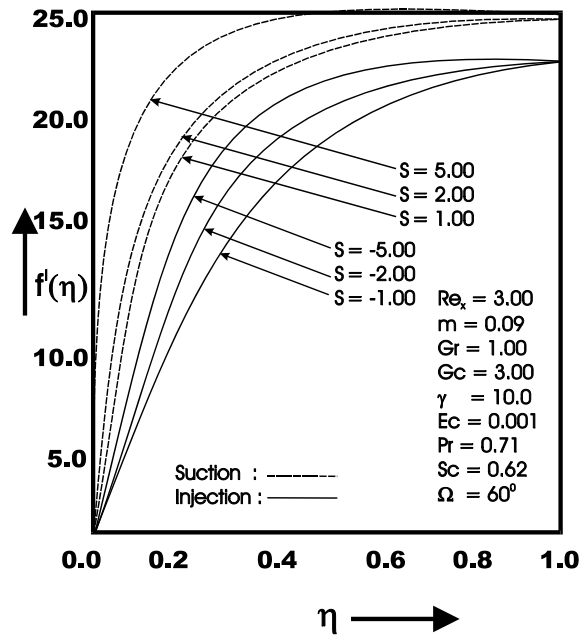


Figure 2. Velocity profiles for different values of suction/injection

Figure 2 depicts the dimensionless velocity profiles $f'(\eta)$ for different values of suction parameter ($S > 0$) and injection parameter ($S < 0$), respectively. It is observed that the velocity component of the fluid along the wall of the wedge increases with increase of suction and decreases with increase of injection at the wall of the wedge. On the contrary, the dimensionless temperature $\theta(\eta)$ and concentration $\phi(\eta)$ of the fluid reduce with increase of suction and increase with increase of injection and these are shown in Figures 3 and 4, respectively. So, the increase of suction accelerates the fluid motion and decreases the temperature distribution and concentration of the fluid along the wall of the wedge. On the other hand, the increase of injection decelerates the fluid motion and increases the temperature distribution and concentration of the

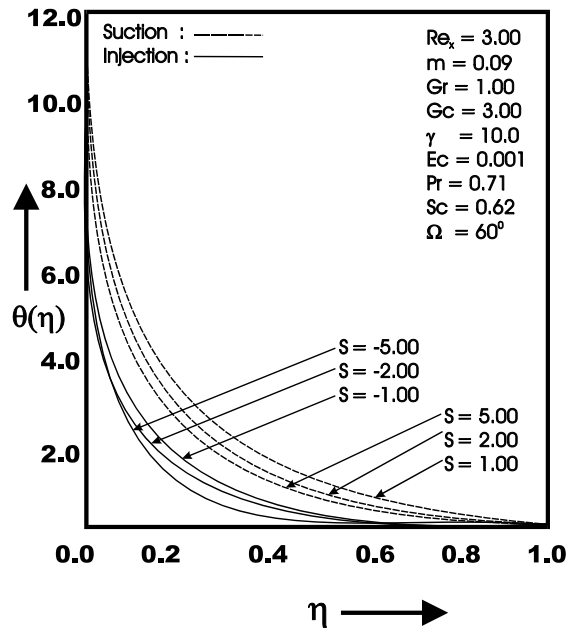


Figure 3. Temperature profiles for different values of suction/injection

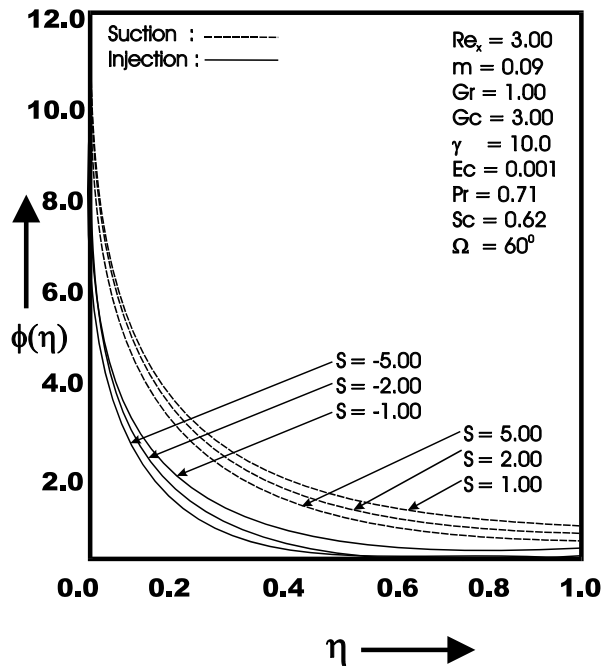


Figure 4. Concentration profiles for different values of suction/injection

fluid along the wall of the wedge. All this physical behavior is due to the combined effects of magnetic field, suction or injection and chemical reaction.

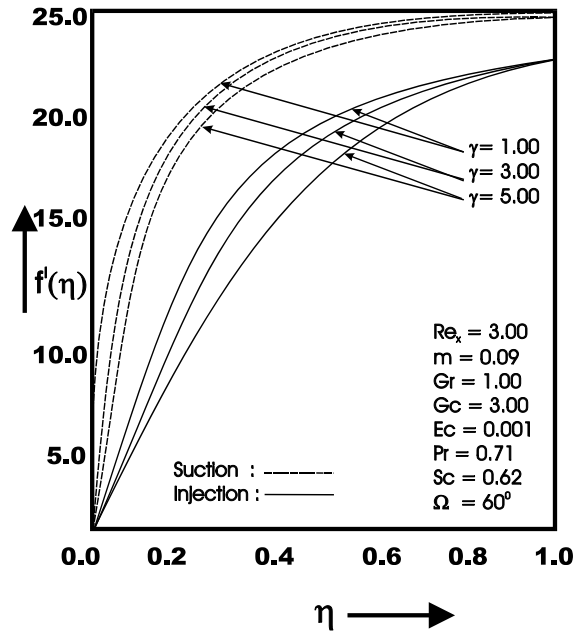


Figure 5. Influence of chemical reaction over the velocity profiles

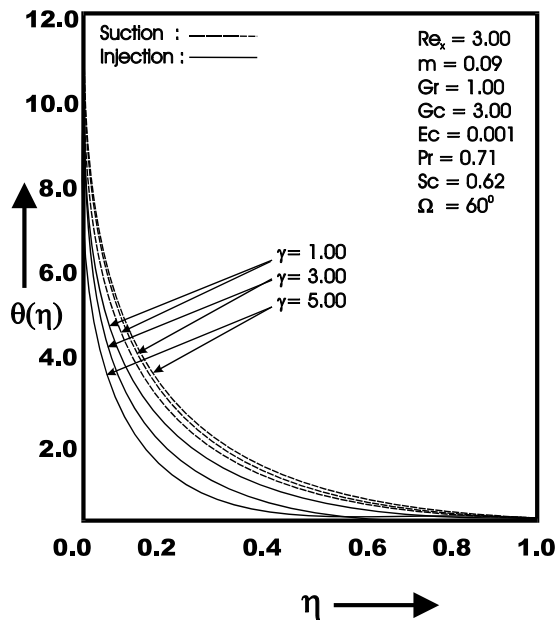


Figure 6. Effects of chemical reaction over the temperature profiles

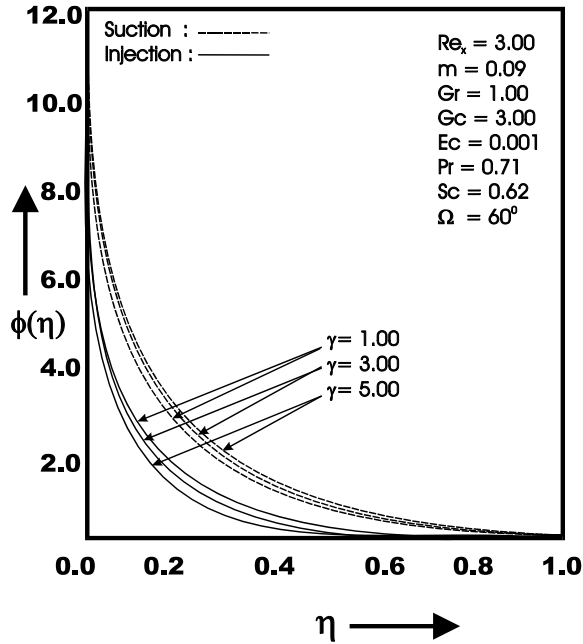


Figure 7. Effects of chemical reaction over the concentration profiles

The effects of chemical reaction over velocity, temperature and concentration of the fluid along the wall of the wedge are shown through Figures 5, 6 and 7.

4. Conclusion

We conclude the following from the above results and discussions:

- In the presence of uniform chemical reaction, the fluid flow along the wall of the wedge accelerates with increase of suction and decelerates with increase of injection. On the other hand, the temperature and concentration of the fluid reduce with increase of suction and increase with increase of injection of the fluid along the wall of the wedge. All these facts clearly depict the combined effects of chemical reaction and suction/injection.
- Due to the uniform magnetic field, in the case of suction, the increase of chemical reaction decelerates the fluid motion, temperature distribution and concentration of the fluid along the wall and for injection, it accelerates the fluid motion, temperature distribution and concentration of the fluid along the wall of the wedge, which affects the consumption reactions of the chemical reaction parameter.

Acknowledgement. One of the authors (R.K) wishes to thank Dr. R. Vadivel, Principal and Dr. K. Periyasamy, Assistant Professor of chemistry, IRTT, Erode, for their encouragement.

References

1. FALKNER, V.M. and SKAN, S.W.: *Some approximate solutions of the boundary equations*. Philos. Mag., **12**, (1931), 865–867.
2. CEBECI, T. and BRADSHAW, L.H.: *Physical and Computational Aspects of Convective Heat Transfer*, Springer-Verlag, New York, 1984.
3. SCHLICHTING, H.: *Boundary Layer Theory*, McGraw Hill Inc., 1979.
4. YIH, K. A.: *Uniform suction/blowing effects on forced convection about a wedge*. Acta Mech., **128**, (1998), 173–181.
5. WATANABE, T.: *Thermal boundary-layer over a wedge with uniform suction or injection in forced flow*. Acta Mech., **83**, (1990), 119–126..
6. KAFOUSSIAS, N. G. and NANOUSIS, N. D.: *Magnetohydrodynamic laminar boundary layer flow over a wedge with suction or injection*. Can. J. Phys., **75**, (1997), 733–745.
7. ANJALI DEVI, S. P. and KANDASAMY, R.: *Effects of thermal stratification on laminar boundary layer flow over a wedge with suction or injection*. Mechanics Research Communications, **28**, (2001), 349–354.
8. BYRON B. R., STEWART W. E. and LIGHTFOOT E. N.: *Transport Phenomena*, John Wiley and Sons, New York, 1992.

FINITE ELEMENT ANALYSIS OF STRUCTURES ON THE BASE OF HETEROGENEOUS MODELS

LÁSZLÓ ECSI AND PÁL ÉLESZTŐS

Faculty of Mechanical Engineering, Slovak University of Technology in Bratislava
Námestie slobody 17, 812 31 Bratislava 1, Slovak Republic

ladislav.ecsi@stuba.sk, pavel.elesztos@stuba.sk

[Received: October 13, 2003]

Abstract. In the paper a simple fracturing model is presented using the 2D discrete element method capable of simulating large-scale brittle fracturing. It uses the combined Mohr-Coulomb and Rankine material model and mode I fracturing in the Rankine corner based on the rotating crack model. In the interactions between the bodies, the Coulomb friction model is considered by using a contact interface element and utilizing the penalty method in its formulation. The modified central difference scheme is used to solve the above explicit dynamic problem.

Mathematical Subject Classification: 74R99, 74S05

Keywords: DEM, brittle fracturing, multi-surface plasticity and softening, explicit dynamic formulation, Coulomb friction contact

1. Introduction

Fracturing simulation presents a challenging task in mechanical engineering. There are various approaches [5], [11] to describe and solve the above problem, however none of their applicabilities is in general straightforward. One of the methods to simulate fracturing is the Discrete Element Method (DEM). Its attractiveness lies first of all in its relatively easy mathematical formulation and computational implementation, and it requires for its material model only a few parameters, which are in general easily measurable. The DEM is an extension of the Finite Element Method (FEM). It can be considered to be a FEM enriched by the contact between the discrete bodies. Due to the contact and the possible softening in the material model and to the possibility of having an unconstrained body among the discrete bodies during the calculation, it requires an explicit dynamic formulation and corresponding central difference scheme for its solution.

2. Mathematical formulation

2.1. The node facet contact based on the penalty method. The most essential part of the DEM is the contact formulation [1],[6]. The contact problem can be

viewed as a specific restraint imposition problem of the discretised continuum system of bodies in contact. The most widespread method in restraint imposition is the penalty method. The potential energy increase corresponding to the contact (see also Figure 1) can be written as follows:

$$\delta A^c = \delta \left(\frac{1}{2} \alpha_n g_n^2 + \frac{1}{2} \alpha_t g_t^2 \right), \quad (2.1)$$

where $\alpha_n, \alpha_t, g_n, g_t$ are the normal (tangential) penalties and actual normal (tangential) gaps.

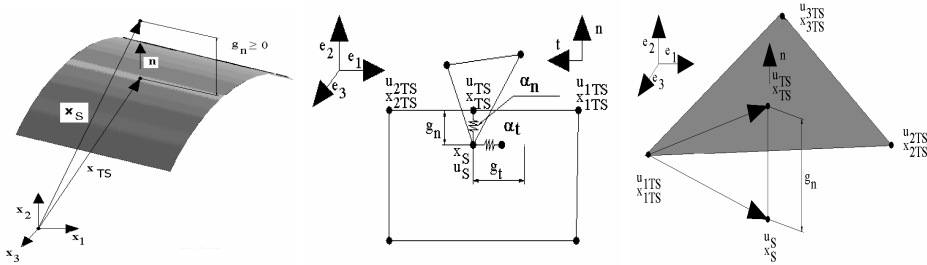


Figure 1. Positive sign convention and node to facet contact 2D and 3D implementation

The principle of minimum potential energy states the contact internal force vector as the first derivative of the contact potential energy according to the contact displacement vector given by the following formula:

$$\mathbf{f}_c^{\text{int}} = \frac{\partial A^c}{\partial \mathbf{u}_c} = \alpha_n g_n \frac{\partial g_n}{\partial \mathbf{u}_c} + \alpha_t g_t \frac{\partial g_t}{\partial \mathbf{u}_c} = \mathbf{f}_{c_n}^{\text{int}} + \mathbf{f}_{c_t}^{\text{int}}. \quad (2.2)$$

2.1.1. Normal and tangential gap calculation and discretization. The discretization of the system requires defining a pair of contact nodes given by the Euler coordinates \mathbf{x}_S of a contractor node and the corresponding target or defense node given by \mathbf{x}_{TS} as a normal projection of the contractor node to the facet. By using shape functions, Lagrange coordinates and deflections for the actual normal and tangential gaps, the following expressions can be written:

$$g_n = (\mathbf{x}_S - \mathbf{x}_{TS}) \cdot \mathbf{n} = (\mathbf{X}_S + \mathbf{u}_S - \sum_{i=1}^{n_{\text{facet}}} N_i(\mathbf{X}_i + \mathbf{u}_i)) \cdot \mathbf{n}, \quad (2.3)$$

$$g_t = (\mathbf{x}_S - \mathbf{x}_{TS}) \cdot \mathbf{t} = (\mathbf{X}_S + \mathbf{u}_S - \sum_{i=1}^{n_{\text{facet}}} N_i(\mathbf{X}_i + \mathbf{u}_i)) \cdot \mathbf{t}. \quad (2.4)$$

By using equations (2.3) and (2.4), the derivatives for the contact force calculation can be calculated as follows:

$$\frac{\partial g_n}{\partial \mathbf{u}_c} = \frac{\partial(\mathbf{x}_S - \mathbf{x}_{TS})}{\partial \mathbf{u}_c} \cdot \mathbf{n} + (\mathbf{x}_S - \mathbf{x}_{TS}) \cdot \frac{\partial \mathbf{n}}{\partial \mathbf{u}_c}, \quad (2.5)$$

$$\frac{\partial g_t}{\partial \mathbf{u}_c} = \frac{\partial(\mathbf{x}_S - \mathbf{x}_{TS})}{\partial \mathbf{u}_c} \cdot \mathbf{t} + (\mathbf{x}_S - \mathbf{x}_{TS}) \cdot \frac{\partial \mathbf{t}}{\partial \mathbf{u}_c}. \quad (2.6)$$

For deformations where the unit normal (tangential) vector change is negligible, further simplifications are possible. These simplifications are assumed as a result of the stability requirements of the central difference scheme, which require extremely small time steps during the solution.

$$\frac{\partial g_n}{\partial \mathbf{u}_c} \cong \frac{\partial(\mathbf{x}_S - \mathbf{x}_{TS})}{\partial \mathbf{u}_c} \cdot \mathbf{n} = \begin{bmatrix} \mathbf{n} \\ -N_1 \mathbf{n} \\ -N_{n_{\text{facet}}} \mathbf{n} \end{bmatrix}, \quad (2.7)$$

$$\frac{\partial g_t}{\partial \mathbf{u}_c} \cong \frac{\partial(\mathbf{x}_S - \mathbf{x}_{TS})}{\partial \mathbf{u}_c} \cdot \mathbf{t} = \begin{bmatrix} \mathbf{t} \\ -N_1 \mathbf{t} \\ -N_{n_{\text{facet}}} \mathbf{t} \end{bmatrix}.$$

By using expressions (2.7), the internal contact force vector (2.2) can be easily calculated.

The above derivation corresponds to sticking contact. If friction has to be considered between the surfaces in contact, a Coulomb plasticity model extends the contact force derivation, which is briefly outlined in Appendix D.

2.2. Multi-surface plasticity model. In the calculation, a classical multi-surface plasticity theory was utilized in the material model derivation [2], [3]. The following section briefly outlines the essentials of the non-associative multi-surface plasticity model, while a detailed derivation can be found for the combined Mohr-Coulomb and Rankine model in Appendices A-C.

2.2.1. Plastic velocity strain. The evolution of plastic velocity strain for non-associative multi-surface plasticity is defined as:

$$\mathbf{D}^p = \sum_{\alpha=1}^m \dot{\gamma}^\alpha \cdot \partial_{\boldsymbol{\sigma}} r_\alpha(\boldsymbol{\sigma}, \mathbf{q}), \quad (2.8)$$

where $\dot{\gamma}^\alpha, r_\alpha(\boldsymbol{\sigma}, \mathbf{q})$ are an unknown plastic multiplier and the non-associative plastic potential function, respectively.

The evolution equations for the hardening variables can be described according to the following formula:

$$\dot{\mathbf{q}} = - \sum_{\alpha=1}^m \dot{\gamma}^\alpha \cdot \mathbf{h}_\alpha(\boldsymbol{\sigma}, \mathbf{q}), \quad (2.9)$$

where $\mathbf{h}_\alpha(\boldsymbol{\sigma}, \mathbf{q}) = \frac{\partial \mathbf{q}}{\partial \dot{\gamma}^\alpha} = \frac{\partial \dot{\mathbf{q}}}{\partial \dot{\gamma}^\alpha}$ contains the instantaneous hardening modulus.

2.2.2. *Complementary and consistency requirements.* The complementary conditions state the requirements for the plastic multiplier γ^α calculation, and define the admissible stress space $\mathbb{J}_{\text{adm}} := \{\beta \in [1, 2, \dots, m_{\text{adm}}] | f_\beta(\boldsymbol{\sigma}, \mathbf{q}) \leq 0\}$, respectively for the stress calculation as follows:

$$\text{For } \alpha = 1, 2, \dots, m, \quad \gamma^\alpha \geq 0, \quad f_\alpha(\boldsymbol{\sigma}, \mathbf{q}) \leq 0. \quad (2.10)$$

2.2.3. *The consistency requirement summarize the complementary requirements in a short form with the following formula:*

$$\text{For } \alpha = 1, 2, \dots, m, \quad \gamma^\alpha \cdot f_\alpha(\boldsymbol{\sigma}, \mathbf{q}) \equiv 0. \quad (2.11)$$

2.2.4. *Plastic multiplier calculation.* The active stress space condition $\mathbb{J}_{\text{act}} := \{\beta \in \mathbb{J}_{\text{adm}} | \dot{f}_\beta(\boldsymbol{\sigma}, \mathbf{q}) = 0\}$ implies the following formulation for the plastic multiplier calculation:

$$\text{For } \alpha = 1, 2, \dots, m_{\text{adm}}, \\ f_\alpha(\boldsymbol{\sigma}, \mathbf{q}) = 0; \quad \dot{f}_\alpha(\boldsymbol{\sigma}, \mathbf{q}) = 0 \Rightarrow \sum_{\beta \in \mathbb{J}_{\text{adm}}} g_{\alpha\beta}(\boldsymbol{\sigma}, \mathbf{q}) \cdot \dot{\gamma}^\beta = \partial_{\boldsymbol{\sigma}} f_\alpha(\boldsymbol{\sigma}, \mathbf{q}) : \mathbf{C}_{el}^{\sigma G} : \mathbf{D}, \quad (2.12)$$

$$g_{\alpha\beta}(\boldsymbol{\sigma}, \mathbf{q}) = \partial_{\boldsymbol{\sigma}} f_\alpha(\boldsymbol{\sigma}, \mathbf{q}) : \mathbf{C}_{el}^{\sigma G} : \partial_{\boldsymbol{\sigma}} r_\beta(\boldsymbol{\sigma}, \mathbf{q}) + \partial_{\mathbf{q}} f_\alpha(\boldsymbol{\sigma}, \mathbf{q}) \cdot \mathbf{h}_\beta(\boldsymbol{\sigma}, \mathbf{q}).$$

Equation (2.12) represents a system of $\alpha = m_{\text{act}}$ equations with $\alpha = m_{\text{act}}$ unknowns whose solution for the plastic multipliers implies:

$$\dot{\gamma}^\beta = 0, \quad \text{if } \beta \notin \mathbb{J}_{\text{act}}, \quad (2.13)$$

$$\dot{\gamma}^\alpha = \sum_{\beta \in \mathbb{J}_{\text{act}}} g^{\alpha\beta}(\boldsymbol{\sigma}, \mathbf{q}) \cdot [\partial_{\boldsymbol{\sigma}} f_\beta(\boldsymbol{\sigma}, \mathbf{q}) : \mathbf{C}_{el}^{\sigma G} : \mathbf{D}], \quad \text{if } \alpha \in \mathbb{J}_{\text{act}}, \quad (2.14)$$

where: $g^{\alpha\beta}(\boldsymbol{\sigma}, \mathbf{q})$ are the components of the $[g_{\alpha\beta}(\boldsymbol{\sigma}, \mathbf{q})]^{-1}$ tensor.

2.2.5. *Elastic-plastic tangent modulus.* The elastic-plastic tangent modulus can be calculated by back substitution for $\dot{\gamma}^\alpha$ as follows:

$$\mathbf{C}_{ep}^{\sigma G} = \mathbf{C}_{el}^{\sigma G} - \sum_{\alpha, \beta \in \mathbb{J}_{\text{act}}} g^{\alpha\beta}(\boldsymbol{\sigma}, \mathbf{q}) [\mathbf{C}_{el}^{\sigma G} : \partial_{\boldsymbol{\sigma}} r_\alpha(\boldsymbol{\sigma}, \mathbf{q})] \otimes [\mathbf{C}_{el}^{\sigma G} : \partial_{\boldsymbol{\sigma}} f_\beta(\boldsymbol{\sigma}, \mathbf{q})], \quad \text{if } \mathbb{J}_{\text{act}} \neq 0 \quad (2.15)$$

or

$$\mathbf{C}_{ep}^{\sigma G} = \mathbf{C}_{el}^{\sigma G}, \quad \text{if } \mathbb{J}_{\text{act}} = 0. \quad (2.16)$$

Note: If $\mathbf{h}_\beta(\boldsymbol{\sigma}, \mathbf{q}) \neq \text{const}$, then the system of equations (2.12) is non-linear and iterations are needed to calculate the value of the plastic multiplier. The elastic-plastic tangent modulus is then calculated as $\mathbf{C}_{ep}^{\sigma G} = \frac{\partial \dot{\boldsymbol{\sigma}}}{\partial \mathbf{D}}$, after back substitution for the plastic multiplier in $\dot{\boldsymbol{\sigma}}$.

2.3. Stress update. Due to the non-objectivity of the stress measure used in the updated Lagrange formulation, the stress update uses the Green-Naghdi objective rate

$$\boldsymbol{\sigma}^{\nabla G} = \frac{D\boldsymbol{\sigma}}{Dt} - \boldsymbol{\Omega} \cdot \boldsymbol{\sigma} - \boldsymbol{\sigma} \cdot \boldsymbol{\Omega}^T = \mathbf{R} \cdot \frac{D\boldsymbol{\sigma}}{Dt} \cdot \mathbf{R}^T, \quad (2.17)$$

which after the numerical integration at the midpoint of the time increment can be expressed in the elastic case as

$$\boldsymbol{\sigma}^{t_n+\Delta t} = \mathbf{R}^{t_n+\Delta t} \cdot \left[\mathbf{C}_{el}^{\sigma G} : \left(\mathbf{R}^{(t_n+\frac{\Delta t}{2})^T} \cdot \mathbf{D}(t_n+\frac{\Delta t}{2}) \cdot \mathbf{R}^{(t_n+\frac{\Delta t}{2})} \right) \Delta t + \right. \\ \left. + \mathbf{R}^{t_n^T} \cdot \boldsymbol{\sigma}^{t_n} \cdot \mathbf{R}^{t_n} \right] \cdot \mathbf{R}^{t_n+\Delta t^T}, \quad (2.18)$$

and in the plastic case as

$$\boldsymbol{\sigma}^{t_n+\Delta t} = \mathbf{R}^{t_n+\Delta t} \cdot \left[\mathbf{C}_{el}^{\sigma G} : \left(\mathbf{R}^{(t_n+\frac{\Delta t}{2})^T} \cdot (\mathbf{D}(t_n+\frac{\Delta t}{2}) - \mathbf{D}^p(t_n+\frac{\Delta t}{2})) \cdot \mathbf{R}^{(t_n+\frac{\Delta t}{2})} \right) \Delta t + \right. \\ \left. + \mathbf{R}^{t_n^T} \cdot \boldsymbol{\sigma}^{t_n} \cdot \mathbf{R}^{t_n} \right] \cdot \mathbf{R}^{t_n+\Delta t^T}, \quad (2.19)$$

where

$$\hat{\mathbf{D}}^p(t_n+\frac{\Delta t}{2}) = \mathbf{R}^{(t_n+\frac{\Delta t}{2})^T} \mathbf{D}^p(t_n+\frac{\Delta t}{2}) \mathbf{R}^{(t_n+\frac{\Delta t}{2})} = \sum_{\alpha=1}^m \gamma^\alpha \cdot \partial_{\boldsymbol{\sigma}r\alpha} \left(\hat{\boldsymbol{\sigma}}^{t_n+\Delta t}, \hat{\mathbf{q}}^{t_n+\Delta t} \right) \quad (2.20)$$

is a co-rotational plastic velocity strain, $\hat{\boldsymbol{\sigma}}^{t_n+\Delta t}$, $\hat{\mathbf{q}}^{t_n+\Delta t}$ and \mathbf{R} stand for the co-rotational Cauchy stress, the co-rotational vector of hardening variables and the rotation tensor, respectively.

2.4. Fracturing. Mode I fracturing is present only in the Rankine plastic corner. If the first principal plastic strain value reaches the critical fracturing strain value $\varepsilon_c^f = \frac{f_c}{H}$, the fracture is inserted. The most meaningful quasi-brittle damage indicator or so-called failure factor is the ratio of the inelastic fracturing strain ε^f to the critical fracturing strain ε_c^f . The local fail factor F_k at Gauss point k is given by

$$F_k = (\varepsilon^f / \varepsilon_c^f)_k. \quad (2.21)$$

The weighted-average failure factor \bar{F}_p and fracture direction $\bar{\theta}_p$ at node p are given by

$$\bar{F}_p = \sum_{k=1}^{N_{adj}} F_k w_k \Big/ \sum_{k=1}^{N_{adj}} w_k, \quad (2.22)$$

$$\bar{\theta}_k = \sum_{k=1}^{N_{adj}} \theta_k w_k \Big/ \sum_{k=1}^{N_{adj}} w_k, \quad (2.23)$$

where N_{adj} is the number of immediately adjacent Gauss points and w_k is a weighting factor usually taken as the element volume. The fracture direction angle is allowed to change during the whole period of softening as far as the fracture is inserted. That

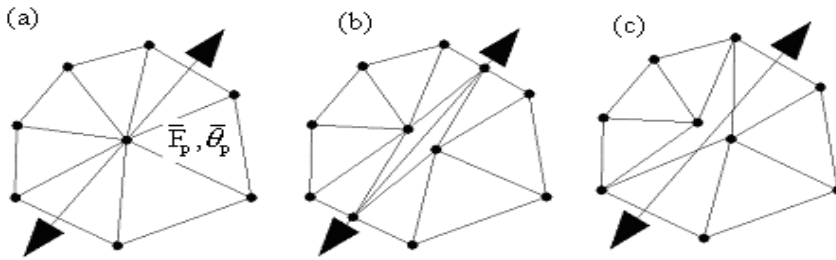


Figure 2. (a) Weighted-average nodal failure direction (b) Intra-element fracturing (c) Inter-element fracturing

is why this kind of fracturing is designated as the rotating crack model. Contact damping can be used on the border between the bodies in contact as a further improvement. The solution uses the modified central difference scheme [4], whose stability sets severe criteria on the time step value.

3. Simulation of real caving

There are several material models which treat the discontinuities by introducing various parameters and do the stress update as in the classical plasticity formulation limited to the FEM formulation. All of these models however assume homogenous discontinuity distribution within the element. In rock fracturing this assumption is not necessarily correct [7], [8]. Figure 3 depicts a typical sample of a rock block in reality, its approximated geometry and the further simplified model geometry using two sets of discontinuities. By using the DEM, the above problem can easily be avoided by combining the classical model with homogenous discontinuities and the real discontinuities as shown in Figure 3b,c. One such typical application of the method is the Block caving method, where, during the mining, large blocks of the mined rock fracture into small pieces and flow as a result of the gravity forces. The flow itself is initiated by the material integrity weakening of a supporting layer under the mined rock by its gradual drilling and blasting.

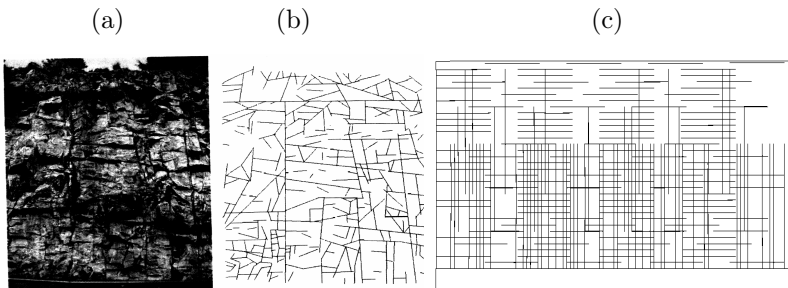


Figure 3. (a) Real geometry, (b) approximated geometry, (c) model geometry

3.1. Description of the numerical model. The 2D plane-strain model represents a 200m x 100m rock block with two sets of discontinuities. The vertical set is composed of 60m long discontinuities (persistence), with 30m spacing along the discontinuity between the adjacent ends (bridges) and 2m spacing (spacing) in the perpendicular direction between the adjacent discontinuities. The corresponding horizontal set can be described by the following parameters: persistence x bridges x spacing = 30m x 15m x 3m. The caving initialization is realized by a gradual deactivation of supporting elements at the bottom of the model by 10m increments in both directions from the midline of the model. The model uses one Gauss point triangular elements with linear shape functions. The triangular element is advantageous in fracturing, since during the fracturing only further triangular elements can be created, which is a huge simplification and which significantly speeds up the calculation. However, this type of element has an obvious drawback, namely its poor performance in high stress gradient areas.

4. Numerical Results

4.1. Material parameters and loading. The material properties [9], [10] used in the calculation are based on the real data obtained from the South-African Palabora copper mine and shown in the following Table:

Material property / loadings:	Value:
Young's modulus	60 GPa
Poisson's ratio	0.25
Density	3100 kg/m ³
Cohesion stress	8 MPa
Friction angle	55 deg.
Dilatancy angle	9 deg.
Tension cut off stress	1MPa
Fracture energy	70 N/m
Friction angle (between the joints)	33 deg.
Cohesion stress (between the joints)	50 000 Pa
Surface contact damping coefficient	0.5
Model size:	200 x 100 m,
Face loading	15.2 MPa
Body force	30.41 kN/ m ³

Table 1. Material properties of the caved rock

Figure 4 shows the first principal stress distribution which controls the fracturing. The undercut was gradually increased up to 160m. There is no restriction on the flow, the material is allowed to fall freely. In the caved area the lowered density as a result of increasing void ratio can be seen. The numerical simulation shows the extensive fracturing in the caving zone above the undercut area. In mines where the block

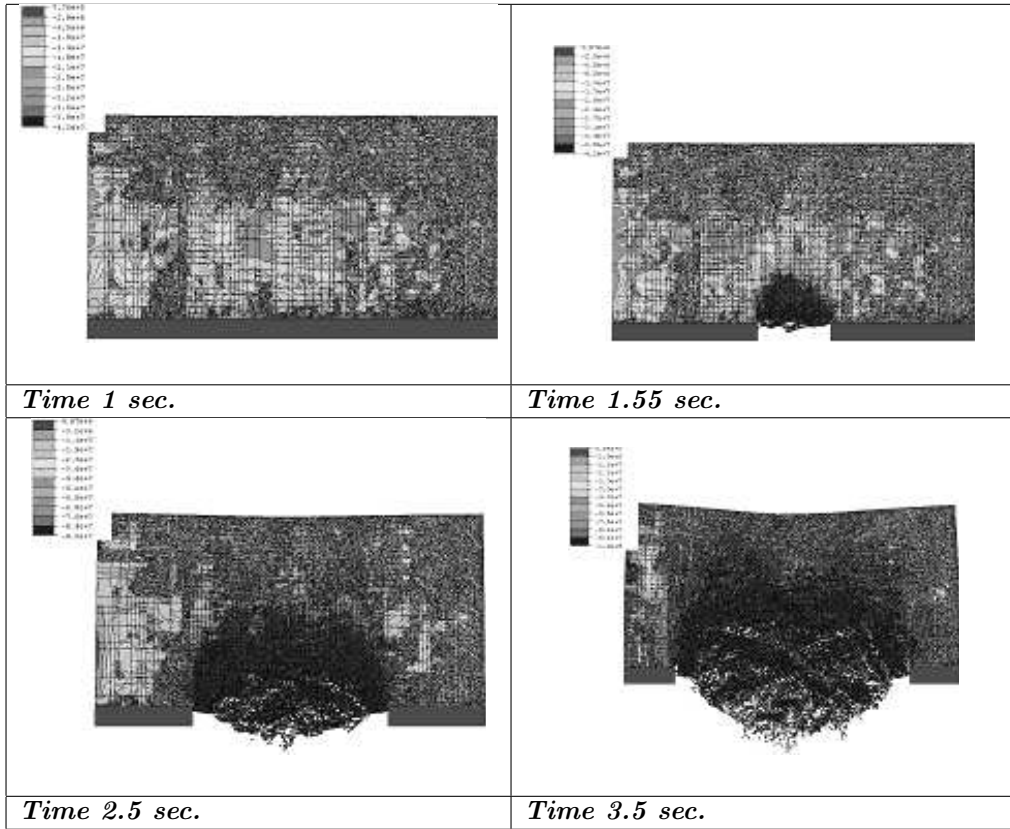


Figure 4. First principal stress distribution

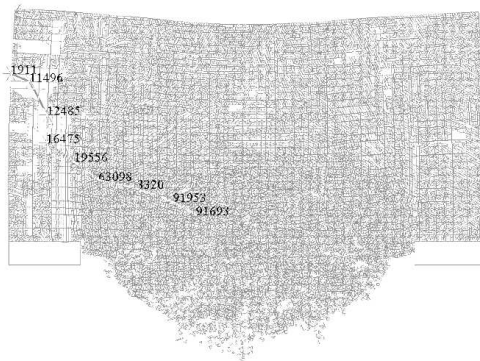


Figure 5. Continuum caving scenario with fracturing at 3.5 sec

caving method is employed, the same effect was observed, as there were not any extremely large pieces of rocks on the operation level during the haulage.

Figure 5 shows the fractured rock flow at time 3.5 sec.

4.2. Stress states at selected points. The following Table shows some typical stress values for the selected points in Figure 5 at time 3.5 sec.

	x [m]	y [m]	σ_{xx} [MPa]	σ_{yy} [MPa]	σ_{zz} [MPa]	σ_{xy} [MPa]
Node 91693	77.58	-533.76	-1.298	-1.107	-0.792	-0.611
Node 91953	67.44	-529.09	0.011	0.074	-0.335	0.087
Node 3320	51.00	-520.00	-1.535	0.015	-0.236	-0.613
Node 63098	38.20	-520.40	-9.079	-5.526	-3.651	-6.747
Node 19556	27.71	-514.65	-9.312	-34.463	-10.944	-12.985
Node 16475	16.00	-507.00	-20.551	-51.560	-18.028	-10.029
Node 12485	16.00	-495.00	-30.486	-63.564	-23.512	3.075
Node 11496	8.00	-481.00	-23.092	-17.362	-10.113	3.266
Node 1911	0.00	-478.00	-21.642	-0.274	-5.479	1.536

Table 2. Stress values at selected nodes

5. Conclusion

The biggest advantage of the method presented is the ability to model extensive fracturing. The method allows us to model situations where the conventional finite element method would fail. The calculation uses explicit dynamic formulation of equations of motion and the combined Mohr-Coulomb and Rankine plasticity model with mode I fracturing based on the rotating crack model. Due to the stability requirements and the extensive contact search between the discrete bodies, even 2D calculations with a relatively small number (several ten thousands) of elements appear to be very expensive. A similar 3D simulation without sorting out the parallel processing of the code is thus unimaginable.

Acknowledgement. Funding provided by Rio Tinto and VEGA SR is gratefully acknowledged.

References

1. BELYTSCHKO, T., WAM KAM LUI and MORAN, B.: *Nonlinear Finite Element Analysis for Continua and Structures*. Chichester, John Wiley & Sons, 1999.
2. HINTON, E. and OWEN, R.: *Computational Modelling of Reinforced Concrete Structures*. Swansea, Pineridge Press, 1986.
3. SIMO, J. C. and HUGHES, J. R.: *Computational Inelasticity*. New York, Springer-Verlag, 1998.
4. COOK, R. D., MALKUS, D. S., and PLESHA, M. E.: *Concepts and Applications of Finite Element Analysis*, New York, N.Y., John Wiley & Sons, 1989.

5. CLERK, P. A.: *The Finite Element Modelling of Discrete Fracture in Quasi-Brittle Materials*. Thesis, Dept. of Civil Engineering, UW Swansea, 2000.
6. YU, J. G.: *A contact interaction framework for numerical simulation of multi body problems and aspects of damage and fracture for brittle materials*. Thesis, Dept. of Civil Engineering, UW Swansea, 1995.
7. TINTO R.: *Caving Study*. End of Project Report, Nov. 1997 to Nov. 2000.
8. BRADY, B. H. G. and BROWN, E. T.: *Rock mechanics for underground mining*, 2nd. edition, Chapman & Hall, 1993
9. PETER, J. and GASH S.: *In situ stress measurement*. Palabora Underground Mining Project, 1999.
10. ITASCA CONSULTING GROUP, *Examination of the Caving Potential for the Palabora Underground Mine*, Internal report, 1995.
11. BAZANT, Z. P. and PLANAS, J.: *Fracture and size effect in concrete and other quasibrittle materials*, CRC Press LLC, 1998.

Appendix A.

In the sequel we briefly outline the combined Mohr-Coulomb and Rankine plasticity model. Depending on which part of the plasticity surface is active the following possibilities can be distinguished.

A.1. Mohr-Coulomb constitutive model. The Mohr-Coulomb plasticity surface usually becomes active if the principal stresses are compressive. As a simplification perfect plasticity was considered, which means the plasticity surface is static. The following cases can be distinguished and are depicted in the π - plane (Figure 6):

If $\sigma_1 \geq \sigma_2 \geq \sigma_3$ are the principal stresses and c_0, φ, ψ are the cohesion stress, friction angle and dilatation angle, the plasticity surface equation is given as follows:

$$\frac{1}{2}(\sigma_1 - \sigma_3) + \frac{1}{2}(\sigma_1 + \sigma_3) \sin \varphi = c_0 \cos \varphi \quad (\text{A.1})$$

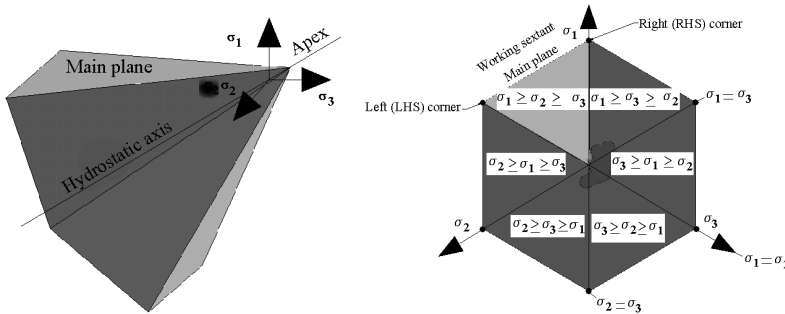


Figure 6. (a) The 3-D Mohr-Coulomb yield-surface in principal stress spaces (b) The π -plane representation.

- *Plastic flow from the main plane.* This is the simplest case, depicted in Figure 7. The trial stress crosses only one stress space, and only this stress space is active at one time. The active stress space is given by function f_1 , the plastic potential function by r_1 and the hardening variables by h_1 .

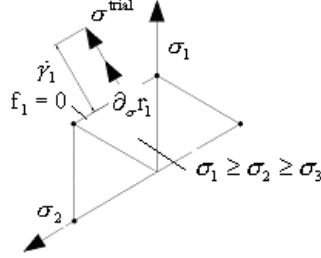


Figure 7. Main plane plasticity flow representation

$$m_{\text{act}} = 1, \quad f_1 = \frac{1}{2}(\sigma_1 - \sigma_3) + \frac{1}{2}(\sigma_1 + \sigma_3) \sin \varphi - c_o \cos \varphi = 0 \quad (\text{A.2a})$$

$$r_1 = \frac{1}{2}(\sigma_1 - \sigma_3) + \frac{1}{2}(\sigma_1 + \sigma_3) \sin \psi - c_o \cos \psi = 0 \quad (\text{A.2b})$$

For $c_o = \text{const}$, $\varphi = \text{const}$ and $\psi = \text{const}$ - these conditions ensure that the plasticity surface is static.

$$\mathbf{q}^T = [c_o \quad \varphi \quad \psi] \quad - \text{vector of state variables,} \quad \mathbf{h}_1^T = [0 \quad 0 \quad 0] \quad (\text{A.2c})$$

- *Plastic flow from the right corner (RHS)* The corner points represent the state where a number of stress spaces might be active at one time. At the right corner (Fig. 8) two stress spaces are active given by functions f_1, f_2 , the plastic potential functions are given by r_1, r_2 and the hardening variables by h_1, h_2 .

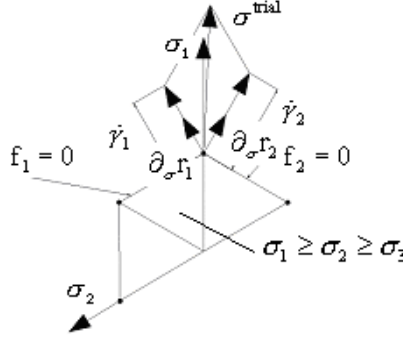


Figure 8. Right corner plasticity flow representation

$$m_{\text{act}} = 2, \quad f_1 = \frac{1}{2}(\sigma_1 - \sigma_3) + \frac{1}{2}(\sigma_1 + \sigma_3) \sin \varphi - c_o \cos \varphi = 0 \quad (\text{A.3a})$$

$$r_1 = \frac{1}{2}(\sigma_1 - \sigma_3) + \frac{1}{2}(\sigma_1 + \sigma_3) \sin \psi - c_o \cos \psi = 0 \quad (\text{A.3b})$$

$$f_2 = \frac{1}{2}(\sigma_1 - \sigma_2) + \frac{1}{2}(\sigma_1 + \sigma_2) \sin \varphi - c_o \cos \varphi = 0 \quad (\text{A.3c})$$

$$r_2 = \frac{1}{2}(\sigma_1 - \sigma_2) + \frac{1}{2}(\sigma_1 + \sigma_2) \sin \psi - c_o \cos \psi = 0 \quad (\text{A.3d})$$

for $c_o = \text{const}$, $\varphi = \text{const}$ and $\psi = \text{const}$

$$\mathbf{q}^T = [c_o \quad \varphi \quad \psi], \quad \mathbf{h}_1^T = \mathbf{h}_2^T = [0 \quad 0 \quad 0] \quad (\text{A.3e})$$

- *Plastic flow from the left corner (LHS)* It is analogous to the plastic flow from the right corner (Figure 9).

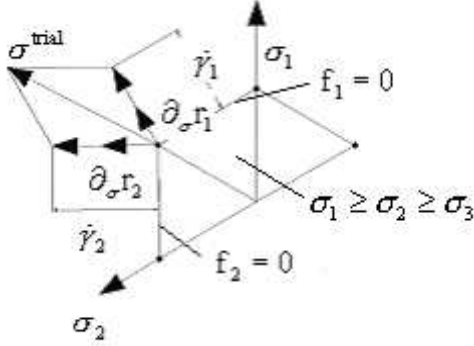


Figure 9. Left corner plasticity flow representation

$$m_{\text{act}} = 2, \quad f_1 = \frac{1}{2} (\sigma_1 - \sigma_3) + \frac{1}{2} (\sigma_1 + \sigma_3) \sin \varphi - c_o \cos \varphi = 0 \quad (\text{A.4a})$$

$$r_1 = \frac{1}{2} (\sigma_1 - \sigma_3) + \frac{1}{2} (\sigma_1 + \sigma_3) \sin \psi - c_o \cos \psi = 0 \quad (\text{A.4b})$$

$$f_2 = \frac{1}{2} (\sigma_2 - \sigma_3) + \frac{1}{2} (\sigma_2 + \sigma_3) \sin \varphi - c_o \cos \varphi = 0 \quad (\text{A.4c})$$

$$r_2 = \frac{1}{2} (\sigma_2 - \sigma_3) + \frac{1}{2} (\sigma_2 + \sigma_3) \sin \psi - c_o \cos \psi = 0 \quad (\text{A.4d})$$

for $c_o = \text{const}$, $\varphi = \text{const}$ and $\psi = \text{const}$

$$\mathbf{q}^T = [c_o \quad \varphi \quad \psi], \quad \mathbf{h}_1^T = \mathbf{h}_2^T = [0 \quad 0 \quad 0] \quad (\text{A.4e})$$

- *Plastic flow from the apex.* At the apex (Figure 10) two stress spaces corresponding to the hydrostatic and deviatoric stress are active and given by functions f_1, f_2 , as well as the plastic potential functions by r_1, r_2 and the hardening variables by h_1, h_2 .

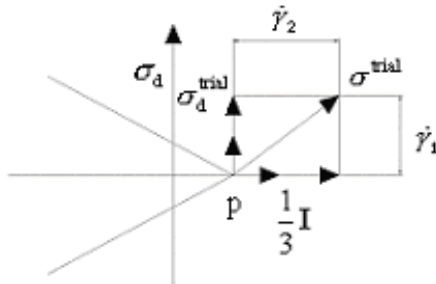


Figure 10. Plastic flow from the apex representation

$$m_{\text{act}} = 2, \quad f_1 = f_a^{\text{DEV}}(\boldsymbol{\sigma}, \varepsilon^p) = \boldsymbol{\sigma}_d = 0, \quad (\text{A.15})$$

$$r_1 = f_1; \quad f_2 = f_b^{\text{HYD}}(\boldsymbol{\sigma}, \varepsilon^p) = p - c_o \cot \varphi = 0; \quad r_2 = f_2, \quad (\text{A.16})$$

where $\boldsymbol{\sigma}_d = \text{dev}[\boldsymbol{\sigma}] = \boldsymbol{\sigma} - p\mathbf{I}$ and $p = \text{tr}[\boldsymbol{\sigma}] = (\sigma_1 + \sigma_2 + \sigma_3)/3$ for

$$c_o = \text{const}, \quad \varphi = \text{const}; \quad \mathbf{q}^T = [c_o \quad \varphi], \quad \mathbf{h}_1^T = \mathbf{h}_2^T = [0 \quad 0]. \quad (\text{A.17})$$

Appendix B. Rankine constitutive model

The Rankine failure model (Figure 11) governs the failure of brittle material in tension. When fracturing is considered, the FEM applications usually distinguish between the so-called fixed and rotating crack models.

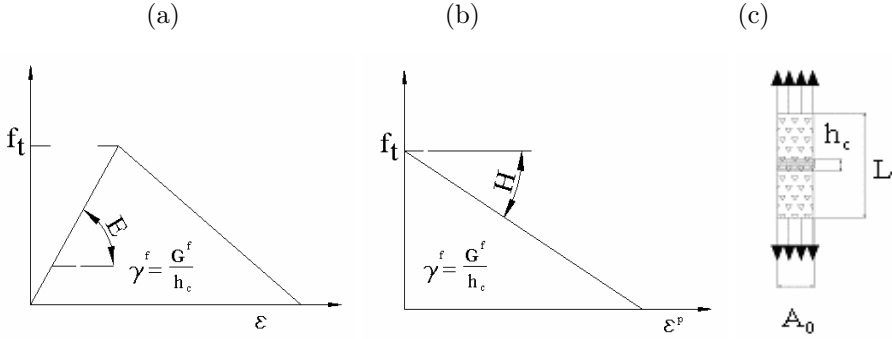


Figure 11. a) Stress strain curve, b) Stress plastic strain curve, c) Uniaxial specimen with crack band

The material behavior and the first principal stress value on the element level, is linear up to the so-called uniaxial tension strength, then it softens as is shown in Figure 11. The fixed crack model direction remains fixed after the peak value of the first principal stress has been reached, while in the case of the rotating crack model the fracture angle is allowed to change while the material softens as far as the crack is inserted.

$$\text{If } \sigma_1 \geq \sigma_2 \geq \sigma_3; \quad m_{\text{act}} = 1; \quad f_1 = \sigma_1 - \sigma_y(\varepsilon^p) = 0; \quad r_1 = f_1; \quad (\text{B.1})$$

$$\frac{\partial \varepsilon(\gamma^1)^p}{\partial \gamma^1} = 1, \quad q = \sigma_y(\varepsilon^p); \quad h_1(\boldsymbol{\sigma}, q) = h_1(\boldsymbol{\sigma}, \varepsilon^p) = \frac{\partial \sigma_y}{\partial \varepsilon^p} \cdot \frac{\partial \varepsilon^p}{\partial \gamma^1} = -H. \quad (\text{B.2})$$

Evolution of the tensile strength:

$$\sigma_y = \sigma_y(\varepsilon^p) = f_t - H\varepsilon^p. \quad (\text{B.3})$$

From the equivalence of the area, which represents the fracture energy per unit length to create a crack surface of uniform area, the softening modulus can be calculated as follows:

$$\frac{1}{2} \cdot \frac{f_t^2}{H} = \frac{G_f}{h_c^{(e)}} \Rightarrow H = -\frac{d\sigma_y}{d\varepsilon^p} = \frac{h_c^{(e)} \cdot f_t^2}{2 \cdot G_f} \quad (\text{B.4})$$

where

$$h_c^{(e)} \approx \sqrt{4A^{(e)}/\pi} \quad \text{for 2 - D triangular elements and} \quad (\text{B.5a})$$

$$h_c^{(e)} \approx \sqrt[3]{6V^{(e)}/\pi} \quad \text{for 3 - D tetrahedral elements.} \quad (\text{B.5b})$$

It is assumed, that the micro cracks in the fracture process zone are distributed over a band of width h (Figure 11c), hence the name crack band model (CBM). The technique, where the deformations are smeared over the element is called the smeared crack approach. In the FEM application the following technique was used for the equivalent crack band calculation (See Figure 12 and equations (B.5)).

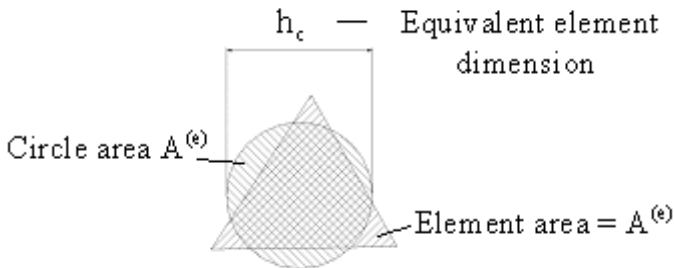


Figure 12. The approximate (equivalent) element dimension for a plane triangular element

Appendix C. Combined Mohr-Coulomb and Rankine constitutive model

It describes the plastic behavior of the model at the places where the Mohr-Coulomb and Rankine plasticity surfaces intersect each other (see Figure 13). As can be seen in the Figure, in compression there is always a stress space where the material remains elastic.

Single vector return mapping to the σ_1 tensile plane (for the interior of the ACD triangle see Figure 13): It is analogous to the Rankine constitutive model.

Two vector return mapping to the intersection of the σ_1 and σ_2 tensile planes (for the interior of the AD line see Figure 13) In the tensile corner it is assumed that the yield surfaces are independent of each other so if one surface softens, the remaining one does not change its position.

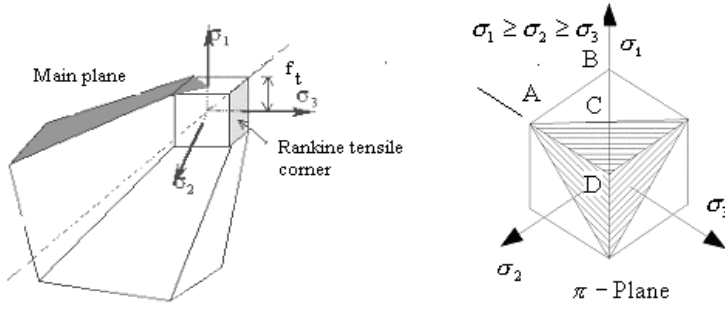


Figure 13. Combined Mohr-Coulomb and Rankine constitutive model representation

$$m_{\text{act}} = 2; \quad f_1 = \sigma_1 - \sigma_{y1}(\varepsilon_1^p) = 0; \quad r_1 = f_1; \quad f_2 = \sigma_2 - \sigma_{y2}(\varepsilon_2^p) = 0; \quad r_2 = f_2; \quad (C.1)$$

$$\frac{\partial \varepsilon_1(\gamma^1)^p}{\partial \gamma^1} = 1; \quad \frac{\partial \varepsilon_2(\gamma^2)^p}{\partial \gamma^2} = 1; \quad \sigma_{y1} = \sigma_{y1}(\varepsilon_1^p) = f_t - H\varepsilon_1^p; \quad \sigma_{y2} = \sigma_{y2}(\varepsilon_2^p) = f_t - H\varepsilon_2^p; \quad (C.2)$$

$$\mathbf{q}^T = [\sigma_{y1} \quad \sigma_{y2}]; \quad \mathbf{h}_1^T = [-H \quad 0]; \quad \mathbf{h}_2^T = [0 \quad -H]. \quad (C.3)$$

Three vector return mapping to the Rankine tensile corner apex (for point D see Figure 13):

$$m_{\text{act}} = 3; \quad f_1 = \sigma_1 - \sigma_{y1}(\varepsilon_1^p) = 0; \quad r_1 = f_1; \quad f_2 = \sigma_2 - \sigma_{y2}(\varepsilon_2^p) = 0; \quad (C.4)$$

$$r_2 = f_2; \quad f_3 = \sigma_3 - \sigma_{y3}(\varepsilon_3^p) = 0; \quad r_3 = f_3; \quad (C.5)$$

$$\frac{\partial \varepsilon_1(\gamma^1)^p}{\partial \gamma^1} = 1; \quad \frac{\partial \varepsilon_2(\gamma^2)^p}{\partial \gamma^2} = 1; \quad \frac{\partial \varepsilon_3(\gamma^3)^p}{\partial \gamma^3} = 1; \quad \sigma_{y1} = \sigma_{y1}(\varepsilon_1^p) = f_t - H\varepsilon_1^p; \quad (C.6)$$

$$\sigma_{y2} = \sigma_{y2}(\varepsilon_2^p) = f_t - H \cdot \varepsilon_2^p; \quad \sigma_{y3} = \sigma_{y3}(\varepsilon_3^p) = f_t - H \cdot \varepsilon_3^p; \quad (C.7)$$

$$\mathbf{q}^T = [\sigma_{y1} \quad \sigma_{y2} \quad \sigma_{y3}]; \quad \mathbf{h}_1^T = [-H \quad 0 \quad 0]; \quad (C.8)$$

$$\mathbf{h}_2^T = [0 \quad -H \quad 0]; \quad \mathbf{h}_3^T = [0 \quad 0 \quad -H]. \quad (C.9)$$

Two vector return mapping to the intersection of the Mohr-Coulomb main plane and the σ_1 tensile plane (for the interior of the line AC see Figure 13):

$$m_{\text{act}} = 2; \quad f_1 = \frac{1}{2}(\sigma_1 - \sigma_3) + \frac{1}{2}(\sigma_1 + \sigma_3) \sin \varphi - c_o \cos \varphi = 0; \quad f_2 = \sigma_1 - \sigma_y(\varepsilon^p) = 0; \quad (C.10)$$

$$r_1 = \frac{1}{2}(\sigma_1 - \sigma_3) + \frac{1}{2}(\sigma_1 + \sigma_3) \sin \psi - c_o \cos \psi = 0; \quad r_2 = f_2; \quad (C.11)$$

for $c_o = \text{const}$, $\varphi = \text{const}$ and $\psi = \text{const}$. The Mohr-Coulomb plasticity surface does not change:

$$\mathbf{q}^T = [c_o \quad \varphi \quad \psi \quad \sigma_y \varepsilon^p]; \quad \mathbf{h}_1^T = [0 \quad 0 \quad 0 \quad 0]; \quad \mathbf{h}_2^T = [0 \quad 0 \quad 0 \quad -H] \quad (C.12)$$

Three vector return-mapping to the intersection of the right edge of the Mohr-Coulomb main-plane and the σ_1 tensile plane (for point C see Figure 13)

$$\mathbf{m}_{\text{act}} = 3; \quad \mathbf{f}_1 = \frac{1}{2}(\sigma_1 - \sigma_3) + \frac{1}{2}(\sigma_1 + \sigma_3) \sin \varphi - c_o \cos \varphi = 0; \quad (\text{C.13})$$

$$\mathbf{f}_2 = \frac{1}{2}(\sigma_1 - \sigma_2) + \frac{1}{2}(\sigma_1 + \sigma_2) \sin \varphi - c_o \cos \varphi = 0; \quad \mathbf{f}_3 = \sigma_1 - \sigma_y(\varepsilon^p) = 0; \quad (\text{C.14})$$

$$\mathbf{r}_1 = \frac{1}{2}(\sigma_1 - \sigma_3) + \frac{1}{2}(\sigma_1 + \sigma_3) \sin \psi - c_o \cos \psi = 0; \quad (\text{C.15})$$

$$\mathbf{r}_2 = \frac{1}{2}(\sigma_1 - \sigma_2) + \frac{1}{2}(\sigma_1 + \sigma_2) \sin \psi - c_o \cos \psi = 0; \quad \mathbf{r}_3 = \mathbf{f}_3; \quad (\text{C.16})$$

for $c_o = \text{const}$, $\varphi = \text{const}$ and $\psi = \text{const}$

$$\mathbf{q}^T = [c_o \quad \varphi \quad \psi \quad \sigma_y(\varepsilon^p)]; \quad \mathbf{h}_1^T = [0 \quad 0 \quad 0 \quad 0]; \quad (\text{C.17})$$

$$\mathbf{h}_2^T = [0 \quad 0 \quad 0 \quad 0]; \quad \mathbf{h}_3^T = [0 \quad 0 \quad 0 \quad -H]. \quad (\text{C.18})$$

Four vector return-mapping to the intersection of the left edge of the Mohr-Coulomb main-plane and the σ_1 and σ_2 tensile planes (point A see Figure 13)

$$\mathbf{m}_{\text{act}} = 4; \quad \mathbf{f}_1 = \frac{1}{2}(\sigma_1 - \sigma_3) + \frac{1}{2}(\sigma_1 + \sigma_3) \sin \varphi - c_o \cos \varphi = 0; \quad (\text{C.19})$$

$$\mathbf{f}_2 = \frac{1}{2}(\sigma_2 - \sigma_3) + \frac{1}{2}(\sigma_2 + \sigma_3) \sin \varphi - c_o \cos \varphi = 0; \quad \mathbf{f}_3 = \sigma_1 - \sigma_{y1}(\varepsilon_1^p) = 0; \quad (\text{C.20})$$

$$\mathbf{f}_4 = \sigma_2 - \sigma_{y2}(\varepsilon_2^p) = 0; \quad \mathbf{r}_1 = \frac{1}{2}(\sigma_1 - \sigma_3) + \frac{1}{2}(\sigma_1 + \sigma_3) \sin \psi - c_o \cos \psi = 0; \quad (\text{C.21})$$

$$\mathbf{r}_2 = \frac{1}{2}(\sigma_2 - \sigma_3) + \frac{1}{2}(\sigma_2 + \sigma_3) \sin \psi - c_o \cos \psi = 0; \quad \mathbf{r}_3 = \mathbf{f}_3; \quad \mathbf{r}_4 = \mathbf{f}_4; \quad (\text{C.22})$$

$$\mathbf{q}^T = [c_o \quad \varphi \quad \psi \quad \sigma_{y1}(\varepsilon_1^p) \quad \sigma_{y2}(\varepsilon_2^p)]; \quad \mathbf{h}_1^T = [0 \quad 0 \quad 0 \quad 0 \quad 0]; \quad (\text{C.23})$$

$$\mathbf{h}_2^T = [0 \quad 0 \quad 0 \quad 0 \quad 0], \quad \mathbf{h}_3^T = [0 \quad 0 \quad 0 \quad -H \quad 0], \quad \mathbf{h}_4^T = [0 \quad 0 \quad 0 \quad 0 \quad -H]. \quad (\text{C.24})$$

Appendix D. Tangential interaction law - The Coulomb friction model

The tangential interaction law describes the friction contact if a friction slip occurs between the bodies. It is formulated as follows:

$$\mathbf{g}_t = \mathbf{g}_t^e + \mathbf{g}_t^p; \quad \mathbf{f}_{c_t}^{\text{int}} = \alpha_t \mathbf{g}_t^e \mathbf{t} = \alpha_t (\mathbf{g}_t - \mathbf{g}_t^p) \mathbf{t}, \quad (\text{D.1})$$

where \mathbf{g}_t is the tangential gap and \mathbf{t} is the unit tangential vector at the place of contact.

The Coulomb friction phenomenon can be described as:

$$\mathbf{f}_1 = \|\mathbf{f}_{c_t}^{\text{int}}\| - (\mathbf{f}_{c_n}^{\text{int}} \mu + C_0) \leq 0, \quad (\text{D.2})$$

where μ is the friction coefficient and C_0 is the cohesion force.

The non-associative plastic flow (slip) potential function is:

$$\mathbf{r}_1 = \|\mathbf{f}_{c_t}^{\text{int}}\|; \quad \Delta \mathbf{g}_t^p = \Delta \lambda \frac{\partial \mathbf{r}_1}{\partial \mathbf{f}_{c_t}^{\text{int}}} = \Delta \lambda \frac{\mathbf{f}_{c_t}^{\text{int}}}{\|\mathbf{f}_{c_t}^{\text{int}}\|} = \Delta \lambda \mathbf{t}; \quad \Delta \mathbf{f}_{c_n}^{\text{int}} = \alpha_n \Delta \mathbf{g}_n \quad (\text{D.3})$$

The slipping/sticking conditions can be formulated in the discrete Kuhn-Tucker form with the following complementary and consistency requirements:

$$\mathbf{f}_1 \leq 0, \quad \Delta \lambda \geq 0, \quad \Delta \lambda \cdot \mathbf{f}_1 = 0. \quad (\text{D.4})$$

TRANSVERSE SHEAR AND NORMAL DEFORMATION THEORY FOR VIBRATION ANALYSIS OF CURVED BANDS

BÉLA KOVÁCS

Institute of Mathematics, University of Miskolc
3515 Miskolc-Egyetemváros, Hungary
matkb@gold.uni-miskolc.hu

[Received: May 5, 2003]

Dedicated to Professor József FARKAS on the occasion of his seventyfifth birthday

Abstract. A new laminate model is presented for the dynamic analysis of laminated curved bands. The collocation curved band is used to denote a cylinder panel in the plane strain state. The differential equations which govern the free vibrations of a curved band and the associated boundary conditions are derived by Hamilton's principle considering bending, shear and normal deformation of all layers. The author used a new iterative process to successively refine the stress/strain field in the sandwich curved band. The model includes the effects of transverse shear and rotary inertia. The iterative model is used to predict the modal frequencies and damping of simply supported sandwich curved band. The solutions for a three-layer curved band are compared to a three-layer approximate model.

Mathematical Subject Classification: 74H45, 74K10

Keywords: dynamic analysis, vibrations, layered band, damping

1. Introduction

Laminated composite curved beams have been used in engineering applications for many years. Design applications of isotropic and curved bars, rings and arches of arbitrary shape are assisted by a well-developed theory and proven design guidelines [1 – 4]. The development of the theory and design guidelines for composite curved beams is much less satisfactory. Earlier works are related to sandwich beams or closed composite rings [5 – 9]. The finite element method was used to study the dynamic response of sandwich curved beams by Ahmed [5 – 6]. Free and forced vibrations of a three-layer damped ring were investigated by Di Taranto [7]. Lu and Douglas [8] investigate the damped three-layered sandwich ring subjected to a time harmonic radially concentrated load. The paper gives an analytical solution for the mechanical impedance at an arbitrary point on the surface of the damped structure as a function of the forcing frequency. Furthermore, an experimental procedure is employed to measure the driving point mechanical impedance as a verification of the calculated

results. Transient response was studied for three-layer closed rings by Sagartz [9]. Damping properties of curved sandwich beams with viscoelastic layer were studied by Tatemichi et al. [10]. Viscoelastic damping in the middle core layer was emphasized.

Nelson and Sullivan [11] analyzed the complete circular ring consisting of a layer soft viscoelastic material sandwiched between two hard elastic layers. The equations which govern the forced vibration of a damped circular ring were solved by the method of damped forced modes. The essence of the damped forced mode method is the use of harmonic forcing functions which are in-phase with local velocity and proportional to local inertia loads. The constant of proportionality is the loss factor of the composite structure, η_n . A clear alternative to a damped forced mode solution is to set all the forcing functions to zero and solve the resulting complex eigenvalue problem. Isvan and Nelson [12] investigated the natural frequencies and composite loss factors of free vibration of a soft cored circular arch simply supported at each end. Although harmonic motion is assumed, what is not stated is that some harmonic excitation is required to maintain such motion in the presence of damping. The dynamic eigenvalue problem is then posed for an unforced system. Kovacs [13] solved the problem of free vibrations of a stiff cored sandwich circular arch. All the tangential displacement components are assumed to be piecewise linear across the thickness, thus implying the inclusion of shear deformations and rotary inertia.

The incremental equations of motion based on the principle of virtual displacements of a continuous medium are formulated using the total Lagrangian description by Liao and Reddy [14]. They developed a degenerate shell element with a degenerate curved beam element as a stiffener for the geometric non-linear analysis of laminated, anisotropic, stiffened shells. Bhimaraddi et al. [15] presented a 24-d.o.f. of isoparametric finite element for the analysis of generally laminated curved beams. The rotary inertia and shear deformation effects were considered in this study. Qatu developed a consistent set of equations for laminated shallow [16] and deep arches [17]. Exact solutions are presented for laminated arches having general boundary conditions by Qatu and Elsharkawy [18]. The in-plane free vibrational analysis of symmetric cross-ply laminated circular arches is studied by Yildirim [19]. The free vibration equations are derived based on the distributed parameter model. The transfer matrix method is used in the analysis. The rotary inertia, axial and shear deformation effects are considered in the Timoshenko analysis by the first-order shear deformation theory. Vaswani, Asnani and Nakra [20] derived a closed form solution for the system loss factors and resonance frequencies for a curved sandwich beam with a viscoelastic core by the Ritz method. Rao and He [21] used the energy method and Hamilton's principle to derive the governing equation of motion for the coupled flexural and longitudinal vibration of a curved sandwich beam system. Both shear and thickness deformations of the adhesive core are included. Equations for obtaining the system modal loss factors and resonance frequencies are derived for a system having simply supported ends by the Ritz method.

It is well-known that the accurate determination of the stress field in the laminate configurations is particularly important for 'stress critical' calculations such as damping and delamination. Zapfe and Lesieutre [22] developed an iterative process to

refine successively the shape of the stress/strain distribution for the dynamic analysis of laminated beams. The iterative model is used to predict the modal frequencies and damping of simply supported beams with integral viscoelastic layers.

The eigenproblem of the plane bending of circular arch shaped layered beams was investigated by using the finite element method [23]. The finite element model of the structure has two-two elements along the face thickness and three elements along the thickness of the core. The two edges of the circular arch are simply supported. The corresponding model is formed by eight node hexahedron elements (280 pcs.).

Flexure of the three-layer sandwich arch results in energy dissipation due to strains induced in the viscoelastic layer. In a symmetrical arrangement with identical elastic layers, most of the damping is due to shear of the viscoelastic layer. In an unsymmetrical arrangement, with dissimilar elastic layers, one might expect damping due to direct strain as well as shear in the viscoelastic layer, the former being known as extensional damping and the latter as shear damping. Both these effects have been included by Kovacs [24]. However, the stress-strain law assumed for the viscoelastic layer was not strictly correct and was only an approximation if extensional effects were considered. An analysis of the vibration of transversely isotropic beams, which have small constant initial curvature was presented in Rossettos [25], Rossettos and Squires [26]. A closed-form general solution to the governing equations was derived. Natural modes and frequencies were determined for both clamped and simply supported end conditions. In Khdeir and Reddy [27], an analysis of the vibration of slightly curved cross-ply laminated composite beams is presented. Hamilton's principle is used to derive the equations of motions of four theories. Exact natural frequencies are determined for various end conditions using the state space concept. The combined effects of initial curvature, transverse shear deformation, orthotropy ratio, stacking sequence and boundary conditions are evaluated and discussed. Yildirim [28] offers a comprehensive analysis of free vibration characteristics of symmetric cross-ply laminated circular arches vibrating perpendicular to their planes. Governing equations of symmetric laminated circular arches made of a linear, homogeneous, and orthotropic material are obtained in a straightforward manner based on the classical beam theory. The transfer matrix method is used for the free vibration analysis of the continuous parameter system.

The present research offers a new laminated model for the dynamic analysis of laminated curved bands, which includes both transverse shear and transverse normal effects. The differential equations which govern the free vibrations of a curved band and the associated boundary conditions are derived by Hamilton's principle considering bending, shear and normal deformation of all layers. The author used a new iterative process to successively refine the stress/strain fields in the sandwich band. The model includes the effects of transverse shear and rotary inertia. The current model is developed for the specific case of a simply supported curved band with uniform properties along the length.

2. Governing equations of motion

The geometry of interest and the notations used are shown in Figure 1. As indicated in the Figure, the curved band ends are simply supported. The collocation curved band is used to denote a cylinder panel in the plane strain state. Consider the curved band with a cylinder middle surface and the radius of curvature R of the middle surface. The curved band consists of three different layers of homogeneous materials bonded together to form a composite structure. Subscript i , where $i = 1, 2, 3$ is used to denote quantities in the various layers, starting from the outermost layer, so that layers 1,3 represent the elastic layers while layer 2 represents the viscoelastic layer. A state of plane strain is assumed, as well as the fact that the materials in each layer of the band are homogeneous and isotropic. Perfect bonding of the layers and linear elasticity are also assumed in the analysis. The composite band is lightly damped and it is assumed that all the energy dissipated is dissipated in the viscoelastic layer.

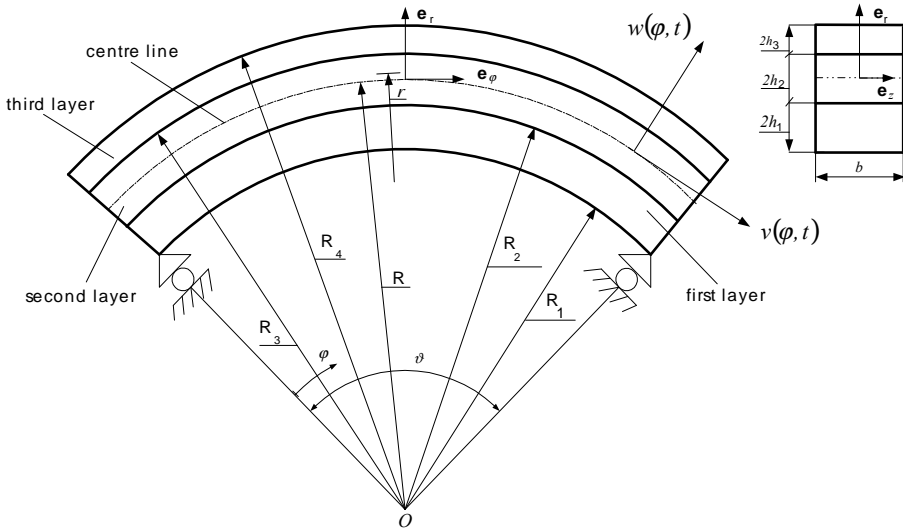


Figure 1. Geometry of the laminated curved band

The form of the displacement field over the domain of the curved band is

$$\begin{aligned} \mathbf{t}(r, \varphi, t) &= u(r, \varphi, t)\mathbf{e}_\varphi + w(r, \varphi, t)\mathbf{e}_r = \\ &= \left[v_0(\varphi, t) - \frac{r - R}{R} \left(\frac{\partial w_0}{\partial \varphi} - v_0(\varphi, t) \right) + f(r)v_1(\varphi, t) \right] \mathbf{e}_\varphi + [w_0(\varphi, t) + g(r)w_1(\varphi, t)] \mathbf{e}_r \end{aligned} \quad (2.1)$$

where $f(R) = 0$ and $g(R) = 0$, so (v_0, w_0) denote the displacement of a point (R, φ) of the centre-surface along the circumferential and radial directions, respectively.

The terms $f(r)v_1(\varphi, t)$ and $g(r)w_1(\varphi, t)$ can be thought to be correction to account for transverse shear and normal deformation effects, respectively. The functions $f(r)$ and $g(r)$ represent the shape of the corrections through the thickness of the curved

band, while $v_1(\varphi, t)$ and $w_1(\varphi, t)$ determine its distribution along the circumferential direction. The solution of a given problem requires the determination of the unknown functions $v_0(\varphi, t)$, $v_1(\varphi, t)$, $w_0(\varphi, t)$, $w_1(\varphi, t)$, $f(r)$ and $g(r)$. By using the standard expressions

$$\mathbf{t} = w\mathbf{e}_r + u\mathbf{e}_\varphi, \quad \varepsilon_\varphi = \frac{1}{r} \frac{\partial u}{\partial \varphi} + \frac{w}{r}, \quad \gamma_{r\varphi} = \frac{1}{r} \frac{\partial w}{\partial \varphi} + \frac{\partial u}{\partial r} - \frac{u}{r}, \quad \varepsilon_r = \frac{\partial w}{\partial r},$$

the strain tensor of each layer can be computed from equations (2.1):

$$\varepsilon_\varphi = \frac{1}{r} \left[\frac{\partial v_0}{\partial \varphi} - \frac{r-R}{R} \left(\frac{\partial^2 w_0}{\partial \varphi^2} - \frac{\partial v_0}{\partial \varphi} \right) + f(r) \frac{\partial v_1}{\partial \varphi} + w_0 + g(r) w_1(\varphi, t) \right], \quad (2.2)$$

$$\gamma_{r\varphi} = \left[\frac{df}{dr} - \frac{f(r)}{r} \right] v_1(\varphi, t) + \frac{g(r)}{r} \frac{\partial w_1}{\partial \varphi}, \quad (2.3)$$

$$\varepsilon_r = \frac{dg}{dr} w_1(\varphi, t), \quad (2.4)$$

where

$$f(r) = \begin{cases} f_1(r) & \text{if } R_1 \leq r \leq R_2 \\ f_2(r) & \text{if } R_2 \leq r \leq R_3 \\ f_3(r) & \text{if } R_3 \leq r \leq R_4 \end{cases}$$

and

$$g(r) = \begin{cases} g_1(r) & \text{if } R_1 \leq r \leq R_2 \\ g_2(r) & \text{if } R_2 \leq r \leq R_3 \\ g_3(r) & \text{if } R_3 \leq r \leq R_4 \end{cases}$$

are single-valued functions defined at each point through the thickness.

From equation (2.3), it can be seen that the functions $\frac{df}{dr} - \frac{f}{r}$ and $\frac{dg}{dr}$ represent the shape of the transverse shear strain field through the thickness of the curved band at a given φ -location. While the assumed form of the functions, $f(r)$ and $g(r)$ changes from one iteration to the next, at any given iteration they can be treated as known functions.

The curved band vibrates in the $r\varphi$ -plane. It is assumed that the plane strain state occurs within the structure and thus within each i -th layer. By treating the problem as a plane strain one and assuming that the materials in each layer are homogeneous and isotropic, we have the following stress-strain relations:

$$\sigma_{ri} = \frac{E_i}{(1-2\nu_i)(1+\nu_i)} ((1-\nu_i)\varepsilon_{ri} + \nu_i\varepsilon_{\varphi i}), \quad (2.5)$$

$$\sigma_{\varphi i} = \frac{E_i}{(1-2\nu_i)(1+\nu_i)} ((1-\nu_i)\varepsilon_{\varphi i} + \nu_i\varepsilon_{ri}), \quad (2.6)$$

$$\tau_{r\varphi i} = G_i \gamma_{r\varphi i}, \quad (2.7)$$

where E_i is the Young's modulus and G_i is the shear modulus within the i -th layer of the structure. Also ν_i is the Poisson's coefficient, which characterises the compression in the radial direction due to tension in the circumferential direction, and vice versa. In addition the stresses $\tau_{\varphi zi}, \tau_{rzi}$ are equal to zero.

The strain energy stored in the curved band is given by:

$$U = \frac{b}{2} \sum_{i=1}^3 \int_{\varphi=0}^{\vartheta} \int_{R_i}^{R_{i+1}} [\sigma_{r_i} \varepsilon_{r_i} + \sigma_{\varphi_i} \varepsilon_{\varphi_i} + \tau_{r\varphi_i} \gamma_{r\varphi_i}] r dr d\varphi. \quad (2.8)$$

The kinetic energy, which includes components associated with transverse, in plane and rotary inertia, is given by

$$T = \frac{b}{2} \sum_{i=1}^3 \int_{\varphi=0}^{\vartheta} \int_{R_i}^{R_{i+1}} \rho_i \left(\dot{\mathbf{t}}_i \right)^2 r dr d\varphi, \quad (2.9)$$

where the dots over \mathbf{t}_1 , \mathbf{t}_2 and \mathbf{t}_3 denote the partial derivative with respect to time. The differential equations of motion and boundary conditions are derived using Hamilton's principle. The equations of motion for the four unknown functions, $w_0(\varphi, t)$, $w_1(\varphi, t)$, $v_0(\varphi, t)$ and $v_1(\varphi, t)$ are

$$\begin{aligned} & A_{11} \frac{\partial^4 w_0}{\partial \varphi^4} + A_{12} \frac{\partial^2 w_0}{\partial \varphi^2} + A_{13} \frac{\partial^3 v_0}{\partial \varphi^3} + A_{14} \frac{\partial^3 v_1}{\partial \varphi^3} + A_{15} \frac{\partial v_0}{\partial \varphi} + A_{16} \frac{\partial v_1}{\partial \varphi} + A_{17} \frac{\partial^2 w_1}{\partial \varphi^2} + \\ & + A_{18} w_0 + A_{19} w_1 = D_{11} \frac{\partial^4 w_0}{\partial \varphi^2 \partial t^2} + D_{12} \frac{\partial^3 v_0}{\partial \varphi \partial t^2} + D_{13} \frac{\partial^3 v_1}{\partial \varphi \partial t^2} + D_{14} \frac{\partial^2 w_0}{\partial t^2} + D_{15} \frac{\partial^2 w_1}{\partial t^2}, \end{aligned} \quad (2.10)$$

$$\begin{aligned} & A_{21} \frac{\partial^3 w_0}{\partial \varphi^3} + A_{22} \frac{\partial w_0}{\partial \varphi} + A_{23} \frac{\partial^2 v_0}{\partial \varphi^2} + A_{24} \frac{\partial^2 v_1}{\partial \varphi^2} + A_{25} \frac{\partial w_1}{\partial \varphi} + A_{26} v_1 = \\ & = D_{21} \frac{\partial^3 w_0}{\partial \varphi \partial t^2} + D_{22} \frac{\partial^2 v_0}{\partial t^2} + D_{23} \frac{\partial^2 v_1}{\partial t^2}, \end{aligned} \quad (2.11)$$

$$A_{31} \frac{\partial^2 w_0}{\partial \varphi^2} + A_{32} \frac{\partial^2 w_1}{\partial \varphi^2} + A_{33} \frac{\partial v_0}{\partial \varphi} + A_{34} \frac{\partial v_1}{\partial \varphi} + A_{35} w_0 + A_{36} w_1 = D_{31} \frac{\partial^2 w_0}{\partial t^2} + D_{32} \frac{\partial^2 w_1}{\partial t^2}, \quad (2.12)$$

$$\begin{aligned} & A_{41} \frac{\partial^3 w_0}{\partial \varphi^3} + A_{42} \frac{\partial w_0}{\partial \varphi} + A_{43} \frac{\partial^2 v_0}{\partial \varphi^2} + A_{44} \frac{\partial^2 v_1}{\partial \varphi^2} + A_{45} \frac{\partial w_1}{\partial \varphi} = \\ & = D_{41} \frac{\partial^3 w_0}{\partial \varphi \partial t^2} + D_{42} \frac{\partial^2 v_0}{\partial t^2} + D_{43} \frac{\partial^2 v_1}{\partial t^2}, \end{aligned} \quad (2.13)$$

where A_{ij} and D_{ij} are given in the Appendix. K_{1-18} and M_{1-8} are section stiffness and mass coefficients, given by

$$K_{[1,\dots,7]} = b \sum_{i=1}^3 \int_{R_i}^{R_{i+1}} \frac{E_i (1 - \nu_i)}{(1 - 2\nu_i)(1 + \nu_i)} \left[1, r, \frac{1}{r}, f_i, g_i, \frac{1}{r} f_i, \frac{1}{r} g_i \right] dr, \quad (2.14)$$

$$K_{[8,17,18]} = b \sum_{i=1}^3 \int_{R_i}^{R_{i+1}} G_i \left[\frac{1}{r} g_i^2, r \left(\frac{df_i}{dr} - \frac{f_i}{r} \right)^2, \left(\frac{df_i}{dr} - \frac{f_i}{r} \right) g_i \right] dr, \quad (2.15)$$

$$K_{[9,\dots,12]} = b \sum_{i=1}^3 \int_{R_i}^{R_{i+1}} \frac{E_i(1-\nu_i)}{(1-2\nu_i)(1+\nu_i)} \left[\frac{1}{r} f_i^2, \frac{1}{r} g_i^2, \frac{1}{r} f_i g_i, \frac{1}{r} \left(\frac{dg_i}{dr} \right)^2 \right] dr \quad (2.16)$$

$$K_{[13,\dots,16]} = b \sum_{i=1}^3 \int_{R_i}^{R_{i+1}} \frac{E_i \nu_i}{(1-2\nu_i)(1+\nu_i)} \left[r \frac{dg_i}{dr}, \frac{dg_i}{dr}, f_i \frac{dg_i}{dr}, g_i \frac{dg_i}{dr} \right] dr, \quad (2.17)$$

$$M_{[1,2,3,4,5,6,7,8]} = b \sum_{i=1}^3 \int_{R_i}^{R_{i+1}} \rho_i [r, r^2, r^3, r f_i, r^2 f_i, r f_i^2, r g_i, r g_i^2] dr, \quad (2.18)$$

where $f_i = f_i(r)$ and $g_i = g_i(r)$. The kinematic and natural boundary conditions specified at $\varphi = 0$ and $\varphi = \vartheta$, are given by

KINEMATIC	NATURAL
$v_0 = 0$	or $F_{11} \frac{\partial^2 w_0}{\partial \varphi^2} + F_{12} \frac{\partial v_0}{\partial \varphi} + F_{13} \frac{\partial v_1}{\partial \varphi} + F_{14} w_0 + F_{15} w_1 = 0,$
$w_0 = 0$	or $F_{21} \frac{\partial^3 w_0}{\partial \varphi^3} + F_{22} \frac{\partial^2 v_0}{\partial \varphi^2} + F_{23} \frac{\partial^2 v_1}{\partial \varphi^2} + F_{24} \frac{\partial^3 w_0}{\partial \varphi^2 \partial t} +$ $+ F_{25} \frac{\partial^2 v_0}{\partial t^2} + F_{26} \frac{\partial^2 v_1}{\partial t^2} = 0,$ (2.19)
$v_1 = 0$	or $F_{31} \frac{\partial^2 w_0}{\partial \varphi^2} + F_{32} \frac{\partial v_0}{\partial \varphi} + F_{33} \frac{\partial v_1}{\partial \varphi} + F_{34} w_0 + F_{35} w_1 = 0,$
$\frac{\partial w_0}{\partial \varphi} = 0$	or $F_{41} \frac{\partial^2 w_0}{\partial \varphi^2} + F_{42} \frac{\partial v_0}{\partial \varphi} + F_{43} \frac{\partial v_1}{\partial \varphi} + F_{44} w_0 + F_{45} w_1 = 0,$
$w_1 = 0$	or $F_{51} \frac{\partial w_1}{\partial \varphi} + F_{52} v_1 = 0,$

where F_{ij} are constants. For the special case of a simply supported curved band, the first, third and fourth natural boundary conditions are combined with the kinematic condition, $w_0 = w_1 = 0$.

3. Solution for a simply supported curved band

Sinusoidal mode shapes that satisfy the boundary conditions are assumed. Consequently, the assumed displacements are:

$$w_0(\varphi, t) = W_0 \cdot \sin(k_n \varphi) e^{i\omega_n t}, \quad (3.1)$$

$$w_1(\varphi, t) = W_1 \cdot \sin(k_n \varphi) e^{i\omega_n t}, \quad (3.2)$$

$$v_0(\varphi, t) = V_0 \cdot \cos(k_n \varphi) e^{i\omega_n t}, \quad (3.3)$$

$$v_1(\varphi, t) = V_1 \cdot \cos(k_n \varphi) e^{i\omega_n t}, \quad (3.4)$$

where $k_n = (n\pi)/\vartheta$. Since the motion is now harmonic, it is justified to admit hysteretic damping into the viscoelastic layer by putting complex moduli. The Young's and shear modulus of the constituent materials are represented by the complex quantities

$$E_2^* = E_2(1 + i\alpha_2), \quad G_2^* = G_2(1 + i\beta_2), \quad (3.5)$$

where α_2 and β_2 denote the material loss factors in extension and shear, respectively. Since G_2^* and E_2^* are used as complex moduli of the middle layer, the differential equations of motion will have complex coefficients. The substitution of equations (3.1),

(3.2), (3.3) and (3.4) into equations (2.10-2.13), will result in a set of four simultaneous, homogeneous algebraic equations with symmetric and complex coefficients. In matrix form, these equations are

$$[-\omega_n^2 [M] + [Y]] \{U\} = 0, \quad \{U\} = \{V_0, V_1, W_0, W_1\} \quad (3.6)$$

where M_{ij} and Y_{ij} are in the Appendix. The complex eigenvalues give the desired natural frequencies and mode shapes with their phase relations. The natural frequency is approximately equal to the square root of the real part of the eigenvalue. The modal loss factor for the n -th mode is approximately equal to the ratio of the imaginary part of the eigenvalue to the real part of the eigenvalue

$$\eta_n = \text{Im}(\omega_n^2) / \text{Re}(\omega_n^2). \quad (3.7)$$

4. Improved estimate for shear correction functions $f(r)$ and $g(r)$

An improved estimate for the correction functions $f(r)$ and $g(r)$ is derived from the equation of elementary stress equilibrium. The equations of motion in plane strain

$$\frac{\partial}{\partial r} [r^2 \tau_{r\varphi}] + r \frac{\partial \sigma_\varphi}{\partial \varphi} = r^2 \rho \frac{\partial^2 u}{\partial t^2}, \quad (4.1)$$

$$r \frac{\partial \sigma_r}{\partial r} + \sigma_r + \frac{\partial \tau_{r\varphi}}{\partial \varphi} - \sigma_\varphi = r \rho \frac{\partial^2 w}{\partial t^2}, \quad (4.2)$$

applied to the layered curved band with $\sigma_{\varphi i} = E_i(\varepsilon_{\varphi i} + \nu_i \varepsilon_{r i}) / (1 - \nu_i^2)$ expressions, are now in the form

$$\begin{aligned} \frac{\partial}{\partial r} (r^2 \tau_{r\varphi i}) + \frac{E_i (1 - \nu_i)}{(1 - 2\nu_i)(1 + \nu_i)} \left[\frac{r}{R} \frac{\partial^2 v_0}{\partial \varphi^2} - \frac{r - R}{R} \frac{\partial^3 w_0}{\partial \varphi^3} + \right. \\ \left. + f_i(r) \frac{\partial^2 v_1}{\partial \varphi^2} + \frac{\partial w_0}{\partial \varphi} + g_i(r) \frac{\partial w_1}{\partial \varphi} \right] + r \frac{E_i \nu_i}{(1 - 2\nu_i)(1 + \nu_i)} \frac{dg_i}{dr} \frac{\partial w_1}{\partial \varphi} = \\ = r^2 \rho_i \left[\frac{\partial^2 v_0}{\partial t^2} - \frac{r - R}{R} \left(\frac{\partial^3 w_0}{\partial \varphi \partial t^2} - \frac{\partial^2 v_0}{\partial t^2} \right) + f_i(r) \frac{\partial^2 v_1}{\partial t^2} \right], \quad (4.3) \end{aligned}$$

$$\begin{aligned} r \frac{\partial \sigma_r}{\partial r} + \sigma_r - \frac{1}{r} \frac{E_i (1 - \nu_i)}{(1 - 2\nu_i)(1 + \nu_i)} \left[\frac{r}{R} \frac{\partial v_0}{\partial \varphi} - \frac{r - R}{R} \frac{\partial^2 w_0}{\partial \varphi^2} + f_i(r) \frac{\partial v_1}{\partial \varphi} + w_0 + g_i(r) w_1 \right] - \\ - \frac{E_i \nu_i}{(1 - 2\nu_i)(1 + \nu_i)} \frac{dg_i}{dr} w_1 + \frac{\partial \tau_{r\varphi i}}{\partial \varphi} = r \rho_i \left(\frac{\partial^2 w_0}{\partial t^2} + g_i(r) \frac{\partial^2 w_1}{\partial t^2} \right), \quad (4.4) \end{aligned}$$

where $i = 1, 2, 3$ and $R_i \leq r \leq R_{i+1}$.

Using equations (2.3), (3.1), (3.2), (3.3) and (3.4), it is obvious that equations (4.3) and (4.4) can be written the following form

$$\begin{aligned} \frac{d}{dr} (r^2 \tau_{r\varphi i}^\circ) + \frac{E_i (1 - \nu_i)}{(1 - 2\nu_i)(1 + \nu_i)} \left[-\frac{r}{R} k_n^2 V_0 + \frac{r - R}{R} k_n^3 W_0 - f_i(r) k_n^2 V_1 + \right. \\ \left. + k_n^2 W_0 + g_i(r) k_n^2 W_1 \right] + r \frac{E_i \nu_i}{(1 - 2\nu_i)(1 + \nu_i)} \frac{dg_i}{dr} k_n W_1 = \end{aligned}$$

$$= -r^2 \rho_i \omega_n^2 \left[V_0 - \frac{r-R}{R} (k_n W_0 - V_0) + f_i(r) V_1 \right], \quad (4.5)$$

$$\begin{aligned} r \frac{d\sigma_{ri}^\circ}{dr} + \sigma_{ri}^\circ(r) - \frac{1}{r} \frac{E_i(1-\nu_i)}{(1-2\nu_i)(1+\nu_i)} \left[-\frac{r}{R} k_n V_0 + \frac{r-R}{R} k_n^2 W_0 - f_i(r) k_n V_1 + \right. \\ \left. + W_0 + g_i(r) W_1 \right] - \frac{E_i \nu_i}{(1-2\nu_i)(1+\nu_i)} \frac{dg_i}{dr} W_1 - k_n \tau_{r\varphi i}^\circ(r) = -r \rho_i \omega_n^2 (W_0 + g_i(r) W_1), \end{aligned} \quad (4.6)$$

where $\tau_{r\varphi i}(r, \varphi, t) = \tau_{r\varphi i}^\circ(r) \cos(k_n \varphi) e^{i\omega_n t}$ and $\sigma_{ri}(r, \varphi, t) = \sigma_{ri}^\circ(r) \sin(k_n \varphi) e^{i\omega_n t}$. The shape of the shear stress distribution can be found by integrating equation (4.5) through the thickness

$$\begin{aligned} \tau_{r\varphi i}^\circ(r) = -\frac{1}{r^2} \int_{R_i}^r \left\{ r^2 \rho_i \omega_n^2 \left[V_0 - \frac{r-R}{R} (k_n W_0 - V_0) + f_i(r) V_1 \right] + \right. \\ \left. + r \frac{E_i \nu_i}{(1-2\nu_i)(1+\nu_i)} \frac{dg_i}{dr} k_n W_1 - \frac{E_i(1-\nu_i)}{(1-2\nu_i)(1+\nu_i)} \left[\frac{r}{R} k_n^2 V_0 - \frac{r-R}{R} k_n^3 W_0 + f_i(r) k_n^2 V_1 \right. \right. \\ \left. \left. - k_n^2 W_0 - g_i(r) k_n^2 W_1 \right] \right\} dr + \frac{1}{r^2} c_i, \end{aligned} \quad (4.7)$$

where

$$c_1 = 0, \quad c_2 = R_2^2 \tau_{r\varphi 1}^\circ(R_2), \quad c_3 = R_3^2 \tau_{r\varphi 2}^\circ(R_3). \quad (4.8)$$

Then if equation (4.7) is used in equation (4.6), the shape of the normal stress distribution can be found by integrating equation (4.6) through the thickness

$$\begin{aligned} \sigma_{ri}^\circ(r) = -\frac{1}{r} \int_{R_i}^r \left\{ r \rho_i \omega_n^2 (W_0 + g_i(r) W_1) - \frac{E_i \nu_i}{(1-2\nu_i)(1+\nu_i)} \frac{dg_i}{dr} W_1 - k_n \tau_{r\varphi i}^\circ(r) - \right. \\ \left. - \frac{1}{r} \frac{E_i(1-\nu_i)}{(1-2\nu_i)(1+\nu_i)} \left[-\frac{r}{R} k_n V_0 + \frac{r-R}{R} k_n^2 W_0 - f_i(r) k_n V_1 + W_0 + g_i(r) W_1 \right] \right\} dr + \frac{1}{r} d_i, \end{aligned} \quad (4.9)$$

where

$$d_1 = 0, \quad d_2 = R_2 \sigma_{r1}^\circ(R_2), \quad d_3 = R_3 \sigma_{r2}^\circ(R_3). \quad (4.10)$$

The shape of the tensile strain distribution ε_{ri} is calculated using equation (4.9) and the constitutive equation (2.5)

$$\varepsilon_{ri}^\circ(r) = (1 - \nu_i^2) \frac{\sigma_{ri}^\circ(r)}{E_i} - \nu_i \varepsilon_{\varphi i}^\circ(r), \quad (4.11)$$

where $\varepsilon_{ri}(r, \varphi, t) = \varepsilon_{ri}^\circ(r) \sin(k_n \varphi) e^{i\omega_n t}$ and $\varepsilon_{\varphi i}(r, \varphi, t) = \varepsilon_{\varphi i}^\circ(r) \sin(k_n \varphi) e^{i\omega_n t}$.

Upon substitution of equation (4.11) into equation (2.4), the new estimate for the normal correction function $g(r)$ obtained by integrating equation (2.4) through the thickness, is given by

$$g_1(r) = \int_R^{R_2} \frac{1}{W_1} \varepsilon_{r2}^\circ(r) dr + \int_{R_2}^r \frac{1}{W_1} \varepsilon_{r1}^\circ(r) dr, \quad R_1 \leq r \leq R_2, \quad (4.12)$$

$$g_2(r) = \int_R^r \frac{1}{W_1} \varepsilon_{r2}^\circ(r) dr, \quad R_2 \leq r \leq R_3, \quad (4.13)$$

$$g_3(r) = \int_R^{R_3} \frac{1}{W_1} \varepsilon_{r2}^\circ(r) dr + \int_{R_3}^r \frac{1}{W_1} \varepsilon_{r3}^\circ(r) dr, \quad R_3 \leq r \leq R_4. \quad (4.14)$$

Evidently $g(R) = g_2(R) = 0$ at the reference axis.

The shape of the shear strain distribution is calculated using equation (4.7) and the constitutive relation

$$\gamma_{r\varphi i}^\circ(r) = \frac{\tau_{r\varphi i}^\circ(r)}{G_i}, \quad i = 1, 2, 3 \quad (4.15)$$

where $\gamma_{r\varphi i}(r, \varphi, t) = \gamma_{r\varphi i}^\circ(r) \cos(k_n \varphi) e^{i\omega_n t}$.

Upon substitution of equation (4.15) into equation (2.3) and using equations (4.12-4.14), the new estimate for the shear correction function $f(r)$ obtained by integrating equation (2.3) through the thickness, is given by

$$f_1(r) = r \left[\int_R^{R_2} \frac{1}{r} \left[\frac{\gamma_{r\varphi 2}^\circ(r)}{G} - k_n \frac{W_1 g_2(r)}{rG} \right] dr + \int_{R_2}^r \frac{1}{r} \left[\frac{\gamma_{r\varphi 1}^\circ(r)}{G} - k_n \frac{W_1 g_1(r)}{rG} \right] dr \right], \quad (4.16)$$

where $R_1 \leq r \leq R_2$

$$f_2(r) = r \int_R^r \frac{1}{r} \left[\frac{\gamma_{r\varphi 2}^\circ(r)}{G} - k_n \frac{W_1 g_2(r)}{rG} \right] dr, \quad R_2 \leq r \leq R_3 \quad (4.17)$$

and

$$f_3(r) = r \left[\int_R^{R_3} \frac{1}{r} \left[\frac{\gamma_{r\varphi 2}^\circ(r)}{G} - k_n \frac{W_1 g_2(r)}{rG} \right] dr + \int_{R_3}^r \frac{1}{r} \left[\frac{\gamma_{r\varphi 3}^\circ(r)}{G} - k_n \frac{W_1 g_3(r)}{rG} \right] dr \right] \quad (4.18)$$

where $R_3 \leq r \leq R_4$ and evidently $f(R) = f_2(R) = 0$ at the reference axis. The integrals in equations (4.7-4.18) are evaluated numerically using a trapezoidal method and $f(r)$ and $g(r)$ can be complex quantities. This new estimates of $f(r)$ and $g(r)$ are used as the correction functions for the next iteration. As with any smeared laminate model, there are two distinct ways to calculate the shear stress distribution: from the material constitutive relations; or by the elementary stress equilibrium. The ultimate goal of the iterative analysis is the determination of the functions, $f(r)$ and $g(r)$, that cause the two stress distributions to be equal. This defines the convergence point for the iterative functions $f(r)$ and $g(r)$, the point at which the stresses and strains are self-consistent.

Table 1

Variation of the lowest frequency and the loss factor with adhesive shear modulus

G_2 [N/m^2]	[20]		Present theory	
	f [Hz]	η	f [Hz]	η
$6,88 \cdot 10^4$	7,898	0,0644	7,508	0,0624
$6,88 \cdot 10^5$	11,36	0,2504	10,72	0.248
$6,88 \cdot 10^6$	20,94	0,1696	19,81	0.173
$6,88 \cdot 10^7$	25,8	0,0272	24,55	0.0281
$6,88 \cdot 10^8$	26,47	0,0029	25,23	0,00348

5. Results and discussion

Numerical results were generated to observe the effects of curvature, core thickness and adhesive shear modulus on the system natural frequencies ω_n and modal loss factors η_n . Vaswani et al. [20] assembled a series of design curves for the dynamic characterization of a three-layer damped circular ring segment which is simply supported at each end, see Fig.1. The model assumes that all transverse shear deformation and energy dissipation occurs in the core material. The dissipation is modeled using a complex modulus formulation. The resonant frequencies and the associated system loss factor have been experimentally determined for four sandwich beam specimens and the values compared with those obtained theoretically. Reasonably good agreement is seen between the theoretical and experimental results. However, the model of Vaswani et al. overpredicts natural frequencies by 5%, approximately. The present smeared laminate model was compared to the design curves of Vaswani et al. for the first transverse modes presented in the paper by Vaswani et al., with simply supported boundary conditions.

Table 2

Variation of the lowest frequency with adhesive thickness

$2h_2$ [mm]	[20]	Present theory
	f [Hz]	f [Hz]
1,0	17,981	17,028
2,0	19,1	18,125
3,0	20,09	19,04
4,0	20,94	19,81
5,0	21,66	20,47

The adhesive shear modulus plays a very important role in the damping of a sandwich curved band. The variations of the lowest natural frequency and the associated loss factor with respect to the shear modulus G_2 (= real part of G_2^*) are given in Table 1 for the three layer arch using the design curves of Vaswani et al. and the present laminate model. The input data used here were $h_1 = h_2 = h_3 = 2.0$ mm, $\nu = 1.0$, $\alpha_2 = \beta_2 = 0.5$, $R = 1.0$ m, $E_1 = E_3 = 6.88 \cdot 10^{10}$ N/m², $G_1 = G_3 = 2.75 \cdot 10^{10}$ N/m²,

$\rho_1 = \rho_3 = 2.7 \cdot 10^3 \text{ kg/m}^3$, $\rho_2 = \rho_1/2$. G_2 varied from $6.88 \cdot 10^4 \text{ N/m}^2$ to $6.88 \cdot 10^8 \text{ N/m}^2$ and $E_2 = 2.5 \cdot G_2$. The present smeared laminate model frequency predictions are generally consistent with the results of Vaswani et al. The slight discrepancy is due to facesheet shear and rotary inertia, effects which the model of Vaswani *et al.* does not consider. The model of Vaswani et al. overpredicts natural frequencies by 5%, approximately. The modal loss factors predicted by the present laminate model are also in good agreement with the results of Vaswani et al. The variation of the system loss factor η with the shear modulus G_2 is similar to that obtained for straight sandwich beams. For each core thickness, a maximum is observed which increases as the core thickness increases and is also seen to occur at higher values of the shear modulus. At low values of the shear modulus, although the deformations are large, shear stiffness is small, hence low damping is observed. At very high values of the shear modulus, the shear stiffness is high and the deformations are small, again resulting in low damping.

Table 3

Variation of the loss factor with adhesive thickness

	[20]	Present theory
$2h_2$ [mm]	η	η
1,0	0,0546	0.0562
2,0	0,1	0.102
3,0	0,138	0.141
4,0	0,1696	0.173
5,0	0,196	0,199

The effects of the adhesive thickness $2h_2$ on the system natural frequencies and loss factors are also studied. The input data in this case were $h_1 = h_3 = 2.0 \text{ mm}$, $\nu = 1.0$, $\alpha_2 = \beta_2 = 0.5$, $R = 1.0 \text{ m}$, $E_1 = E_3 = 6.88 \cdot 10^{10} \text{ N/m}^2$, $G_1 = G_3 = 2.75 \cdot 10^{10} \text{ N/m}^2$, $\rho_1 = \rho_3 = 2.7 \cdot 10^3 \text{ kg/m}^3$, $\rho_2 = \rho_1/2$, $G_2 = 6.88 \cdot 10^4 \text{ N/m}^2$, $E_2 = 2.5 \cdot G_2$. The thickness $2h_2$ was increased from 1.0 mm to 5.0 mm in steps of 1.0 mm . The variations of f and η with $2h_2$ are given in Tables 2-3. It can be seen from these Tables that both f and η increase with $2h_2$.

Table 4

Variation of the lowest frequency with radius R

	[20]	Present theory
R [mm]	f [Hz]	f [Hz]
800	29,75	28,1
900	24,78	23,42
1000	20,94	19,81
1100	17,9	16,95
1200	15,469	14,658

The third parameter which effects the system natural frequencies and modal loss factors is the radius of curvature R of the middle surface of the adhesive layer. In this case, the angle v is kept constant, while changing R . This means the total length of the sandwich arch system will change with R . The variations of f and η with R are shown in Tables 4-5. The input data was $h_1 = h_2 = h_3 = 2.0 \text{ mm}$, $v = 1.0$, $\alpha_2 = \beta_2 = 0.5$, $E_1 = E_3 = 6.88 \cdot 10^{10} \text{ N/m}^2$, $G_1 = G_3 = 2.75 \cdot 10^{10} \text{ N/m}^2$, $\rho_1 = \rho_3 = 2.7 \cdot 10^3 \text{ kg/m}^3$, $\rho_2 = \rho_1/2$, $G_2 = 6.88 \cdot 10^4 \text{ N/m}^2$, $E_2 = 2.5 \cdot G_2$. R varied from 800 mm to 1200 mm in steps of 100 mm. It can be seen that f decreases with R . The variations of f with R are obvious, as the total length of the curved sandwich beam system increases with any increase in R .

Table 5

Variation of the loss factor with radius R .

R [mm]	[20]	Present theory
	η	f [Hz]
800	0,211	0,214
900	0,1895	0,193
1000	0,1696	0,173
1100	0,1516	0,155
1200	0,1357	0,1388

6. Conclusions

A new iterative laminate model has been presented for a thin sandwich arch that can accurately determine the dynamic stress distribution in soft as well as hard cored sandwich arches. This represents an advance over previous smeared laminate models, in which accurate estimates of the stress field were only possible if the assumed displacement field was a reasonable approximation of the actual displacement field.

References

1. CHIDAMPARAM, P. and LEISSA, A.W.: Vibrations of planar curved beams, rings, and arches. *Applied Mechanics Review*, **46**, (1993), 467-483.
2. LAURA, P.A.A. and MAURIZI, M.J.: Recent research on vibrations of arch-type structures. *The Shock and Vibration Digest*, **19**, (1987), 6-9.
3. MARKUS, S. and NANASI, T.: Vibrations of curved beams. *The Shock and Vibrations Digest*, **7**, (1981), 3-14.
4. DAVIS, R., HENSHELL, R.D. and WARBURTON, G.B.: Constant curvature beam finite elements for in-plane vibration. *Journal Sound and Vibrations*, **25**, (1972), 561-576.
5. AHMED, K.M.: Free vibrations of curved sandwich beams by the method of finite elements. *Journal Sound and Vibrations*, **18**, (1971), 61-74.
6. AHMED, K.M.: Dynamic analysis of sandwich beams. *Journal Sound and Vibrations*, **21**, (1972), 263-276.

7. DITARANTO, R.A.: Free and forced response of a laminated ring. *Journal of Acoustical Society of America*, **53**, (1973), 748-757.
8. LU, Y.P. AND DOUGLAS, B.E.: On the forced vibrations of three-layer damped sandwich ring. *Journal Sound and Vibrations*, **32**, (1974), 513-516.
9. SAGARTZ, M.J.: Transient response of three-layered rings. *Journal Applied Mechanics*, **44**, (1977), 299-304.
10. TATEMACHI, A., OKAZAKI, A. and HIKAYAMA, M.: Damping properties of curved sandwich beams with viscoelastic layer. *Bulletin of Nagaya Institute*, **29**, (1980), 309-317.
11. NELSON, F. C. and SULLIVAN, D.F.: The Forced vibrations of a three-layer damped circular ring. *Journal of American Society of Mechanical Engineers*, **154**, (1977), 1-8.
12. ISVAN, O. and NELSON, F. C.: Free vibrations of a three-layer damped circular ring segment. *Mecanique Materiaux Electricite*, **394-395**, (1982), 447-449.
13. KOVACS, B.: Free vibrations of a layered damped arch. *Publications of the University of Miskolc*, **36**, (1996), 65-76.
14. LIAO, C. and REDDY, J.N.: Analysis of anisotropic, stiffened composite laminates using a continuum-based shell element. *Computers and Structures*, **34**, (1990), 805-815.
15. BHIMARADDI, A., CARR, A.J. and MOSS, P.J.: Generalized finite element analysis of laminated curved beams with constant curvature. *Computers and Structures*, **31**, (1989), 309-317.
16. QATU, M.S.: In-plane vibration of slightly curved laminated composite beams. *Journal of Sound and Vibrations*, **159**, (1992), 327-338.
17. QATU, M.S. and ELSHARKAWY, A.A.: Vibration of laminated composite arches with deep curvature and arbitrary boundaries. *Computers and Structures*, **47**, (1993), 305-311.
18. QATU, M.S.: Equations for the analysis of thin and moderately thick laminated composite curved beams. *International Journal of Solid and Structures*, **30**, (1992), 2743-2756.
19. YILDIRIM, V.: Rotary inertia, axial and shear deformation effects on the in-plane natural frequencies of symmetric cross-ply laminated circular arches. *Journal of Sound and Vibration*, **224**, (1999), 575-589.
20. VASWANI, J., ASNANI, N.T. and NAKRA, B.C.: Vibration and damping analysis of curved sandwich beams with a viscoelastic core. *Composite structures*, **10**, (1988), 231-245.
21. HE, S. and RAO, M.D.: Prediction of loss factors of curved sandwich beams. *Journal of Sound and Vibration*, **159**, (1992), 101-113.
22. ZAPFE, J. A. and LESIEUTRE, G. A.: Vibration analysis of laminated beams using an iterative smeared laminate model. *Journal of Sound and Vibration*, **199**, (1997), 275-284.
23. KOVACS, B., SZABO, F.J. and DOBROCZONI, A.: Free vibrations of a layered circular ring segment. *microCAD-SYSTEM '93 International Computer Science Meeting Proceeding*, Miskolc, Hungary, (1993), 65-77.
24. KOVACS, B.: *Vibration and stability of layered circular arch*, Ph.D. thesis, Hungarian Academy of Sciences, Budapest, (1992). (in Hungarian)
25. ROSSETTOS, J.N.: Vibration of slightly curved beams of transversely isotropic composite materials. *American Institute of Aeronautics and Astronautic Journal*, **9**, (1971), 2273-2275.

26. ROSSETTOS, J.N. and SQUIRES, D.C.: Modes and frequencies of transversely isotropic slightly curved Timoshenko beams. *Journal of Applied Mechanics*, **40**, (1973), 1029-1033.
27. KHDEIR, A.A. and REDDY, J.N.: Free and forced vibration of cross-ply laminated composite shallow arches. *International Journal of Solids and Structures*, **34**, (1997), 1217-1234.
28. YILDIRIM, V. : Out-of-plane free vibration characteristics of symmetric cross-ply laminated composite arches with deep curvature. *Journal of the Mechanical Behavior of Materials*, **10**, (1999), 165-186.

Appendix A. NOMENCLATURE

b	width of the curved band
E_i	elastic modulus of layer i
E_2^*	complex modulus in tension
\mathbf{e}_r	unit vector in the radial direction
\mathbf{e}_φ	unit vector in the transverse direction
\mathbf{e}_z	unit vector in the z-direction
$\varepsilon_{\varphi i}$	tensile strain of layer i in the transverse direction
$\varepsilon_{r i}$	tensile strain of layer i in the radial direction
$f(r)$	shear correction function
$g(r)$	normal correction function
$\gamma_{r\varphi i}$	shear strain of layer i
G_2^*	complex modulus in shear
G_i	shear modulus of layer i
h_i	half-thickness of layer i
φ	circumferential coordinate
n	mode number
r	cylindrical coordinate
R	radius of middle surface of the curved band
T	kinetic energy
$\sigma_{\varphi i}$	tensile stress of layer i in the transverse direction
$\sigma_{r i}$	tensile stress of layer i in the radial direction
$\tau_{r\varphi i}$	shear stress of layer i
\mathbf{t}_i	displacement vector of layer i
R_1	radius at the bottom of the first layer
R_2	radius at the top of the first layer
R_3	radius at the bottom of the third layer
R_4	radius at the top of the third layer
α_2	material loss factor in tension of the second layer
β_2	material loss factor in shear of the second layer
η_n	composite loss factor for the n -th mode
ω_n	frequency of oscillation in radians for the n -th mode
f_n	frequency of oscillation in Hertz for the n -th mode
ρ_i	density of layer i

ϑ	opening angle of the curved band
v_0	tangential displacement of the middle surface
w_0	radial displacement of the middle surface

Appendix B. Definitions for the various coefficients

Equations (2.10) to (2.13) in the main text contain certain A_{ij} and D_{ij} terms which are defined as follows:

$$\begin{aligned}
A_{11} &= K_3 + K_2/R^2 - 2K_1/R, & A_{12} &= 2K_3 - 2K_1/R, & A_{13} &= -K_2/R^2 + K_1/R \\
A_{14} &= K_6 - K_4/R, & A_{15} &= K_1/R, & A_{16} &= K_6, & A_{17} &= K_{14} + K_7 - K_{13}/R - K_5/R \\
A_{18} &= K_3, & A_{19} &= K_{14} + K_7, & A_{21} &= K_4/R - K_6, & A_{22} &= -K_6, & A_{23} &= -K_4/R, \\
A_{24} &= -K_9, & A_{25} &= K_{18} - K_{15} - K_{11}, & A_{26} &= K_{17} \\
A_{31} &= -K_{13}/R + K_{14} - K_5/R + K_7, & A_{32} &= -K_8, & A_{33} &= K_{13}/R + K_5/R \\
A_{34} &= K_{15} + K_{11} - K_{18}, & A_{35} &= K_7 + K_{14}, & A_{36} &= K_{12} + 2K_{16} + K_{10} \\
A_{41} &= K_2/R^2 - K_1/R, & A_{42} &= -K_1/R, & A_{43} &= -K_2/R^2, & A_{44} &= -K_4/R \\
A_{45} &= -K_{13}/R - K_5/R \\
D_{11} &= M_1 - 2M_2/R + M_3/R^2, & D_{12} &= M_2/R - M_3/R^2, & D_{13} &= M_4 - M_5/R \\
D_{14} &= -M_1, & D_{15} &= -M_7, & D_{21} &= -M_4 + M_5/R, & D_{22} &= -M_5/R \\
D_{23} &= -M_6, & D_{31} &= -M_7, & D_{32} &= -M_8, & D_{41} &= -M_2/R + M_3/R^2 \\
D_{42} &= -M_3/R^2, & D_{43} &= -M_5/R.
\end{aligned}$$

Equation (3.6) in the main text contain Y_{ij} and M_{ij} terms which are defined as follows:

$$\begin{aligned}
Y_{11} &= (2k_n^2 - 2k_n^4) K_1/R + k_n^4 K_2/R^2 + (1 - 2k_n^2 + k_n^4) K_3 \\
Y_{12} &= Y_{21} = -k_n K_6 + k_n^3 (K_6 - K_4/R), \\
Y_{14} &= Y_{41} = -k_n K_1/R + k_n^3 (K_1/R - K_2/R^2), \\
Y_{13} &= Y_{31} = K_{14} + K_7 - k_n^2 (K_{14} + K_7 - K_{13}/R - K_5/R), & Y_{22} &= K_{17} + k_n^2 K_9 \\
Y_{23} &= Y_{32} = k_n (K_{18} - K_{15} - K_{11}), & Y_{24} &= Y_{42} = k_n^2 K_4/R, & Y_{44} &= k_n^2 K_2/R^2 \\
Y_{33} &= K_{12} + 2K_{16} + K_{10} + k_n^2 K_8, & Y_{34} &= Y_{43} = -k_n (K_{13}/R + K_5/R) \\
M_{11} &= M_1 + k_n^2 (M_1 + M_3/R^2 - 2M_2/R), & M_{12} &= M_{21} = k_n (M_4 - M_5/R) \\
M_{13} &= M_{31} = M_7, & M_{14} &= M_{41} = k_n (M_2/R - M_3/R^2), & M_{22} &= M_6 \\
M_{24} &= M_{42} = M_5/R, & M_{33} &= M_8, & M_{44} &= M_3/R^2 \\
M_{23} &= M_{32} = M_{24} = M_{42} = 0.
\end{aligned}$$

MOBILITY AND STRESS ANALYSIS OF HIGHLY SYMMETRIC GENERALIZED BAR-AND-JOINT STRUCTURES

FLÓRIAN KOVÁCS

Research Group for Computational Mechanics, Hungarian Academy of Sciences
Department of Structural Mechanics, Budapest University of Technology and Economics
Műegyetem Rkp. 3–5, H-1521 Budapest, Hungary
kovacs@ep-mech.me.bme.hu

[Received: September 18, 2003]

Abstract. This paper discusses the possibility of detecting mechanisms with second-order stiffness (resistance to the excitation of an infinitesimal mechanism) imposed by self-stresses in highly symmetric structures. Coupled application of symmetry adapted first-order matrix analysis and a second-order stiffness analysis is performed, then the symmetry adapted form of that second-order analysis is presented, specifying conditions under which the stiffening effect of multiple states of self-stress can be analyzed. Finally, a generalized bar-and-joint model containing new kinematic scalar constraints and variables is proposed, with respect to their applicability in symmetry adapted and second-order analyses. The results are illustrated on structural models of viruses in biology with icosahedral symmetry.

Mathematical Subject Classification: 74A05

Keywords: symmetry, polyhedral, finite mechanism, second-order stiffness, product force

1. Introduction

Living systems in nature and engineering structures - consequently, their mechanical models as well - often show certain symmetry: it is enough to mention flowers, leaves, micro-organisms and architectonical solutions. These models, for having some degree of kinematical and statical indeterminacy, are usually highly indeterminate due to a high order of symmetry. Inclusion of symmetry properties in the computation can therefore be useful for two reasons: on the one hand, a given problem can often be reduced to a simpler one with less computational work by symmetry considerations, and on the other hand, clear description and physical interpretation of a multi-parameter system of self-stresses and displacements can hardly be made without using symmetry.

Since the first aim of this paper is to present a tool only for the detection and categorization of these mechanisms and states of self-stress, all further arguments and examples are based on the assumption of a perfectly rigid material behavior.

In the starting sections, a short review of existing analytical methods and a theoretical introduction of new ones are presented for classical bar-and-joint structures,

even if this simple model is not always applicable (or practical) for many structures. Our second aim is therefore to extend these analytical methods to generalized models containing various kinematic constraints instead of the only classical constant bar length, as well as to set up basic conditions for the type of extension that can match the original symmetry adapted techniques.

2. First-order calculations in symmetry adapted coordinate systems

If a compatibility or equilibrium matrix of a structure is given in an arbitrary coordinate system, it is a very simple task to determine the number of independent infinitesimal mechanisms and states of self-stress, since it depends only on the rank and dimensions of the matrix in case. Difficulties arise, however, when an attempt is made to characterize these mechanisms given on a general basis, knowing that all their linear combinations constitute another infinitesimal mechanism. A possible solution to this problem can be the choice of a special, symmetry adapted basis in which the compatibility matrix \mathbf{C} (consequently, equilibrium and stiffness matrices \mathbf{G} and \mathbf{R} as well) appears in a block-diagonal form according to symmetry properties.

The method of obtaining these bases was developed by Kangwai and Guest [1, 2] and it is built upon the foundations of group representation theory. In order to justify some of the later arguments, it is necessary to reassume the essential definitions, theorems and notations in this field.

Connection to group theory comes from the fact that symmetry can be interpreted as a set of symmetry operations like rotation or reflection, etc, applied to a geometrical object. It is a trivial statement that there always exists the identity operation and if two of all existing operations are done successively, the resultant operation is always found to be equivalent to one operation of the original set. For any operation there must also exist an inverse operation such that its application to the original one results in the identity operation. Fulfilling these conditions, symmetry operations of an object constitutes a group, and it is possible to assemble the full multiplication table of all operations of the group [3].

Operations in general have different representations among which the most common one is the so-called matrix representation: an operation is represented by a matrix multiplication that can express in the most natural way, for example, a coordinate-transformation in 3D space. It is very important, however, that any set of square matrices that obeys the multiplication table forms a matrix representation of the group. Among the infinite number of representations, there is, for example, a natural representation of the geometrical object that expresses transformations of all specific coordinates (in bar-and-joint structures, these are nodal coordinates). This representation is called external, in contrast to a similar possible representation that concerns transformations among internal forces and internal deformations belonging to the respective constraints. For illustration, let us consider a simple planar structure in Figure 1 with a classical - and instructive - C_{3v} symmetry. In this symmetry group, there are six operations: two rotations (by 120° and 240° , denoted as C_3 and C_3^2), three reflections (σ_v) and the identity (E). Concentrating on a simple operation

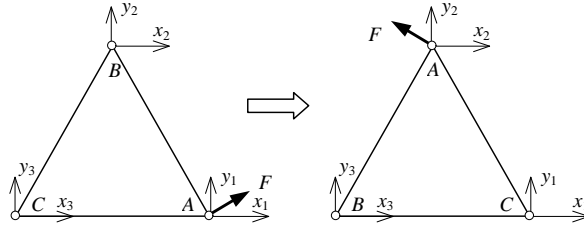


Figure 1. A structure with C_{3v} symmetry – rotation by 120° counter-clockwise

(counter-clockwise rotation by 120 degrees), one can observe what happens, for instance, to force F acting at node A . Looking only at the direction, new coordinates can be obtained from a multiplication by the matrix of rotation by 120° as follows:

$$\begin{bmatrix} x_{new} \\ y_{new} \end{bmatrix} = \begin{bmatrix} \cos 120^\circ & -\sin 120^\circ \\ \sin 120^\circ & \cos 120^\circ \end{bmatrix} \begin{bmatrix} x_{old} \\ y_{old} \end{bmatrix} = \mathbf{M}_{C3} \begin{bmatrix} x_{old} \\ y_{old} \end{bmatrix}. \quad (2.1)$$

Transformation matrices like in (2.1) can also be generated for all other operations in C_{3v} - these form a 2-by-2 representation of the group C_{3v} in general. Taking into account that a rotation of the object also shifts the nodes, equation (2.1) needs correction:

$$\begin{bmatrix} x_2^{new} \\ y_2^{new} \end{bmatrix} = \mathbf{M}_{C3} \begin{bmatrix} x_1^{old} \\ y_1^{old} \end{bmatrix}, \quad (2.2)$$

and since all the three nodes move, rotation of the whole object is described by

$$\begin{bmatrix} x_1^{new} \\ y_1^{new} \\ \vdots \\ y_3^{new} \end{bmatrix} = \begin{bmatrix} 0 & 0 & \mathbf{M}_{C3} \\ \mathbf{M}_{C3} & 0 & 0 \\ 0 & \mathbf{M}_{C3} & 0 \end{bmatrix} \begin{bmatrix} x_1^{old} \\ y_1^{old} \\ \vdots \\ y_3^{old} \end{bmatrix}, \quad (2.3)$$

where the 6-by-6 matrix is an external representation of the object under C_3 operation.

If internal forces and deformations are considered, the same rotation moves bar b_1 into bar b_2 etc., hence

$$\begin{bmatrix} b_1^{new} \\ b_2^{new} \\ b_3^{new} \end{bmatrix} = \begin{bmatrix} 0 & 0 & 1 \\ 1 & 0 & 0 \\ 0 & 1 & 0 \end{bmatrix} \begin{bmatrix} b_1^{old} \\ b_2^{old} \\ b_3^{old} \end{bmatrix} \quad (2.4)$$

and the 3-by-3 matrix is an internal representation of the object under the same operation. Note that general symbol b can refer to bar forces or elongations as well, while x_i, y_i may equally denote nodal force or displacement coordinates.

Matrix representations - as it happens to quadratic matrices - can undergo unitary transformations that generate another representation of the group. Some of them have all matrices in block-diagonal form but usually it is impossible to diagonalise all matrices of a representation with the same transformation. A set of blocks that cannot be split into smaller blocks is called ‘irreducible representation’ but since a set of n -by- n matrices can be operated on by further unitary transformations, the number

of irreducible representations is still infinite. Within this infinite set, there can be chosen only a few representations that cannot be transformed into each other by a unitary transformation. Their name is ‘non-equivalent irreducible representation’ [3] (note that the matrix forms of these few representations still depend on the vector basis, therefore it is not uniquely defined unless the dimension of matrices is 1 by 1).

From the character tables for group theory [4], the number and matrix dimensions of non-equivalent irreducible representations can be read, but beyond that, the table itself gives the characters (traces of matrices) of each representation row by row: in spite of the form of matrices, these are uniquely defined since left unchanged by unitary transformations. For example, in group C_{3v} there are three non-equivalent irreducible representations, two of them are 1-dimensional and denoted by A_1 and A_2 , the third one (E) is 2-dimensional (dimension numbers of a representation are always equal to the trace under identity in that representation). Since in C_{3v} there are 6 symmetry operations, it means 6 matrices and therefore 6 character values, but some of the operations (those belonging to the same *class*) have regularly the same character that is given in a single column. In our example there are three classes: identity belongs to the first one, while two rotations and three reflections compose the second and third ones, respectively. Thus, the character table for C_{3v} is as shown in Table 1:

	E	$2C_3$	$3\sigma_v$
A_1	1	1	1
A_2	1	1	-1
E	2	-1	0

Table 1. Character table of group C_{3v}

There exists a method for generating also matrix forms of multi-dimensional non-equivalent irreducible representations that are needed for further symmetry-analysis. It is shown in [1] that using the Great Orthogonality Theorem of group theory, it is possible to construct quadratic matrices that transform compatibility and rigidity matrices into a block-diagonal form, once a full set of non-equivalent irreducible representations of the group and an arbitrary internal and external representation of the object are given.

For instance, block-diagonalisation of a compatibility matrix can be written in the form

$$\mathbf{C}^S = \mathbf{V}_f^T \cdot \mathbf{C} \cdot \mathbf{V}_p, \quad (2.5)$$

where superscript S means symmetry adapted form, whilst \mathbf{V}_f and \mathbf{V}_p are orthogonal transformation matrices of internal and external quantities with subscripts f and p referring to internal bar force and external nodal load. The block structure of \mathbf{C}^S is determined by the number and dimension of non-equivalent irreducible representations: each representation means as many blocks as the dimension of its matrices. For illustration, \mathbf{C}^S of a structure with C_{3v} symmetry will assume the form shown in Figure 2:

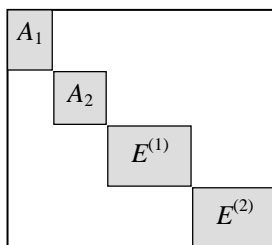


Figure 2. Block structure of compatibility matrix in symmetry adapted form with C_{3v} symmetry

In this symmetry adapted form it is possible to perform an independent analysis of each block that means practically a singular value decomposition: this is because any state of self-stress given by the left nullspace or mechanisms coming from the right nullspace of the matrix is within an invariant subspace associated with one of the blocks.

In addition to the reduced matrix calculations, mechanisms and self-stresses belonging to a given block display well-defined symmetry properties: for example, a mechanism or state of self-stress found in a block A must be left unchanged by any of the symmetry operations, which is why they are said to have full symmetry. Mechanisms and states of self-stress categorized by symmetry provide then a system where physical interpretation of mobility or possibilities of pre-stressing turns out to be more straightforward.

3. Problems of higher-order rigidity

Singular value decomposition accounts only for the existence of states of self-stress and infinitesimal mechanisms. This latter category, however, covers now three different cases. An infinitesimal mechanism can be a [5]

- a) first-order infinitesimal mechanism with additional stiffness provided by pre-stressing,
- b) first-order infinitesimal mechanism without additional stiffness or higher-order infinitesimal mechanism that can never be stiffened by pre-stressing,
- c) finite mechanism, always without additional stiffness.

We notice that an infinitesimal mechanism is of n -th order if there is at least one bar for which in the expansion of the Taylor-series of its elongation, the order of the first non-vanishing term is $n + 1$: a typical example for (a) is a linkage supported at two endpoints, with all nodes lying along a straight line; a first-order infinitesimal mechanism pertaining to case (b) is presented in [6]. In accordance with mechanisms, we define second-order stiffness: when there is a state of self-stress, and an infinitesimal mechanism is activated, unbalanced nodal forces appear. If the virtual work done by this force system on the mechanism is positive, then the self-stress is said to be able to impart second-order stiffness to the mechanism; if it holds for all possible mechanisms, then the whole structure has second-order stiffness.

Interestingly enough, some of the finite mechanisms can be detected even with first-order symmetry-analysis: if a block with full symmetry contains one or more mechanisms but no self-stress, then all displacements in the subspace spanned by vectors of these mechanisms must be finite [7]. Even if this procedure works only for full symmetry, it is possible to find an appropriate group for any symmetric mechanism where the respective mechanism is fully symmetric, and symmetry adapted diagonalization based on this group can also be performed. It is impossible to make a decision in this way about finiteness, however, when at least one fully symmetric state of self-stress appears.

Another approach to the question of rigidity leads to analyses of existence of additional stiffness: once it is proven, finiteness of the motion is ruled out. A method developed for this purpose by Pellegrino and Calladine [8] uses the concept of ‘product force’, defined as a nodal resultant of forces in adjacent bars when a single-parameter state of self-stress and a mechanism is activated to the structure. For example, a collinear linkage supported at two endpoints has a uniform tensional self-stress; moving internal nodes infinitesimally off the axis will induce also product force \mathbf{F}_1 shown in Figure 3.

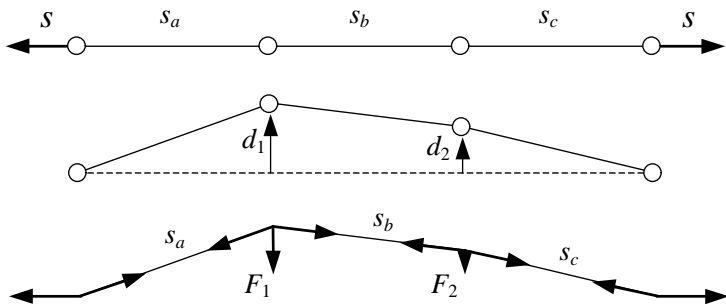


Figure 3. State of self-stress, mechanism and product forces

Magnitude of F_1 can be computed, based on the assumption of small displacements, as

$$F_1 = -d_1 \frac{s_a}{l_a} - d_1 \frac{s_b}{l_b} + d_2 \frac{s_b}{l_b}. \quad (3.1)$$

It can be proved in the same way that a general formula for product force at point P_i is

$$F_{ir} = -d_{ir} \sum_j \frac{s_{ij}}{l_{ij}} + \sum_j d_{jr} \frac{s_{ij}}{l_{ij}}, \quad (3.2)$$

where $r^o = {}^o x, {}^o y, {}^o z$, d_i denotes displacement components at point P_i , while j runs over all adjacent nodes; s_{ij} and l_{ij} are bar forces and lengths, respectively.

Consider a structure with n nodes and b bars. Let \mathbf{S} denote a diagonal matrix of self-stresses containing b diagonal blocks of dimension dim equal to that of the Euclidean space that the structure is defined in: i -th block $\mathbf{S}^{(i)}$ can be obtained as

$$\mathbf{S}_{(dim \times dim)}^{(i)} = \frac{s_i}{l_i} \mathbf{E}_{(dim \times dim)}. \quad (3.3)$$

Now a $(dim \times b)$ -by- $(dim \times n)$ matrix \mathbf{T} can be constructed: let a block t_{ij} be $\mathbf{E}_{(dim \times dim)}$ or $\mathbf{E}_{(dim \times dim)}$ if P_j is starting or endpoint of the i -th bar, respectively. With the help of \mathbf{T} and \mathbf{S} , the complementary stiffness matrix (\mathbf{Q}) of the given structure can be defined:

$$\mathbf{Q} = \mathbf{T}^T \cdot \mathbf{S} \cdot \mathbf{T} , \quad (3.4)$$

and one can verify that if \mathbf{d} is the vector of a mechanism, the product $\mathbf{d}^T \mathbf{Q}$ gives exactly the coordinates of all product forces.

Existence of stiffening by pre-stressing is tested by the following criterion: if the external work done by a displacement on the set of product forces generated by the same displacement vector is zero, no stiffening effect exists [9]. In terms of linear algebra, it means a quadratic form of zero value:

$$w = \mathbf{d}^T \mathbf{Q} \mathbf{d} = 0 . \quad (3.5)$$

The method is applicable also with k mechanisms: if these n column vectors are collected in a matrix \mathbf{D} , then the product

$$\mathbf{d} = \mathbf{D} \mathbf{a} , \quad (3.6)$$

gives their general linear combination ($\mathbf{a}^T = [\alpha_1^0 \dots \alpha_k^0]$). For this particular mechanism, the condition of zero external work (regarding that $(\mathbf{D} \mathbf{a})^T = \mathbf{a}^T \mathbf{D}^T$) yields

$$\mathbf{a}^T \mathbf{D}^T \mathbf{Q} \mathbf{D} \mathbf{a} = 0 . \quad (3.7)$$

Term $\mathbf{D}^T \mathbf{Q} \mathbf{D}$ is a symmetric n -by- n matrix called reduced complementary stiffness matrix [10] and denoted by \mathbf{W} , thus the left-hand side of (3.7) can again be written as a quadratic form $\mathbf{a}^T \mathbf{W} \mathbf{a}$. If coefficients in \mathbf{a} are considered to be variables, the analysis can be extended to all possible mechanisms. In this case, there is additional stiffness for all mechanisms if and only if matrix \mathbf{W} is definite.

Nevertheless, there is still an open question: what happens when self-stresses are multiple? For special two-parameter states of self-stress there can be found particular solutions in [9] but the problem is more complex when a structure has several states of self-stress with different symmetry properties.

4. Symmetry adapted second-order rigidity analysis

As shown, product force analysis does not require necessarily a symmetry adapted treatment but in some cases one can make use of it. In this section, a new symmetry adapted higher-order analysis will be described, pointing out some advantages and restrictions of its application.

To avoid confusion, matrices \mathbf{S} , \mathbf{Q} and \mathbf{W} will be indexed by serial numbers of independent states of self-stress found in the first-order analysis. Suppose that \mathbf{S}_1 is coming from the fully symmetric block: it is easy to see now that \mathbf{Q}_1 expresses full symmetry as well, consequently it can be block-diagonalised with the formula

$$\mathbf{Q}_1^S = \mathbf{V}_p^T \cdot \mathbf{Q}_1 \cdot \mathbf{V}_p , \quad (4.1)$$

while the transformation formula of displacement vectors \mathbf{d}_i into symmetry adapted system is

$$\mathbf{d}_i^S = \mathbf{V}_p^T \cdot \mathbf{d}_i . \quad (4.2)$$

It is possible then to perform the described matrix analysis in symmetry adapted system where displacement vectors have all zero values except for those being in the block of the representation where the displacement was found: in a fully symmetric displacement vector, for instance, only the first few entries are nonzero.

Consider now a matrix \mathbf{D}^S containing vectors that belong to different blocks. The structure of reduced complementary stiffness matrix can be illustrated by the scheme in Figure 4:

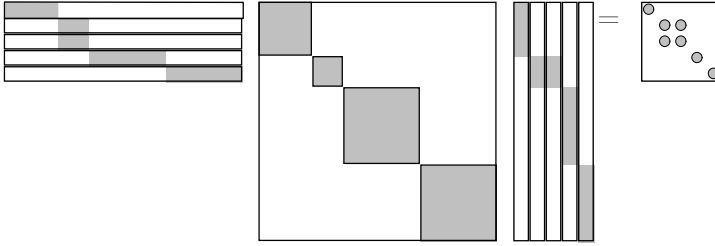


Figure 4. Block structure of product $(\mathbf{D}^S)^T \cdot \mathbf{Q}^S \cdot \mathbf{D}^S = \mathbf{W}^S$

An important conclusion may be drawn at this stage: having a fully symmetric state of self-stress, a reduced complementary stiffness matrix is always obtained in block-diagonal form (note that $\mathbf{W}^{S^o} = {}^o\mathbf{W}$, irrespective of intermediate steps made in the symmetry adapted system), hence a necessary condition for the existence of a global stiffening effect can be formulated as each set of displacements belonging to a given block must be stiffened by self-stress \mathbf{S}_1 , or in other words, blocks in \mathbf{W} must be definite in themselves.

Altogether, it is a true objection that a simple check for definiteness does not justify such amount of symmetry calculations: real applicability of symmetry adapted analysis is experienced when there are multiple states of self-stress.

Imagine a state of self-stress \mathbf{S}_k with lower symmetry than that of \mathbf{S}_1 : formula (4.1) now will not diagonalise the original matrix \mathbf{Q} but \mathbf{Q}^S will show considerable regularity. If there is a mechanism \mathbf{d}_l that belongs to a different representation

	A_1	A_2	E
A_1	A_1	A_2	E
A_2		A_1	E
E			$A_1^o + {}^o[A_2] + E$

Table 2. Direct product table of group C_{3v}

(therefore, certainly to a different block), the product force should ‘mix’ properties of the two symmetries. This effect can be read from direct product tables of groups [4]

and it says what kind of representations can ever appear in a direct product of two objects belonging to two representations. For illustration, Table 2 gives the direct product table of group C_{3v} .

If, for example, \mathbf{S}_k belongs to \mathbf{A}_2 and \mathbf{d}_l to E , representation of the resultant product force system may contain E -blocks only. This property is reflected in the structure of \mathbf{Q}_k in a way that in two block columns pertaining to E there are nonzero blocks only in block rows that belong to E . Matrix \mathbf{Q}_k is therefore still sparse, and it can happen that blocks in the main block diagonal are all empty. This is not simple coincidence, since direct product tables often rule out nonzero blocks in rows and columns pertaining to the same representation (e.g. from Table 2, it follows that a block pertaining to block row and column of A_2 must be empty, since a mechanism that belongs to A_2 cannot generate a product force system belonging to A_2 but A_1). The second reason for frequent appearance of zero diagonal blocks is that in case of representations with multiplicity μ there is a hyperblock of $\mu \times \mu$ blocks pertaining all to the same representation, hence non-empty block(s) can be located off the diagonal.

Finding a matrix \mathbf{Q}_k with empty diagonal blocks, it is easy to see from arguments like in Figure 4 that the main diagonal of \mathbf{W} is empty as well. Since unitary transformations used for the digitalization cannot modify the trace of matrix \mathbf{W} , among the eigenvalues of \mathbf{W} there must appear both positive and negative numbers, which is a proof of indefiniteness.

Consider now a set of states of self-stress ($\mathbf{S}_2, \dots, \mathbf{S}_\nu$) for which all complementary stiffness matrices in symmetry adapted form $\mathbf{Q}_2^S, \dots, \mathbf{Q}_\nu^S$ have empty diagonal blocks. In this case any linear combination of matrices \mathbf{Q}_i^S gives a resultant matrix with empty block-diagonal, therefore the respective matrix \mathbf{W} must also be indefinite. In mechanical aspect it means that *any* linear combination of these self-stresses is insufficient to provide additional stiffness to *any* linear combination of independent displacement vectors included in \mathbf{D}^S .

5. Generalized bar-and-joint structures: extension of results

The higher-order symmetry analysis presented in the previous section uses the supposition of kinematic constraints being constant bar lengths. This section deals with possible extensions of constraint types that fit both symmetry adapted and product force analyses in order that the analysis under Section 4 can also be performed.

Theoretically, symmetry adapted first-order computations are applicable to an arbitrary type of constraints, provided it does not break the symmetry of the whole object, or in other words, if there is an internal matrix representation for the object that gives full account of the topology. Since bar lengths are given by scalars, this representation contained only ones and zeros, but if a definite direction had been associated with the constraints, internal representations should contain minus ones as well (for example, rotation of a straight line segment about a perpendicular bisector seems to do nothing, while the same operation applied to an arrow reverses its direction). From the aspect of nodal coordinates, a generalization is possible by

introduction of single vectors. It will be useful when a folded structure is modelled: folding lines are inclined to each other with a given angle that can be prescribed by constant difference (or constant scalar product) of two vectors of fixed length, lying in the direction of folds. Similarly, an angle between a vector and a bar can also be prescribed by a scalar product or vector difference. There is, however, a necessary additional condition that vector lengths must be kept fixed. Numerically it means a constraint of constant vector norm.

An application of generalized constraints and nodes in first-order analysis is presented in [11, 12], here we restrict ourselves only to presenting a single example.

Consider two nodes P_i and P_j connected by a bar. Let this bar be an edge of a rectangular plate that is determined by a vector \mathbf{v}_k in the model: length and direction of \mathbf{v}_k is equal and parallel to the other edge of the modelled plate (Figure 5).

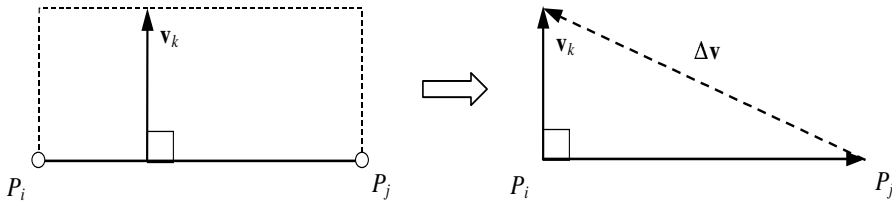


Figure 5. Bar and vector modelling a rectangular plate: difference of vectors \mathbf{v}_k and P_iP_j

It can be guaranteed by three types of constraint functions:

$$f_b = \sqrt{(x_j - x_i)^2 + (y_j - y_i)^2 + (z_j - z_i)^2} - l_{ij} \quad (5.1)$$

is for constant bar length P_iP_j ,

$$f_v = \sqrt{x_k^2 + y_k^2 + z_k^2} - l_k \quad (5.2)$$

fixes Euclidean norm of \mathbf{v}_k (here and in the sequel, x_k , y_k and z_k are relative vector coordinates, in contrast to absolute coordinates indexed by i and j), while

$$f_d = \sqrt{(x_k - (x_j - x_i))^2 + (y_k - (y_j - y_i))^2 + (z_k - (z_j - z_i))^2} - l_{ij,k} \quad (5.3)$$

expresses the constant difference of vectors P_iP_j and \mathbf{v}_k , denoted as $\Delta\mathbf{v}$ in Figure 5. Note that if there is a C_2 axis within the plane of the rectangle that shifts P_i and P_j , representation of f_b and f_v is +1 under this C_2 operation but it is -1 for f_d , otherwise the direction of the difference vector would break the symmetry.

Constraint functions in (5.1-5.2) were all generated in a form of vector difference. This is useful when a product force test is intended to be done. Method of constructing matrix \mathbf{Q} is based now on the same principles as in Section 3: vector norms and differences in constraints of type f_v and f_d generate force-like quantities along the respective directions. Their effect can now be taken into account by assembling matrices \mathbf{T} and \mathbf{S} in the same way as in the case of constraints f_b : a 3-by-3 diagonal block in \mathbf{T} , associated with a function f_v and f_d are filled with +1 if columns refer

to vector coordinates, while constraint of type f_d will mean an additional diagonal block of plus or minus ones in columns of edge starting or endpoints, respectively.

Note that entries of \mathbf{T} divided by vector norms or difference vector lengths can also be obtained as first-order approximation of second derivatives of the respective constraint function according to the variable in question. This approach to the problem of second-order stiffness is based on a regular second-order analysis of the original compatibility matrix of bar-and-joint structures [13]. For example, if f_d and y_k belong to m -th row and n -th column, respectively, of the compatibility matrix of a structure, entry t_{mn} can be obtained from

$$t_{mn} = l_{ij,k} \frac{\partial^2 f_d}{\partial y_k^2} \approx l_{ij,k} \frac{\partial \frac{y_k - (y_j - y_i)}{l_{ij,k}}}{\partial y_k} = +1. \quad (5.4)$$

An important remark: a similar extension of higher-order symmetry analysis is possible by using other constraint functions instead of vector differences (e.g. a scalar product), but the applicability of a product force test requires an exact statical interpretation of self-stress induced by the respective constraint, which is not always an easy problem to solve.

6. Expandedhedra: a numerical example

For better understanding, in this chapter two sample problems will be presented to illustrate practical applications for the theory above. The object of the analysis will be in both cases an assembly with icosahedral symmetry, called expandedhedron [14]. Expandedhedra are constructed to model the swelling of some viruses, and the denomination refers to a fully symmetric finite expansion.

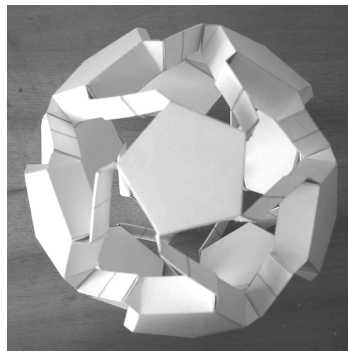
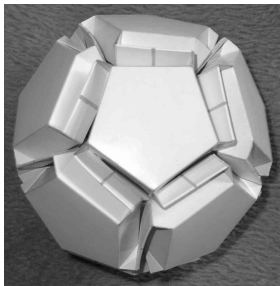


Figure 6. Cardboard model of an icosahedral expandedhedron

6.1. Single-link icosahedral expandedhedron. The assembly consists of rigid pentagonal prisms connected by a triangle-rectangle-triangle folded linkage of C_2 symmetry (connections between rigid elements are all revolute hinges). In the mechanical model, prisms were substituted by determinate bipyramidal bar-and-joint networks built upon the inner pentagonal faces, and new constraints shown in Section 5 were used to reduce matrix dimensions. The physical and mechanical models are sketched

in Figure 7, B and K are vertices of a bipyramid lying on its C_5 -axis, the constant length of dotted difference vector $\Delta \mathbf{v}$ fixes the constant angle of revolute hinges along the two edges of the triangular plates.

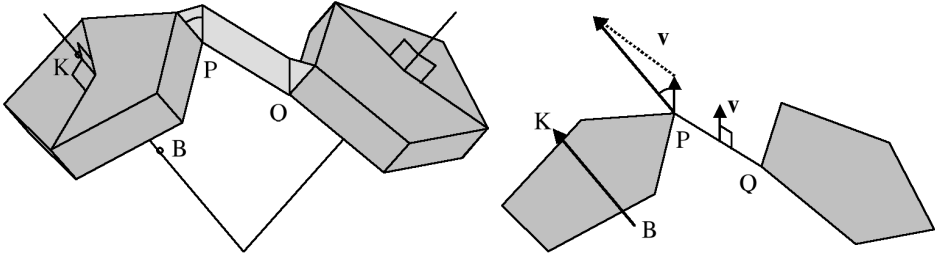


Figure 7. Physical (folded) and mechanical model for a single-link icosahedral expandohedron

Irrespective of the applied numerical model, this expandohedron must have a compatibility matrix with 12 rows less than the number of its columns, which means at least 12 independent displacement systems (six of them are due to rigid body motions). Assuming a general - not fully open - configuration, first-order symmetry adapted analysis showed that there are 9 extra mechanisms with 9 states of self-stress, in the following distribution:

Representation	Number of Blocks	General Configuration	
		Number of Mechanisms	Number of States of Self-stress
A	1	1	1
T_1	3	$3 \times 2 = 6$	0
T_2	3	$3 \times 1 = 3$	$3 \times 1 = 3$
G	4	0	0
H	5	$5 \times 1 = 5$	$5 \times 1 = 5$

Table 3. Mechanisms and states of self-stress of a single-link icosahedral expandohedron

Since there are both a fully symmetric mechanism and a state of self-stress, the finite character of swelling motion cannot be proved by symmetry arguments (nevertheless, there exists a geometrical proof). A simple product force test based on the fully symmetric state of self-stress, however, accounts for the existence of additional stiffness pertaining to all linear combinations of mechanisms except for that containing only the fully symmetric one. In other words: without using serious higher-order symmetry considerations we have proved the existence of exactly one finite (swelling) mechanism, all others can be blocked by self-stresses.

6.2. Double-link icosahedral expandohedron. In this model adjacent pentagonal bipyramids are connected by pairs of ball-jointed bars with C_2 symmetry.

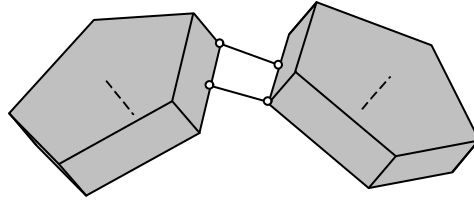


Figure 8. Ball-jointed connection of a double-link icosahedral expandohedron

Apart from rigid body motions, here are obtained six mechanisms again only from counting rows and columns of matrix \mathbf{C} . The result of first-order analysis is as follows:

Representation	Number of Blocks	General Configuration	
		Number of Mechanisms	Number of States of Self-stress
A	1	1	0
T_1	3	$3 \times 1 = 3$	0
T_2	3	0	$3 \times 1 = 3$
G	4	0	0
H	5	$5 \times 1 = 5$	0

Table 4. Mechanisms and states of self-stress of a double-link icosahedral expandohedron

Lack of fully symmetric self-stress indicates now finite expansion directly. The symmetry adapted form of matrices \mathbf{Q} based on each state of self-stress has all the empty diagonal blocks, therefore *neither* of the linear combinations of self-stresses can stiffen *any* linear combinations of mechanisms.

7. Conclusions

Symmetry-adapted higher-order mobility and stiffness analysis covers several sub-methods that were partially developed earlier: the first-order matrix analysis in symmetry adapted coordinate system and the product force test also for asymmetric structures are robust tools for investigation of bar-and-joint structures. It was shown, however, that efficiency can be increased by coupling the two methods: if there exists any, a fully symmetric state of self-stress - which is the most likely to impart second-order stiffness to a structure - can be identified by symmetry analysis. Existence or lack of second-order stiffness, however, can only be decided in a general case for a given state of self-stress by second-order analysis. The symmetry adapted version of this latter method simplifies calculations with fully symmetric states of self-stress and in some cases it accounts for the non-existence of stiffening effect for arbitrary linear combinations of self-stresses with lower symmetry.

A coupled symmetry and second-order stiffness analysis for bar-and-joint structures could be generalized to more complex mechanical models containing free vectors and

kinematic constraints formulated by a vector difference norm but it is possible to use another type of scalar constraints once a product force can be defined and symmetry group representations can be found.

Acknowledgement. The author gratefully acknowledges support from OTKA Grant nos. T031931 and T037880, as well as FKFP Grant no. 0177/2001.

References

1. KANGWAI, R.D.: *The Analysis of Symmetric Structures using Group Representation Theory*. PhD thesis, University of Cambridge, Department of Engineering, 1997.
2. KANGWAI, R.D., and GUEST, S.D.: Symmetry-adapted equilibrium matrices. *Int. J. Solids and Structures*, **37**, (2000), 1525–1548.
3. BISHOP, D.M.: *Group Theory and Chemistry*, Dover Publications Inc., 1974.
4. ATKINS, P.W., CHILD, M.S. and PHILLIPS, C. S. G.: *Tables for Group Theory*, Oxford University Press, 1970.
5. TARNAI, T.: Higher-order infinitesimal mechanisms. *Acta Technica Acad. Sci. Hung.* **102**(3-4), (1989), 363–378.
6. CONNELLY, R. and WHITELEY, W.: Second order rigidity and pre-stress stability for tensegrity frameworks. *SIAM J. Disc. Math.*, **9**, (1996), 453–491.
7. KANGWAI, R.D. and GUEST, S.D.: Detection of finite mechanisms in symmetric structures. *Int. J. Solids and Structures*, **36**, (1999), 5507–5527.
8. PELLEGRINO, S. and CALLADINE, C.R.: Matrix analysis of statically and kinematically indeterminate frameworks. *Int. J. Solids and Structures*, **22**, (1986), 409–428.
9. CALLADINE, C.R. and PELLEGRINO, S.: First-order infinitesimal mechanisms. *Int. J. Solids and Structures*, **27**, (1991), 505–515.
10. TARNAI, T. and SZABÓ, J.: *Rigidity and stability of prestressed infinitesimal mechanisms*. In: *New Approaches to Structural Mechanics, Shells and Biological Structures* (eds.: H.R. Drew and S. Pellegrino), Kluwer Academic Publishers, (2002), 245–256.
11. KOVÁCS, F., HEGEDŰS, I. and TARNAI, T.: *Movable Pairs of Regular Polyhedra*. In: *Proceedings of International Colloquium on Structural Morphology* (eds.: J.C. Chilton, B.S. Choo, W.J. Lewis and O. Popovic), Nottingham, (1997), 123–129.
12. KOVÁCS, F. and TARNAI, T.: An expandable dodecahedron. *HyperSpace*, **10**, (2001), 13–20.
13. SZABÓ, J. and ROLLER, B.: *Anwendung der Matrizenrechnung auf Stabwerke*, Akadémiai Kiadó, Budapest, 1978.
14. KOVÁCS, F., TARNAI, T., FOWLER, P.W. and GUEST, S.D.: A class of expandable polyhedral structures. *Int. J. of Solids and Structures* (2003, accepted for publication).

OPTIMUM DESIGN OF A COMPOSITE MULTICELLULAR PLATE STRUCTURE

GYÖRGY KOVÁCS

Department of Materials Handling and Logistics, University of Miskolc
3515 Miskolc-Egyetemváros, Hungary
altkovac@uni-miskolc.hu

[Received: November 27, 2003]

Dedicated to Professor József FARKAS on the occasion of his seventy-fifth birthday

Abstract. This study presents the optimal design of a new complex structural model [laminated carbon fiber reinforced plastic (CFRP) deck plates with aluminium (Al) stiffeners] which is depicted in Figure 1. The structure was designed both for minimal cost and minimal weight. Design constraints on maximum deflection of the total structure, buckling of the composite plates, buckling of the Al webs, stress in the composite plates and stress in the Al stiffeners are considered in the calculation. The Rosenbrock's Hillclimb algorithm is used in the optimization process.

Mathematical Subject Classification: 74P05

Keywords: multicellular plate structure, optimal design

1. Introduction

Sandwich structures utilize the advantages of different structural components. These components can have different structural configurations (e.g. plates or beams) or different material properties (e.g. density or damping coefficients). In the design of layered beams, plates and shells, one can exploit the different beneficial characteristics of these components. Prime examples are orthotropic sandwich structures, which have a high ratio of bending stiffness to density. Hence they are often used in light-weight structures.

Recent literature reviews [1, 2] highlight the significant effort directed at the design, analysis, and application of sandwich structures. Examples include a bending theory for sandwich beams with thick faces in [3]. Notable work is reflected in [4, 5], as well as the proceedings of international conferences on sandwich constructions [6, 7, 8, 9]. There is also a report on marine applications of sandwich construction [10].

The optimum design of specialized welded sandwich panels for ship floors was treated in [11], while a five layer beam was analysed and optimized in [12, 13]. This

beam consists of a rubber layer, two aluminium profile beams and two CFRP deck layers.

In the present study a new structural model is investigated. Sandwich plates have deck layers made of metal or FRP (fiber reinforced plastic) plates, and their inner layer is usually made of foam or honeycomb. On the contrary, cellular plates consist of metal deck plates and metal stiffeners welded into the deck plates. Our new structural model combines sandwich and cellular plates, since it has FRP deck plates and two or more aluminium square hollow section stiffeners riveted into the deck plates. So it is a new combination of materials, stiffeners and fabrication technology.

The multicellular sandwich plate is constructed from a number of longitudinal Al (aluminium) square hollow section beams and two laminated CFRP deck plates (Figure 1). The connection between the beams and deck plates is effected through riveting. This type of sandwich plate can be applied in many engineering load carrying structures such as ship floors, bridges, airplanes, building floors, etc.

The main aim of the present study is to work out an optimum design procedure for such a structural model. In doing so, design constraints are formulated on the buckling strength of the compressed deck plate, the local buckling of the aluminium square hollow section plate elements, stress in the composite plates and in the Al stiffeners as well as the deflection of the simply supported beams subjected to distributed pressure acting on the total surface.

In order to achieve cost savings in the design stage, a cost function is formulated on the basis of material and fabrication cost analysis. The mass function used in the optimization process includes the sum of the mass of CFRP plates and beams.

Mathematical programming methods for constrained function minimization are an integral part of the procedure. The Rosenbrock's Hillclimb algorithm [14] is used for the determination of the optimal dimensions of the structural model.

2. A new multicellular sandwich plate model

The sandwich plate model under consideration is depicted in Figure 1. The CFRP plates are constructed from laminated layers. The fiber volume fraction is 61% and

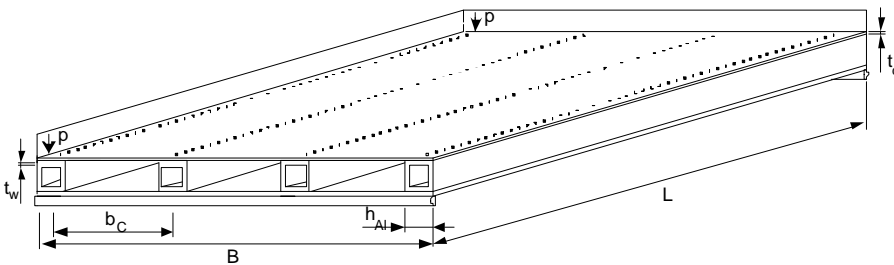


Figure 1. Multicellular sandwich plate structure

the matrix volume fraction is 39%. All of the fibers of a layer and laminate are arranged in the longitudinal direction. The plates are riveted to the upper and lower flanges of the aluminium square hollow section (SHS) profiles. The calculated required distance between the rivets is 31 mm.

The material parameters of a pre-impregnated CFRP layer are given as follows: the thickness of a layer $t = 0.2$ mm, longitudinal Young's modulus $E_x = E_c = 120$ GPa and the transverse modulus $E_y = 9$ GPa. The mass of the CFRP plate is $\rho^* = 180$ g/m², and Poisson's ratios are $\nu_{xy} = 0.25$ and $\nu_{yx} = 0.019$.

3. Optimization

3.1. Cost function. The structure is optimized with respect to minimum cost K , which can be formulated as the sum of the material and manufacturing costs [15],

$$\begin{aligned} f(x) = K = & K_{CFRP} + K_{Al} + K_{\text{heat treatment}} + K_{\text{manufacturing}} \\ K(\text{Euro}) = & 2(31.047n) + k_{Al}[n_s(\rho_{Al}4h_{Al}t_wL)] + \\ & + 2n \frac{525}{528} + k_f [n14_{\min} + n_s26_{\min} + 110_{\min}] , \end{aligned} \quad (1)$$

where n represents the number of CFRP layers, n_s the number of stiffeners, ρ_{Al} the density of the Al profile, h the height and t_w thickness of the SHS Al profiles.

The main contribution to the material cost arises from the raw material for the composite plates. In our case this cost reached 31.047 Euro/layer. The cost of the Al profile is 4.94 Euro/kg. The specific fabrication cost is $k_f=0.6$ Euro/min.

The cost of heat treatment depends on the volume of deck plates to be heat treated and the type of the resin matrix. In our case these cost components can be calculated as a function of layer number and plate dimension. The heat treatment cost of a manufactured 220x1200x2mm CFRP plate is known, so compared to it the cost of the examined plates based on volume can be calculated. The resulting ratio can be seen in eq. (1).

The total fabrication cost (as the function of time [min]) is the sum of the cost required for the manufacturing of the CFRP plates ($n14_{\min} + 110_{\min}$), the cutting cost of the Al profiles (n_s6_{\min}) and the total assembly costs (n_s20_{\min}). The time associated with manufacturing of the CFRP plates consists of the time lost in press form preparation, layer cutting, layer sequencing and final working. Final assembly consists of drilling of the CFRP plates and the Al profiles, and also riveting. Drilling of the holes is an implicit function of the number of layers.

The design variables are the height h and thickness t_w of the SHS Al profiles, the number of layers n of the CFRP plates and the number of stiffeners n_s . The fiber orientation is fixed for all layers (0°) as described above.

3.2. Mass function. The total cost of the structure is the sum of the CFRP and Al components:

$$m = 2\rho_c [BL(nt^*)] + n_s\rho_{Al} [L(4h_{Al}t_w - 4t_w^2)] , \quad (2)$$

where t^* is the thickness of a laminate.

3.3. Constraints.

3.3.1. Deflection of the total structure.

$$w_{\max} = \frac{5pL^4}{384(E_c I_c + E_{Al} n_s I_{Al})} + \frac{5\Delta M L^2}{48(E_c I_c + E_{Al} n_s I_{Al})} \leq \frac{L}{200}, \quad (3)$$

where:

I_c, I_{Al} : moment of inertia of the CFRP plate and Al profile,
 E_c, E_{Al} : reduced modulus of elasticity of the CFRP lamina and Young's modulus of Al profile.

There is the effect of the relative movement between the components, and is expressed as a function of the differences in predicted stresses in the middle of Al profile and CFRP plate. Due to difference in stress ($\Delta\sigma$) there is a corresponding difference in the equivalent applied moment (ΔM). So the second part of the equation is the additional deflection due to the sliding.

3.3.2. Composite plate buckling [15].

$$\left(\frac{b_c}{nt^*} \right) \leq \sqrt{\frac{\pi^2}{6\sigma_{\max}(1 - \nu_{xy}\nu_{yx})} \left[\sqrt{E_x E_y} + E_x \nu_{xy} + 2G_{xy}(1 - \nu_{xy}\nu_{yx}) \right]}, \quad (4)$$

where:

b_c : plate width between stiffeners,
 σ_{\max} : maximum stress in the CFRP lamina,
 E_x, E_y, G_{xy} : laminate moduli,
 ν_{xy}, ν_{yx} : Poisson's ratios.

3.3.3. Web buckling in the Al profiles [16].

$$\frac{h_{Al}}{t_w} \leq 42 \sqrt{\frac{235E_{Al}}{240E_{Steel}}}, \quad (5)$$

where: E_{Al}, E_{Steel} : Young's modulus of elasticity of Al and Steel.

3.3.4. *Stress in the composite plates.* The moment acting on the total structure is distributed on the components of the structure. So it can be calculated as the sum of the distributed moment components acting on the composite plates and Al profiles.
 $M = X_c M + X_{Al} M$

$$\frac{X_c M}{I_c} \frac{h_{Al} + nt^*}{2} \leq \sigma_{Call}, \quad (6)$$

where:

$$X_c = \frac{E_c I_c}{E_{Al} n_s I_{Al} + E_c I_c}; \quad M = \frac{pL^2}{8}; \quad \sigma_{Call} = \frac{\sigma_T}{\gamma_c}$$

σ_{Call} : allowable stress,
 $X_c M$: moment acting on composite plate,

σ_T : tensile strength of composite lamina,
 γ_c : safety factor (=2).

Because of the high number of stiffeners in the case of optimum design, the stress due to the transversal bending moment can be neglected.

3.3.5. Stress in the Al stiffeners.

$$\frac{X_{Al}M}{n_s I_{Al}} \frac{h_{Al}}{2} \leq \sigma_{Alall}, \quad (7)$$

where:

$$X_{Al} = \frac{E_{Al} n_s I_{Al}}{E_{Al} n_s I_{Al} + E_c I_c}; \quad \sigma_{Alall} = \frac{f_y}{\gamma_{Al}},$$

σ_{Alall} : allowable stress,

$X_{Al}M$: moment acting on Al tube,

f_y : yield stress of Al,

γ_{Al} : safety factor (=1.5).

3.3.6. Size constraints for the design variables.

$$\begin{aligned} 10 &\leq h_{Al} \leq 100, \\ 2 &\leq t_w \leq 6, \\ 2 &\leq n \leq 32, \\ 7 &\leq n_s \leq 20. \end{aligned} \quad (8)$$

These represent physical limitations on the design variables [mm], taking economic and manufacturing aspects into consideration.

3.4. Problem formulation. The optimum design problem under consideration is mathematically stated as:

Find

$$x^* = (x_1, x_2, \dots, x_n) \in R^n \quad (9)$$

that minimizes a cost function $f(x)$ subject to the constraints

$$\begin{aligned} g_j(x) &\leq 0, \quad j = 1, 2, \dots, m, \\ h_j(x) &\leq 0, \quad j = 1, 2, \dots, r, \end{aligned} \quad (10)$$

where $f(x), g_j(x), h_j(x)$ are scalar functions of the design variables x . The optimum solution is denoted by x^* .

3.5. Rosenbrock's non-linear mathematical programming method. The Rosenbrock's direct search non-linear mathematical programming method is used to determine the optimal geometric values, required number of Al stiffeners and the values of the objective functions.

Rosenbrock's method [14] is a simple but efficient mathematical programming method, which uses derivative-free direct searches. Instead of continuous line searches, the algorithm takes discrete steps during searches in orthogonal search directions. In each iteration, the procedure searches successively along n linearly independent and

orthogonal directions. When a new point is reached at the end of an iteration, a new set of orthogonal search vectors is constructed. Boundary zones are introduced to slow down the algorithm when it approaches the constraint boundaries.

A modified objective function, using penalty functions, is used to accommodate the constraints. Instead of continually searching in the coordinate space corresponding to the directions of the independent variables, the method achieves an improvement after one cycle of coordinate searches through alignment of the search directions in an orthogonal system. Here, the overall step of a previous stage is used as the first building block for the new set of orthogonal directions. After iteration k^{th} , Rosenbrock's method locates $x^{(k+1)}$ after completing unidimensional searches from the previous point $x^{(k)}$ along a set of orthonormal directions. The method is easy to implement, and attractive for many problems in engineering, even though the method may converge to local minima instead of the global minimum.

4. Numerical results

4.1. Mass optimization. Table 1 shows the result of mass optimization of the examined structure according to the mass function (eq. 2) and design constraints (eq. 3-8). The obtained optimal number and standard geometries of the stiffeners for the case of different numbers of layers (12-32 pieces) of CFRP deck panels can be seen in Table 1.

Table 1. Result of mass optimization

Number of layers n [pieces]	Optimal discrete stiffener numbers and geometries			Mass [kg]
	h_{AL} [mm]	t_w [mm]	n_s [mm]	
12	60	3	19	98.391
14	60	3	17	93.32
16	60	3	15	88.25
18	60	3	13	83.179
20	60	3	13	86.419
22	60	3	10	77.193
24	60	3	9	76.278
26	50	2.5	9	68.091
28	50	2.5	8	68.445
30	50	2.5	7	68.799
32	40	2.5	7	67.787

The global mass optimum is obtained in case of a laminate of 32 layers and 7 pieces (limited in size constraints) of 40x40x2.5 mm stiffeners. This optimum is a global optimum only for the examined interval of n (Figure 2), but it is clear that the total stiffness of the examined structure can be increased by the continuous increase of the number of layers of the deck panel which causes a reduction in the number and geometry of stiffeners. So a lighter structure can be constructed in this way, but the cost will be extremely high.

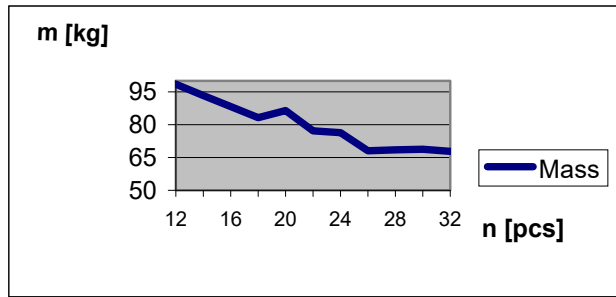


Figure 2. Mass of the structure versus number of CFRP layers

The obtained optimal mass structure of Table 1 was compared to the mass of a total steel multicellular plate structure (Figure 3) optimized in [11]. The dimension (B, L) of the steel structure and the applied pressure (p) are the same as in case of the sandwich plate structure described above.

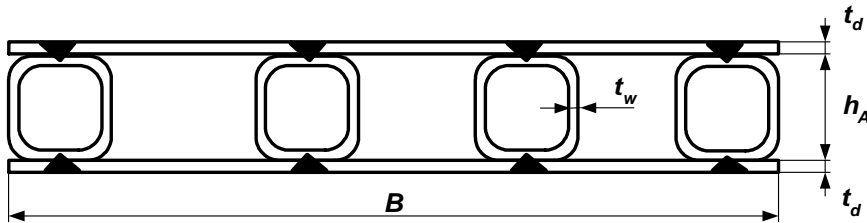


Figure 3. Steel multicellular plate structure

Table 2 summarizes the mass comparison of optimized plate structures made of steel or sandwich.

Table 2. Mass comparison of optimized plate structures made of steel or sandwich

	Optimal discrete stiffener numbers and geometries			Thickness of deck plates	Mass kg	Mass ratio [%]
	$h_S; h_{AL}$ [mm]	t_w [mm]	n_s [mm]	t_d [mm]		
Steel structure ($f_y=355$ Mpa)	40	2	6	2	517	100
Composite structure	40	2.5	7	6.4	67.787	13.11

It can be seen that an extremely high mass reduction can be achieved by the application of a modern light-weight structure instead of a traditional steel structure. This numerical example proves that 86.89 % mass saving can be realized by the application of a CFRP-Al sandwich plate structure instead of a total steel structure.

4.2. Cost optimization. Cost saving can be a prime design aim of sandwich structures because composite materials are very expensive. Table 3 shows the result of cost optimization of the analyzed structure based on the cost function (eq. 1) and design constraints (eqs. 3-8). The optimal number and standard geometries of the stiffeners obtained and total costs for different numbers of layers (12-32 pieces) are as follows:

Table 3. Result of cost optimization

Number of layers n [pieces]	Optimal discrete stiffener numbers and geometries			Cost [Euro]
	h_{AL} [mm]	t_w [mm]	n_s [mm]	
22	90	4	7	2072
24	60	3	9	2140
26	50	2.5	9	2226
28	60	3	7	2356
30	60	3	6	2464
32	60	3	5	2572

Table 4. Cost components

Number of layers [pieces]	Cost of CFRP deck panels [Euro]	Cost of Al stiffeners [Euro]	Cost of heat treatment [Euro]	Cost of fabrication [Euro]	Total cost [Euro]
22	1366	302.5	43.75	360	2072.25
24	1490	194.5	48	408	2140.5
26	1614	135	52	425	2226
28	1739	151	56	410	2356
30	1863	130	60	411.6	2464
32	1987	108	64	413	2572

Table 4 and Figure 4 show the optimum values and cost components of the optimized structures. It can be seen that the biggest part of the total cost is the cost of the composite deck plates, mainly in case of a high number of layers, while the other components are much smaller compared to it. It can also be seen that increasing the number of deck layers will increase the plate cost to a large extent, so the material cost of CFRP plates is the most decisive cost component. Based on these facts the structure having the smallest layer number is considered to be the most economical.

Because of the high number of stiffeners in case of a small layer number of deck plates a limitation should be defined for the number of stiffeners ($n_s \leq 11$). According to this limitation stating that the minimal number of stiffeners is equal to or smaller than 11, the optimum is a laminated plate with 18 layers and 11 pieces of 70x70x4 mm stiffeners.

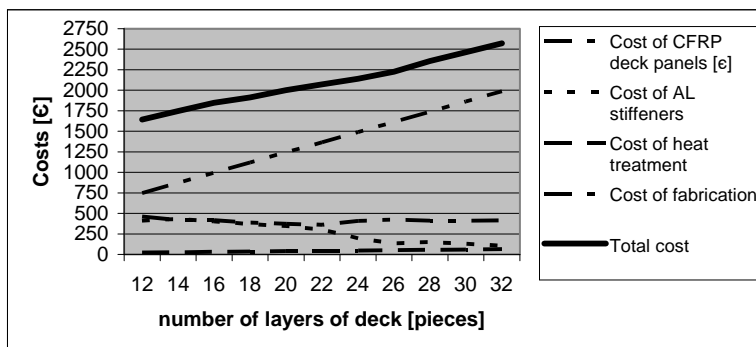


Figure 4. Cost components

The optimal cost obtained – see Table 1 – is also compared to the cost of a total steel multicellular plate structure (Figure 3).

Table 5. Cost comparison of the optimised plate structures made of steel or sandwich

	Optimal discrete stiffener numbers and geometries			Thickness of deck plates	Cost [Euro]	Cost ratio [%]
	$h_S; h_{AL}$ [mm]	t_w [mm]	n_s [mm]	t_d [mm]		
Steel structure ($f_y=355$ Mpa)	40	2	5	2.5	1014	100
Composite structure	90	4	7	4.4	2072	204

The attainable significant mass saving achieved by the application of modern composite materials causes high additional costs. In our example this extra cost of the optimized composite structure is 104 % compared to the steel structure.

So it can be summarized as follows – based on the mass saving and the disadvantageous extra cost – the application of fibre reinforced laminates is recommended in applications where mass saving is the prime design aim and cost saving is only secondary (e.g.: space flight, air-, water- and land vehicles, building parts, etc.).

Additional advantageous characteristics of these composite structures include vibration damping and corrosion resistance. Due to corrosion resistance, surface treatment and painting can be neglected, which can result in significant cost saving.

5. Conclusion

A new structural model of a sandwich plate riveted from two aluminium square hollow section rods and two CFRP deck plates is investigated by an optimization procedure.

In an optimum design procedure the dimensions and number of stiffeners and number of layers of sandwich plates are determined, which fulfil the design constraints and minimize the cost and mass. It is shown that significant mass and cost savings can be achieved in the design stage through optimization.

Acknowledgement. The research work was supported by the Hungarian Scientific Research Foundation grants OTKA T38058, and T37941. The author gratefully acknowledges the help of Profs. József Farkas and Károly Jármai formulating the problem.

References

1. NOOR, A.K., BURTON, W.S., and BERT, C.W.: Computational models for sandwich panels and shells. *Appl. Mech. Rev.*, **49**(3), (1996), 155-199.
2. VINSON, J.R.: Sandwich structures. *Appl. Mech. Rev.*, **54**(3), (2001), 201-214.
3. STAMM, K., and WITTE, H.: *Sandwich-Konstruktionen*. Springer, Berlin, 1974.
4. ZENKERT, D.: *An introduction to sandwich construction*. EMAS Publ., W Midlands, UK, 1995.
5. VINSON, J. R.: *The behaviour of sandwich structures of isotropic and composite materials*. Technomic Publ., Lancaster PA., 1999.
6. Olsson, K.A., and Reichard, R.P. (eds.): Sandwich Constructions 1, Proc. 1st Int. Conf. on Sandwich Constructions, Stockholm. EMAS Ltd. Solibull, UK, 1989.
7. Weissman-Berman, D., and Olsson, K.A. (eds.): Sandwich Constructions 2. Proc. 2nd Int. Conf. on Sandwich Constructions, EMAS Publ., UK, 1992.
8. Allen, H.: Sandwich constructions 3. Proc. 3rd Int. Conf. on Sandwich Constructions. Southampton, UK. EMAS, UK, 1996.
9. Olsson, K.A. (ed.): Sandwich Constructions 4. Proc. 4th Int. Conf. on Sandwich Constructions, Stockholm. EMAS, UK, 1998.
10. KNOX, E.M., and COWLING, M.J.: Adhesively bonded steel corrugated core sandwich construction for marine applications. *Marine Structures.*, **11**(4-5), (1998), 185-204.
11. JARMAI, K., FARKAS, J., and PETERSHAGEN, H.: Optimum design of welded cellular plates for ship deck panels. *Welding in the World.*, **43**(1), (1999), 51-54.
12. FARKAS, J., and JARMAI, K.: Minimum material cost design of five-layer sandwich beams. *Structural Optimization*, **15**(3-4), (1998), 215-220.
13. FARKAS, J., and JARMAI, K.: *Economic design of metal structures*. Millpress, Rotterdam, 2003.
14. ROSENBROCK, H.: An automatic method for finding the greatest or least value of a function. *Comp. J.*, **3**, (1960), 175-184.
15. BARBERO E.J.: *Introduction to composite materials design*. Taylor & Francis, USA, 1999.
16. FARKAS, J., and JARMAI, K.: *Analysis and optimum design of metal structures*. Balkema, Rotterdam-Brookfield, 1997.

QUASI-EVOLUTIONARY POLYOPTIMIZATION OF SPATIAL TRUSSES

WITOLD M. PACZKOWSKI, ADRIAN SILICKI

Department of Theory of Structure, Technical University of Szczecin
Szczecin, Poland
optim@ps.pl

STEFAN JENDO

Institute of Fundamental Technological Research, Polish Academy of Sciences
Warsaw, Poland
sjendo@ippt.gov.pl

[Received: March 17, 2003]

Dedicated to Professor József FARKAS on the occasion of his seventy-fifth birthday

Abstract. In the paper the discrete quasi-evolutionary polyoptimization process is presented and illustrated with the optimization of an orthogonal double-layer spatial truss. The problem is solved in six cycles of evolution. During the analysis, values of the most important design variables connected with the structure of the object are obtained. As the result of the analysis, the cover that satisfies in the best way all considered requirements is obtained.

Mathematical Subject Classification: 65M06, 35L65, 35L67

Keywords: quasi-evolutionary optimization, polyoptimization, spatial trusses

1. Introduction

A modern large-scale object must satisfy many requirements, such as load bearing capacity and serviceability conditions and requirements of the investor and user. The structure has to be light, functional, friendly to the natural environment, and easy to maintain. All the requirements have influence on the economic aspect of the investment, like costs of erection, exploitation and utilization. Another important requirement is the attractive architecture form. The shape, dimensions and the general appearance of the structure should make an appropriate impression. In the first stage of the process of designing, architect's, user's, engineer's and investor's ideas of the structure come together [1, 2]. Those ideas are most frequently contradictory and the final concept of the structure must be a compromise that is sometimes very difficult to achieve. In such a situation optimization becomes an indispensable tool [3–6]. But in the case of complex problems some difficulties appear. Due to the necessity to consider many decision variables, the feasible range of solutions is quite numerous. Also, a considerable number of constraints must be taken into account. The choice of

the best solution should be based on several criteria to make it satisfy all significant conditions and requirements in the best way. Solving that sort of problems only with methods based on a traditional approach to optimization may cause some difficulties. A quasi-evolutionary approach seems to be more effective.

2. Qasi-evolutionary polyoptimization

The quasi-evolutionary approach to solving optimization problems comes from observations of the outer world. In nature as well as in the history of human civilization one can notice continuous development, with trends to better and more complex forms. During the evolution, solutions that are difficult, poor or less functional are eliminated by stronger, lighter and more suitable ones for the purpose they are designed for. When new solutions are created, knowledge and experience from former attempts are applied. A similar approach may be employed when optimization problem is considered. It is useful, especially in the case of complex objects.

The quasi-evolutionary optimization process consists of few cycles, each of them being a standard numerical problem. The term 'quasi-evolutionary' is used here to avoid mistaking it for the traditional evolutionary optimization procedure in which genetic algorithms are required. In the quasi-evolutionary formulation, each solution gives information and experience that allow one to form better assumptions, select more effective methods of solution and help to exclude any insignificant elements of the solution. On the basis of the former results the problem is analyzed again in the next cycle. In this context, the quasi-evolutionary approach is similar to evolution in the world of nature, where only better adapted forms give start to a next generation [6].

3. Problem statement

The paper presents the process of a polyoptimal design of a cover of a sports hall. Dimensions of the space to cover are: width – 60 m, length – 105 m, height – 8 m. The only input requirement is that the cover should be realized as a two-layer spatial truss made of steel tubes. Values of all remaining variables describing the structure are to be obtained as results of the polyoptimization analysis. Since the object of the analysis is rather complex, solving the problem formulated in a traditional way may cause some difficulties. They can come from the fact that many decision variables must be considered, which leads to a considerable domain of feasible solutions. In process of design of the structure many requirements and conditions must be satisfied. It leads to a considerable number of constraints and criteria. In order to obtain the solution in a reasonable period of time, application of the quasi-evolutionary approach to the polyoptimization is highly recommended.

4. Solution of the problem

4.1. General algorithm. The problem is solved in six evolution cycles. Each cycle is a standard polyoptimization problem. In most cases the enumeration method is

employed to analyze the problem. The objective result is a set of nondominated evaluations and nondominated solutions. From these sets a preferred evaluation and its inverse image – a preferred solution are selected. The preferred solution from the former cycle is the starting point for the next one. The starting point of the first cycle is chosen arbitrarily. In this cycle the polyoptimal catalogue is searched. In the second one, shape of the cover and the manner of support are analyzed. The third cycle concerns the rise of the truss, the fourth one – the depth of the truss and the distance between nodes. The next one chooses the grade of steel and the last one – selects catalogue again. In this way, the complex problem is divided into several relatively simple problems coordinated naturally by the idea of evolution.

4.2. The OPTYTRUSS system. Numerical analysis of the structure is performed by the OPTYTRUSS system. The system enables computation of internal forces in the truss bars on the basis of the matrix displacement method, the choice of the appropriate profile for each bar, and optimization analysis of different variants of the structure. The profiles are selected from the catalogue provided. Such an approach makes the problem a discrete one, because the space of solutions contains a finite number of variants. Since every analyzed variant of structure is built of profiles that are commercially available this way of optimum design is technologically correct.

In the system all loadings typical of the covers may be applied, i.e. deadweight, snow load, wind load and loads arising from mounted installations or devices. The loads are realized by several simple types of loads: uniformly distributed load, trapezoidal load, triangular load and concentrated load. The loads may be imposed in the upper or lower layer. There are two means of imposing the distributed loads: they can be vertical or normal to the surface of the cover. The concentrated load is expressed by its three components, so the force may be imposed in any direction. Every load is reduced to a nodal load.

There are four types of profiles available: circular tube, circular, square tube and square (Figure 1). For every type a catalogue with cross-sections of different sizes may be applied.

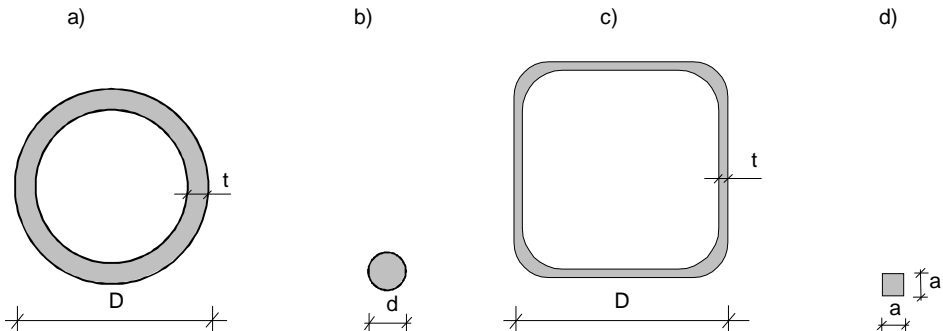


Figure 1. Types of profiles available in the OPTYTRUSS system

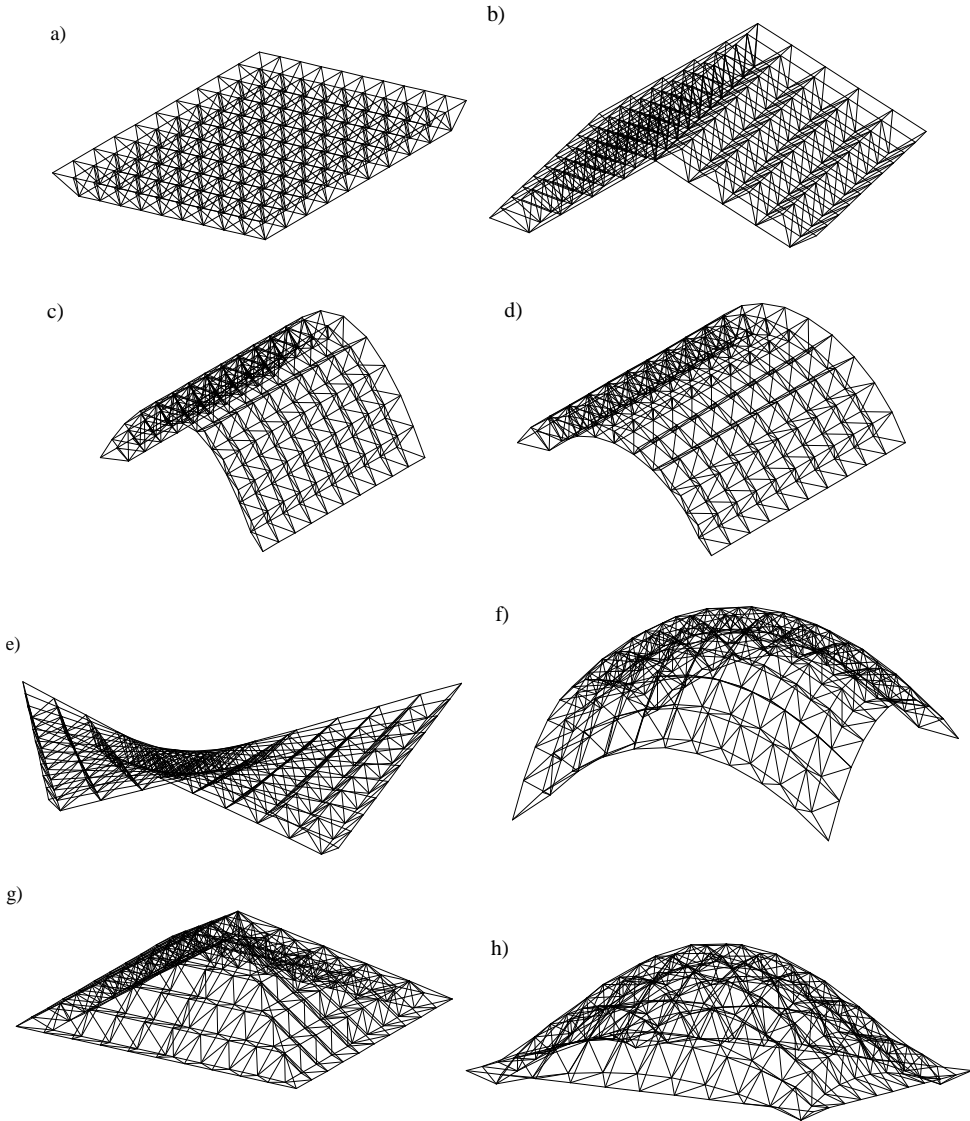


Figure 2. Analyzed shapes of the cover: a) plane, b) double slope, c) a parabolic arc, d) circular arc, e) hyperbolic paraboloid, f) dome-shaped with arc edges, g) four slope, h) dome-shaped with flat edges

The OPTYTRUSS system facilitates analysis of the two-layer spatial trusses based on the orthogonal grid of nodes in both layers. There are eight shapes of analyzed covers available: plane, double slope, parabolic arc, circular arc, hyperbolic paraboloid, dome-shaped with arc edges, four slope, and dome-shaped with flat edges (Figure

2). Six objective functions are computed for every solution: the volume of material of truss members per one square meter of projection of the cover, the strain energy per one square meter of projection of the cover, the greatest displacement, average use of cross-sections and two objective functions that may be created by the user. There are three methods of optimization built-in: exhaustive search, crude Monte Carlo and modified Monte Carlo. The system computes values of objective functions for every analyzed solution, therefore other methods may also be used, but this cannot be performed automatically. In order to choose the preferred evaluation the distance method is applied. As a reference point the ideal evaluation or the Nadir evaluation may be used.

4.3. The first evolution cycle. The starting point in the first evolution cycle is the plate spatial truss with an orthogonal grid of nodes and a depth of 3 m. The distance between nodes is 3.75 m. The truss is made of steel with the yield stress equal to 225 MPa. The cover is supported in the upper layer by posts placed on the external longer edges of the truss. The distance between the supports is 15 m.

The first evolution cycle considers the catalogue of steel profiles. At the start, a catalogue containing 72 elements is assumed. This catalogue is a representative sample of the metallurgical assortment available in Poland. On the basis of the starting catalogue, sixteen other catalogues are created. They are formed with regard to the frequency of choice of particular profiles by the designing system. The initial catalogue is used for designing the analyzed structure. Then the elements that are not chosen or are rarely chosen by the designing system are discarded from the initial catalogue. In that way the second catalogue (second solution analyzed in this evolution cycle) is obtained. It is applied in the system during designing the analyzed structure and the process is repeated. It is stopped when the one-element catalogue is obtained. In this way the discrete 17-element domain of feasible solutions is obtained.

$$\mathbf{x}_{(l)} = \{x_{i(l)}\} \quad i = 1, \dots, 17 \quad (4.1)$$

where the number in brackets in subscript denotes the number of the evolution cycle.

Definition of the vector of constraints is not required in this cycle, because all created catalogues facilitate designing a structure correctly. Each solution is evaluated with regard to three criteria of optimization that are expressed formally as the vector of objective functions

$$f_{(l)}(\mathbf{x}_{(l)}) = \{f_{1(l)}(\mathbf{x}_{(l)}), f_{2(l)}(\mathbf{x}_{(l)}), f_{3(l)}(\mathbf{x}_{(l)})\} \quad (4.2)$$

where

- $f_{1(l)}(\mathbf{x}_{(l)})$ – mass of the structure per one square meter of projection of the cover (in kg/m^2),
- $f_{2(l)}(\mathbf{x}_{(l)})$ – the greatest displacement (in cm),
- $f_{3(l)}(\mathbf{x}_{(l)})$ – the number of profiles in the catalogue (as the technological criterion).

All the functions are minimized. The diagram of the objective functions is presented in Figure 3.

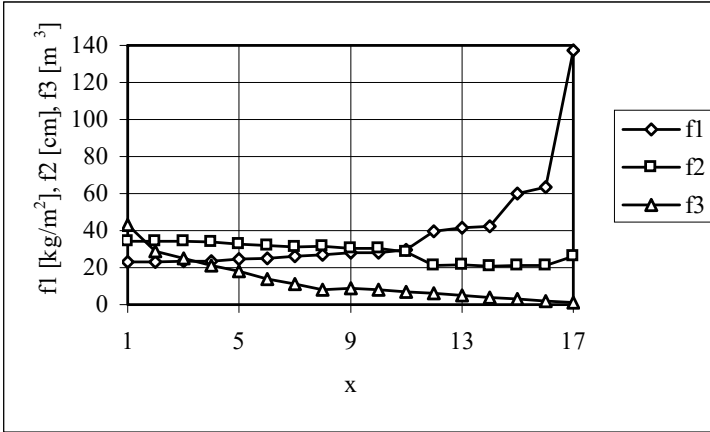


Figure 3. Diagram of the objective functions

From the set of evaluations the nondominated ones are selected and normalized. Then the preferred evaluation is chosen with the use of distance function method with the norm $\|p\| = 2$ [6]. The inverse image of the preferred evaluation is the preferred solution that determines the catalogue consisting of four elements (Table 1).

Table 1. The preferred catalogue

Number of element	Diameter[mm]	Thickness of the wall[mm]
1	51.0	2.9
2	88.9	3.6
3	159.0	4.5
4	323.9	8.0

The values of the objective functions for the preferred solution form the vector

$$fp_{(l)} = \{42.17, 20.96, 4\} . \quad (4.3)$$

During the analysis it has been noticed that from profiles with the same diameter those with the thinnest walls are most frequently chosen by the designing system. It is due to the smaller slenderness ratio of bars made of such profiles (when bars with the same cross-sectional area are considered).

4.4. The second evolution cycle. In the second evolution cycle, the polyoptimal manner of support and shape of the cover are selected. Four shapes are considered: plane, double slope, parabolic arc, and circular arc (Fig. 2), and three manners of support: one-point supports at the external edge of the upper or lower layer and four-point supports in the lower layer (Fig. 4). Every shape (excluding the planar one) is analyzed with three different rises of 3, 6 and 9 m in order to establish its approximate value.

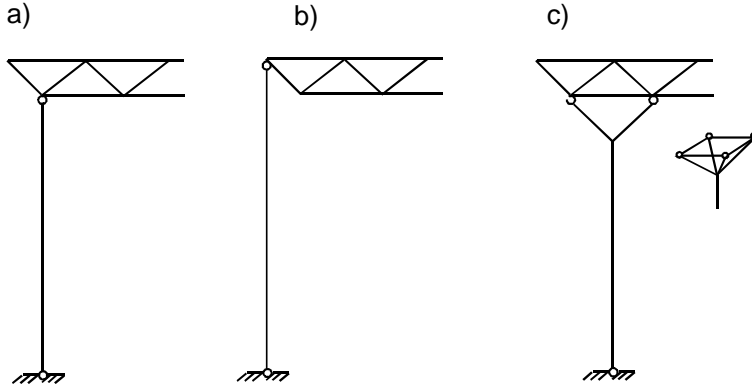


Figure 4. Analyzed manners of support: a) one–point support in the lower layer, b) one–point support in the upper layer, c) four–point support

The analyzed variants of the cover are represented by the vector of decision variables $\mathbf{x}_{(2)}$:

$$\mathbf{x}_{(2)} = \{x_{1(2)}, x_{2(2)}\}, \tag{4.4}$$

where:

- $x_{1(2)}$ – shape of the cover,
- $x_{2(2)}$ – manner of support.

Three criteria of evaluation are assumed: minimum of the mass of the structure per one square meter of projection, minimum of the greatest displacement and minimum of increase of the space volume arising from changing the shape of the cover (in reference to the volume of the starting point structure). Minimizing the volume is important because of maintenance costs (space that needs heating in the winter). The vector of objective functions is presented below:

$$\mathbf{f}_{(2)}(\mathbf{x}_{(2)}) = \{f_{1(2)}(\mathbf{x}_{(2)}), f_{2(2)}(\mathbf{x}_{(2)}), f_{3(2)}(\mathbf{x}_{(2)})\} \tag{4.5}$$

where

- $f_{1(2)} = f_{1(1)}$ and $f_{2(2)} = f_{2(1)}$,
- $f_{3(2)}(\mathbf{x}_{(2)})$ – increase in volume in reference to the volume of the starting point structure (in m^3).

In order to solve the problem, the exhaustive search method is employed. The feasible domain contains 30 elements. The computations are performed with the use of the catalogue obtained as a result of the former cycle. Diagrams of the 3D–space of evaluations are presented in Figure 5.

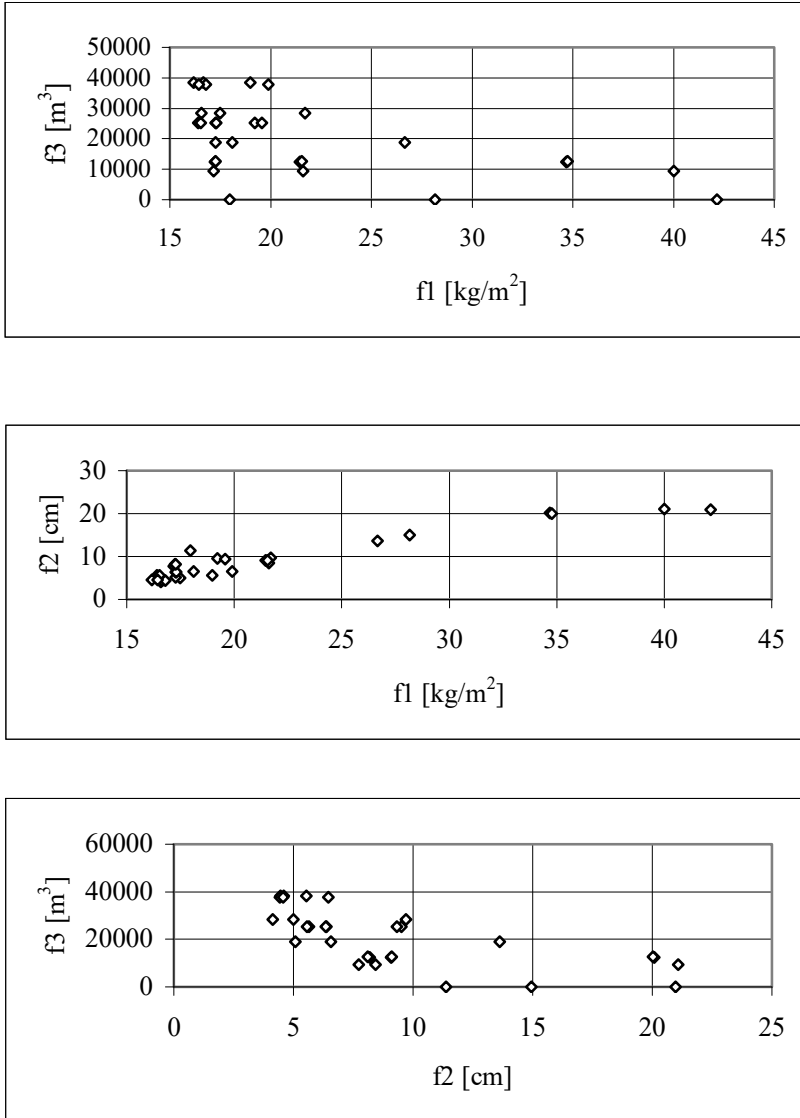


Figure 5. Diagrams of the 3D space of evaluations

After the polyoptimization analysis, the preferred solution is obtained: – a double slope cover with a rise of 3 m, supported in the lower layer by the four-point supports. The vector of objective functions for the preferred solution is presented below:

$$\mathbf{fp}_{(2)} = \{17.18, 7.72, 9450\} . \quad (4.6)$$

A fragment of the obtained structure is presented in Figure 6.

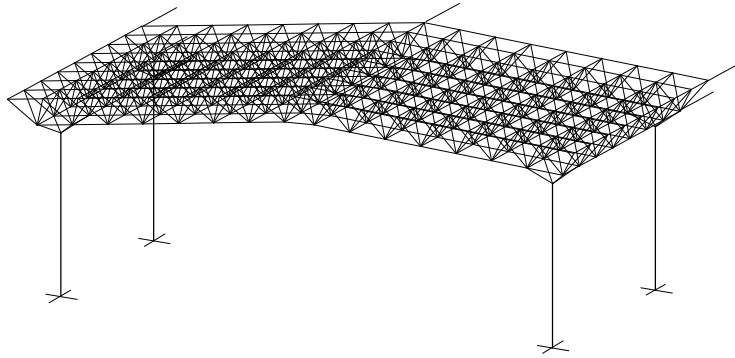


Figure 6. A fragment of the structure being the result of the second evolution cycle

4.5. **The third evolution cycle.** In this cycle, only one decision variable is analyzed: the rise of the cover in order to establish its precise value. The vector of decision variables is therefore a one-element one:

$$\mathbf{x}_{(3)} = \{x_{l(3)}\}, \tag{4.7}$$

where $x_{l(3)}$ is the rise. The decision variable is discretized and some constraints are imposed on it:

$$x_{1(3)} = n \cdot 0.6m, \quad n = 2, 3, \dots, 8. \tag{4.8}$$

The vector of objective functions is the same as in the former cycle. The diagram of the objective functions is presented in Figure 7.

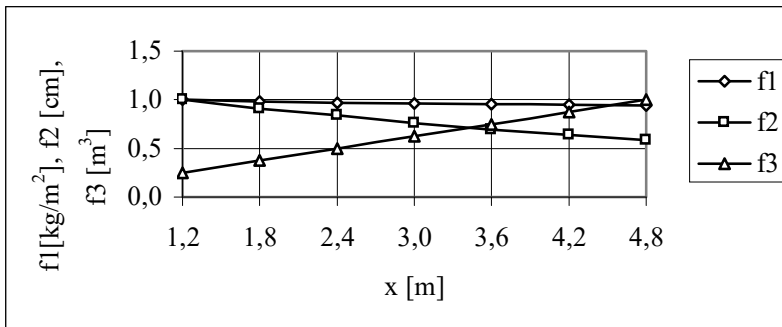


Figure 7. The diagram of objective functions

After the polyoptimization analysis the preferred solution is obtained:

$$\mathbf{x}_{p(3)} = \{1.8\}. \tag{4.9}$$

It means that a rise of 1.8 m satisfies the assumed criteria in the best way. The values of objective functions are as follows:

$$\mathbf{f}p_{(3)} = \{17.57, 9.20, 5670\} . \tag{4.10}$$

4.6. The fourth evolution cycle. The fourth cycle concerns the depth of the truss and the distance between nodes. A two–element vector of decision variables is assumed: The fourth cycle concerns the depth of the truss and the distance between nodes.

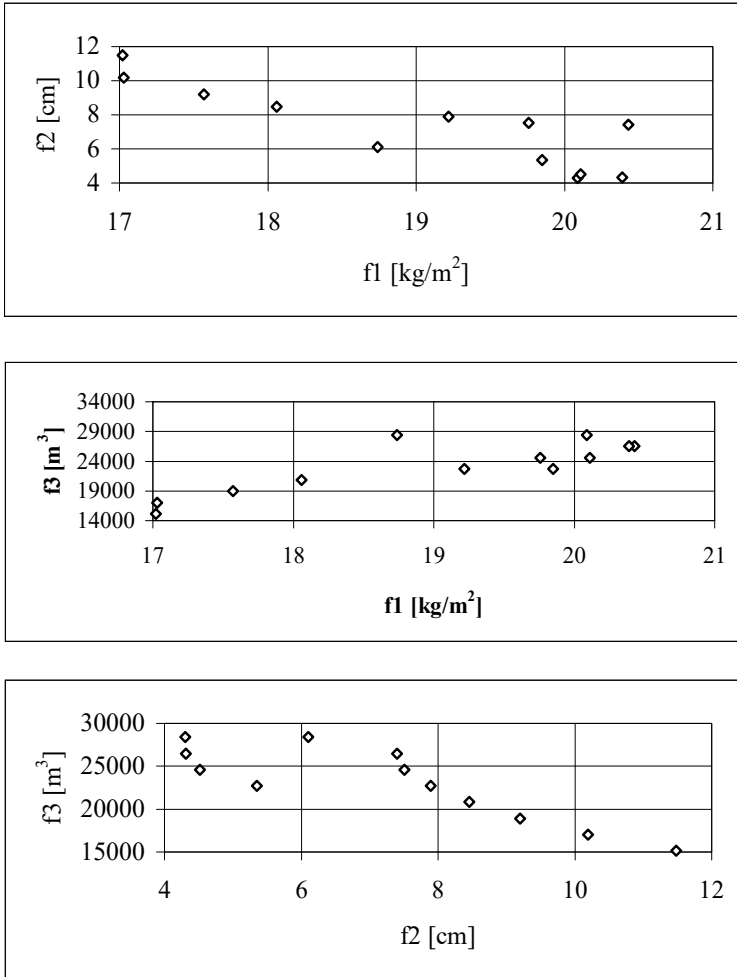


Figure 8. Diagrams of the 3D space of evaluations

A two–element vector of decision variables is assumed:

$$\mathbf{x}_{(4)} = \{x_{1(4)}, x_{2(4)}, \} \tag{4.11}$$

where

$x_{1(4)}$ – depth of the truss (in m)

$$x_{1(4)} = n \times 0.3m, \quad n = 8, 9, \dots, 15 \quad (4.12)$$

$x_{2(4)}$ – distance between nodes (in m)

$$x_{2(4)} = 3.00, 3.75, 5.00 \text{ m} . \quad (4.13)$$

In order to make a solution technologically correct, angles between a cross brace and the layer of the truss must be included between 30° and 60° . This fact is one of the constraints of the feasible domain.

The objective functions are analogous to those from the former cycle. The only difference is that the considered increase of the volume arises here from changing the value of the truss depth. In order to solve the problem, the Gauss–Seidel method is used. Diagrams of the 3D space of evaluations are presented in Figure 8.

As a result of the analysis, the 12–element set of nondominated evaluations and the set of nondominated solutions are obtained. The preferred solution is chosen by the use of the distance method:

$$\mathbf{x}_{p(4)} = \{3.6, 5.0\} . \quad (4.14)$$

The preferred evaluation is:

$$\mathbf{f}_{p(4)} = \{19.85; 5.35; 22, 720\} . \quad (4.15)$$

4.7. The fifth evolution cycle. The aim of this cycle is the choice of the grade of steel. Two grades of steel are considered, with the yield stress of the first equal to 225 MPa and that of the second one 210 MPa. Thus, only one decision variable is considered here:

$$\mathbf{x}_{(5)} = \{x_{1(5)}\} \quad (4.16)$$

where

$$x_{1(5)} = 210, 225 \text{ MPa} . \quad (4.17)$$

The problem is analyzed with regard to two criteria: minimum of the structure mass and minimum of the greatest displacement, defined in the vector of objective functions

$$\mathbf{f}_{(5)}(\mathbf{x}_{(5)}) = \{f_{1(5)}(\mathbf{x}_{(5)}), f_{2(5)}(\mathbf{x}_{(5)})\} , \quad (4.18)$$

where $f_{1(5)} = f_{1(4)}$ and $f_{2(5)} = f_{2(4)}$.

The evaluations of the solutions analyzed are contained in Table 2.

Table 2. Evaluations of the solutions analyzed

Yield stress [MPa]	Structure mass [kg/m ²]	Greatest displacement [cm]
210	20.02	4.92
225	19.85	5.35

The preferred solution is chosen on the basis of the results discussion. Using steel with the lower yield stress leads to an increase of structure mass of 0.9 % and a decrease of the greatest displacement of 8.0 %. Therefore, the preferred solution is:

$$\mathbf{x}_{p(5)} = \{210\} \tag{4.19}$$

and the preferred evaluation:

$$\mathbf{f}p_{(5)} = \{18.70, 6.07\} . \tag{4.20}$$

4.8. The sixth evolution cycle. In this last cycle the catalogue is considered again. 24 three-, four- and five-element catalogues, similar to the one obtained in the first cycle, are analyzed with the exhaustive search method. The criteria of evaluation are analogous to the ones from the former cycle. After the polyoptimization analysis the preferred catalogue is established (Tab. 3). The catalogues obtained in the first (T1) and discussed sixth cycle (T2) are presented in Figure 9.

Table 3. The preferred catalogue

Number of element	Diameter [mm]	Thickness of the wall [mm]
1	54.0	2.9
2	101.6	3.6
3	168.3	5.0
4	273.0	7.1

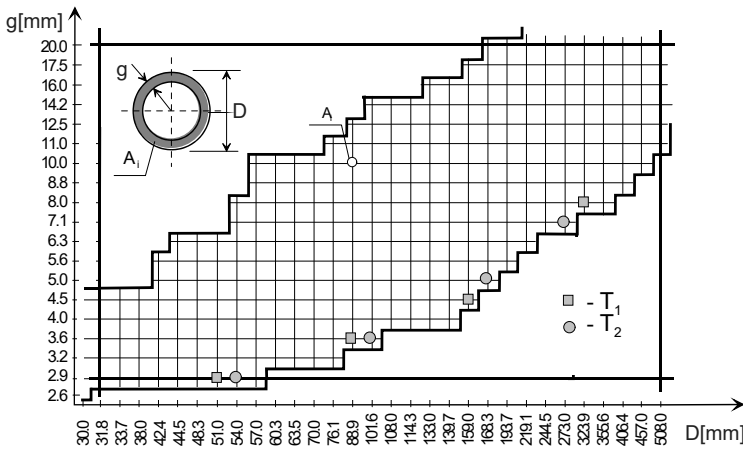


Figure 9. The catalogues obtained in the first and sixth cycles of evolution

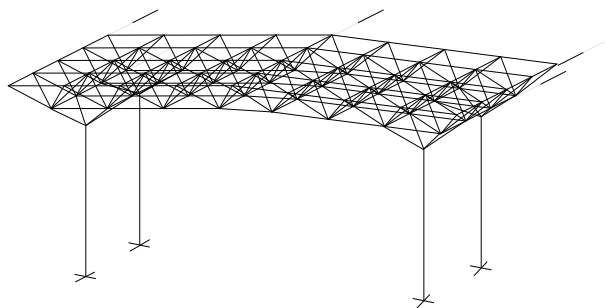


Figure 10. A fragment of the structure being the result of quasi-evolutionary polyoptimization

The preferred evaluation is:

$$\mathbf{fp}_{(6)} = \{17.00, 5.33\} . \quad (4.21)$$

5. Conclusions

The quasi-evolutionary approach to optimization problems leads to better results than the ones obtained with a traditional analysis. In case of complex problems, it is possible to divide them into several simple ones. The numerical example shows that the proposed method is efficient enough to analyze large-scale truss systems (Figure 11). The structure that fulfils the assumed criteria best is a double-sloped truss supported by four-point supports with a rise of 1.8 m, a depth of 3.6 m and a distance between nodes 5.0 m, made of steel with a yield stress 210 MPa and four kinds of profiles. The fact that every next cycle is based on the information obtained in the former ones leads to permanent development of the problem formulation. It also facilitates analysis from general issues to details and may be easily applied in engineering practice.

References

1. MAKOWSKI, Z. S.: *Space structures of today and tomorrow: A brief review of their present development and a glance into their future use*, In H. Nooshin (ed.), *Space structures*; Proc. of the Third Int. Conf., University of Surrey, Guildford, UK, 11–14 Sept. 1984, London – New York, Elsevier Applied Science Publisher, (1984), 1–8.
2. REBIALAK, J.: *Space Structures of Large Span*, Scientific Works of Technical University of Wrocław, No 27, Wrocław, 1992, (in Polish)
3. AMELJAŃCZYK, A.: *Multicriteria Optimization in the Control and Management Problems*, Ossolineum, Wrocław, 1984, (in Polish)
4. JENDO, S.: *Multiobjective optimization*, In M. Save & W. Prager (eds), *Structural Optimization, Vol. 2: Mathematical Programming*, Plenum Press, New York, (1990), 311–342.
5. JENDO, S. and PACZKOWSKI, W. M.: *Multicriterion discrete optimization of space trusses with stiffness variations*, In J. B. Obrębski (ed) *Lightweight Structures in Civil Engineering*, Int. Conf. on LSCE, Warsaw, Poland, 25–29 September 1995, (1995), 109–114.

6. PACZKOWSKI, W. M.: *Chosen Problems of Discrete Evolutionary Optimization*, Scientific Works of Technical University of Szczecin, No 544, Szczecin, 1999 (in Polish).

LOCALLY ORTHOTROPIC FEMUR MODEL

PÉTER PÁLFI

Department of Structural Mechanics, Budapest University of Technology and Economics
Műegyetem rkp. 3-5, 1111 BUDAPEST, Hungary
palfi@ep-mech.me.bme.hu

[Received: September 22, 2003]

Abstract. The ability of spongy bone, which specifies the direction of trabeculae to be parallel to the local principal stress directions is called, Wolff's law [1]. Based on this statement we can create a simple model using an easy iterative method which is called locally orthotropic femur model [2]. The gist of the iteration is the following: in an FE model according to the actual loading, first the material directions are engaged to be parallel to the calculated principal stress for every element, then the principal stress directions are calculated again and the material directions are modified. (The initial material orientations are parallel to each other, or random.) The obtained iterative method is strongly convergent, after six iteration loops the material angles do not change more than a few tenths and after the fifteenth iteration are practically constant. Therefore the advantages of this iterative method are its speed, effectiveness and similarity to real bone's trabeculae structure. We are planning to extend the 2D model to 3D, or rather to use the model obtained to the validation process of femur prosthesis.

Mathematical Subject Classification: 74M99, 74S05

Keywords: orthotropic, femur, FEM, biomechanics

1. Introduction

Remodelling theories represent one of the most important branches of bone biomechanical research. They are primarily aimed at the modelling of the processes happening in cancellous bone tissue, because this part of the bone remodels approximately six to eight times faster than compact bone tissue. Among the existing models there are micro and macro models. Micro models attempt to model the most complex microbiological properties of spongy bone while macro models reflect only the most fundamental properties of bones. This obviously means that the micro models are much more complex and therefore require a much more extensive computer capacity. (Some models takes several months to run on a 16-processor supercomputer, see Huiskes [3].)

The aim of our research team is to apply the created model to test the stability of femur prosthesis. Due to the large number of implantations to be tested there is no time for several months running. So we wanted to create a femur model that reflects as many properties of the bone as possible but at the same time allows a relatively fast

calculation. On the other hand, the exclusion of remodelling processes would be an unjustifiable negligence on our part, considering the fact that this is one of the most fundamental characteristics of bones. Accordingly, we concluded that the application of a macro model would be most reasonable.

The structure of spongy bone and at the same time the remodelling processes were first examined by Wolff. In his research he observed that the bone trabeculae form their orientation in such a way that they are parallel to the local principal stresses at every point. He stated this observation as a law that received the name Wolff's law. One of the most important conclusions of Wolff's law is that bones build up their internal structure according to the actual loading present for a longer period of time. This simple but very important property can easily be incorporated into a FEM model. The acquired model is the so-called locally orthotropic bone model, which was developed by Thomas J. Impelluso [2]. The model is fast and can easily be applied, therefore it was reasonable to choose it for our research. We improved this conception for 2D and 3D generic problems and three BASIC scripts were written, which are able to automate the iteration in Nastran for Windows systems.

2. Locally Orthotropic Bone Model

As mentioned above, the locally orthotropic bone model is aimed to apply Wolff's law in practice. This is achieved through a simple iteration procedure. As the name of the model suggests, the procedure requires the application of orthotropic materials; based on our knowledge of literature data this consideration fits well the real behavior of the bone, thus this is a reasonable simplification. Consequently, according to the present state of science, regarding bones as orthotropic materials we obtain a very good approximation [1].

The steps of the iteration are as follows:

1. In an orthotropic FEM model the original material orientations are chosen parallel to each other or even at random.
2. The principal stress directions are determined for each element according to actual loading.
3. Material orientations are modified to be parallel to the principal stress directions in each element.
4. If the magnitude of changes in material orientation exceeds the value preset by us, then the calculation is repeated from step 2.

3. Mathematical background

The iteration in 2D can easily be incorporated into the Nastran for Windows FEM code on Windows platforms, because the program makes the changing of material orientations and polling of principal stress directions possible. Consequently, creating a relatively simple BASIC script is enough. However, in 3D it is not possible to change material orientations and poll principal stress directions using a single BASIC function. Therefore first principal stress directions must be determined based on the

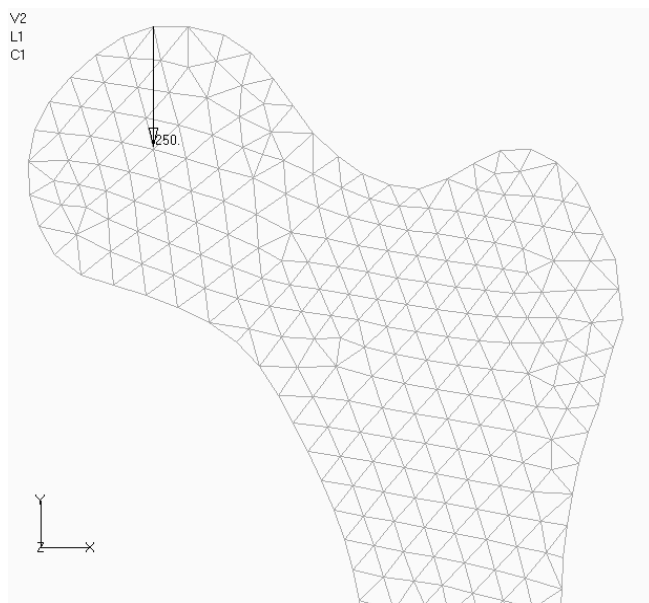


Figure 1. (a). The force was applied in bilateral body posture

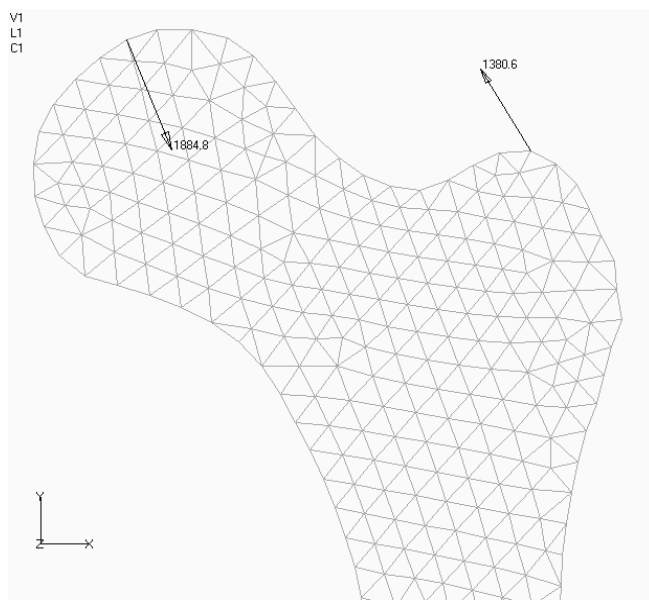


Figure 1. (b). The force was applied in unilateral body posture

As already mentioned, in 2D it is possible to poll principal stress directions and to set material orientations using simple functions. Therefore to realize local orthotropy, three Basic scripts were written. The first nullifies material orientations for every element (or sets them to any other angle), creating original material orientations parallel to each other. The second sets original material directions at random for every element. The third polls the direction of the highest principal stress for each element and modifies material orientations accordingly.

Unfortunately, in 3D the setting of material directions according to principal stress directions is much more complicated, because in the program the direction and coordinates of principal stress vectors cannot be polled, the material orientations can not be set, so in this case the transformation mentioned earlier must be applied.

5. Results

5.1. Load states. The 2D model was tested for two fundamental load states: based on literature data examining bilateral and unilateral body postures. The applied forces are shown in Figure 1a.

For bilateral body posture (when we are standing on two legs) we used a very simple model. The weight of the upper body is split equally into the two legs. The bodyweight of an average person is 70 *kg* and the weight of the upper body is two thirds of the total bodyweight, thus 50 *kg*, consequently 250 *N* acts on each leg. We applied this load on one node in the midsection of the femur head and the hip joint.

The unilateral body posture is very similar to the bilateral body posture. When standing on one leg we need a muscle force to keep the balance, thus based on literature data we applied two loads: a contact force at the midsection of the femur head and the hip joint (1884.8*N*) and a muscle force (1380.6*N*).

In both cases, the original material orientation was taken in five different ways: parallel (0°, 45°, 75°, 90°) and randomly. The acquired results are alike, the only difference is in the number of steps required for the final result. (The originally parallel material orientations reached the final results in 10 or 11 iteration steps while the random running required 12 or 13 steps.) However, in the presentation of results only the data acquired from random original orientation are described because ‘changes’ are most striking here.

The material parameters were taken from the book [2]:

$$E_1 = 17 \text{ GPa}, \quad E_2 = 11 \text{ GPa}, \quad G_{12} = 3.3 \text{ GPa}, \quad \nu_{12} = 0,41 .$$

5.2. Bilateral body posture. In a bilateral body posture the bone carries smaller loads than in a unilateral body posture, therefore the stresses in the bone are also smaller. The result of the procedure is the decrease of stresses and ‘smoothing’ of local stress peaks in the bone model as described later. First take a look at the distribution of material orientations as these show the method’s effectiveness to a greater extent. Figure 2 shows the material orientation in every element, with random original orientation (a), after the first iteration step (b), and after 20 iteration steps (c).

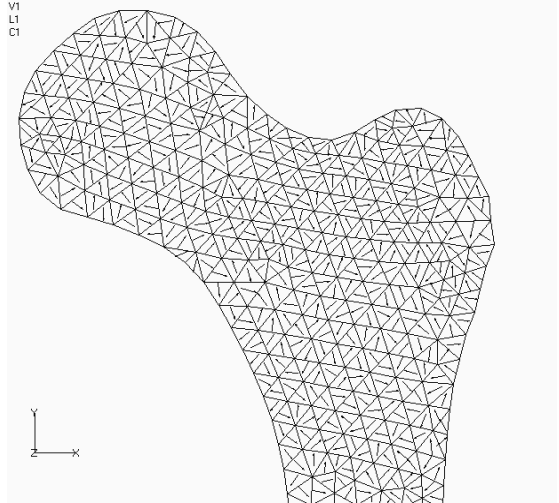


Figure 2. (a). Random material directions in the elements

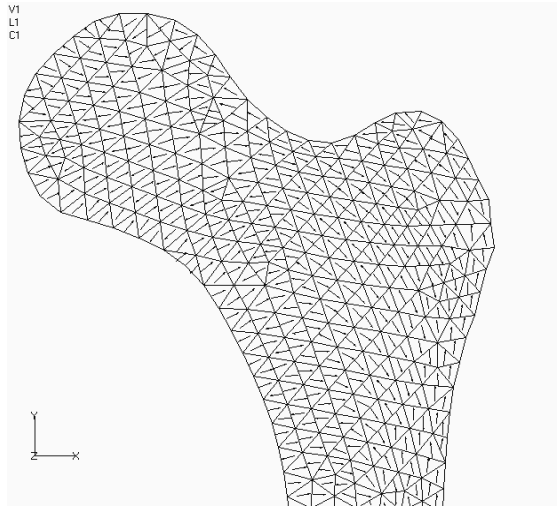


Figure 2. (b). Material directions in the elements after the first iteration step

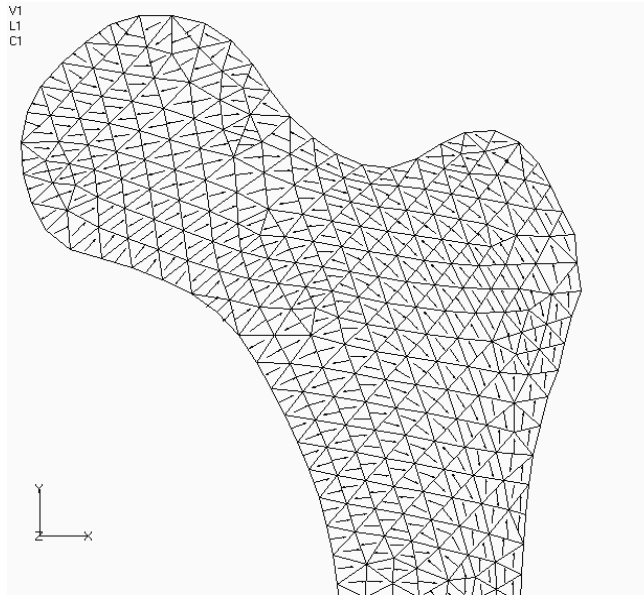


Figure 2. (c). Material directions in the elements after the 20th iteration steps

As can be seen, the material orientations do not change considerably (c) compared to the first iteration step (b). If calculations are carried out twice (only the first iteration step is finished), it already gives a good approximation, therefore this procedure provides very fast results. 15 iteration steps are enough for a very accurate calculation. Besides it also can be seen that the resulting material orientation diagram is very similar to the Culmann-trajectory and the actual form of trabeculae in real bones.

Figure 3 shows the above mentioned stress decreasing effect. Figure 3a shows top major principal stresses calculated with original material orientations set at random, while Figure 3b shows top major principal stress distribution after the 20th iteration.

The changes in stress values are more visible if a stress diagram is produced. This is shown in Figure 4. The red diagram 'in the background' shows the top major principal stress distribution with original material orientations set at random, while the blue diagram shows the situation after the 20th iteration. In both cases the x coordinates of the elements are on the horizontal axis and all elements are represented. It is possible to realise that this method 'smoothens' and decreases by approximately

10% the stress peaks critical for fracture, so really an effect similar to real behavior is shown.

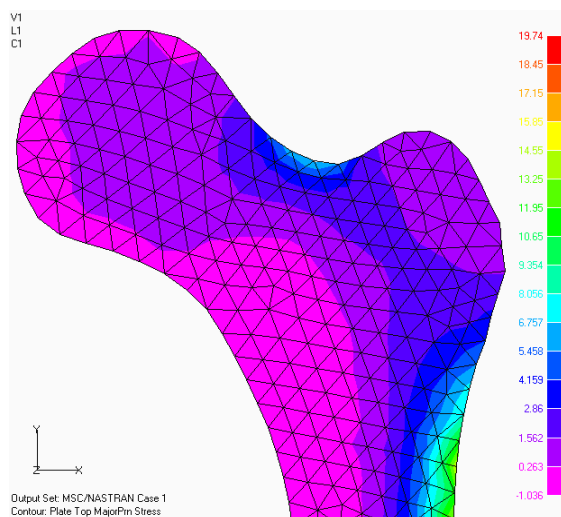


Figure 3. (a). Distribution of the top major principal stress with original material directions [MPa]

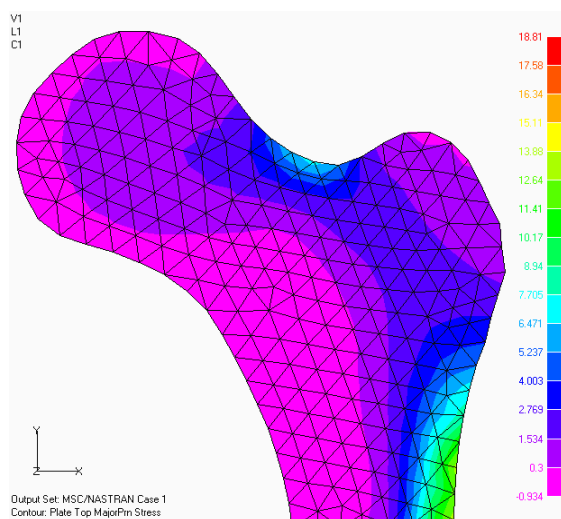


Figure 3. (b). Distribution of the top major principal stress after the 20th iteration steps [MPa]

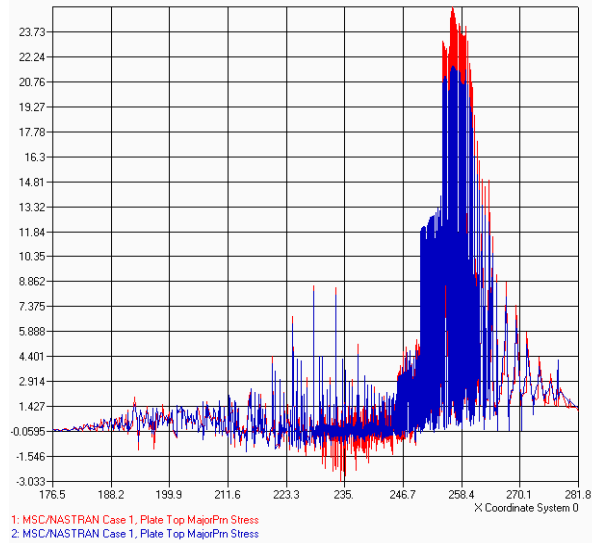


Figure 4. Top major principal stress distribution diagram versus the x coordinate. [MPa]

5.3. Unilateral body posture. Unilateral body posture is very similar to bilateral, but the forces are greater. Because a force exerted by the muscles is taken into

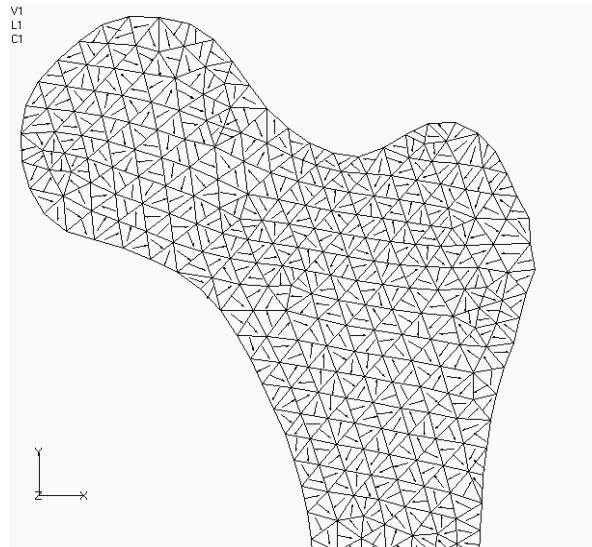


Figure 5. (a). Random Material directions in the elements

consideration and with this, balance can only be maintained if the forces acting at the hip-joint are increased. The top major principal stress distributions are a little bit different here, but their form is very similar and the evaluations of the results are also the same. The procedure was repeated for 20 iterations here as well because in

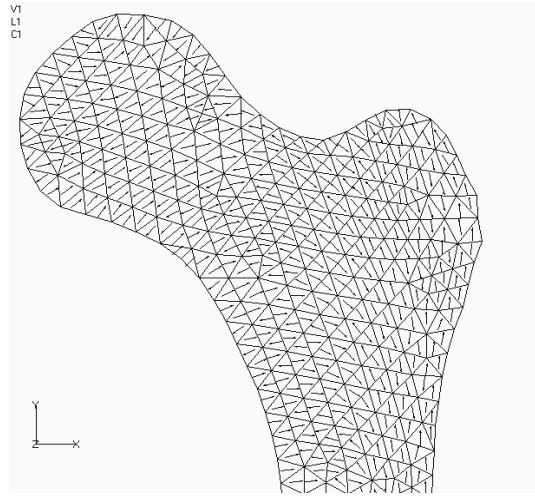


Figure 5. (b). Material directions in the elements after the first iteration step

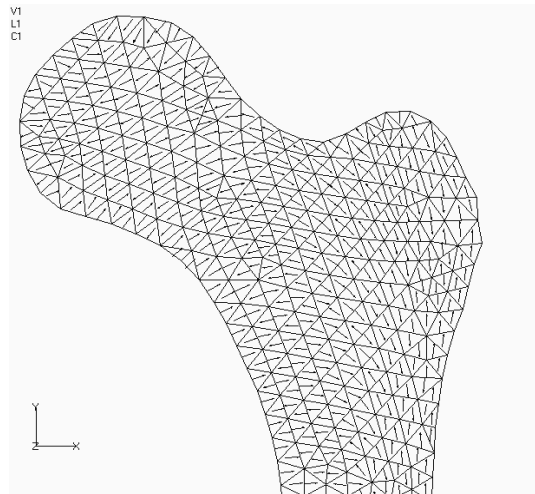


Figure 5. (c). Material directions in the elements after the 20th iteration step

this case iteration converged perfectly for any original condition and any load situation. The results here also show that the method strives for the decreasing of high stress peaks; we also emphasize that stress levels are much smoother, rounder.

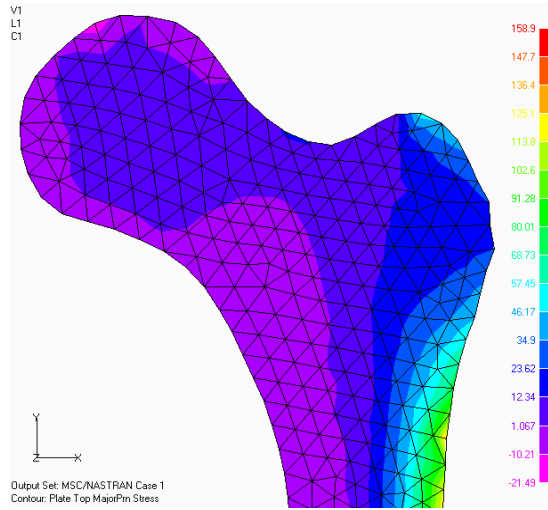


Figure 6. (a). Distribution of the top major principal stress with original material directions [MPa]

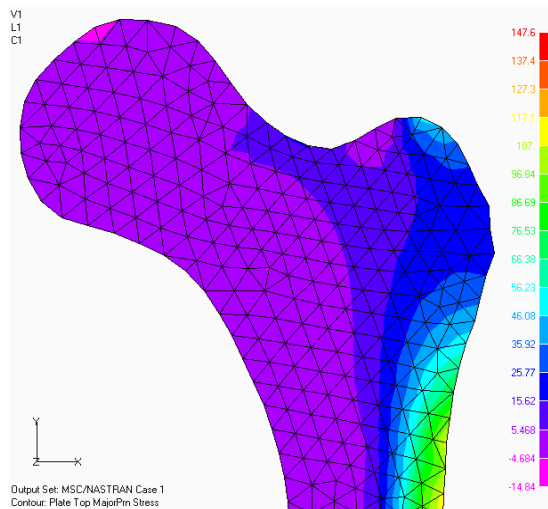


Figure 6. (b). Distribution of the top major principal stress after the 20th iteration step [MPa]

The material orientations follow the Culmann-trajectory again, so they are very similar to the real case. Therefore they are only shown here, because the evaluations of the results are the same as for bilateral body posture. (Please refer to them.)

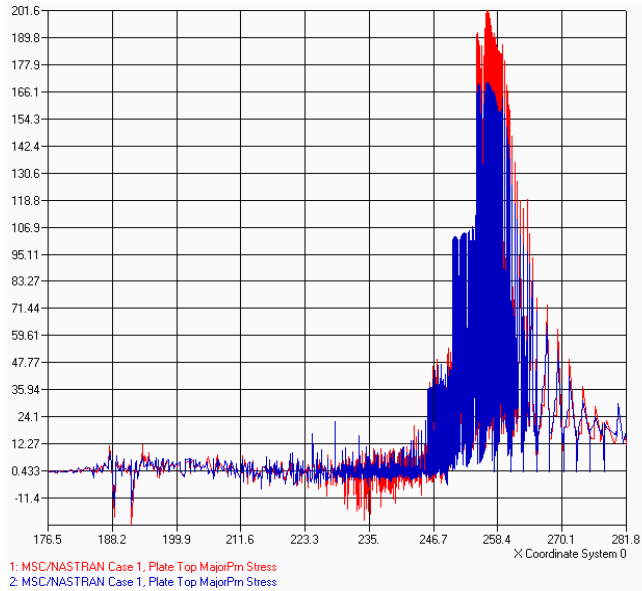


Figure 7. Top major principal Stress distribution diagram as the function of the x coordinate [MPa].

It can be recognized that the method is not sensitive to the applied loads and constraints comparing the two cases of loading. As we can see in Figures 2*a*, *b* and *c* and Figures 5*a*, *b* and *c* the evolving material orientations are similar to each other and also to the Culmann-trajectory. So we can apply any kind of loads and constraints: nodal forces, forces on surface, pressure, nonlinear forces, nodal constraints, constraints on surface and any combination of these. (Note: this property of the method follows from the way of realization.)

6. Concluding remarks

The creation steps of a local orthotropic femur model were described in detail and the results acquired from application were analyzed for two types of load. Based on these it can be seen that the model shows very well what we expect from it on the basis of physiological considerations, and that the acquired material direction ‘trajectories’ obtained are very similar to the real ones and correlate well with the most fundamental assumptions of bone biomechanics. Based on this the model is considered suitable to be included in implantation stability investigation. In the near future by building up the 3D model and adding properties like the separation of the mechanical properties of solid and spongy bone tissues and their marking based

on CT diagrams, and taking the dependence of material properties on density into consideration (thus creating an opportunity to characterize mechanical properties as function of position), probably one of the most detailed femur models will be acquired, which will hopefully be a suitable basis for a numerical implantation investigation. Obviously in the case of such a serious project we cannot rely solely on numerical calculations, so simultaneously with these a research series is also started, which will partly be a reference to simulations, partly provide those with material properties.

References

1. BRONZINO, J.D.: *Biomedical Engineering Handbook*. Vol. 1, CRC Press, 1999. (ISBN/ISSN: 084930461X)
2. IMPELLUSO, T.J.: *Locally Orthotropic Femur Remodeling*. Department of Mechanical Engineering, San Diego State University.
<http://asb-biomech.org/onlineabs/abstracts2001/pdf/035.pdf>.
3. J. HOMMINGA, J., MCCREADIE, B. R., CIARELLI, T. E., WEINANS, H., GOLDSTEIN, S. A. and HUISKES, R.: Cancellous Bone Mechanical Properties From Normals and Patients With Hip Fractures Differ on the Structure Level, Not on the Bone Hard Tissue Level. *Bone*, **30**(5), (2002), No. 2759764., 214–228
4. POPPER GY., and CSIZMÁS F.: *Numerical Methods*, Akadémiai Kiadó, 1993. (in Hungarian)
5. ZIENKIEWITCZ, O.C. and TAYLOR, L.R.: *The Finite Element Method, Vol. 1: The Basis*. Fifth Edition, Butterworth–Heinemann Press, 2000.
6. RAO, S.S.: *The Finite Element Method in Engineering*. Second Edition, Pergamon Press, 1999.
7. BUDINAS, R. G.: *Advanced Strength and Applied Stress Analysis*, Second Edition, WCB, McGraw–Hill, 1999.
8. STOLK, J., VERDONSCHOT, N., CRISTOFOLINI, L., TONI, A. and HUISKES, R.: Finite element and experimental models of cemented hip joint reconstructions can produce similar bone and cement strains in pre-clinical tests. *Journal of Biomechanics*, **35**, (2002), 499–510.

CHANGING THE CONNECTIONS OF STRUCTURAL ELEMENTS DURING AN OPTIMIZATION PROCESS

VANDA POMEZANSKI

Research Group for Computational Structural Mechanics, Hungarian Academy of Sciences
Budapest University of Technology and Economics
Műegyetem rkp. 3. Km.f.35., 1111 Budapest, Hungary
vpomezanski@epito.bme.hu

[Received: November 6, 2002]

Abstract. Optimization of internal joint connections is the inverse problem of structural optimization. There are three types of internal joints: rigid connection, flexible connection and no connection. A continuous function is chosen to design the type of every joint. These functions are determined by the optimization. The methods presented in this paper can be used for topological design as well. The paper presents the mathematical formulation. The examples shown are compared with the usual topological optimization forms.

Mathematical Subject Classification: 74P10

Keywords: cross-section, connection, optimization, topological optimization, mathematical programming

1. Introduction

The boundary conditions, defined as external foundations and/or internal joint connections, basically determine the shape and design of structures. Earlier analysis is presented in [1] and [2], and a summary is given in [3]. In practice the boundaries are given, and the calculations are carried out in order to find a minimal weight design without changing the earlier defined form and stress distribution of the structure. The topology optimization methods modify the stress distribution by changing the value of the cross-sectional area. By using the method the area of all unnecessary elements will converge to zero while the other elements will approach full stress. The disadvantage of those optimization forms – *cross-section optimization* in the following - is that they keep and use the unnecessary elements. The aim of this paper is to define a topological optimization form based on the internal joint connections – referred to as *connection optimization* in the following - and compare it to cross-section optimization. Both optimizations are analyzed in the case of *bar structures*. Section 2 presents the mathematical background. Section 3 is devoted to topological optimization and the corresponding examples.

The analysis we have presented is based on the equilibrium and compatibility equations of bar structures. The problem formulations are based on the following preconditions:

- the geometrical data are known,
- the external loads are given,
- the external supports are given,
- the material is homogeneous and linearly elastic,
- the displacements are small,
- buckling is not treated.

The state equation of FEM analysis concerns the displacements only. To take the internal forces as optimization limits into consideration, it is useful to separate the equilibrium and compatibility equations (1.1). Thus the equation system is:

$$\begin{bmatrix} \mathbf{C} & \mathbf{G} \\ \mathbf{G}^T & \mathbf{F} \end{bmatrix} \begin{bmatrix} \mathbf{v} \\ \mathbf{s} \end{bmatrix} = \begin{bmatrix} \mathbf{q} \\ \mathbf{0} \end{bmatrix}, \quad (1.1)$$

where \mathbf{C} is the diagonal matrix of the displacement supports, \mathbf{G} and its transpose are the geometrical matrices, \mathbf{F} is the flexibility matrix, \mathbf{v} is the vector of node displacements, \mathbf{s} is the vector of the internal forces acting in the bars and \mathbf{q} is the external load vector [4]. We assume that there are no permanent deformations and initial displacements at the supports: $\mathbf{0}$.

2. The connection/disconnection problem

2.1. General formulations for the connection modification. In FEM design the connections between the nodes and elements are defined fix as default. Other types of connections (e.g. hinge, elastic, etc. can be taken into consideration by subtracting a suitable dyad from the stiffness matrix \mathbf{K} :

$$\tilde{\mathbf{K}} = \mathbf{K} - \frac{1}{k_{ii}} \mathbf{k}_i \mathbf{k}_i^T, \quad (2.1)$$

where k_{ii} is an element in the main diagonal of \mathbf{K} , \mathbf{k}_i and \mathbf{k}_i^T are the column and the row in \mathbf{K} that involve k_{ii} . The flexible connections are defined by the spring constants ρ_i and are taken into consideration via a dyad which is also to be subtracted from \mathbf{K} :

$$\tilde{\mathbf{K}} = \mathbf{K} - \frac{\rho_i}{1 + \rho_i k_{ii}} \mathbf{k}_i \mathbf{k}_i^T. \quad (2.2)$$

For $\rho_i \rightarrow \infty$ the limit of equation (2.2) coincides with equation (2.1) [4] – see Figure 1 for details which graphically represent the connection.

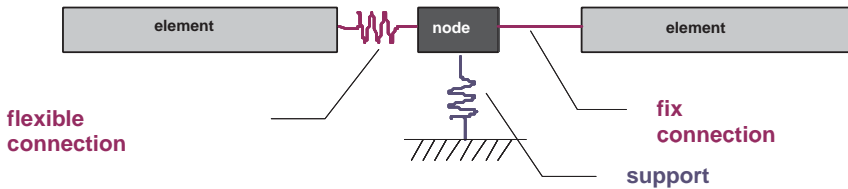


Figure 1. Model of supports and connections in FEM design

To present the same effect in the separated equation system (1.1), the symmetric flexibility matrix \mathbf{F} of a structural element has to be diagonalized:

$$\mathbf{F} = \mathbf{U}\langle\hat{\mathbf{F}}\rangle\mathbf{U}^T, \tag{2.3}$$

where $\langle\hat{\mathbf{F}}\rangle$ is the diagonal flexibility matrix and \mathbf{U} and its transpose \mathbf{U}^T are the matrices of the transformation. By adding the spring variable ρ_i to $\langle\hat{\mathbf{F}}_i\rangle$ we have

$$\langle\tilde{\mathbf{F}}\rangle = \langle\hat{\mathbf{F}}\rangle + \langle\rho\rangle. \tag{2.4}$$

Generating the stiffness matrix we obtain (a) equation (2.1) if $\rho_i = -\frac{1}{\langle\hat{\mathbf{F}}_i\rangle}$ (b) \mathbf{K} if $\rho_i = 0$ and (c) equation (2.2) otherwise. The system we have generated can be used for *connection optimization* design.

2.2. The example structure. The structure we shall analyze as an example is a well known nine-bar truss [5]. The optimal form of the structure is taken from literature [6] – see Figure 2. These two forms are used for making comparisons. The advantage of the example structure is that the flexibility matrix is a diagonal one. Consequently, there is no need for a diagonalization. The values of the vertical loads acting on the nodes 2 and 3 are the same, i.e., 400kN. The Young modulus of all elements is $2.1 \cdot 10^5$ MPa. The initial cross-sectional area is 85 cm^2 , $\sigma_e = 160 \text{ MPa}$ is the elastic stress limit and the largest bar force equals 1333 kN.

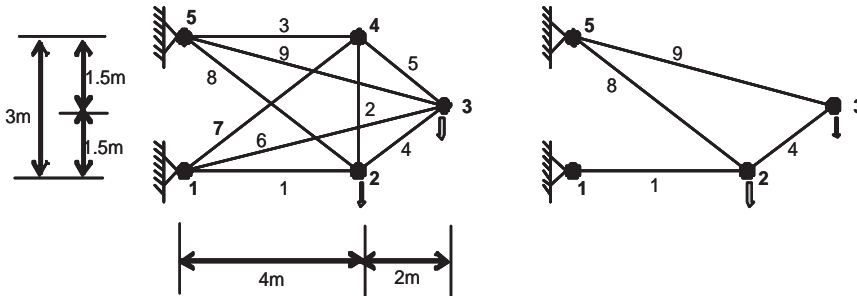


Figure 2. The nine bar truss to be investigated and its optimal form

2.3. Cross-section modification in case of the example structure. In case of the example structure the flexibility matrix of an element contains only one element, $\langle F_i \rangle = \frac{l_i}{EA_i}$, where the Young modulus E and the length of the bar l_i are constant values. A_i is the cross-sectional area. Multiplying the element $\langle F_i \rangle$ by $\rho_i \in 1..1e4$ or regarding the problem as a simple inverse one and dividing by spring variable $\hat{\rho}_i \in 1e - 4..1$, we obtain

$$\langle\tilde{F}_i\rangle = \langle F_i \rangle \langle \rho_i \rangle = \frac{l_i \rho_i}{EA_i} \tag{2.5}$$

or

$$\langle \tilde{F}_i \rangle = \frac{\langle F_i \rangle}{\langle \hat{\rho}_i \rangle} = \frac{l_i}{EA_i \hat{\rho}_i}, \quad i = 1..9. \quad (2.6)$$

The system we have generated is adaptable for cross-section modification, thus usable for a *cross-section optimization* design.

2.4. Comparison. To check formulas (2.4) and (2.5), the admissible form of the example structure is solved in three different ways, see Figure 2 and Table 1. The results obtained by comparing the different techniques (Section 2.1, 2.3) for the example structure (presented in Section 2.2) show that disconnecting the elements unused the bar forces and the displacements at the fixed points are much closer to the real values in Table 1.

		9 bar structure	4 bar structure		
			using eq. (2.5)	using eq. (2.4)	analytical solution
Displacements (cm)	1x	.1333e-2	.1333e-2	.1333e-3	.1333e-2
	1y	-.3879e-3	-.1037e-6	-.2824e-11	0
	2x	-.1188	-.2974	-.2987	-.2975
	2y	.4027	.9385	.9426	.9387
	3x	-.7124e-2	-.1629	-.1629	-.1629
	3y	.5847	1.235	1.240	1.235
	4x	.1173	.1862	.2154	
	4y	.3743	.8034	.7621	
	5x	-.1333e-2	-.1333e-2	-.1333e-3	-.1333e-2
	5y	-.4121e-3	-.7999e-3	-.8000e-4	-.8000e-3
Forces in Members (kN)	1	-536.0	-1333.	-1333.	-1333.
	2	168.5	.8037e-1	.1805e-4	
	3	529.5	.8370e-1	.2155e-4	
	4	-142.1	-499.9	-500.0	-500.0
	5	190.5	-.1466e-1	-.1571e-5	
	6	-433.2	-.1324	-.4590e-4	
	7	-471.4	-.1193	-.2851e-4	
	8	527.9	1166.	1167.	1167.
	9	393.3	412.4	412.3	412.3

Table 1. Results obtained by applying different techniques

3. The optimization problem with examples

The optimization was carried out for the example structure in Figure 2 with both methods mentioned in Section 2. The aim of the design was to find the best statically determinate form of the structure.

The optimization is implemented by a sequential quadratic programming method for solving nonlinear problems. The following variables are the unknowns in the program developed:

- $\rho_{1..9}$ are the variables to be modified,
- $v_{1..10}$ are the node displacements,
- $s_{1..9}$ are the values of the bar forces.

$$\begin{aligned}
 obj1 &= \sum_{i=1}^9 s_i & obj4 &= \sum_{i=1}^9 (s_i - \rho_i) \\
 obj2 &= - \sum_{i=1}^9 \rho_i & obj5 &= \sum_{i=1}^9 (s_i - s_i^2 \langle \tilde{\mathbf{F}}_i \rangle) \\
 obj3 &= -\mathbf{s}^T \langle \tilde{\mathbf{F}} \rangle \mathbf{s} = - \sum_{i=1}^9 s_i^2 \langle \tilde{\mathbf{F}}_i \rangle & obj6 &= - \sum_{i=1}^9 (s_i^2 \langle \tilde{\mathbf{F}}_i \rangle + \rho_i)
 \end{aligned}$$

Table 2. The objective functions

There are six objective functions given in Table 2, defined as a summation of the internal bar forces, of the spring variables, of the compliance and of three of their variations, respectively.

In both cases of topological optimization, the mathematical programming problems are formulated as follows:

$$\begin{aligned}
 \text{obj } n &= \min! && \text{Objective function from Table 2} \\
 \mathbf{C}\mathbf{v} + \mathbf{G}\mathbf{s} - \mathbf{q} &= \mathbf{0} && \text{Equalities} \\
 \mathbf{G}^T\mathbf{v} + \langle \tilde{\mathbf{F}} \rangle \mathbf{s} &= \mathbf{0} && \\
 LL \leq \rho_{i=1..9} &\leq 1e4 && \text{Inequalities} \\
 -1.8 \leq v_{i=1..10} &\leq 1.8 \quad [\text{cm}] && \\
 -1335 \leq s_{i=1..9} &\leq 1335 \quad [\text{kN}] &&
 \end{aligned} \tag{3.1}$$

The lower limit LL is zero for connection optimization and is equal to one for cross-sectional optimization.

Note: The value of the variables to be modified should fall between two positive limits. The admissible form needs a higher value. Therefore a negative sign is used to ensure the minimal optimum.

	9 bar structure	4 bar structure		
		using eq. (2.5)	using eq. (2.4)	analytical solution
Compliance	398.8	873.0	873.6	873.6
$\sum s_i$	227.0	-254.6	-253.7	-253.7
$\sum s_i, s_i > 0$	1809.7	1578.4	1579.3	1579.3
$\sum s_i, s_i < 0$	-1582.7	-1833.1	-1833	-1833

Table 3. Results obtained by the three different techniques

The comment on the positive and negative signs of other objective functions is in Table 3. The compliance of a statically determinate structure is much higher than that of an indeterminate one. A negative sign is used to present the maximum value in a minimization process, $obj3$. The sum of the internal bar forces is less, negative,

in case of a statically determinate structure. The number of bars in compression is more than that of the bars in tension. In addition the compressive stress is quite large. Since the bars are in compression the sign of the normal stress is neglected when we seek for a minimum, *obj1*.

Results: The *cross-section optimization* gives four different results, three statically determinate structures and an indeterminate one – see Table 4, 6 – 14. The statically indeterminate form is due to compliance *obj3*. The simple summation *obj1* and *obj2*, and the combination *obj4* are the dominant objective functions. Compliance *obj3* only slightly modifies the result.

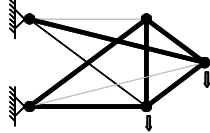
Cross-section optimization										
ρ_i [dimensionless]						v_i [cm]		s_i [kN]		
1	1	4	1	7	1	1x	.133e-2	1	-725.5	
2	1	5	1	8	57	1y	-.451e-3	2	894.0	
3	557	6	120	9	1	2x	-.161	3	4.953	
						2y	1.32	4	-865.1	
						3x	.031	5	-742.0	
						3y	1.78	6	-9.635	
						4x	.617	7	-748.2	
						4y	1.17	8	41.7	
						5x	-.133e-2	9	1335	
						5y	-.348e-3			

Table 4. Results of the mathematical programming problem (3.1) with (2.5) and *obj1* from Table 2

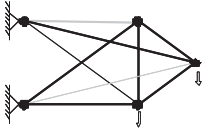
Connection optimization										
ρ_i [dimensionless]						v_i [cm]		s_i [kN]		
1	2e-5	4	0	7	0	1x	.133e-2	1	-729.0	
2	0	5	0	8	.016	1y	-.453e-3	2	900.6	
3	.083	6	2.1	9	0	2x	-.174	3	7.52	
						2y	1.33	4	-872.8	
						3x	.025	5	-745.8	
						3y	1.8	6	-.197	
						4x	.622	7	-755.2	
						4y	1.18	8	38.49	
						5x	-.133e-2	9	1335	
						5y	-.347e-3			

Table 5. Results of the mathematical programming problem (3.1) with (2.4) and *obj1* from Table 2

Cross-section optimization										
ρ_i [dimensionless]						v_i [cm]		s_i [kN]		
1	9.4	4	1e4	7	1e4	1x	.133e-2	1	-532.0	
2	1e4	5	1e4	8	1	1y	-.200e-3	2	.144	
3	1e4	6	1	9	2	2x	-1.12	3	.163	
						2y	1.8	4	.728	
						3x	.156	5	-.016	
						3y	1.8	6	-826.0	
						4x	.363	7	-.219	
						4y	1.56	8	655.7	
						5x	-.133e-2	9	825.4	
						5y	-.599e-3			

Table 6. Results of the mathematical programming problem (3.1) with (2.5) and *obj2* from Table 2

Connection optimization										
ρ_i [dimensionless]						v_i [cm]		s_i [kN]		
1	0	4	3e-5	7	0	1x	.133e-2	1	-536.0	
2	2e-5	5	2e-5	8	~ 0	1y	-.388e-3	2	168.5	
3	0	6	~ 0	9	~ 0	2x	-.119	3	529.5	
						2y	.406	4	-142.1	
						3x	-.008	5	190.5	
						3y	.593	6	-433.2	
						4x	.117	7	-471.4	
						4y	.374	8	527.9	
						5x	-.133e-2	9	393.3	
						5y	-.412e-3			

Table 7. Results of the mathematical programming problem (3.1) with (2.4) and *obj2* from Table 2

Cross-section optimization										
ρ_i [dimensionless]						v_i [cm]		s_i [kN]		
1	~ 1	4	~ 1	7	5.69	1x	.133e-2	1	-536.0	
2	13.8	5	~ 1	8	6.67	1y	-.388e-3	2	168.6	
3	~ 1	6	3.85	9	2.19	2x	-.119	3	529.4	
						2y	1.8	4	-142.1	
						3x	-.144	5	190.4	
						3y	1.8	6	-433.2	
						4x	.117	7	-471.4	
						4y	1.41	8	527.8	
						5x	-.133e-2	9	393.4	
						5y	-.412e-3			

Table 8. Results of the mathematical programming problem (3.1) with (2.5) and *obj3* from Table 2

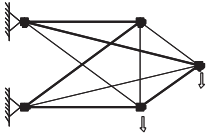
Connection optimization										
ρ_i [dimensionless]						v_i [cm]		s_i [kN]		
1	0	4	~ 0	7	$5e-5$	1x	.133e-2	1	-536.0	
2	.008	5	.003	8	.002	1y	-.388e-3	2	168.5	
3	0	6	.001	9	$4e-4$	2x	-.119	3	529.5	
						2y	1.8	4	-142.1	
						3x	-.144	5	190.5	
						3y	1.8	6	-433.2	
						4x	.117	7	-471.4	
						4y	.414	8	527.9	
						5x	-.133e-2	9	393.3	
						5y	-412e-3			

Table 9. Results of the mathematical programming problem (3.1) with (2.4) and *obj3* from Table 2

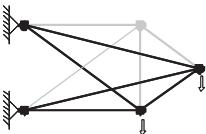
Cross-section optimization										
ρ_i [dimensionless]						v_i [cm]		s_i [kN]		
1	144	4	23	7	$1e4$	1x	.133e-2	1	-38.18	
2	$1e4$	5	$1e4$	8	1	1y	-.324e-3	2	.191	
3	$1e4$	6	1	9	1	2x	-1.23	3	.125	
						2y	1.8	4	309.3	
						3x	-.046	5	-.082	
						3y	1.72	6	-1335	
						4x	.278	7	-.238	
						4y	1.48	8	357.0	
						5x	-.133e-2	9	1080	
						5y	-.476e-3			

Table 10. Results of the mathematical programming problem (3.1) with (2.5) and *obj4* from Table 2

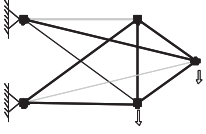
Connection optimization										
ρ_i [dimensionless]						v_i [cm]		s_i [kN]		
1	$2e-5$	4	0	7	0	1x	.133e-2	1	-735.8	
2	0	5	0	8	.012	1y	-.448e-3	2	895.0	
3	1.6	6	.56	9	0	2x	-.176	3	.396	
						2y	1.33	4	-872.4	
						3x	.025	5	-745.6	
						3y	1.8	6	-.735	
						4x	.623	7	-746.1	
						4y	.118	8	47.40	
						5x	-.133e-2	9	1335	
						5y	-.352e-3			

Table 11. Results of the mathematical programming (3.1) with (2.4) and *obj4* from Table 2

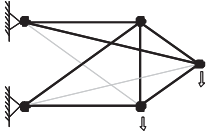
Cross-section optimization										
ρ_i [dimensionless]						v_i [cm]		s_i [kN]		
1	1	4	1	7	1.07	1x	.133e-2	1	-680.0	
2	1	5	1	8	1e4	1y	-.476e-3	2	923.2	
3	71.1	6	1317	9	1	2x	-.155	3	38.12	
						2y	1.36	4	-872.3	
						3x	.025	5	-745.5	
						3y	1.8	6	-895	
						4x	.606	7	-793.2	
						4y	1.2	8	.243	
						5x	-.133e-2	9	1335	
						5y	-.324e-3			

Table 12. Results for the mathematical programming problem (3.1) with (2.5) and *obj5* from Table 2

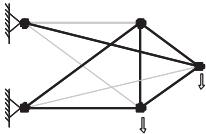
Connection optimization										
ρ_i [dimensionless]						v_i [cm]		s_i [kN]		
1	0	4	0	7	3e-5	1x	.133e-2	1	-705.5	
2	0	5	0	8	.04	1y	-.466e-3	2	908.8	
3	.024	6	.04	9	0	2x	-.158	3	24.76	
						2y	1.36	4	-864.9	
						3x	.025	5	-741.8	
						3y	1.8	6	-9.99	
						4x	.604	7	-772.8	
						4y	1.2	8	16.95	
						5x	-.133e-2	9	1335	
						5y	-.334e-3			

Table 13. Results of the mathematical programming problem (3.1) with (2.4) and *obj5* from Table 2

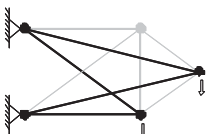
Cross-section optimization										
ρ_i [dimensionless]						v_i [cm]		s_i [kN]		
1	9.4	4	1e4	7	1e4	1x	.133e-2	1	-532.0	
2	1e4	5	1e4	8	1	1y	-.200e-3	2	.147	
3	1e4	6	1	9	2.1	2x	-1.12	3	.167	
						2y	1.8	4	.728	
						3x	.156	5	-.018	
						3y	1.8	6	-826.0	
						4x	.373	7	-.227	
						4y	1.55	8	665.7	
						5x	-.133e-2	9	825.4	
						5y	-.600e-3			

Table 14. Results of the mathematical programming problem (3.1) with (2.5) and *obj6* from Table 2

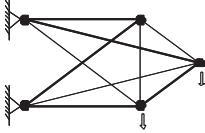
Connection optimization									
ρ_i [dimensionless]					v_i [cm]		s_i [kN]		
1	0	4	~ 0	7	3e-5	1x	.133e-2	1	-536.0
2	.009	5	.003	8	.002	1y	-.388e-3	2	168.5
3	0	6	.001	9	4e-4	2x	-.119	3	529.5
						2y	1.8	4	-142.1
						3x	-.145	5	190.5
						3y	1.8	6	-433.2
						4x	.117	7	-471.4
						4y	.399	8	527.9
						5x	-.133e-2	9	393.3
						5y	-.412e-3		

Table 15. Results of the mathematical programming problem (3.1) with (2.4) and *obj6* from Table 2

The *connection optimization* gives three different solutions: a statically determinate structure and two indeterminate ones – see Tables 5, 7 and 15. In this case the sum of internal bar forces *obj1*, and the compliance *obj3* are the useful functions.

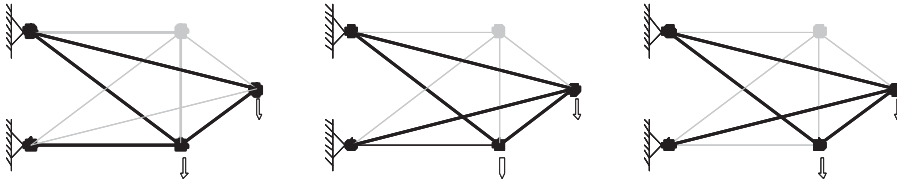


Figure 3. The results of limit modifications

The limits, used in inequalities, are important for the optimal form as well. Increasing the positive displacement limit and/or reduces the negative internal force limit the optimal statically determinate form can change. In the case of the example structure Figure 3 using *obj4* the following happens: the result is the left figure if the vertical displacement limit is 1.3cm and the internal bar force limit is 1335kN, the middle structure if the displacement limit is increased to 1.8 cm, and finally the right form if the internal force limit is changed to -1375kN.

The results of the optimization process with limits of (2.5) are presented in Tables 4 – Table 15.

4. Conclusion

The method we have presented in this paper is capable of solving the connection – disconnection problem in structural design. From a mechanical point of view the

problem is an inverse one. Mathematically it is not a convex problem. The optimization algorithm can find as many solutions as the number of the possible statically determinate structures. The results of the optimization process are determined by the objective functions. The limits set up for the displacement and the internal forces influence the local optima.

The main objective of the analysis was to formulate and try a solution technique. Thus the stability, safety and economy requirements are not fulfilled.

The method we have presented is developed for numerical optimization problems. The example structure is a well-known one from the literature, and is practical for demonstrating that the connection optimization technique developed gives good solutions. The advantages of that simple structure are that the calculations can easily be controlled, and the results obtained can easily be compared with those found in the literature [5],[6] and [7].

Acknowledgement. The author wishes to thank Prof. Anna Vászárhelyi for the idea of this research and her continuous support. The support provided by the Hungarian National Research Foundation (OTKA T029638) is gratefully acknowledged.

References

1. POMEZANSKI, V. and VÁSÁRHELYI, A.: *Shape design of bar structures by boundary optimization*. Proceedings of the 3rd International PhD Symposium in Civil Engineering, Vienna, Oct. 5-7, 2000., Volume 1., 261-266.
2. VÁSÁRHELYI, A. and POMEZANSKI, V.: *Topology design of the joint types and boundary conditions of the discretized structures by mathematical programming*. G.I.N. Rozvany and N. Olhoff (eds.), *Topology Optimization of Structures and Composite Continua*, Kluwer Academic Publishers, Netherlands, 2000, 383-385.
3. POMEZANSKI, V.: *Optimization tasks*, Műszaki Mechanika 2002. MTA-BME Mechanika Kutatóközösség Konferenciájának kiadványa, Budapest, January 30, 2002. 73-78. (in Hungarian)
4. GÁSPÁR Zs.: *Structural Analysis III, (Beam Structures)*, J95006. Műegyetemi Kiadó (Publishing House of the Budapest University of Technology and Economics), 1993, 83-93. (Lecture notes in Hungarian)
5. KALISZKY S. and LÓGÓ J.: Optimal plastic limit and shakedown design of bar structures with constraints on plastic deformation. *Engineering Structures*, **19**(1), (1997), 19–27.
6. LÓGÓ J. and IVÁNYI P.: *Topology Optimization of Simple Structures by Mathematical Programming*, Proceedings of 5th CAD/CAM International Conference and Trade Show, Budapest, Sept. 12-14, 1995, 144-155.
7. CSÉBFALVI A.: Discrete optimal weight design of geometrically nonlinear truss-structures. *Computer Assisted Mechanics and Engineering Sciences*, **6**, (1999), 313–320.

FINITE ELEMENT ANALYSIS BASED ON HETEROGENEOUS MODELS

YAREMA H. SAVULA AND NESTOR YA. SAVULA
Department of Applied Mathematics and Computer Science
Ivan Franko National University of L'viv, Ukraine
savula@franko.lviv.ua, savula@lviv.farlep.net

VALENTINE SHCHUKIN
Department of Environmental Engineering and Chemical Technology
University of Veszprém, Veszprém, Hungary

[Received: April 22, 2003]

Dedicated to Professor József FARKAS on the occasion of his seventy-fifth birthday

Abstract. A heterogeneous mathematical model (elastic body - Timoshenko shell) has been applied for the analysis of some elastic structures. The boundary and variational formulation of the heterogeneous mathematical problem are presented. Bubble functions – Finite Element Method – have been applied for the numerical analysis.

Mathematical Subject Classification: 74K25, 74S05

Keywords: heterogeneous mathematical problem, finite element method, bubble functions

1. Formulation of the problem

1.1. Introductory remarks. Many structures encountered in engineering practice consist of shell parts linked to the solid continua. In the numerical analysis these structures cannot be approximated well with the lower dimensional theories of shells. If the reliability and accuracy of the computed data are to be ensured, one must use multifield modelling in numerical simulation of the structures [1]. An approach to the analysis of multistructures, based on the asymptotic theory of shells and the theory of elasticity was suggested in the work by P. Siarlet [2]. D - adaptive analysis of multistructures is considered in the work by E. Stein [3]. Here we suggest another approach to the analysis of multistructures, which is based on the Timoshenko shell theory and the theory of elasticity.

Let the elastic continuum occupy the bounded and connected domain $\Omega_1 \cap \Omega_2^*$, (Figure 1), where Ω_1, Ω_2^* are three-dimensional domains with the Lipschitz boundaries Γ_1, Γ_2^* . Let us suppose, that the three-dimensional domain Ω_1 is referred to a Cartesian coordinate system x_1, x_2, x_3 . The three mutually orthogonal unit vectors on the

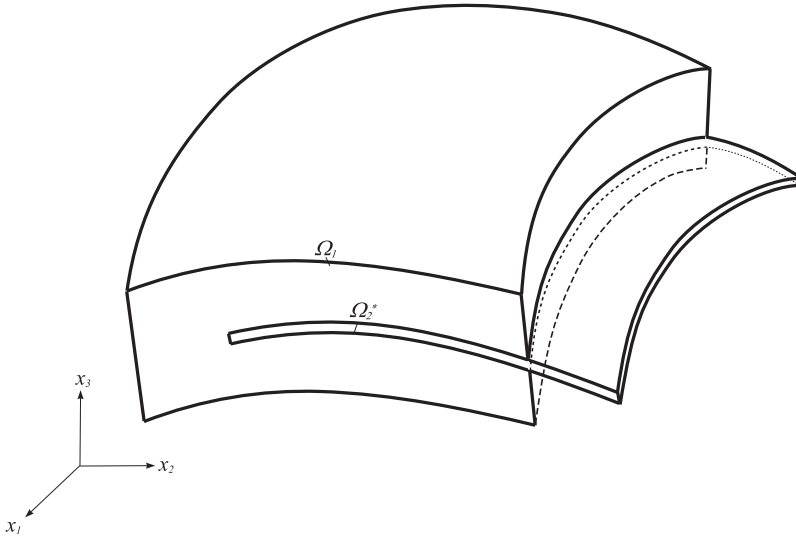


Figure 1. Thin shell embedded into a 3D body

boundary Γ_1 are denoted by $\vec{\nu}_1, \vec{\nu}_2, \vec{\nu}_3$ ($\vec{\nu}_1$ is the outer normal to Γ_1). We also suppose that the three-dimensional domain Ω_2^* is thin, i.e., one of its dimensions, the thickness h , is considerably smaller than the two others. We refer the domain Ω_2^* to the curvilinear coordinate system $\zeta_1, \zeta_2, \zeta_3$

$$\Omega_2^* = \left\{ \zeta_1, \zeta_2, \zeta_3 : \zeta_1, \zeta_2 \in \Omega_2, -\frac{h}{2} \leq \zeta_3 \leq \frac{h}{2} \right\},$$

defined on the middle surface $S \subset \mathbf{R}^3$, which is an image of the set $\Omega_2 \subset \mathbf{R}^2$ (with the boundary Γ_2) through a map

$$x_i = \varphi_i(\zeta_1, \zeta_2), \quad \zeta_1, \zeta_2 \in \Omega_2, \quad i = 1, 2, 3. \quad (1)$$

Let us denote the three orthogonal right-handed unit vectors on the curve ∂S (∂S is the map of Γ_2 with respect to (1)) by $\vec{\mathbf{n}}_1, \vec{\mathbf{n}}_2, \vec{\mathbf{n}}_3$, where $\vec{\mathbf{n}}_1$ is the unit normal to $\partial\Gamma_2$ that lies in the tangent plane of the middle surface S ; $\vec{\mathbf{n}}_2$ is the unit tangent to the curve Γ_2 ; and $\vec{\mathbf{n}}_3$ is a unit normal to the middle surface S .

1.2. Equations of the theory of elasticity. Let

$$\mathbf{u} = (u_1(x), u_2(x), u_3(x)), \quad x = x_1, x_2, x_3, \quad (2)$$

be the displacement vector of the elastic continuum. The components $e_{ij}(u)$ of the deformation tensor are given by the relations

$$e_{ij} = \frac{1}{2} \left(\frac{\partial u_i}{\partial x_j} + \frac{\partial u_j}{\partial x_i} \right), \quad i, j = 1, 2, 3. \quad (3)$$

The stress components are denoted by σ_{ij} . The stress strain relations are of the form

$$\sigma_{ij} = \sum_{k,l=1}^3 c_{ijkl}(x) e_{kl}, \quad (4)$$

where c_{ijkl} stands for the elastic parameters. For a homogeneous and isotropic continuum equation (4) can be rewritten in the form

$$\begin{aligned} \sigma_{ii} &= \lambda\theta + 2\mu e_{ii}, \quad i = 1, 2, 3; \\ \sigma_{ij} &= 2\mu e_{ij}, \quad i \neq j, \quad i, j = 1, 2, 3; \end{aligned} \quad (5)$$

where

$$\theta = e_{11} + e_{22} + e_{33},$$

while

$$\lambda = \frac{E\nu}{(1+\nu)(1-2\nu)} \quad \text{and} \quad \mu = \frac{E}{2(1+\nu)}$$

are the Lamé coefficients.

The components of the stress tensor satisfy the equilibrium equations

$$\sum_{k=1}^3 \frac{\partial \sigma_{ik}}{\partial x_k} + f_i = 0, \quad i = 1, 2, 3; \quad (6)$$

where f_i denote the components of the body forces applied to the elastic continuum in the domain Ω_1 .

1.3. Equations of the Timoshenko shell theory [5]. The vector defined by the equation

$$\mathbf{v} = (v_1(\xi), v_2(\xi), w(\xi), \gamma_1(\xi), \gamma_2(\xi)), \quad \xi = \xi_1, \xi_2, \quad (7)$$

involves the displacements $v_1(\xi), v_2(\xi), w(\xi)$ and the angles of rotations $\gamma_1(\xi), \gamma_2(\xi)$ on the middle surface.

The deformation of a shell is described by the characteristics

$$\begin{aligned} \varepsilon_{\alpha\alpha} &= \frac{1}{A_\alpha} \partial_\alpha v_\alpha + \frac{1}{A_\alpha A_\beta} v_\beta \partial_\beta A_\alpha + k_\alpha w, \\ 2\varepsilon_{\alpha\beta} &= \frac{A_\alpha}{A_\beta} \partial_\beta \frac{v_\alpha}{A_\alpha} + \frac{A_\beta}{A_\alpha} \partial_\alpha \frac{v_\beta}{A_\beta}, \\ \varepsilon_{\alpha 3} &= -k_\alpha u_\alpha + \frac{1}{A_\alpha} \partial_\alpha w + \gamma_\alpha, \\ \chi_{\alpha\alpha} &= \frac{1}{A_\alpha} \partial_\alpha \gamma_\alpha + \frac{1}{A_\alpha A_\beta} \gamma_\beta \partial_\beta A_\alpha \\ 2\chi_{\alpha\beta} &= \frac{k_\alpha}{A_\beta} \partial_\beta \gamma_\alpha - \frac{k_\beta}{A_\alpha A_\beta} v_\alpha \partial_\beta A_\alpha + \frac{k_\beta}{A_\alpha} \partial_\alpha \gamma_\beta - \\ &\quad - \frac{k_\alpha}{A_\alpha A_\beta} \gamma_\beta \partial_\alpha A_\beta + \frac{A_\alpha}{A_\beta} \partial_\beta \frac{\gamma_\alpha}{A_\alpha} + \frac{A_\beta}{A_\alpha} \partial_\alpha \frac{\gamma_\beta}{A_\beta}, \end{aligned} \quad (8)$$

where $\alpha, \beta \in \{1, 2\}; \alpha \neq \beta.$, $\partial_\alpha = \frac{\partial}{\partial \xi_\alpha}$, A_α, k_α are Lamé coefficients and main curvatures of the middle surface of the shell, respectively.

The force and moment characteristics $T_{\alpha\beta}$, $T_{\alpha 3}$, $M_{\alpha\beta}$ can be given in terms of the deformation characteristics of the shell $\varepsilon_{\alpha\beta}$, $\varepsilon_{\alpha 3}$, $\chi_{\alpha\beta}$, $\alpha, \beta \in \{1, 2\}$ via the material law:

$$\begin{aligned} T_{\alpha\alpha} &= \frac{Eh}{1-\nu^2} (\varepsilon_{\alpha\alpha} + \nu\varepsilon_{\beta\beta}), \\ T_{\alpha\beta} &= \frac{Eh}{2(1+\nu)} \varepsilon_{\alpha\beta}, \\ T_{\alpha 3} &= k'G'h\varepsilon_{\alpha 3}, \\ M_{\alpha\alpha} &= \frac{Eh^3}{12(1-\nu^2)} (\chi_{\alpha\alpha} + \nu\chi_{\beta\beta}), \\ M_{\alpha\beta} &= \frac{Eh^3}{12(1+\nu)} \chi_{\alpha\beta}, \end{aligned} \quad (9)$$

where k' is the shear coefficient, G' is the shear module. For isotropic materials

$$k' = \frac{5}{6}, \quad G' = \frac{E}{2(1+\nu)}.$$

The force and moment characteristics introduced should satisfy the equilibrium equations

$$\begin{aligned} &\frac{1}{A_\alpha A_\beta} \partial_\alpha A_\beta T_{\alpha\alpha} - \frac{1}{A_\alpha A_\beta} \partial_\alpha (A_\beta) T_{\beta\beta} + \frac{1}{A_\alpha^2 A_\beta} \partial_\beta A_\alpha^2 T_{\alpha\beta} + k_\alpha T_{\alpha 3} + \\ &\quad + \frac{1}{A_\alpha A_\beta} \partial_\beta A_\alpha k_\alpha M_{\alpha\beta} + \frac{k_\beta}{A_\alpha A_\beta} \partial_\beta (A_\alpha) M_{\alpha\beta} + p_\alpha = 0, \\ &\quad -k_1 T_1 - k_2 T_2 + \frac{1}{A_1 A_2} \partial_1 A_2 T_{13} + \frac{1}{A_1 A_2} \partial_2 A_1 T_{23} + p_3 = 0, \\ &-T_{\alpha 3} + \frac{1}{A_\alpha A_\beta} \partial_\alpha A_\beta M_{\alpha\alpha} - \frac{1}{A_\alpha A_\beta} \partial_\alpha (A_\beta) M_{\beta\beta} + \frac{1}{A_\alpha^2 A_\beta} \partial_\beta A_\alpha^2 M_{\alpha\beta} + m_\alpha = 0, \end{aligned} \quad (10)$$

where

$$\begin{aligned} p_i &= \left(1 + k_1 \frac{h}{2}\right) \left(1 + k_2 \frac{h}{2}\right) \sigma_{i3}^+ + \left(1 - k_1 \frac{h}{2}\right) \left(1 - k_2 \frac{h}{2}\right) \sigma_{i3}^- + \\ &\quad + \int_{-h/2}^{h/2} (1 + k_1 \zeta_3) (1 + k_2 \zeta_3) f_i d\zeta_3, \quad i = 1, 2, 3; \\ m_i &= \left(1 + k_1 \frac{h}{2}\right) \left(1 + k_2 \frac{h}{2}\right) \frac{h}{2} \sigma_{j3}^+ - \left(1 - k_1 \frac{h}{2}\right) \left(1 - k_2 \frac{h}{2}\right) \frac{h}{2} \sigma_{j3}^- + \\ &\quad + \int_{-h/2}^{h/2} (1 + k_1 \zeta_3) (1 + k_2 \zeta_3) f_i \zeta_3 d\zeta_3, \quad j = 1, 2; \end{aligned} \quad (11)$$

in which f_i stands for the components of body forces in the domain Ω_2 , σ_{i3}^+ , σ_{i3}^- are the components of the surface forces on the shell surfaces $\zeta_3 = +h/2$, $\zeta_3 = -h/2$.

1.4. Boundary and junction conditions. We shall assume that boundary Γ_1 consists of parts $\Gamma_1^{(i)}$, that is

$$\Gamma_1 = \bigcup_{i=1}^5 \Gamma_1^{(i)}, \quad \bigcap_{\substack{i,j=1, \\ i \neq j}}^5 \Gamma_1^{(j)} = \emptyset. \tag{12}$$

Boundary Γ_2^* of the thin domain Ω_2^* consists of the side surface Γ_2^c and the two face surfaces Γ_2^+, Γ_2^- . The side surface Γ_2^c is a cylindrical one, which is generated by the motion of the normal to the middle surface S along the boundary ∂S of the middle surface. The boundary ∂S of the middle surface is the curve $\partial S \subset \mathbf{R}^3$, which is the map (1) $\Gamma_2 \subset \mathbf{R}^2$. Let us suppose that Γ_2 consists of parts $\Gamma_2^{(i)}$, which satisfy conditions

$$\Gamma_2 = \bigcup_{i=1}^3 \Gamma_2^{(i)}, \quad \bigcap_{\substack{i,j=1, \\ i \neq j}}^3 \Gamma_2^{(j)} = \emptyset. \tag{13}$$

The following boundary conditions are imposed on the parts of the boundary $\Gamma_1^{(1)}, \Gamma_1^{(2)}, \Gamma_2^{(1)}, \Gamma_2^{(2)}$:

$$u_1^\nu = 0, \quad u_2^\nu = 0, \quad u_3^\nu = 0, \quad x \in \Gamma_1^{(1)}; \tag{14}$$

$$\sigma_{11}^\nu = 0, \quad \sigma_{12}^\nu = 0, \quad \sigma_{13}^\nu = 0, \quad x \in \Gamma_1^{(2)}; \tag{15}$$

$$v_1^n = 0, \quad v_2^n = 0, \quad w = 0, \quad \gamma_1^n = 0, \quad \gamma_2^n = 0, \quad \zeta_1, \zeta_2 \in \Gamma_2^{(1)}; \tag{16}$$

$$T_{11}^n = 0, \quad T_{12}^n = 0, \quad T_{13}^n = 0, \quad M_{11}^n = 0, \quad M_{12}^n = 0, \quad \zeta_1, \zeta_2 \in \Gamma_2^{(2)}, \tag{17}$$

where $u_1^\nu, u_2^\nu, u_3^\nu, v_1^n, v_2^n, \gamma_1^n, \gamma_2^n$ are the normal deflections and rotation angles on the boundaries Γ_1 and Γ_2 ; $\sigma_{ij}^\nu, T_{\alpha\beta}^n, T_{\alpha 3}^n, M_{\alpha\beta}^n$ are the normal stresses, forces and moments on the boundaries Γ_1 and Γ_2 .

We shall also assume that $\Gamma_1^{(3)}$ and $\Gamma_2^{(3)}$ satisfy the relations

$$\Gamma_1^{(3)} = \left\{ \zeta_1, \zeta_2, \zeta_3 : \zeta_1, \zeta_2 \in \Gamma_2^{(3)}, -\frac{h}{2} \leq \zeta_3 \leq \frac{h}{2} \right\}.$$

On this part of the boundary perfect contact of two elastic continua, which occupy domains Ω_1, Ω_2^* , is carried out. On the part of the boundary the following relations exist (Figure 2)

$$\vec{\nu}_1 = -\vec{n}_1, \quad \vec{\nu}_2 = -\vec{n}_2, \quad \vec{\nu}_3 = \vec{n}_3.$$

On the boundary $\Gamma_1^{(3)}$ we specify the following junction conditions.

Geometrical conditions:

$$\begin{aligned} u_1^\nu &= -v_1^n - \zeta_3 \gamma_1^n, \\ u_2^\nu &= -v_2^n - \zeta_3 \gamma_2^n, \\ u_3^\nu &= w. \end{aligned} \tag{18}$$

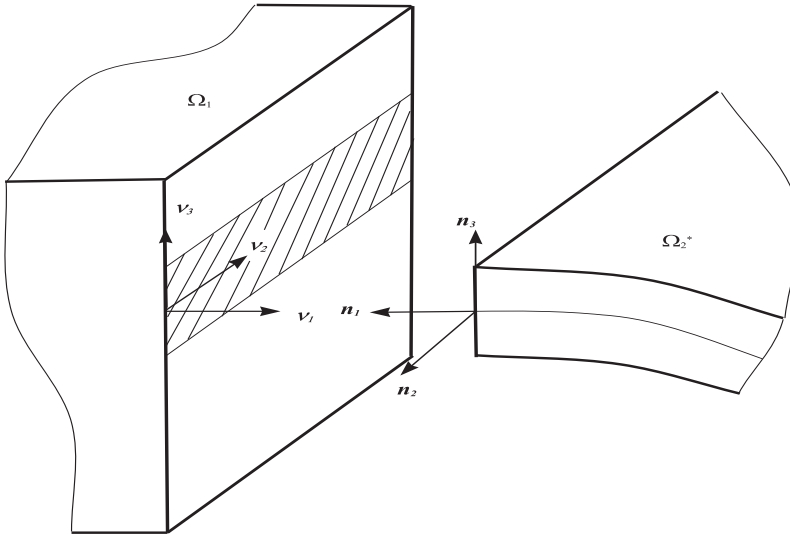


Figure 2. Junction of a thin shell to a 3D elastic body

Statical conditions:

$$\begin{aligned}
 - \int_{-h/2}^{h/2} \sigma_{11}^\nu (1 + k_\nu \zeta_3) d\zeta_3 &= T_{11}^n, & - \int_{-h/2}^{h/2} \sigma_{12}^\nu (1 + k_\nu \zeta_3) d\zeta_3 &= T_{12}^n, \\
 \int_{-h/2}^{h/2} \sigma_{33}^\nu (1 + k_\nu \zeta_3) d\zeta_3 &= T_{13}^n, & & (19) \\
 - \int_{-h/2}^{h/2} \sigma_{11}^\nu \zeta_3 (1 + k_\nu \zeta_3) d\zeta_3 &= M_{11}^n, & - \int_{-h/2}^{h/2} \sigma_{12}^\nu \zeta_3 (1 + k_\nu \zeta_3) d\zeta_3 &= M_{12}^n,
 \end{aligned}$$

where k_ν is the curvature of the normal section along the boundary curve of the shell.

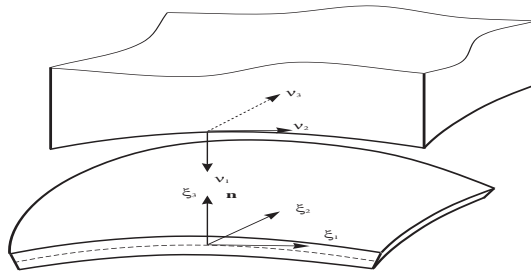


Figure 3. Embedding of a thin shell into a 3D elastic body on the upper face

Let us define junction conditions on the surfaces $\Gamma_1^{(4)} = \Gamma_2^+$ (see Figure 3). They have the following forms:

Geometrical conditions:

$$u_1^\nu = -w, \quad u_2^\nu = u_1^n + \frac{h}{2}\gamma_1^n, \quad u_3^\nu = u_2^n + \frac{h}{2}\gamma_2^n. \tag{20}$$

Statical conditions:

$$\sigma_{11}^\nu = -\sigma_{33}^+, \quad \sigma_{12}^\nu = \sigma_{13}^+, \quad \sigma_{13}^\nu = \sigma_{23}^+. \tag{21}$$

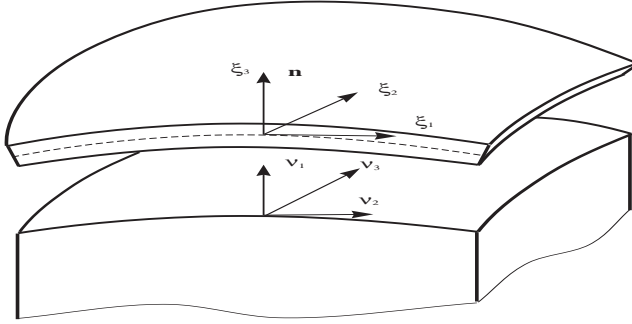


Figure 4. Embedding of a thin shell into a 3D elastic body on the lower face

We shall also define junction conditions on the surfaces $\Gamma_1^{(5)} = \Gamma_2^-$ (see Figure 4).

Geometrical conditions:

$$u_1^\nu = w, \quad u_2^\nu = u_1^n - \frac{h}{2}\gamma_1^n, \quad u_3^\nu = u_2^n - \frac{h}{2}\gamma_2^n. \tag{22}$$

Statical conditions:

$$\sigma_{11}^\nu = p_n^-, \quad \sigma_{12}^\nu = p_1^-, \quad \sigma_{13}^\nu = p_2^-. \tag{23}$$

Thus heterogeneous mathematical model [6] consists of the equations (6), (3) - (5), (8) - (10); boundary conditions (14) - (17); and junction conditions (18) - (23).

2. Variational formulation

Let us consider the function space

$$V = \left\{ \mathbf{U} = (\mathbf{u}, \mathbf{v}), \mathbf{u} = (u_1, u_2, u_3), \mathbf{v} = (v_1, v_2, w, \gamma_1, \gamma_2), \mathbf{u} \in \mathbf{W}_2^{(1)}(\Omega_1), \right. \\ \left. \mathbf{v} \in \mathbf{W}_2^{(1)}(\Omega_2), \text{ conditions (14), (16), (18), (20), (22)} \right\}.$$

We shall formulate two equivalent variational problems for the heterogeneous mathematical model: theory of elasticity and Timoshenko shell theory in displacements. Find a solution \mathbf{U} which minimizes the functional (principle of the minimum of potential energy)

$$F(\mathbf{U}) \rightarrow \min, \quad \mathbf{U} \in V \tag{24}$$

and find a \mathbf{U} , which satisfies the variational equation (weak formulation):

$$a_1(\mathbf{u}, \tilde{\mathbf{u}}) + a_2(\mathbf{v}, \tilde{\mathbf{v}}) = (\mathbf{P}, \tilde{\mathbf{U}}), \quad \mathbf{U} = (\mathbf{u}, \mathbf{v}) \in \mathbf{V}, \quad \forall \tilde{\mathbf{U}} = (\tilde{\mathbf{u}}, \tilde{\mathbf{v}}) \in V. \quad (25)$$

Here

$$\begin{aligned} F(\mathbf{U}) &= a_1(\mathbf{u}, \mathbf{u}) + a_2(\mathbf{v}, \mathbf{v}) - 2(\mathbf{P}, \mathbf{U}), \\ a_1(\mathbf{u}, \tilde{\mathbf{u}}) &= 2 \int_{\Omega_1} W_1(\mathbf{u}, \tilde{\mathbf{u}}) d\Omega_1, \\ W_1(\mathbf{u}, \tilde{\mathbf{u}}) &= \frac{1}{2} [e_{11}(\mathbf{u}) \sigma_{11}(\tilde{\mathbf{u}}) + \dots + e_{23}(\mathbf{u}) \sigma_{23}(\tilde{\mathbf{u}})], \\ a_2(\mathbf{v}, \tilde{\mathbf{v}}) &= 2 \int_{\Omega_2} W_2(\mathbf{v}, \tilde{\mathbf{v}}) d\Omega_2, \\ W_2(\mathbf{v}, \tilde{\mathbf{v}}) &= \frac{1}{2} [\varepsilon_{11}(\mathbf{v}) T_{11}(\tilde{\mathbf{v}}) + \varepsilon_{22}(\mathbf{v}) T_{22}(\tilde{\mathbf{v}}) + \varepsilon_{12}(\mathbf{v}) T_{12}(\tilde{\mathbf{v}}) + \\ &+ \varepsilon_{13}(\mathbf{v}) T_{13}(\tilde{\mathbf{v}}) + \varepsilon_{23}(\mathbf{v}) T_{23}(\tilde{\mathbf{v}}) + \chi_{11}(\mathbf{v}) M_{11}(\tilde{\mathbf{v}}) + 2\chi_{12}(\mathbf{v}) M_{12}(\tilde{\mathbf{v}})], \\ (\mathbf{P}, \tilde{\mathbf{U}}) &= \int_{\Omega_1} \sum_{i=1}^3 u_i f_i d\Omega_1 + \int_{\Omega_2} (v_1 p_1 + v_2 p_2 + w p_3 + \gamma_1 m_1 + \gamma_2 m_2) d\Omega_2. \end{aligned} \quad (26)$$

3. Penalty variational formulation

Consider a penalty variational formulation of the heterogenous mathematical model in the following two forms:

$$F_\varepsilon(\mathbf{U}_\varepsilon) \rightarrow \min, \quad \mathbf{U}_\varepsilon \in V_\varepsilon, \quad \varepsilon \rightarrow 0 \quad (27)$$

and

$$a_1(\mathbf{u}_\varepsilon, \tilde{\mathbf{u}}) + a_2(\mathbf{v}_\varepsilon, \tilde{\mathbf{v}}) + \frac{1}{\varepsilon} a_3(\mathbf{U}_\varepsilon, \tilde{\mathbf{U}}) = (\mathbf{P}, \tilde{\mathbf{U}}), \quad (28)$$

$$\mathbf{U}_\varepsilon = (\mathbf{u}_\varepsilon, \mathbf{v}_\varepsilon), \quad \mathbf{U}_\varepsilon \in V_\varepsilon, \quad \varepsilon > 0, \quad \varepsilon \rightarrow 0,$$

$$\forall \tilde{\mathbf{U}} \in V_\varepsilon,$$

$$\begin{aligned} V_\varepsilon = \left\{ \mathbf{U} = (\mathbf{u}, \mathbf{v}), \quad \mathbf{u} = (u_1, u_2, u_3), \quad \mathbf{v} = (v_1, v_2, w, \gamma_1, \gamma_2), \quad \mathbf{u} \in \mathbf{W}_2^{(1)}(\Omega_1), \right. \\ \left. \mathbf{v} \in \mathbf{W}_2^{(1)}(\Omega_2), \text{ conditions (14), (16), (20), (22)} \right\}. \end{aligned}$$

Here

$$\begin{aligned} F_\varepsilon(\mathbf{U}_\varepsilon) &= a_1(\mathbf{u}_\varepsilon, \mathbf{u}_\varepsilon) + a_2(\mathbf{v}_\varepsilon, \mathbf{v}_\varepsilon) + \frac{1}{\varepsilon} a_3(\mathbf{U}_\varepsilon, \mathbf{U}_\varepsilon) - 2(\mathbf{P}, \mathbf{U}_\varepsilon), \\ a_3(\mathbf{U}_\varepsilon, \tilde{\mathbf{U}}_\varepsilon) &= \int_{\Gamma_1^{(3)}} \{ (u_1^\nu + v_1^n + \zeta_3 \gamma_1^n) (\tilde{u}_1^\nu + \tilde{v}_1^\nu + \zeta_3 \tilde{\gamma}_1^\nu) + \\ &+ (u_2^\nu + v_2^n + \zeta_3 \gamma_2^n) (\tilde{u}_2^\nu + \tilde{v}_2^\nu + \zeta_3 \tilde{\gamma}_2^\nu) + (u_3^\nu - w) (\tilde{u}_3^\nu - \tilde{v}_3^\nu) \} d\Gamma. \end{aligned}$$

The penalty item $\frac{1}{\varepsilon} a_3(\mathbf{U}_\varepsilon, \mathbf{U}_\varepsilon)$ is introduced to avoid satisfying the geometrical conditions on the boundary $\Gamma_1^{(3)}$

$$u_1^\nu = -v_1^n - \zeta_3 \gamma_1^n,$$

$$u_2^\nu = -v_2^n - \zeta_3 \gamma_2^n,$$

$$u_3^\nu = w,$$

which are difficult to satisfy in a finite element algorithm.

4. Numerical examples

4.1. **Example 1.** As a test problem we shall consider a one-dimensional problem, i.r. a plate subjected to uniform pressure $p_0 = const$. The plate is simply supported.

It's well known [5], [7] that there appears the locking effect if we use the FEM to the analysis of shells on the base of Timoshenko's shell theory, To remove the inaccuracy in results generated by the locking effect, we suggest to use bubble-approximation for the unknown displacements.

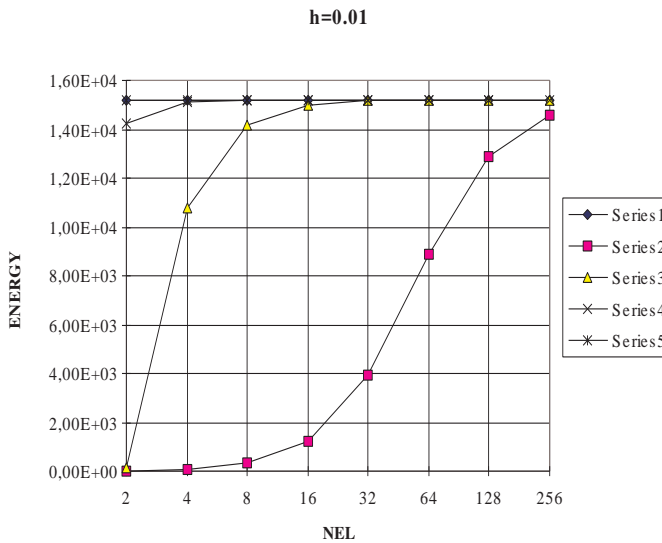


Figure 5. Convergence of the FEM solution

We map the finite element

$$\Omega_k = \{\zeta_1 : \zeta_1^{k-1} \leq \zeta_1 \leq \zeta_1^k\}$$

onto the standard element

$$\Omega_{st} = \{\xi : -1 \leq \xi \leq 1\}$$

with the mapping

$$\zeta_1 = \frac{1 - \xi}{2} \zeta_1^{k-1} + \frac{1 + \xi}{2} \zeta_1^k,$$

and select the following shape functions [4]

$$\varphi_1 = \frac{1 - \xi}{2}, \quad \varphi_2 = \frac{1 + \xi}{2}, \quad \varphi_i = \Phi_{i-1}(\xi) \quad i = 3, 4, \dots, m,$$

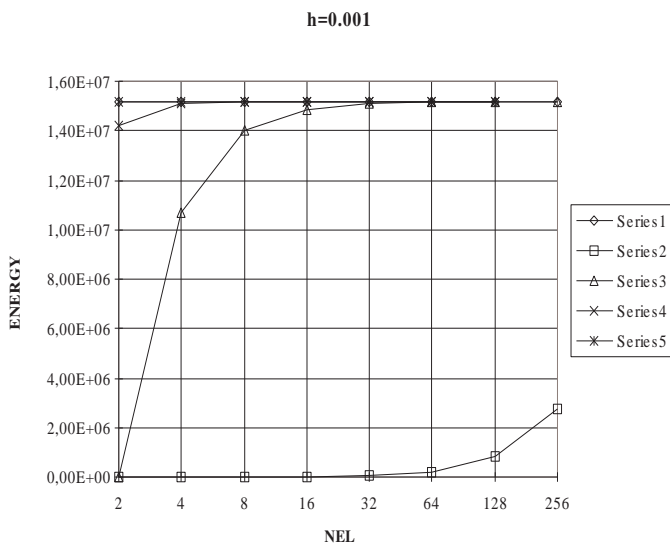


Figure 6. Convergence of the FEM solution

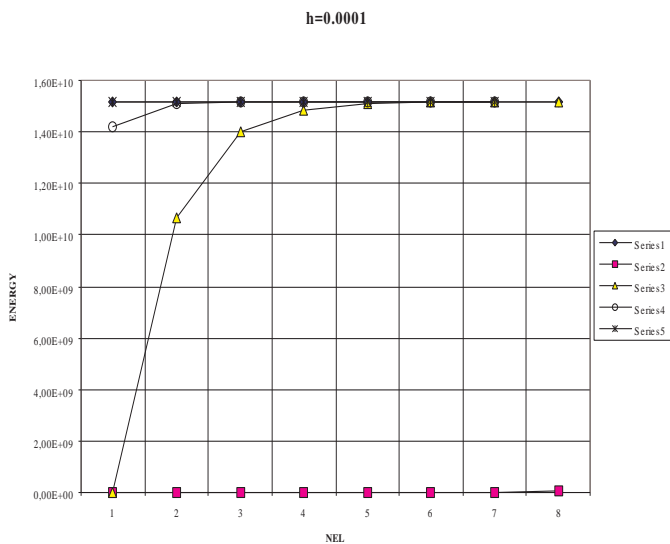


Figure 7. Convergence of the FEM solution

where

$$\Phi_j = \sqrt{\frac{2j-1}{2}} \int_{-1}^{\xi} P_{j-1}(t) dt, \quad j = 2, 3, \dots$$

in which P_j is the j -th Legendre polynomial.

Figures 5-7 illustrate the convergence of the FEM solution in energy norm for different thicknesses (h/l) depending on the number of elements (Series 1: exact value; Series 2: $m = 2$; Series 3: $m = 3$; Series 4: $m = 4$; Series 5: $m = 5$).

4.2. **Example 2.** Let us apply the heterogeneous mathematical model for the numerical analysis of a tube junction (Figure 8) which is subjected to inner pressure[8].

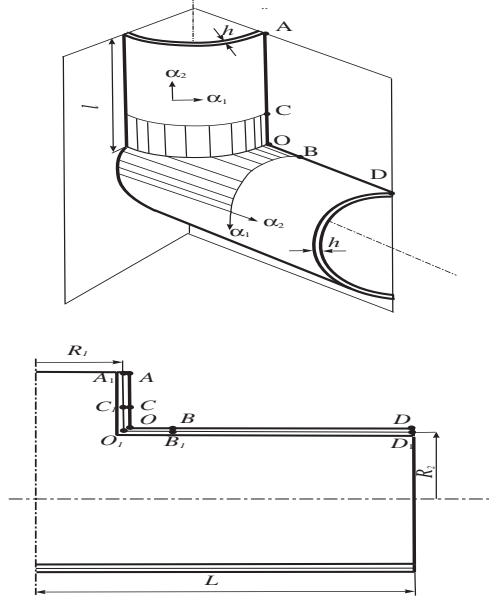


Figure 8. Tube junction

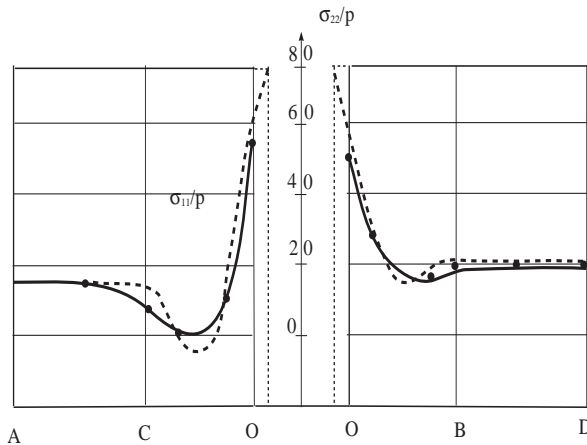


Figure 9. Graphs of stresses in the tube junction

The data are as follows:

$$R_1 = 0.5R_2, \quad h = 0.05R_2, \quad l = 1.7R_2, \quad L = 2.2R_2, \\ E = 2.1 \times 10^5 p, \quad \nu = 0.3, \quad \varepsilon = 10^{-4}$$

For the analysis we used FEM with quadratic approximation on two-dimensional (theory of shell) and three-dimensional (theory of elasticity in shaded region).

In Figure 9 the graphs of stresses σ_{22}/p along the line ACOBD are shown. The solid line corresponds to the analysis by the FEM based on the heterogeneous model. The dotted line corresponds to the analysis by the FEM based on the theory of coupled shells. The point O_1 is the point where the middle surfaces meet. The value of stresses in this point obtained using the theory of coupled shells is not adequate. Bold dots represent the results of experimental data.

Acknowledgement. The support provided by the University of Veszprém, Hungary and NATO grant: 3015/02/HY is gratefully acknowledged.

References

1. QUARTERONI, A.: Multifields modelling in numerical simulation of partial differential equations. GAMM - Mitteilungen, ZAMM, Heft 1, (1996), 45–63.
2. CIARLET P. G.: *Plates and Junctions in Elastic Multi-Structures. An Asymptotic Analysis*. Paris, Springer-Verlag, 1990.
3. STEIN, E., and OHNIMUS, S.: *Concept and realization of integrated adaptive finite element methods in solid and structural - mechanics*. Numerical Methods in Engineering '92, Proceedings of the First European Conference on Numerical Methods in Engineering 7-11 by ECCOMAS September 1992, Brussels, Belgium, Elsevier Science Publisher B.V., 63-170.
4. SZABÓ, B. and BABUŠKA, I.: *Finite Element Analysis*. John Wiley & Sons, 1991.
5. SAVULA YA. H. and FLEISHMAN, N. P.: *Analysis and Optimal Control of Shells with the Monge's Middle Surfaces*. Lviv, 1989.
6. GRIGORENKO, YA. M., SAVULA, YA. H. and MUKHA, I. S.: Linear and non-linear problems of elastic deformation of shells of complicated form and method of numerical analysis. *Applied Mechanics*, **36**(8), (2000), 3–27.
7. SCHWAB, C. and MANIL, M.: Locking and boundary layer effects in the finite element approximation on the Reissner - Mindlin plate model. Proceedings of Symposia in Applied Mathematics, American Mathematical Society, **48**, (1994), 367–371.
8. SAVULA YA. H. and SAVULA, N. YA.: *Static analysis of structures on the base of a heterogeneous model* published in Metal Structures, Design, Fabrication Economy edited by K. Jármai and J. Farkas. Millpress, Rotterdam, Netherlands, (2003), 381–385.

CALCULATION OF STRESSES IN ISOTROPIC PLATES WITH TWO CIRCULAR HOLES

VALENTINE SHCHUKIN

Center of Mathematical Modelling, National Academy of Science of Ukraine
79005, Lviv, 15 Dudayev Str.

IMRE TIMÁR

University of Veszprém
10 Egyetem út, 8200 Veszprém, Hungary
timari@almos.vein.hu

[Received: September 4, 2003]

Dedicated to Professor József FARKAS on the occasion of his seventy-fifth birthday

Abstract. The paper presents an efficient method for the solution of the isotropic plate problem with two circular holes. The aim of the method is the conformal mapping of the exterior of a single circle into the domain of the plate. The paper presents some practical examples for the elastic equilibrium of isotropic plates with two circular holes stiffened by elastic rings. The stresses and deformations of the bodies in contact are evaluated and illustrated. For the strength calculation of plates the theory of small deformation of thin curved bars was used.

Mathematical Subject Classification: 74B05

Keywords: stress distribution, plate with circular holes, stiffened holes

1. Introduction

In engineering, solving the elastic plane problems for a plate with multiple holes is of considerable interest [1-4]. The closed form solution to stress concentration around a hole in an infinite orthotropic plate was first obtained by [5] and [6] using the complex potential method. A series of analytic techniques has been devoted to treating the problem of interacting holes in an infinite plate. The complex potentials and the appropriate superposition procedure was used to formulate the approximate solution for the calculation of the stress field in plates containing any number of holes [7]. In the paper [8] the series solution to the stress concentration of finite composite laminates with elliptical holes was proposed. Several iterative methods for the contact problems with friction are compared in [9].

2. Mathematical background

We consider the problem of the plate containing two circular holes of the same radius ($r_1 = r_2$) stiffened by an elastic ring. The thickness of the plate is $2h$ and the distance

between the centers of the holes is $2l$. Let the boundaries of the hole be L_1 and L_2 (Figure 1). The friction along the contact line can be neglected. The cross-section of the rings is symmetrical about the central plane of the plate. The stress-strain state of the rings is described by the theory of thin curved bars. Since the elastic rings are in the holes of the plate, around the boundaries L_1 and L_2 , the following equations should be satisfied

$$\begin{aligned} u_n - u_{1n} &= \epsilon_1^*(t), \\ u_n - u_{2n} &= \epsilon_2^*(t), \\ \sigma_{r1}^{(i)} &= \sigma_{r2}^{(i)} = \sigma_r^{(i)}, \\ \tau_{r\Theta 1}^{(i)} &= \tau_{r\Theta 2}^{(i)} = 0, \end{aligned} \quad (1)$$

where u_n is the normal component of displacement at the contour points of the plate, u_{1n} and u_{2n} are the normal components of displacements at the contour points of rings, $\sigma_r^{(i)}$ is the normal component of contact stresses,

$$\epsilon_1^*(t) \quad \text{and} \quad \epsilon_2^*(t)$$

are the normal components of displacement jumps around the boundaries L_1 and L_2 , respectively. In this case

$$\epsilon_1^*(t) = \epsilon_2^*(t) = \epsilon^*(t),$$

where t is a parameter of the arc.

In case of a symmetrically loaded plate it is sufficient to satisfy the boundary conditions related to one (right) hole.

The unknown potential functions $\varphi(z)$ and $\psi(z)$ can be expressed according to [10] as follows

$$\begin{aligned} \varphi(z) &= \varphi^*(z) + \varphi^o(z), \\ \psi(z) &= \psi^*(z) + \psi^o(z), \end{aligned} \quad (2)$$

where

$$\begin{aligned} \varphi^o(z) &= \sum_{k=1}^{\infty} a_k r_1^k [(z-l)^{-k} + (-1)^{k+1}(z+l)^{-k}], \\ \Psi^o(z) &= \sum_{k=1}^{\infty} b_k r_1^k [(z-l)^{-k} + (-1)^{k+1}(z+l)^{-k}], \end{aligned} \quad (3)$$

The coefficients a_k and b_k are complex numbers. The smooth contact around the contour of hole L_1 can be expressed in integral form as follows [11]

$$\begin{aligned} \int_{L_1} u \overline{F'(t)} d\bar{t} &= - \int_{L_1} \sigma_r^{(i)} \overline{F(t)} dt, \\ \int_{L_1} u F'(t) dt &= - \int_{L_1} \sigma_r^{(i)} F(t) dt, \\ \int_{L_1} F(t) d[\operatorname{Re}(v)] &= 2G \int_{L_1} F(t) d[u_{1n} + \epsilon(t)], \end{aligned} \quad (4)$$

where

$$u = \varphi(t) + t\overline{\varphi'(t)} + \overline{\psi(t)},$$

$$v = i\dot{t} \left[\kappa\varphi(t) - t\overline{\varphi'(t)} - \overline{\psi(t)} \right],$$

and

$$e^{-i\Theta} = i\dot{t}, \quad \dot{t} = \frac{dt}{ds_1} = ie^{i\Theta},$$

$t = l + r_1 e^{i\Theta}$ is the affix of the contour point on L_1 , ds_1 is the increase of the arc, $F(z)$ is the arbitrary holomorphic function of complex variable ($z = x + iy$) on the domain of the plate S_1 , F' is the derivate function, \overline{F} is the conjugate function, G is the shear modulus of the plate,

$$\kappa = \frac{3 - \nu}{1 + \nu}$$

is a coefficient for plane stresses and ν is the Poisson ratio.

The normal component of displacement at the contour points of the ring can be expressed in the following way [11]

$$u_{1n} = \text{Re} \left\{ i\dot{t} \int_{t_o}^t \left[\frac{r_o}{r_1} \epsilon_o + \dot{t}(r_1 - r_o) \frac{d\Theta_b}{dt} + i\Theta_b \right] dt + \dot{t} \text{const} \right\}, \quad (5)$$

where ϵ_o is the strain of the neutral line L_o (in case of simple bending), Θ_b is the slope of the cross section of the ring and r_o is the radius of the neutral line.

The normal stress component in the cross-section of ring can be expressed as follows

$$\sigma_k = E \left[\frac{r_o}{r} \epsilon_o + (r - r_o) \dot{t} \frac{d\Theta_b}{dt} \right], \quad (6)$$

where E is the elasticity modulus of the ring, r is the radius of an arbitrary line of the bar.

The stress-strain relation (without an external load on the ring) for the contact stresses is given by

$$\sigma_r^{(i)} = -\frac{1}{2h} \text{Re} \frac{d}{dt} \left\{ \frac{d}{d\dot{t}} \left[EA(r_o - r_1) \epsilon_o + EA\eta_c r_1 \dot{t} \frac{d\Theta_b}{dt} \right] + iEA\epsilon_o \dot{t} \right\} \quad (7)$$

where A is the cross-section of the ring, η_c is the distance between the neutral line L_o and the central axis of the ring.

Besides equation (4) we take into consideration the uniqueness condition by

$$\int_{L_1} \left[\frac{r_o}{r_1} \epsilon_o + (r_1 - r_o) \dot{t} \frac{d\Theta_b}{dt} + i\Theta_b \right] dt = 0. \quad (8)$$

Let $z = \omega(\zeta)$ be the function mapping conformly the exterior of unit circle γ , ($|\zeta| \geq 1$), onto the domain of the plate S . In this case the boundary conditions for the transformed domain are expressed as

$$\begin{aligned}
& \int_{\gamma} F'(\sigma) \operatorname{Re} \left\{ \frac{\overline{\omega'(\sigma)}}{\sigma |\omega'(\sigma)|} \left[\kappa \varphi(\sigma) - \frac{\overline{\omega(\sigma)}}{\omega'(\sigma)} \overline{\varphi'(\sigma)} \right] d\sigma - \overline{\Psi(\sigma)} \right\} = \\
& = 2G \int_{\gamma} F'(\sigma) \left\{ \operatorname{Re} \frac{\overline{\omega(\sigma)}}{\sigma |\omega'(\sigma)|} \int_{\sigma_o}^{\sigma} \left[\frac{r_o}{r_1} \epsilon_o + i\Theta_b + \frac{(r_1 - r_o)i\sigma}{|\omega'(\sigma)|} \frac{d\Theta_b}{d\sigma} \right] \omega'(\sigma) d\sigma - \right. \\
& \quad \left. - i c_o \frac{\overline{\omega(\sigma)}}{\sigma |\omega'(\sigma)|} \right\} d\sigma + 2G \int_{\gamma} \epsilon^*(\sigma) F'(\sigma) d\sigma, \\
& \int_{\gamma} \overline{F'(\sigma)} \left[\varphi(\sigma) + \frac{\omega(\sigma)}{\omega'(\sigma)} \overline{\varphi'(\sigma)} + \overline{\psi(\sigma)} \right] d\overline{\sigma} = \\
& = -\frac{EA}{2h} \int_{\gamma} \left[\frac{\epsilon_o}{r_1} - \frac{\sigma}{|\omega'(\sigma)|} \frac{d}{d\sigma} \left(\frac{r_1 \sigma}{|\omega'(\sigma)|} \frac{d\epsilon_o}{d\sigma} \right) \right] \overline{F(\sigma)} \omega'(\sigma) d\sigma, \quad (9)
\end{aligned}$$

$$\begin{aligned}
& \int_{\gamma} F'(\sigma) \left[\varphi(\sigma) + \frac{\omega(\sigma)}{\omega'(\sigma)} \overline{\varphi'(\sigma)} + \overline{\psi(\sigma)} \right] d\sigma = \\
& = -\frac{EA}{2h} \int_{\gamma} \left[\frac{\epsilon_o}{r_1} - \frac{\sigma}{|\omega'(\sigma)|} \frac{d}{d\sigma} \left(\frac{r_1 \sigma}{|\omega'(\sigma)|} \frac{d\epsilon_o}{d\sigma} \right) \right] F(\sigma) \omega'(\sigma) d\sigma,
\end{aligned}$$

where

$$\sigma = e^{i\Theta}$$

is the affix of the contour point on γ , c_o is a constant, Θ is the polar angle in the transformed domain ζ and

$$\varphi(\sigma) = \varphi_1[\omega(\sigma)], \quad \psi(\sigma) = [\omega(\sigma)], \quad F(\sigma) = F_1[\omega(\sigma)].$$

Let ϵ_o and Θ_b be, respectively, the quantities in the form of complex Fourier series describing the deformations of beam (ring) on the boundary γ

$$\begin{aligned}
\epsilon_o &= \alpha_o + \sum_{k=1}^{\infty} \alpha_k (\sigma^k + \sigma^{-k}), \\
\Theta_b &= \beta_o + \sum_{k=1}^{\infty} \beta_k (\sigma^k + \sigma^{-k}).
\end{aligned} \quad (10)$$

The arbitrary function $F(\sigma)$ can also be written as

$$F(\sigma) = \sum_{k=0}^{\infty} E_k \sigma^{-k}$$

where E_k are coefficients.

Curvature of contour L_1 can be calculated by

$$\frac{1}{r_1} = \frac{1}{\omega'(\sigma)} \frac{d}{d\sigma} \left[\frac{\sigma\omega'(\sigma)}{|\omega'(\sigma)|} \right]. \tag{11}$$

When equations (2), (10), (11) are substituted in equation (9) and after integration along the contour γ , we have an infinite inhomogeneous linear algebraic equation system.

The contact condition between the plate and ring along the contours L_1 and L_2 is given as

$$\sigma_r^{(i)} \leq 0.$$

The minimal value of fit ϵ_{\min}^* can be calculated, when the contact stress is zero in one or several points of the contour L_1

$$\sigma_r^{(i)}(\Theta^*) = 0,$$

where Θ^* is the polar angle.

3. Illustrative examples

3.1. Data of the examples. We show some practical examples for copper plate, containing two circular holes stiffened by an elastic steel ring with rectangular cross-section ($A = 2h^*b$, where h^* is the height and b is the width of the ring).

The main data of the examples are as follows: $G = 43.4\text{GPa}$; $\nu = 0.3$; $\kappa = 2.08$, $E = 206\text{GPa}$.

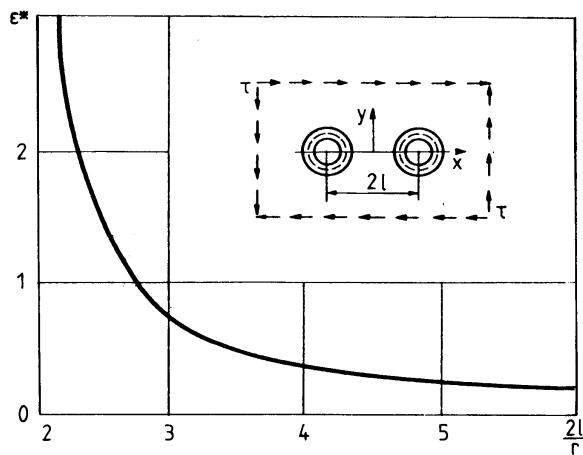


Figure 1. The minimal value of ring fit ϵ^* versus distance between the centres of two holes

3.2. Stresses in a plate subjected to shear. The shear load of the plate considered is shown in Figure 1. The functions $\varphi^*(z)$ and $\psi^*(z)$ can be written as follows

$$\varphi^*(z) = 0, \quad \psi^*(z) = i\tau z,$$

where

$$\tau_{xy}^\infty = \tau, \quad \sigma_x^\infty = 0, \quad \sigma_y^\infty = 0.$$

Table 1. The tangential stresses σ_t around the boundary of the right-hand hole

Θ	$2l/r$				
	∞	4	3	2.5	2.2
0	0.059	0.111	0.268	0.606	1.016
$\pi/12$	-1.911	-1.965	-1.853	-1.548	-1.158
$\pi/6$	-3.353	-3.514	-3.456	-3.201	-2.848
$\pi/4$	-3.882	-4.143	-4.158	-3.977	-3.687
$\pi/3$	-3.353	-3.701	-3.811	-3.739	-3.550
$5\pi/12$	-1.911	-2.308	-2.537	-2.622	-2.580
$\pi/2$	0.059	-0.312	-0.668	-0.963	-1.163
$7\pi/12$	2.030	1.804	1.377	0.853	0.343
$2\pi/3$	3.472	3.548	3.230	2.601	1.794
$3\pi/4$	4.000	4.476	4.588	4.268	3.464
$5\pi/6$	3.472	4.236	4.976	5.532	5.334
$11\pi/12$	2.030	2.669	3.611	4.879	5.500
π	0.059	0.134	0.398	1.167	2.973
$13\pi/12$	-1.911	-2.418	-2.906	-2.950	-1.407
$7\pi/6$	-3.353	-4.024	-4.467	-4.387	-3.620
$5\pi/4$	-3.882	-4.302	-4.247	-3.694	-2.987
$4\pi/3$	-3.353	-3.395	-2.964	-2.225	-1.589
$17\pi/12$	-1.911	-1.655	-1.108	-0.420	0.094
$3\pi/2$	0.059	0.470	0.983	1.559	1.988
$19\pi/12$	2.030	2.480	2.911	3.398	3.793
$5\pi/3$	3.472	3.889	4.241	4.673	5.066
$\pi 7/4$	4.000	4.346	4.634	5.034	5.436
$11\pi/6$	3.472	3.727	3.966	4.345	4.757
$23\pi/12$	2.030	2.185	2.382	2.743	3.159
2π	0.059	0.111	0.268	0.606	1.016

Tables 1 and 2 illustrate the calculated tangential and radial stresses σ_t and σ_r (in ratio of τ) around the boundary of the right-hand circular hole, respectively ($h^* = h$ and $b = 0.2r$). In this case h and h^* are the heights of plate and ring, respectively.

Figure 1 shows the minimal value of ring fit ϵ_{\min}^* as function of distance between the centers of two holes ($b = 0.2r$). Values of fit are given in ratio of $10^{-11}r\tau$.

On the basis of Figure 1 we can conclude that the minimal values of ring fit increase as the distance between the centers of holes decreases. When the gap appears between the ring and the boundary of the right-hand hole the angle is equal to $\theta^* \cong 10\pi/9$.

Table 2. The radial stresses σ_r around the boundary of right holes

Θ	$2l/r$				
	∞	4	3	2.5	2.2
0	-0.059	-0.096	-0.214	-0.446	-0.683
$\pi/12$	-0.030	-0.067	-0.185	-0.418	-0.654
$\pi/6$	-0.008	-0.046	-0.165	-0.398	-0.635
$\pi/4$	0.000	-0.038	-0.158	-0.392	-0.630
$\pi/3$	-0.008	-0.045	-0.167	-0.403	-0.643
$5\pi/12$	-0.030	-0.064	-0.187	-0.426	-0.670
$\pi/2$	-0.059	-0.089	-0.207	-0.448	-0.698
$7\pi/12$	-0.089	-0.110	-0.214	-0.442	-0.685
$2\pi/3$	-0.110	-0.131	-0.208	-0.390	-0.583
$3\pi/4$	-0.118	-0.157	-0.238	-0.375	-0.495
$5\pi/6$	-0.110	-0.189	-0.359	-0.624	-0.886
$11\pi/12$	-0.089	-0.177	-0.429	-0.919	-1.360
π	-0.059	-0.097	-0.221	-0.479	-0.824
$13\pi/12$	-0.030	-0.017	-0.006	0	-0.009
$7\pi/6$	-0.008	-0.003	-0.064	-0.242	-0.392
$5\pi/4$	0.0	-0.033	-0.181	-0.484	-0.891
$4\pi/3$	-0.008	-0.060	-0.214	-0.488	-0.759
$17\pi/12$	-0.030	-0.082	-0.212	-0.450	-0.685
$3\pi/2$	-0.059	-0.103	-0.221	-0.448	-0.679
$19\pi/12$	-0.089	-0.128	-0.242	-0.470	-0.704
$5\pi/3$	-0.110	-0.147	-0.262	-0.492	-0.728
$7\pi/4$	-0.118	-0.154	-0.270	-0.501	-0.738
$11\pi/6$	-0.146	-0.263	-0.495	-0.732	-0.732
$23\pi/12$	-0.089	-0.125	-0.242	-0.475	-0.711
2π	-0.059	-0.096	-0.214	-0.446	-0.683

3.3. **Pure bending of strip.** The bending load of strip having two circular holes considered is shown in Figure 2. The functions $\varphi^*(z)$ and $\psi^*(z)$ may be written as

$$\varphi^*(z) = \frac{iM}{8I} z^2,$$

$$\psi^*(z) = -\frac{iM}{8I} z^2,$$

$M_z^\infty = M$, where M is the bending moment and I is the moment of inertia of the strip-cross section with respect to the neutral axis.

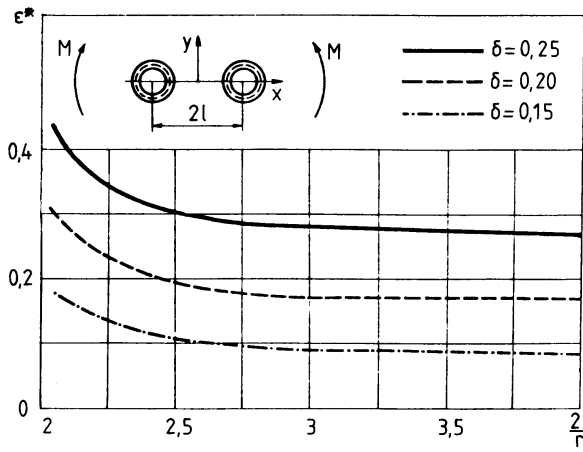


Figure 2. The minimal value of ring fit ϵ^* versus distance between the centers of the two holes

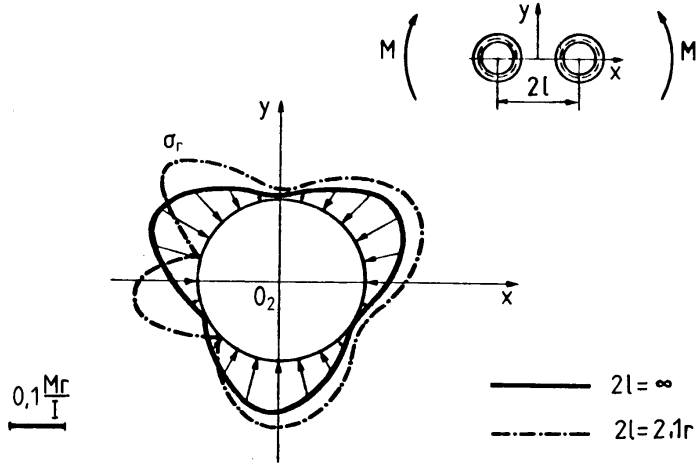


Figure 3. The calculated radial stresses σ_r around the boundary of the right-hand hole

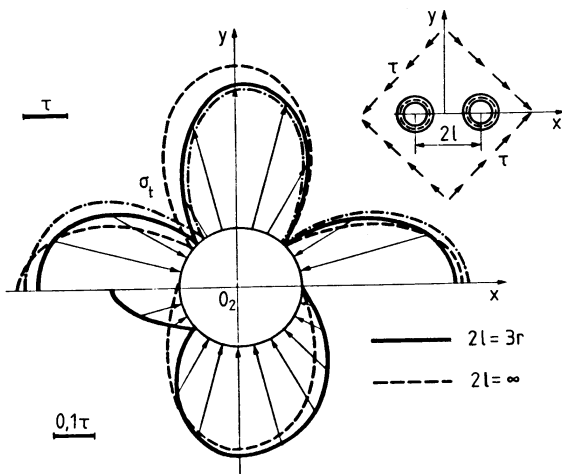


Figure 4. Stress distribution around the boundary of the right-hand hole

Figure 2 depicts the computed minimal values of steel ring fit as a function of distance between the centers of two holes for any values of geometrical parameter $\delta = b/r$. Values of minimal fit are given in ratio of $10^{-11} Mr^2/I$.

Figure 3 shows the calculated radial stresses σ_r around the boundary of the right-hand hole ($h^* = h$; $b = 0.2r$). The results indicate that the distance between the centers of holes has an influence on the stress concentration.

3.4. Stresses in plate subjected to shear with angle. The shear load of plate with angle $\pi/4$ is shown in Figure 4. The complex functions are as follows

$$\varphi^*(z) = 0, \quad \psi^*(z) = -\tau z.$$

The stress components σ_Θ and σ_r around the boundary of the right-hand hole can be expressed as follows

$$\begin{aligned} \sigma_\Theta = & -\tau \cos 2\Theta + \sum_{k=1}^{\infty} \left\langle (k+1) \left\{ a_k \left[\cos(k+1)\Theta + \frac{1}{2\epsilon_1} \cos k\Theta \right] - \right. \right. \\ & -2k \left[a_k \cos(k+1)\Theta + \frac{1}{2} b_k \cos(k-1)\Theta \right] + \sum_{m=1}^{\infty} H_{k,m} m \{ a_k [(m-1)(\cos(m-1)\Theta + \\ & \left. \left. + \frac{1}{2\epsilon_1} \cos m\Theta) + 2 \cos(m-1)\Theta] - b_k \cos(m+1)\Theta \right\} \right\rangle, \\ \sigma_r = & -4 \sum_{k=1}^{\infty} \frac{1}{r} [k a_k \cos(k+1)\Theta - \sum_{m=1}^{\infty} H_{k,m} m a_k \cos(m-1)\Theta] - \sigma_\Theta, \end{aligned}$$

where $\epsilon_1 = r/2l$,

$$H_{k,m} = (-1)^{k+m+1} C_{k+m-1}^m \epsilon_1^{k+m}.$$

and C_{k+m+1}^m refers to combination.

Figure 4 illustrates the stress distribution around the boundary of the right-hand hole. The plate is made of copper and the ring is made of steel ($h^*=h$; $b=0.25r$). The dash and dot lines show the stress distribution around the boundary without ring ($2l=3r$), calculated by [11].

4. Concluding remarks

The present mathematical method is very efficient for the analysis of stress concentration of isotropic plates with two circular holes stiffened by elastic rings.

The radial and tangential stresses around the boundary of holes are given in Tables 1 and 2. Figure 3 and 4 illustrates the stress distribution around the boundary of the right-hand holes.

Formulas for the strength calculation are given according to the theory of complex potential functions.

References

1. PAUL, T. K. and RAO, K. M.: Finite element analysis of laminated composite plates containing two circular holes under transverse loading. *Computers & Structures*, **54**(4), (1995), 671-677.
2. KALTAKCI, M.: *Stress concentrations and failure criteria in anisotropic plates with circular holes subjected to tension or compression*. *Computers & Structures*, **61**(1), (1996), 67-78.
3. TING, K., CHEN, K. T. and YANG, W. S.: *Applied alternating method to analyze the stress concentration around interacting multiple circular holes in an infinite domain*. *Int. J. Solids & Structures*, **36**, (1999), 533-556.
4. SCSUKIN, V. and TIMÁR, I.: *Stress distribution of anisotropic plate with two elliptical holes stiffened by elastic rings*. *Gép*, **50**(1-2), (1998), 55-57. (in Hungarian)
5. LEKHNIKIJ, S. G.: *Anisotropic Plate*, Gordon & Breach, New York, 1968.
6. SAVIN, G. N.: *Stress distribution around a hole*, Pergamon Press, Oxford, 1961.
7. MEGUID, A. and SHEN, C. L.: *On the elastic fields of interacting defnese and main hole systems*. *International Journal of Mechanical Sciences*, **34**(1), (1992), 17-29.
8. XIWU, X., LIANGXIN, S. and XUGI, F.: *Stress concentration of finite composite laminates with elliptical hole*. *Computers & Structures* **57**(1), (1995), 29-34.
9. KOSZMODAMIJANSKIJ, A. S.: *Plane problems of elasticity for plates with holes, cutouts and jumps*, Kijev, Viscsa skola, 1975. (in Russian)
10. ALTENBACH, J., ÉGERT, J. and PÁCZELT, J.: *Vergleich unterschiedlicher Iterationsmethoden zur Lösung elastischer Kontaktaufgaben mit Reibung*, *Zeitschrift für angewandte Mathematik und Mechanik*, **72**(4), (1992), 137-141.
11. MARTYNOVICH, T. L. and ZVARICH, M. K.: *Pressing a closed bar into the circular hole of an isotropic plate*. *Prikladnaja Mekhanika*, **10**(9), (1974), 46-52. (in Russian)

A FINITE ELEMENT MODEL OF DELAMINATION IN CROSS-PLY LAMINATES

JÓZSEF UJ

Department of Applied Mechanics, Budapest University of Technology and Economics

Műegyetem rkp. 3-5, H-1521 Budapest, Hungary

uj@mm.bme.hu

[Received: August 18, 2002]

Abstract. A finite element model was developed for the modelling of progressive delamination in a cross-ply laminate made of polymer composite layers with continuous fibres. Three-dimensional solid elements were used to model the orthotropic layers in the macro-mechanical model. The delamination was initiated by a sharp notch, which was placed at the center part of a rectangular composite plate. The in-plane load was tension, applied incrementally in time. The delamination process was modeled by the help of a meso-scale finite element model, and special interface elements were used in the vicinity of notch tip between the layers. The solid interface elements with special material behavior were applied to model damage progression during the delamination of layers. The analysis predicted a narrow delamination zone at the notch tip, also verified by experimental measurements.

Mathematical Subject Classification: 74A40, 74A45

Keywords: delamination in cross-ply laminates

1. Introduction

Damage in fibre-reinforced composites exhibits a wide range of forms. Various failure modes, which can occur in long fibre composites, were described by Cantwell and Morton [1]. One of the most frequent modes of failure is delamination, which could lead to overall damage of the composite structure. Several kinds of approaches can be found in the literature on this problem. Some authors treat the damage zone as a crack, and apply methods of fracture mechanics. An early work was presented by Griffith et al. [2], who investigated the splitting in a 0° lamina due to tension. Another way is a progressive damage modeling, which predicts the effect of notch size on tensile strength and the behaviour of different lay-ups. Chang and his co-worker [3] applied this method to model the damage process. An energy approach was also used in some models, when the strain energy release rate was investigated during the delamination. A quite new and effective method is the interface modeling approach, which is applied in various finite element models. Special interface elements were used to model the progression of delamination between layers under investigation (Mi et al. [4]). This method was also applied by Wisnom and Fu-Kuo Chang [5], creating a

macro-mechanical model of a notched rectangular plate. Plane stress elements were to represent the plies in the cross-ply laminate, and 2 node non-linear interface elements were to represent the behavior of the inter-laminar matrix and to model the splitting and delamination at the notch tip.

In the present paper a rectangular composite laminate with lay-up $[90/0]_S$ is investigated, and there is a sharp notch at the center (see Figure 1). The notch is extended along all the four layers, and has no gap before loading. The in-plane load increases tension load parallel to x-axis and perpendicular to the notch. First a macro-scale FE model is created to determine the overall behavior of the rectangular plate. Next a meso-scale FE model is applied in the vicinity of notch tip. The finite element analysis is used for modelling the damage process. According to the above mentioned earlier investigations and experimental measurements by Spearing and Beaumont [6], two kinds of damage occur: an axial split of 0° layer and a delamination are progressing near the notch tips. The aim of the analysis is to determine the relationship between the axial load and the extent of the damaged area.

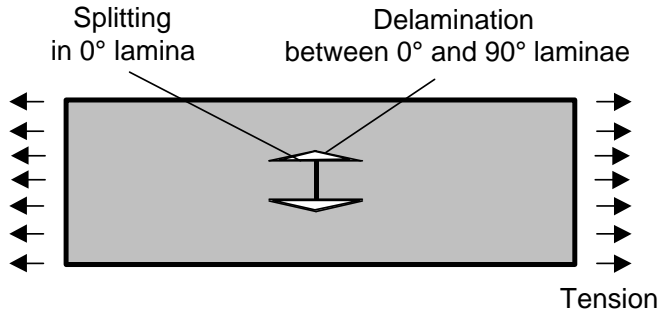


Figure 1. Splitting and delamination in the laminate

The arrangement and dimensions of the plate are given in Figure 2. The x-y plane is the mid-plane of the plate. This structure has three planes of symmetry, therefore

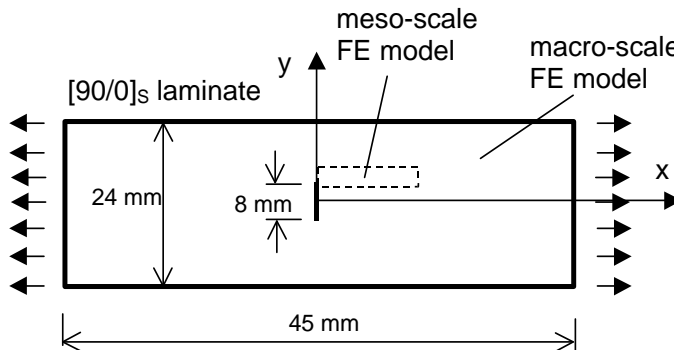


Figure 2. The notched laminate and the FE model

only one eighth of the total is modelled in the macro-scale analysis. The symmetric mechanical behavior is ensured by kinematic boundary conditions along the planes of symmetry. The macro mechanical model consists of two orthotropic layers of 0.14 mm thickness each, which are meshed by 8 node 3D solid elements (see Figure 3).

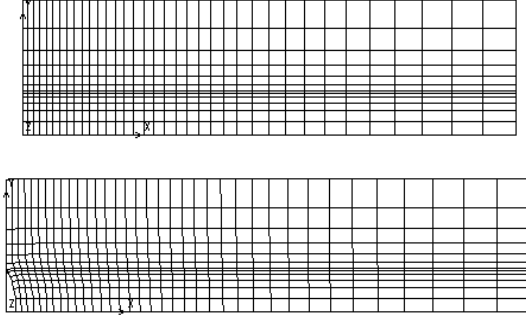


Figure 3. Undeformed and deformed meshes of macro-scale model (hundredfold distortion is for displacements)

The material properties are orthotropic linear elastic ones, for T300/914 composite with 60% fibre volume fraction: $E_{11} = 135$ GPa, $E_{22} = E_{33} = 9.6$ GPa, $G_{12} = G_{13} = 5.8$ GPa, $G_{23} = 3.1$ GPa, $\nu_{12} = \nu_{13} = 0.31$, $\nu_{23} = 0, 38$. This model does not consider any damage process; it is to help the proper selection of borders for the meso-scale analysis. Moreover, the stress-concentration near the notch tip - responsible for split and delamination - can be studied this way.

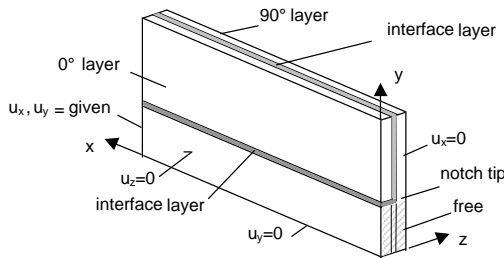


Figure 4. The meso-scale model with the kinematic boundary conditions

The meso-scale model relates to the part of the notch tip, where the damage is expected. It consists of 90° and 0° layers of 0.125 mm thickness each, and an interface layer of 0.03 mm is between them for modeling the delamination. Within the 0° layer, another interface strip of 0.03 mm is placed for modeling the splitting (see Figure 4). Both composite layers and the interface layers are meshed by 3D solid elements with 8 nodes. The composite layers have linear elastic, orthotropic properties with the same elastic constants as in the macro-scale model. The interface elements have isotropic, elasto-plastic damage material properties. Its elastic behaviour is as for

matrix material, plastic yield limit is determined by matrix material yield test. The elasto-plastic deformation in the interface is limited until the strain energy density reaches its critical value. This is determined by the fracture energy density, forming an area under the material curve (Figure 5). As the splitting and delamination processes are controlled by mode II and mode III shear stresses, the fracture energy for those modes is applied in the computation. Referring to Spearing's measurement [6], 0.4 N/mm fracture energy per unit area is applied. The common nodes of the interface elements and the composite elements work together until the damage occurs. After having been damaged, the nodes become inactive, the nodal forces vanish for the interface elements involved.

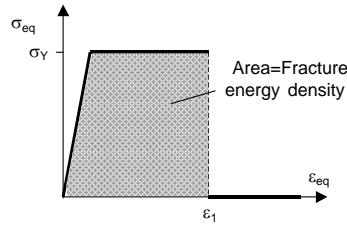


Figure 5. The meso-scale model with the kinematic boundary conditions

The kinematic loads on the surfaces of the meso-scale model are determined by using the macro-scale model, and are applied incrementally starting from zero. Non-linear static analysis was applied, using Cosmos/M software. An external procedure was created for evaluation of the damage criterion of the interface elements, and for modification of the state (from active to inactive) of the damaged nodes, and for restarting the computation. For each load increment, an iteration is necessary to reach an equilibrium.

2. Results

The splitting process starts at the notch tip when the tension load is quite low. Due to the delamination, the damaged nodal points form an increasing narrow, triangular

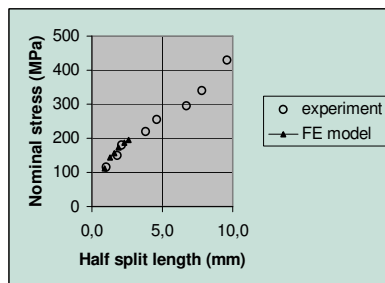


Figure 6. Relationships between half split length and nominal axial stress in the 0° layer, far away from the notch

domain at the notch tip as it was detected by experimental measurement [6] (see Figure 1). As the model dimensions and material behavior parameters in this finite element model were very close to those in the measurement, it became possible to compare the experimental and computational results. The relationship between the half split length and nominal stress (that is x in the 0° layer, far from the notch) is shown for both cases (Figure 6). According to this diagram, the correlation between the computed and measured values is good.

3. Concluding remarks

Macro- and meso-scale finite element models were created for a rectangular plate made of cross-ply laminate with a notch in the center. Using an interface element approach, our models were available for modelling the synchronous damage processes at the notch tips (that is splitting in the 0° layer and delamination between 0° and 90° layers). While other researchers, like Mi et al., [4] applied 4 node solid elements, or Wisnom et al., [5] did 2 node elements, we followed the damage processes by 8 node solid finite elements. The interface elements had special elasto-plastic damage material properties to describe the progressive splitting and delamination. Our model was also suitable for predicting the extent of the damaged domain as function of tension load. The shape and the extent of the delaminated region are in good agreement with the experimental measurement, known from the paper by Spearing and Beaumont [6].

Acknowledgement. The support provided by the Hungarian National Research Foundation (project No. T037 324) is gratefully acknowledged.

References

1. CANTWELL, J. and MORTON, J.: The significance of damage and defects and their detection in composite materials: A review. *Journal of Strain Analysis*, **27**(1), (1992), 29-42.
2. GRIFFIT, W. I., KANNINEN, M. F. and RYBICKI, E. F.: *A fracture mechanics approach to the analysis of graphite/epoxy laminated precracked tension panels*, ASTM STP 696, R.B. Pipes (Ed.), 1979, 185-201.
3. CHANG, F. K. and CHANG K. Y.: A progressive damage model for laminated composites containing stress concentrations. *Journal of Composite Materials*, **21**, (1987) 834-855.
4. MI, Y., CRISFIELD, M. A., DAVIES, G. A. O. and HELLWEG, H. B.: Progressive delamination using interface elements. *Journal of Composite Materials*, **32**(14), (1998), 1246-1272.
5. WISNOM M. R. and CHANG, FU-KUO: Modelling of splitting and delamination in notched cross-ply laminates. *Composites Science and Technology*, **60**, (2000), 2849-2856.
6. SPEARING, S. M. and BEAUMONT, P. W. R.: Fatigue damage mechanics of composite materials. I: Experimental measurement of damage and post-fatigue properties. *Composites Science and Technology*, **44**, (1992), 159-168.

ONSAGER'S RECIPROCAL RELATIONS AND SOME BASIC LAWS

JÓZSEF VERHÁS

Department of Chemical Physics, Budapest University of Technology and Economy
H-1521 Budapest, Hungary
verhas@phy.bme.hu

[Received: September 30, 2003]

Abstract. This paper presents some ideas and doubts about some assumptions on the validity and proofs of the Onsager–Casimir reciprocal relations. Presuming the validity of the Onsager–Casimir reciprocal relations, exact proofs can be constructed for Newton's second and third laws, moreover, for the formula of the Lorentz–force. This way, the axioms of both mechanics and electrodynamics would become theorems in a theory in which the Onsager–Casimir reciprocal relations have been proved phenomenologically. We incline to believe that neither the axioms mentioned nor the Onsager–Casimir reciprocal relation can be proved, nevertheless, they are valid. The statement that if something is true then it can be proved is false.

Mathematical Subject Classification: 70G99

Keywords: Onsager–Casimir reciprocal relations, validity, proofs

1. Introduction

The Onsager–Casimir reciprocal relations play important role in non-equilibrium thermodynamics [1, 2, 3, 4, 5, 6]; their validity deserves attention even if they have been discussed several times, (see e.g. [7, 8, 9, 10, 11] and [12], especially, [13, 14, 15, 16, 17, 18, 19, 20] as well as [21, 22]). Furthermore they are somehow related to the celebrated and persistent problems of the increase in the entropy and thermalization in statistical manifolds [23, 24].

The original proof based on the principle of microscopic reversibility suggests that they hold for statistical ensembles — in accordance with the opinion that entire thermodynamics does — and other methods introducing them did not result in anything new [5]. The generality and some applications hardly belonging to the realm of statistics inspired efforts for a phenomenological proof. The attempts to prove the reciprocal relations on a phenomenological basis have failed. One may think that the failure proves the statistical validity. Here we show that the reciprocal relations are closely related to very basic principles. We show here that the desired phenomenological proof of the reciprocal relations would be equivalent to a proof of fundamental laws of physics.

The equivalence of the reciprocal relations and the principle of detailed balance are well known. What is more the latter has hardly any meaning, e.g., in particle mechanics or in Maxwell's theory. The thermodynamic theory of diffusion—see e.g. [25]—shows that the reciprocal relations for the diffusion coefficients are equivalent to Newton's third law.

Some simple models can elucidate the intimate relation of the reciprocity to Newton's laws and to the fundamental principles of electromagnetism.

2. The diffusion

The entropy production density in an isothermal multicomponent system is (see [5] eq. XI.171, p. 265.)

$$\sigma = \frac{1}{T} \sum_{k=1}^n \mathbf{J}_k^a \{ \mathbf{F}_k - (\text{grad } \mu_k)_T \}, \quad (2.1)$$

where the vectors $\mathbf{J}_k^a = \rho_k(\mathbf{v}_k - \mathbf{v})$ are the diffusion flows with respect to any reference velocity (\mathbf{v}), \mathbf{F}_k stands for the body forces acting on the unit amount of each chemical species in a frame travelling and accelerating together with the local center of mass, the scalars μ_k are the chemical potentials, and T is the thermodynamic temperature. Here ρ_k stands for the densities and \mathbf{v}_k for the velocities of the components. The Onsager equations read

$$\mathbf{F}_i - (\text{grad } \mu_i)_T = \sum_{k=1}^n R_{ik} \mathbf{J}_k^a. \quad (2.2)$$

From the fact that a simple translation of the material does not result in any dissipation,

$$\sum_{k=1}^n R_{ik} \rho_k = 0 \quad (2.3)$$

follows. Eliminating the diagonal elements from the right-hand side of equation (2.2), we get

$$\mathbf{F}_i - (\text{grad } \mu_i)_T = \sum_{k \neq 1} R_{ik} \rho_k (\mathbf{v}_k - \mathbf{v}_i). \quad (2.4)$$

The right-hand side gives account of the forces exerted by the other components on the unit amount of the i -th one. Referring to unit volume, equation (2.4) transforms into

$$\rho_i (\mathbf{F}_i - (\text{grad } \mu_i)_T) = \sum_{k \neq 1} R_{ik} \rho_k \rho_i (\mathbf{v}_k - \mathbf{v}_i). \quad (2.5)$$

One can see that Onsager's reciprocal relations follow from Newton's third law; exactly as Truesdell concluded [25]. To decide whether they are equivalent or not needs a detailed axiomatic investigation difficult for such a complex system. The possibilities are more transparent in case of simpler models.

3. Newton's second law

The simplest model we use is a small – point like – particle and its motion is discussed by recalling the ideas of thermodynamics. The idea of work and Galilean relativity are presumed but Newton's second and third axioms are not. Remember that the idea of work is much older than Newton's theory (Archimedes). The reciprocal relation and the possibility of reversible motion yields Newton's second axiom.

Assume the conservation of energy for a particle. Heat – unlike pure mechanical considerations – is also taken into account as friction or drag may always be present.

$$\frac{de}{dt} = I_q + \mathbf{F}\mathbf{v}. \quad (3.1)$$

Here e is the energy of the thermodynamic system (i.e. the particle and its immediate environment, e.g. in a fluid), I_q is the heat flow into, and \mathbf{F} is the force exerted on it. The entropy is supposed to depend on the energy and on a – not yet specified – β -type vector variable;

$$s = s(e, \beta). \quad (3.2)$$

The Morse – lemma [26] ensures that the form of the above function becomes

$$s = s\left(e - \frac{1}{2}\beta^2\right) \quad (3.3)$$

with a suitable independent variable. The second law of thermodynamics reads

$$\frac{ds}{dt} = \frac{I_q}{T} + P_s \quad (3.4)$$

with non-negative entropy production;

$$P_s \geq 0.$$

If we do not want to take on the difficulties of discussing the possible details of heat exchange we had better suppose reversible heat effects, which results in

$$\frac{\partial s}{\partial e} = \frac{1}{T}.$$

The actual form of the entropy production is

$$P_s = \frac{1}{T} \left\{ \mathbf{F}\mathbf{v} - \beta \frac{d\beta}{dt} \right\}. \quad (3.5)$$

The Onsager equations are

$$\begin{aligned} \mathbf{F} &= R_{11}\mathbf{v} + R_{12}\frac{d\beta}{dt}, \\ -\beta &= R_{21}\mathbf{v} + R_{22}\frac{d\beta}{dt} \end{aligned} \quad (3.6)$$

with Casimir's reciprocal relation

$$R_{21} = -R_{12}. \quad (3.7)$$

The energy dissipation rate $-TP_s$ is given by

$$TP_s = R_{11}\mathbf{v}^2 + R_{22}\left\{\frac{d\boldsymbol{\beta}}{dt}\right\}^2.$$

In the reversible limit both R_{11} and R_{22} equal zero; Onsager's equations turn into

$$\begin{aligned}\mathbf{F} &= R_{12}\frac{d\boldsymbol{\beta}}{dt}, \\ -\boldsymbol{\beta} &= -R_{12}\mathbf{v},\end{aligned}\tag{3.8}$$

which results in

$$\mathbf{F} = R_{12}^2\frac{d\mathbf{v}}{dt};\tag{3.9}$$

obviously, the positive quantity R_{12}^2 is m , the mass of the particle. The dropped coefficient R_{11} may give account of drag if the particle moves in a fluid, while the coefficient R_{22} results in a term approximating electromagnetic radiation [27] or emission of acoustic waves, etc.

The entropy function (3.3) in the reversible case is

$$s = s\left(e - \frac{1}{2}m\mathbf{v}^2\right).$$

Newton's second law has been shown by Onsager's linear theory. The relativistic formulae result in a non-linear theory.

4. Newton's third law

Combining two particles and applying the previous result as well as the homogeneity of space lead to the third axiom if and only if the Onsager–Casimir reciprocal relation holds. For the sake of simplicity, suppose that no external forces act on the particles; the change of the energy is due to heat. The first law of thermodynamics reads

$$\frac{de}{dt} = I_q.\tag{4.1}$$

Take the entropy in the form

$$s = s\left(e - \frac{1}{2}m_1\mathbf{v}_1^2 - \frac{1}{2}m_2\mathbf{v}_2^2, \mathbf{r}_1 - \mathbf{r}_2\right).\tag{4.2}$$

The entropy function expresses the fact that the space is homogeneous and the interaction of the two particles is influenced by their distance. Dropping again the heat effects and evaluating the entropy production leads to

$$TP_s = \boldsymbol{\Gamma}(\mathbf{v}_1 - \mathbf{v}_2) - m_1\mathbf{v}_1\frac{d\mathbf{v}_1}{dt} - m_2\mathbf{v}_2\frac{d\mathbf{v}_2}{dt}$$

or rearranged

$$TP_s = \left(\boldsymbol{\Gamma} - m_1\frac{d\mathbf{v}_1}{dt}\right)\mathbf{v}_1 - \left(\boldsymbol{\Gamma} + m_2\frac{d\mathbf{v}_2}{dt}\right)\mathbf{v}_2,\tag{4.3}$$

where the symbol $\boldsymbol{\Gamma}$ stands for the gradient of the entropy with respect to \mathbf{r}_1 ;

$$\boldsymbol{\Gamma} = \frac{\partial s}{\partial(\mathbf{r}_1 - \mathbf{r}_2)}.$$

The Onsager equations are

$$\begin{aligned} \left(\boldsymbol{\Gamma} - m_1 \frac{d\mathbf{v}_1}{dt} \right) &= R_{11}\mathbf{v}_1 + R_{12}\mathbf{v}_2, \\ - \left(\boldsymbol{\Gamma} + m_2 \frac{d\mathbf{v}_2}{dt} \right) &= R_{21}\mathbf{v}_1 + R_{22}\mathbf{v}_2, \end{aligned} \tag{4.4}$$

where Onsager's reciprocity is not assumed. Galilean invariance requires

$$\begin{aligned} R_{11} + R_{12} &= 0, \\ R_{21} + R_{22} &= 0, \end{aligned}$$

as the left hand sides of the equations (4.4) contain only differences of position vectors and velocities—they are objective— while on the right hand sides absolute velocities stand except the above equalities hold. The sum of the equations—after multiplying both sides by -1 —results

$$m_1 \frac{d\mathbf{v}_1}{dt} + m_2 \frac{d\mathbf{v}_2}{dt} = (R_{21} - R_{12})(\mathbf{v}_1 - \mathbf{v}_2), \tag{4.5}$$

which leads to the conservation of the linear momentum if and only if Onsager's reciprocity holds.

5. Lorentz-force

The idea of the electric field and a β -type field – generated by the motion of charges – is presumed. Onsager's reciprocal relation gives the formula of Lorentz's force together with the definition for the \mathbf{B} -vector.

The balance equation for the internal energy $u = e - 1/2m\mathbf{v}^2$ reads

$$\frac{du}{dt} = I_q + q\mathbf{E}\mathbf{v}, \tag{5.1}$$

where q is the electric charge and \mathbf{E} is the electric field strength. The entropy function is

$$s = s(u) \tag{5.2}$$

and the entropy production reads

$$P_s = \frac{1}{T}q\mathbf{E}\mathbf{v}. \tag{5.3}$$

The form of Onsager's equation is

$$q\mathbf{E} = \mathbf{R}\mathbf{v}, \tag{5.4}$$

where the resistivity tensor \mathbf{R} depends on the aforementioned β -type field quantity $\boldsymbol{\beta}$, the tensorial order of which has not been specified. Onsager's reciprocal relation takes the form

$$\mathbf{R}^T(\boldsymbol{\beta}) = \mathbf{R}(-\boldsymbol{\beta}), \tag{5.5}$$

which says that the skew-symmetric part of the resistivity tensor is an odd function on β while the symmetric part is even. Denote the symmetric part by \mathbf{R}^+ , and the vector invariant of the skew-symmetric part by $-q\mathbf{B}$. Equation (5.4) turns into

$$q\mathbf{E} = \mathbf{R}^+\mathbf{v} - q\mathbf{B} \times \mathbf{v}. \quad (5.6)$$

The last term on the right-hand side is proportional to the charge q ; it can be reasoned the same way as for the electric force $q\mathbf{E}$. The quantity \mathbf{B} is characteristic for the field and may be accepted – trivially – as the magnetic field strength. The first term on the right-hand side gives account of drag.

6. Conclusion

The arguments presented show clearly that a general phenomenological proof for the Onsager–Casimir reciprocal relations would be also proof for Newton’s axioms and for the axioms of electromagnetism.

I hardly believe that it is possible.

Acknowledgement. This work has been supported by the Hungarian National Scientific Research Funds, OTKA (T034715).

References

1. ONSAGER, L.: Reciprocal relations in irreversible processes. i. *Phys. Rev.*, **37**, (1931), 405–426.
2. ONSAGER, L.: Reciprocal relations in irreversible processes. ii. *Phys. Rev.*, **38**, (1931), 2265–2279.
3. ONSAGER, L. and MACLUP, S.: Fluctuations and irreversible processes. *Phys. Rev.*, **91**, (1953), 1505–1512.
4. ONSAGER, L. and MACLUP, S.: Fluctuations and irreversible processes. ii. Systems with kinetic energy. *Phys. Rev.*, **91**, (1953), 1512–1515.
5. DE GROOT S. R. and MAZUR, P.: *Non-Equilibrium Thermodynamics*, North-Holland Publ. Co., Amsterdam, 1962.
6. GYARMATI, I.: *Non-Equilibrium Thermodynamics*, Springer, Berlin, 1970.
7. MEIXNER, J. and REIK, H. G.: *Thermodynamik der irreversiblen Prozesse*. In *Handbuch der Physik.*, Volume III./2, page 413. Springer, Berlin, 1959.
8. GYARMATI, I.: *On the Principles of Thermodynamics*, PhD thesis, Hungarian Academy of Sciences, Budapest, 1958. (in Hungarian)
9. GYARMATI, I.: On the phenomenological basis of irreversible thermodynamics. *Periodica Polytechnica, Ser. Chem. Engng.*, Budapest, **5**, (1961), 219–243, 321–339.
10. RYSELBERGHE, P.: *Thermodynamics of Irreversible Processes*. Herman Paris and Blaisdell Publ. Co., New York, Toronto, London, 1963.
11. LI, J. C. M.: Thermodynamics for nonisothermal systems. The classical formulation. *J. Chem. Phys.*, **29**, (1958), 747–754.
12. VERHÁS, J., Ed.: Cooperation of the Departments of the Technical Universities of Budapest and Berlin, *Periodica Polytechnica, Ser. Chem. Eng., Budapest*, **42**, 1997.

13. CASAS-VAZQUEZ, J., JOU, D. and LEBON, G.: Onsager relations and extended irreversible thermodynamics. *Periodica Polytechnica, Ser. Chem. Eng., Budapest*, **41**, (1997), 143–156.
14. VAN KAMPEN, N. G.: Derivation of nonlinear Onsager relations from statistical mechanics. *Periodica Polytechnica, Ser. Chem. Eng., Budapest*, **41**, (1997), 157–162.
15. MAUGIN, G. A.: Thermomechanics of heterogeneous materials with weakly nonlocal microstructure. *Periodica Polytechnica, Ser. Chem. Eng., Budapest*, **41**, (1997), 163–174.
16. NETTLETON, R. E.: Nonlinear reciprocity: Statistical foundations and applications to nonlinear effects in heat transport and chemical reactions. *Periodica Polytechnica, Ser. Chem. Eng., Budapest*, **41**, (1997), 175–184.
17. LEBON, G., JOU, D., CASAS-VAZQUEZ, J. and MUSCHIK, W.: Heat conduction at low temperature. a non-linear generalization of the Guyer-Krumhansl equation. *Periodica Polytechnica, Ser. Chem. Eng., Budapest*, **41**, (1997), 185–196.
18. MAZUR, P.: Onsager's reciprocal relations and thermodynamics of irreversible processes. *Periodica Polytechnica, Ser. Chem. Eng., Budapest*, **41**, (1997), 197–204.
19. MUSCHIK, W.: A phenomenological foundation of non-linear OC-reciprocal relations. *Periodica Polytechnica, Ser. Chem. Eng., Budapest*, **42**, (1998), 85–96.
20. VÁN, P.: Thermodynamic stability of dia- and paramagnetic materials. *Periodica Polytechnica, Ser. Chem. Eng., Budapest*, **42**, (1998), 97–102.
21. CIANCIO, V. and VERHÁS, J.: On the non-linear generalizations of Onsager's reciprocal relations. *J. Non-Equilib. Thermodyn.*, **19**, (1984), 184–194.
22. VERHÁS, J.: Some non-linear reciprocal relations. *Periodica Polytechnica, Ser. Chem. Eng., Budapest*, **42**, (1998), 65–68.
23. MEIXNER, J.: Consistency of the Onsager-Casimir reciprocal relations. *Adv. Molecular Relax. Proc.*, **5**, (1973), 319–331.
24. MEIXNER, J.: Macroscopic and microscopic reversibility. *Pap. on Math. Phys.*, **7**, (1975), 37–57.
25. TRUESDELL, C.: Mechanical basis of diffusion. *J. Chem. Phys.*, **37**, (1962), 2336–2344.
26. MORSE, M.: Relation between the critical points of a real function of n independent variables. *Trans. Am. Math. Soc.*, **27**, (1925), 345–396.
27. VERHÁS, J.: An application of Gyarmati's wave approach. *Acta Physica Hungarica*, **66**, (1989), 95–97.

OPTIMUM DESIGN OF STIFFENED PLATES FOR DIFFERENT LOADS AND SHAPES OF RIBS

ZOLTÁN VIRÁG

Department of Equipments for Geotechnics, University of Miskolc
3515 Miskolc – Egyetemváros, Hungary
gtbvir@uni-miskolc.hu

[Received: December 1, 2003]

Dedicated to Professor József FARKAS on the occasion of his seventy-fifth birthday

Abstract. In this overview of loaded stiffened plates various plate types, loadings, and stiffener shapes are investigated. Mikami [1] and API [2] methods are used for the optimum design and comparison of the two methods and uniaxially compressed plates stiffened by ribs of various shapes. Both methods consider the effect of initial imperfection and residual welding stresses, but their empirical formulae are different. The elastic secondary deflection due to compression and lateral pressure is calculated using the Paik's solution [3] of the differential equation for orthotropic plates, and the self-weight is also taken into account. Besides this deflection some more deformations are caused by lateral pressure and the shrinkage of longitudinal welds. The unknowns are the thickness of the base plate as well as the dimensions and number of stiffeners. The cost function to be minimized includes two kinds of material and three kinds of welding costs.

Mathematical Subject Classification: 74K20, 74P10

Keywords: stiffened plate, welded structures, stability, residual welding distortion, structural optimization, minimum cost design

1. Introduction

Stiffened welded plates are widely used in various load-carrying structures, e.g. ships, bridges, bunkers, tank roofs, offshore structures, vehicles, etc. They are subject to various loadings, e.g. compression, bending, shear or combined load. The shape of plates can be square, rectangular, circular, trapezoidal, etc. They can be stiffened in one or two directions by stiffeners of flat, L, trapezoidal or other shape.

Various plate types, loadings and stiffener shapes have been investigated. In this paper two kinds of loads are investigated [6], [7]. These are uniaxial compression and lateral pressure. Structural optimization of stiffened plates has been worked out by Farkas [8], Farkas and Jármai [9], and applied to uniaxially compressed plates with stiffeners of various shapes [10], biaxially compressed plates [11].

This paper contains the minimum cost design of longitudinally stiffened plates using the strength calculation methods. Deflections due to lateral pressure, compression stress and shrinkage of longitudinal welds are taken into account in the stress constraint. The self-weight is added to the lateral pressure. The local buckling constraint

of the base plate strips is formulated as well. The cost function includes two kinds of material and three kinds of welding costs. The unknowns are the thickness of the base plate as well as the dimensions and number of stiffeners.

2. Geometric characteristics

The stiffened plates are shown in Figures 1 and 2. The plates are simply supported at four edges. Geometrical parameters of plates with flat, L- and trapezoidal stiffeners can be seen in Figures 3-5.

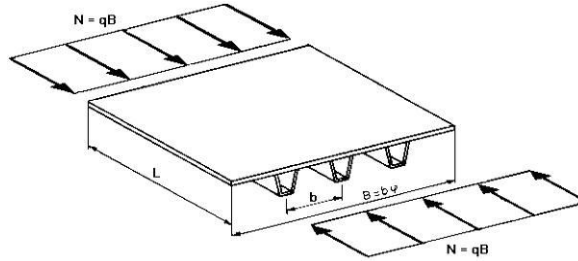


Figure 1. Longitudinally stiffened plate loaded by uniaxial compression

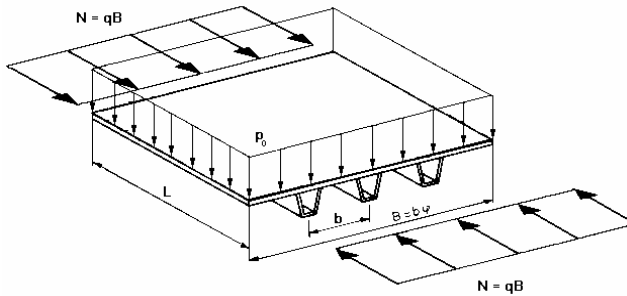


Figure 2. Longitudinally stiffened plate loaded by uniaxial compression and lateral pressure

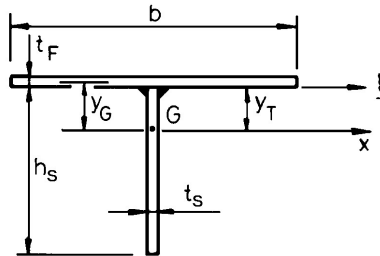


Figure 3. Dimensions of a flat stiffener

The geometrical parameters of the flat stiffener are calculated as follows

$$A_S = h_S t_S, \tag{2.1}$$

$$h_S = 14 t_S \varepsilon, \tag{2.2}$$

$$\varepsilon = \sqrt{235/f_y}, \tag{2.3}$$

$$y_G = \frac{h_S + t_F}{2} \frac{\delta_S}{1 + \delta_S}, \tag{2.4}$$

$$\delta_S = \frac{A_S}{b t_F}, \tag{2.5}$$

$$I_x = \frac{b t_F^3}{12} + b t_F y_G^2 + \frac{h_S^3 t_S}{12} + h_S t_S \left(\frac{h_S}{2} - y_G \right)^2, \tag{2.6}$$

$$I_S = h_S^3 \frac{t_S}{3}, \tag{2.7}$$

$$I_t = \frac{h_S t_S^3}{3}. \tag{2.8}$$

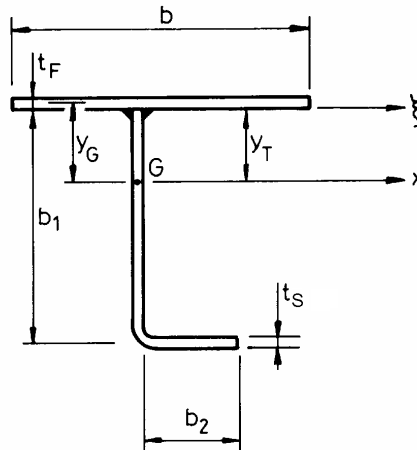


Figure 4. Dimensions of an L-stiffener

The calculations of geometrical parameters of the L-stiffener are

$$A_S = (b_1 + b_2) t_S \tag{2.9}$$

$$b_1 = 30 t_S \varepsilon, \tag{2.10}$$

$$b_2 = 12.5 t_S \varepsilon, \tag{2.11}$$

$$y_G = \frac{b_1 t_S \frac{b_1 + t_F}{2} + b_2 t_S \left(b_1 + \frac{t_F}{2} \right)}{b t_F + A_S}, \tag{2.12}$$

$$I_x = \frac{bt_F^3}{12} + bt_F y_G^2 + \frac{b_1^3 t_S}{12} + b_1 t_S \left(\frac{b_1}{2} - y_G \right)^2 + b_2 t_S (b_1 - y_G)^2, \quad (2.13)$$

$$I_S = \frac{b_1^3 t_S}{3} + b_1^2 b_2 t_S, \quad (2.14)$$

$$I_t = \frac{b_1^3 t_S}{3} + \frac{b_2^3 t_S}{3}. \quad (2.15)$$

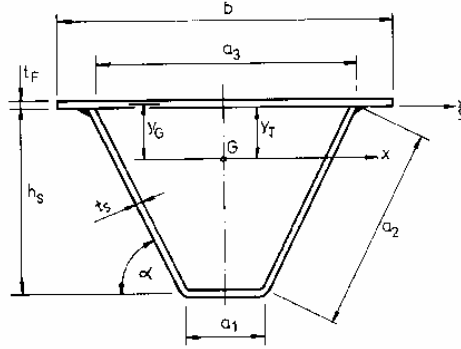


Figure 5. Dimensions of a trapezoidal stiffener

The calculations of geometrical parameters of the trapezoidal stiffener are

$$A_S = (a_1 + 2a_2) t_S, \quad (2.16)$$

$$a_1 = 90 \text{ [mm]}, a_3 = 300 \text{ [mm]}, \text{ thus}$$

$$h_S = (a_2^2 - 105^2)^{1/2}, \quad (2.17)$$

$$\sin^2 \alpha = 1 - \left(\frac{105}{a_2} \right)^2, \quad (2.18)$$

$$y_G = \frac{a_1 t_S (h_S + t_F/2) + 2a_2 t_S (h_S + t_F)/2}{bt_F + A_S} \quad (2.19)$$

$$I_x = \frac{bt_F^3}{12} + bt_F y_G^2 + a_1 t_S \left(h_S + \frac{t_F}{2} - y_G \right)^2 + \frac{1}{6} a_2^3 t_S \sin^2 \alpha + 2a_2 t_S \left(\frac{h_S + t_F}{2} - y_G \right)^2, \quad (2.20)$$

$$I_S = a_1 h_S^3 t_S + \frac{2}{3} a_2^3 t_S \sin^2 \alpha, \quad (2.21)$$

$$I_t = \frac{4A_P^2}{\sum b_i/t_i}, \quad (2.22)$$

$$A_P = h_S \frac{a_1 + a_3}{2} = 195h_S. \quad (2.23)$$

3. Design constraints in case of uniaxial compression

3.1. Global buckling of the stiffened plate. According to Mikami [1] the effect of initial imperfections and residual welding stresses is considered by defining buckling curves for a reduced slenderness

$$\lambda = (f_y/\sigma_{cr})^{1/2}. \tag{3.1}$$

The classical critical buckling stress for a uniaxially compressed longitudinally stiffened plate is

$$\sigma_{cr} = \frac{\pi^2 D}{hB^2} \left(\frac{1 + \gamma_S}{\alpha_R^2} + 2 + \alpha_R^2 \right) \quad \text{for} \quad \alpha_R = L/B < \alpha_{R0} = (1 + \gamma_S)^{1/4}, \tag{3.2}$$

$$\sigma_{cr} = \frac{2\pi^2 D}{hB^2} \left[1 + (1 + \gamma_S)^{1/2} \right] \quad \text{for} \quad \alpha_R \geq \alpha_{R0}. \tag{3.3}$$

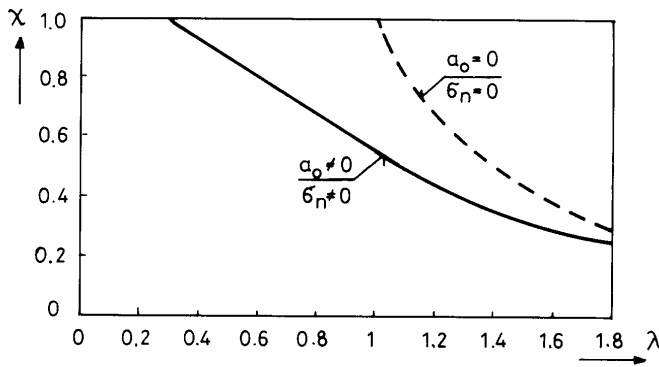


Figure 6. Global buckling curve considering the effect of initial imperfections and residual welding stresses

When the reduced slenderness is known the actual global buckling stress can be calculated according to Mikami [1] as follows

$$\sigma_U/f_y = 1 \quad \text{for} \quad \lambda \leq 0.3, \tag{3.4}$$

$$\sigma_U/f_y = 1 - 0.63(\lambda - 0.3) \quad \text{for} \quad 0.3 \leq \lambda \leq 1, \tag{3.5}$$

$$\sigma_U/f_y = 1/(0.8 + \lambda^2) \quad \text{for} \quad \lambda > 1. \tag{3.6}$$

The global buckling constraint is defined by

$$\frac{N}{A} \leq \sigma_U \frac{\rho_P + \delta_S}{1 + \delta_S}, \tag{3.7}$$

in which δ_S is given by Equation 2.5,

$$A = Bt_F + (\varphi - 1)A_S, \tag{3.8}$$

and the factor is

$$\rho_p = 1 \quad \text{if} \quad \sigma_{UP} > \sigma_U, \quad (3.9)$$

$$\rho_P = \sigma_{UP}/f_y \quad \text{if} \quad \sigma_{UP} \leq \sigma_U. \quad (3.10)$$

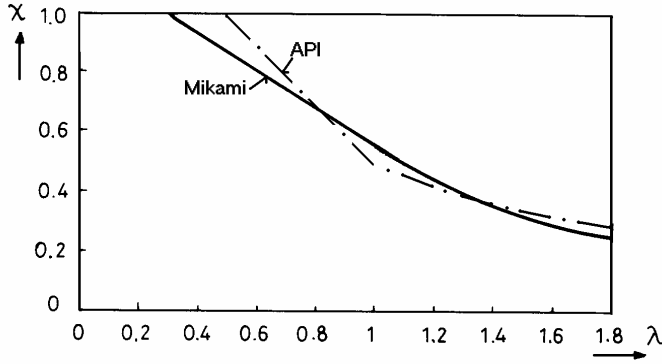


Figure 7. Global buckling curve according to Mikami and API

According to API [2]

$$\sigma_U/f_y = 1 \quad \text{if} \quad \lambda \leq 0.5, \quad (3.11)$$

$$\sigma_U/f_y = 1.5 - \lambda \quad \text{if} \quad 0.5 \leq \lambda \leq 1, \quad (3.12)$$

$$\sigma_U/f_y = 0.5/\lambda \quad \text{if} \quad \lambda > 1. \quad (3.13)$$

The global buckling constraint can be written as follows

$$\frac{N}{A} \leq \sigma_U. \quad (3.14)$$

3.2. Single panel buckling. This constraint eliminates the local buckling of the base plate parts between the stiffeners. From the classical buckling formula for a simply supported panel uniformly compressed in one direction

$$\sigma_{crP} = \frac{4\pi^2 E}{10.92} \left(\frac{t_F}{b} \right)^2, \quad (3.15)$$

the reduced slenderness is

$$\lambda_P = \left(\frac{4\pi^2 E}{10.92 f_y} \right)^{1/2} \frac{b}{t_F} = \frac{b/t_F}{56.8\varepsilon}; \quad \varepsilon = \left(\frac{235}{f_y} \right)^{1/2} \quad (3.16)$$

and the actual local buckling stress considering the initial imperfections and residual welding stresses is

$$\sigma_{UP}/f_y = 1 \quad \text{for} \quad \lambda_P \leq 0.526, \quad (3.17)$$

$$\frac{\sigma_{UP}}{f_y} = \left(\frac{0.526}{\lambda_P} \right)^{0.7} \quad \text{for} \quad \lambda_P > 0.526. \quad (3.18)$$

The single panel buckling constraint is

$$\frac{N}{A} \leq \sigma_{UP}. \tag{3.19}$$

3.3. Local and torsional buckling of stiffeners. These instability phenomena depend on the shape of stiffeners and will be treated separately for L stiffener.

The torsional buckling constraint for open section stiffeners is

$$\frac{N}{A} \leq \sigma_{UT}. \tag{3.20}$$

The classical torsional buckling stress is

$$\sigma_{crT} = \frac{GI_T}{I_P} + \frac{EI_\omega}{L^2 I_P}, \tag{3.21}$$

where $G = E/2.6$ is the shear modulus, I_T is the torsional moment of inertia, I_P is the polar moment of inertia and I_ω is the warping constant. The actual torsional buckling stress can be calculated as a function of the reduced slenderness

$$\lambda_T = (f_y/\sigma_{crT})^{1/2}, \tag{3.22}$$

$$\sigma_{UT}/f_y = 1 \quad \text{for} \quad \lambda_T \leq 0.45, \tag{3.23}$$

$$\sigma_{UT}/f_y = 1 - 0.53(\lambda - 0.45) \quad \text{for} \quad 0.45 \leq \lambda \leq 1.41, \tag{3.24}$$

$$\sigma_{UT}/f_y = 1/\lambda^2 \quad \text{for} \quad \lambda > 1.41. \tag{3.25}$$

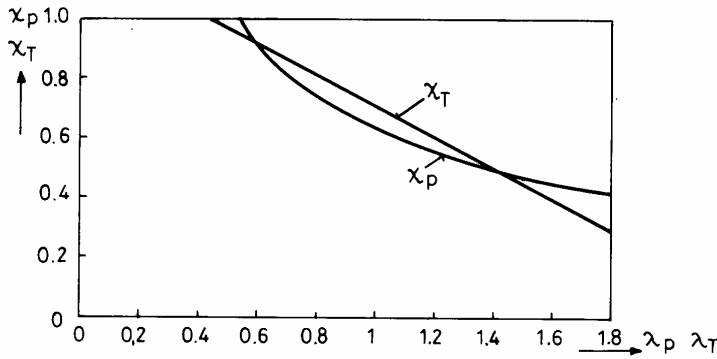


Figure 8. Limiting curves for local plate buckling (χ_P) and torsional buckling of open section ribs (χ_T)

4. Design constraints in case of uniaxial compression and lateral pressure

4.1. Calculation the deflection due to compression and lateral pressure.

Paik et al. [3] used the differential equations of large deflection orthotropic plate theory and the Galerkin method to derive the following cubic equation for the elastic deflection A_m of a stiffened plate loaded by uniaxial compression and lateral pressure

$$C_1 A_m^3 + C_2 A_m^2 + C_3 A_m + C_4 = 0, \quad (4.1)$$

where

$$C_1 = \frac{\pi^2}{16} \left(E_x \frac{m^4 B}{L^3} + E \frac{L}{B^3} \right); \quad C_2 = \frac{3\pi^2 A_{om}}{16} \left(E_x \frac{m^4 B}{L^3} + E \frac{L}{B^3} \right),$$

$$C_3 = \frac{\pi^2 A_{om}^2}{8} \left(E_x \frac{m^4 B}{L^3} + E \frac{L}{B^3} \right) + \frac{m^2 B}{L} \sigma_{xav} + \frac{\pi^2}{t_F} \left(D_x \frac{m^4 B}{L^3} + 2H \frac{m^2}{LB} + D \frac{L}{B^3} \right), \quad (4.2)$$

$$C_4 = A_{om} \frac{m^2 B}{L} \sigma_{xav} - \frac{16LB}{\pi^4 t_F} p,$$

$$E_x = E \left(1 + \frac{n A_S}{B t_F} \right); \quad E_y = E. \quad (4.3)$$

Since the self-weight is taken into account, the lateral pressure is modified as

$$p = p_0 + \frac{\rho V g}{BL}, \quad (4.4)$$

where g is the gravitation constant, 9.81 [m/s²].

The flexural and torsional stiffnesses of the orthotropic plate are as follows:

$$D_x = \frac{Et_F^3}{12(1-\nu_{xy}^2)} + \frac{Et_F y_G^2}{1-\nu_{xy}^2} + \frac{EI_x}{b}, \quad (4.5)$$

$$D_y = \frac{Et_F^3}{12(1-\nu_{xy}^2)},$$

$$\nu_x = \frac{\nu}{0.86} \sqrt{\frac{\frac{E}{E_x} \left(\frac{Et_F^3}{12} + Et_F y_G^2 + \frac{EI_x}{b} \right) - \frac{Et_F^3}{12}}{\frac{EI_x}{b} \left(\frac{E}{E_x} \right)^2}}, \quad (4.6)$$

$$\nu_y = \frac{E}{E_x} \nu_x; \quad \nu_{xy} = \sqrt{\nu_x \nu_y}, \quad (4.7)$$

$$H = \frac{G_{xy} I_t}{b}; \quad G_{xy} = \frac{E}{2(1+\nu_{xy})}, \quad (4.8)$$

$$\sum \frac{b_i}{t_i} = \frac{a_1 + 2a_2}{t_S} + \frac{a_3}{t_F}. \quad (4.9)$$

The deflection due to lateral pressure is

$$A_{om} = \frac{5qL^4}{384EI_x}; \quad q = pb; \quad b = B/\varphi. \quad (4.10)$$

The solution of equation (4.1) is

$$A_m = -\frac{C_2}{3C_1} + k_1 + k_2, \tag{4.11}$$

where

$$k_1 = \sqrt[3]{-\frac{Y}{2} + \sqrt{\frac{Y^2}{4} + \frac{X^3}{27}}}; \quad k_2 = \sqrt[3]{-\frac{Y}{2} - \sqrt{\frac{Y^2}{4} + \frac{X^3}{27}}}, \tag{4.12}$$

$$X = \frac{C_3}{C_1} - \frac{C_2^2}{3C_1^2}; \quad Y = \frac{2C_2^3}{27C_1^3} - \frac{C_2C_3}{3C_1^2} + \frac{C_4}{C_1}. \tag{4.13}$$

4.2. Deflection due to shrinkage of longitudinal welds. According to [9] the deflection of the plate due to longitudinal welds is as follows

$$f_{\max} = CL^2/8, \tag{4.14}$$

where the curvature for steels is

$$C = 0.844x10^{-3}Q_T y_T / I_x, \tag{4.15}$$

Q_T is the heat input, I_x is the moment of inertia of the cross-section containing a stiffener and the base plate strip of width b , y_T is the weld eccentricity

$$y_T = y_G - t_F/2. \tag{4.16}$$

The heat input for a stiffener is

$$Q_T = 2x59.5a_W^2. \tag{4.17}$$

4.3. The stress constraint. The stress constraint includes several effects as follows: the average compression stress and the bending stress caused by deflections due to compression, lateral pressure and the shrinkage of longitudinal welds.

$$\sigma_{\max} = \sigma_{xav} + \frac{M}{I_x} y_G \leq \sigma_{UP}, \tag{4.18}$$

where

$$M = \sigma_{xav} (A_{0m} + A_m + f_{\max}) + \frac{qL^2}{8}, \tag{4.19}$$

According to [1], the calculation of the local buckling strength of a face plate strip of width

$$b_1 = \max(a_3, b - a_3), \tag{4.20}$$

is performed taking into account the effects of initial imperfections and residual welding stresses

$$\sigma_{UP} = f_y \quad \text{when} \quad \lambda_P \leq 0.526, \tag{4.21}$$

$$\sigma_{UP} = \left(\frac{0.526}{\lambda_P}\right)^{0.7} \quad \text{when} \quad \lambda_P \geq 0.526, \tag{4.22}$$

where

$$\lambda_P = \left(\frac{4\pi^2 E}{10.92 f_y}\right)^{1/2} \frac{b_1}{t_F} = \frac{b_1/t_F}{56.8\epsilon}. \tag{4.23}$$

5. Cost function

The objective function to be minimized is defined as the sum of material and fabrication costs

$$K = K_m + K_f = k_m \rho V + k_f \sum T_i, \quad (5.1)$$

or in another form

$$\frac{K}{k_m} = \rho V + \frac{k_f}{k_m} (T_1 + T_2 + T_3), \quad (5.2)$$

where ρ is the material density, V is the volume of the structure, K_m and K_f as well as k_m and k_f are the material and fabrication costs as well as cost factors, respectively, T_i are the fabrication times as follows:

time for preparation, tacking and assembly

$$T_1 = \Theta_d \sqrt{\kappa \rho V}, \quad (5.3)$$

where Θ_d is a difficulty factor expressing the complexity of the welded structure, κ is the number of structural parts to be assembled;

T_2 is time of welding, and T_3 is time of additional works such as changing of electrode, deslagging and chipping. $T_3 \approx 0.3T_2$, thus,

$$T_2 + T_3 = 1.3 \sum C_{2i} a_{wi}^n L_{wi}, \quad (5.4)$$

where L_{wi} is the length of welds, the values of $C_{2i} a_{wi}^n$ can be obtained from formulae or diagrams constructed using the COSTCOMP [4] software, a_w is the weld dimension.

Welding technology	a_w [mm]	$10^3 C_2 a_w^n$
SAW	0-15	$0.2349 a_w^2$
SMAW	0-15	$0.7889 a_w^2$
GMAW-M	0-15	$0.3258 a_w^2$

Table 1. Welding times versus weld size a_w [mm] for longitudinal fillet welds, downhand position

6. Optimization method

Rosenbrock's hillclimb [5] mathematical method is used to minimize the cost function. This is a direct search mathematical programming method without derivatives. The iterative algorithm is based on Hooke & Jeeves searching method. It starts with a given initial value, and takes small steps in the direction of orthogonal coordinates during the search. The algorithm is modified so that secondary searching is carried out to determine discrete values. The procedure finishes when the convergence criterion is satisfied or the iterative number reaches its limit.

7. Numerical data and optimum results

7.1. **Longitudinally stiffened plate loaded by uniaxial compression.** The given data are width $B = 6000$ [mm], length $L = 3000$ [mm], compression force $N = 1.974 \times 10^7$ [N], Young modulus $E = 2.1 \times 10^5$ [MPa] and density $\rho = 7.85 \times 10^{-6}$ [kg/mm³]. The yield stress is $f_y = 355$ [MPa]. The unknowns – the thicknesses of the base plate and the stiffener and the number of the ribs - are limited in size. For without fabrication cost the welding cost is not considered, the material minima is not shown in Tables 4, 5, 6 and 7.

$$\begin{aligned} 3 \leq t_F \leq 40[\text{mm}], \\ 3 \leq t_S \leq 12[\text{mm}], \\ 3 \leq \varphi \leq 10. \end{aligned} \tag{7.1}$$

	k_f/k_m	t_F [mm]	t_S [mm]	ϕ	K/k_m [kg]
Mikami	0	22	6	10	5166
	1	22	6	10	6152
	2	22	6	10	7138
API	0	19	10	10	5224
	1	21	7	10	6249
	2	21	7	10	7367

Table 2. Optimum dimensions with L- stiffener (SAW)

	k_f/k_m	t_F [mm]	t_S [mm]	ϕ	K/k_m [kg]
Mikami	0	9	7	9	3424
	1	12	6	9	4920
	2	17	5	9	6518
API	0	9	7	9	3424
	1	9	7	9	4761
	2	12	6	9	6097

Table 3. Optimum dimensions with trapezoidal stiffener (SAW)

	k_f/k_m	t_F [mm]	t_S [mm]	ϕ	K/k_m [kg]
Mikami	1	22	6	10	7232
	2	24	5	10	8846
API	1	21	7	10	7546
	2	21	7	10	9960

Table 4. Optimum dimensions with L- stiffener (SMAW)

	k_f/k_m	t_F [mm]	t_S [mm]	ϕ	K/k_m [kg]
Mikami	1	19	4	9	6452
	2	19	4	9	8538
API	1	15	5	9	6444
	2	21	3	10	7955

Table 5. Optimum dimensions with trapezoidal stiffener (SMAW)

	k_f/k_m	t_F [mm]	t_S [mm]	ϕ	K/k_m [kg]
Mikami	1	22	6	10	6329
	2	22	6	10	7493
API	1	21	7	10	6462
	2	21	7	10	7793

Table 6. Optimum dimensions with L-stiffener (GMAW-M)

	k_f/k_m	t_F [mm]	t_S [mm]	ϕ	K/k_m [kg]
Mikami	1	11	6	9	4992
	2	16	5	9	6750
API	1	9	7	9	5099
	2	16	5	9	6532

Table 7. Optimum dimensions with trapezoidal stiffener (GMAW-M)

7.2. Longitudinally stiffened plate loaded by uniaxial compression and lateral pressure. The given data are width $B = 4000$ [mm], length $L = 6000$ [mm], compression force $N = 1.974 \times 10^7$ [N], Young modulus $E = 2.1 \times 10^5$ [MPa] and density $\rho = 7.85 \times 10^{-6}$ [kg/mm³]. There are three values of lateral pressure $p_0 = 0.05, 0.1, 0.2$ [MPa] and two values of yield stress $f_y = 255, 355$ [MPa]. The unknowns – the thicknesses of the base plate and the stiffener and the number of the ribs - are limited in size. The results are shown in Tables 8-13. The optimum results are given in bold type.

$$\begin{aligned}
 3 &\leq t_F \leq 40[\text{mm}], \\
 3 &\leq t_S \leq 12[\text{mm}], \\
 3 &\leq \phi \leq 10.
 \end{aligned}
 \tag{7.2}$$

f_y [MPa]	p_0 [MPa]	t_F [mm]	t_S [mm]	ϕ	K/k_m [kg]	
					$k_f/k_m = 0$	$k_f/k_m = 1.5$
235	0.1	38	12	10	8014	11758
235	0.05	30	12	6	6127	8362
355	0.1	28	12	10	6568	10137
355	0.05	20	12	9	4825	7914

Table 8. Optimum dimensions with flat stiffener for $k_f/k_m = 0$, the material minima

f_y [MPa]	p_0 [MPa]	t_F [mm]	t_S [mm]	ϕ	K/k_m [kg]	
					$k_f/k_m = 0$	$k_f/k_m = 1.5$
235	0.1	38	12	10	8014	11758
235	0.05	30	12	6	6127	8362
355	0.1	28	12	10	6568	10137
355	0.05	21	11	8	4852	7312

Table 9. Optimum dimensions with flat stiffener for $k_f/k_m = 1.5$, the cost minima

f_y [MPa]	p_0 [MPa]	t_F [mm]	t_S [mm]	ϕ	K/k_m [kg]	
					$k_f/k_m = 0$	$k_f/k_m = 1.5$
235	0.2	31	12	5	6993	8933
235	0.1	21	12	7	5686	8230
235	0.05	20	10	7	4969	6952
355	0.2	22	12	7	6107	8641
355	0.1	18	9	10	5036	7389
355	0.05	17	7	10	4313	6302

Table 10. Optimum dimensions with L-stiffener for $k_f/k_m = 0$, the material minima

f_y [MPa]	p_0 [MPa]	t_F [mm]	t_S [mm]	ϕ	K/k_m [kg]	
					$k_f/k_m = 0$	$k_f/k_m = 1.5$
235	0.2	34	11	4	7132	8584
235	0.1	27	10	5	5888	7422
235	0.05	24	8	6	5162	6564
355	0.2	28	9	6	6528	8149
355	0.1	22	8	7	5247	6801
355	0.05	19	8	7	4626	6129

Table 11. Optimum dimensions with L-stiffener for $k_f/k_m = 1.5$, the cost minima

f_y [MPa]	p_0 [MPa]	t_F [mm]	t_S [mm]	ϕ	K/k_m [kg]	
					$k_f/k_m = 0$	$k_f/k_m = 1.5$
235	0.2	28	12	4	6974	8549
235	0.1	24	10	4	5723	6975
235	0.05	18	10	5	4993	6466
355	0.2	21	11	5	6108	7780
355	0.1	15	10	6	4944	6635
355	0.05	13	8	7	4148	5611

Table 12. Optimum dimensions with trapezoidal stiffener for $k_f/k_m = 0$, the material minima

f_y [MPa]	p_0 [MPa]	t_F [mm]	t_S [mm]	ϕ	K/k_m [kg]	
					$k_f/k_m = 0$	$k_f/k_m = 1.5$
235	0.2	35	9	3	7250	8223
235	0.1	24	10	4	5723	6975
235	0.05	23	8	4	5122	6132
355	0.2	28	8	4	6530	7589
355	0.1	21	7	5	5111	6284
355	0.05	16	7	6	4264	5560

Table 13. Optimum dimensions with trapezoidal stiffener for $k_f/k_m = 1.5$, the cost minima

8. Conclusions

- The results show that the trapezoidal stiffener is the most economic one. The cost saving can be 69 % compared with various ribs.
- In general the Mikami method gives thinner basic plates than those given by API.
- Materials with higher yield stress give cheaper results. The cost saving can be 40 % compared with the lower one. Higher strength steel is 10 % more expensive.
- In most cases the material and cost minima are different, the number of stiffeners is smaller at cost minima due to welding cost effects. SAW is the cheapest welding process if we do not consider investment cost.
- It can be seen from Tables 8 and 9 that there are no solutions for the highest lateral pressure ($p_0 = 0.2$ [MPa]) for flat stiffeners due to the size limits.
- In case of uniaxially and laterally loaded plate the ratio between material cost and welding cost ranged from 13 % (for flat stiffener, higher yield stress and minimum lateral pressure) to 64 % (in case of trapezoidal stiffener, lower yield stress and maximum lateral pressure).
- For L- and trapezoidal stiffeners the number of stiffeners decreases if the lateral pressure is increased, but it increases if the yield stress of the material is increased.
- For flat stiffeners the number of stiffeners increases if the lateral pressure is increased and the yield stress of the material is increased.

Acknowledgement. The author wishes to acknowledge the guidance of Prof. Károly Jármai and Prof. József Farkas. The research work was supported by the Hungarian Scientific Research Found grants OTKA T38058 and T37941 projects.

References

1. MIKAMI, I., and NIWA, K.: Ultimate compressive strength of orthogonally stiffened steel plates. *J. Struct. Engng ASCE*, **122**(6), (1996), 674–682.
2. American Petroleum Institute API *Bulletin on design of flat plate structures*. Bulletin 2V. Washington, 1987.
3. PAIK, J.K., THAYAMBALLI, A.K. and KIM, B. J.: Large deflection orthotropic plate approach to develop ultimate strength formulations for stiffened panels under combined biaxial compression/tension and lateral pressure. *Thin-Walled Structures*, **39**, (2001), 215–246.
4. COSTCOMP Programm zur Berechnung der Schweisskosten. Deutscher Verlag für Schweisstechnik, Düsseldorf, 1990.
5. ROSENBROCK, H. H.: An automatic method for finding the greatest or least value of a function. *Computer Journal*, **3**, (1960), 175–184.
6. VIRÁG, Z. Minimum cost design of a compressed welded stiffened plate using two different buckling constraints, III. International Conference of PhD. Students, Miskolc, Hungary, 2001, 467–474. (ISBN 963 661 482 2)

7. VIRAG Z. and JÁRMAI K.: Parametric studies of uniaxially compressed and laterally loaded stiffened plates for minimum cost, International Conference on Metal Structures (ICMS), Miskolc, Hungary, Millpress, Rotterdam, 2003, 237–242. (ISBN 90 77017 75 5)
8. FARKAS, J.: *Optimum design of metal structures*. Budapest, Akadémiai Kiadó, Chichester, Ellis Horwood, 1984.
9. FARKAS, J. and JÁRMAI, K.: *Analysis and optimum design of metal structures*, Balkema, Rotterdam-Brookfield, 1997.
10. FARKAS, J. and JÁRMAI, K.: Minimum cost design and comparison of uniaxially compressed plates with welded flat, L- and trapezoidal stiffeners. *Welding in the World*, **44**(3), (2000), 47–51.
11. FARKAS, J., SIMOES, L.M.C., and JÁRMAI, K.: Minimum cost design of a welded stiffened square plate loaded by biaxial compression. WCSMO-4, 4th World Congress of Structural and Multidisciplinary Optimization, Dalian China, Extended Abstracts, 2001, 136–137.
12. FARKAS, J., and JÁRMAI, K.: *Economic design of metal structures*, Millpress, Rotterdam. 2003.

NUMERICAL ANALYSIS OF THE STRESS DISTRIBUTION IN AN ELECTRON BEAM WELDED WORM WHEEL

MICHAL VOREL AND ERHARD LEIDICH

Department of Engineering Design, Technical University Chemnitz

Reichenhainer Str. 70, 09126 Chemnitz, Germany

michal.vorel@mbv.tu-chemnitz.de

[Received: November 11, 2002]

Dedicated to Professor József FARKAS on the occasion of his seventy-fifth birthday

Abstract. In this paper the finite element method was used to determine various stress states in an electron beam welded worm wheel. These are the residual stresses due to the welding process, stress redistribution after teeth milling and another stress redistribution under operation load. It turned out that the maximum principal stress takes up the tangential direction and not the radial direction as was originally assumed. Based on this, the initiation of cracks in the weld can be explained. Teeth milling and applied operation loading proved to have a limited influence on the resulting stress state. Using the time development of residual stresses, an improved welding technology to eliminate the residual stresses was proposed.

Mathematical Subject Classification: 74S05

Keywords: finite element method, residual stresses, worm wheel

1. Introduction

Welded parts often exhibit very complex strain that generally results from residual stresses and stresses from external loading. This is also the case of an electron beam welded worm wheel, the weld of which is strained due to the residual stresses and due to the cyclic loading from the gearing. The wheel is made of a steel hub (S355J2) and a bronze rim (CC484K, Figure 1), which utilizes advantageous wear features of bronze while saving material costs. However, there are always large cracks completely embedded in the weld [1], no matter what the weld depths is. Along with this problem area, a certain minimum thickness of the bronze rim must be considered to prevent tearing off the steel body during operation [2]. Therefore, extensive numerical analyses were performed to explain the form and impact of the arising residual stresses. The objective is rather complex, as the welded joint consists of two very different materials. Furthermore, the unusual round geometry of the weld in a wheel results in even more complicated residual stress fields.

Welding with an electron beam is successfully used in many applications [3]. One of its important advantages is a high energy concentration in the electron beam, which generally leads to low residual stresses in thin weldments. The stress state in thick weldments is, however, more complex and may result in high residual stressing

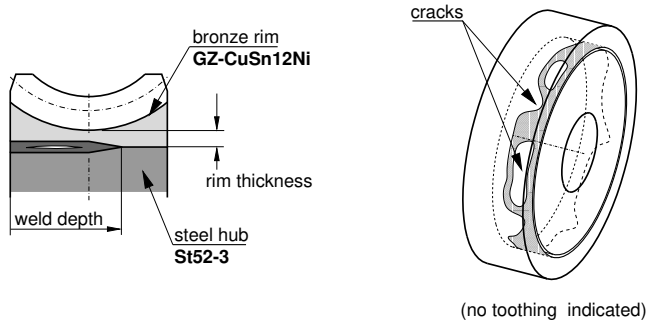


Figure 1. Cracks in an electron beam welded worm wheel.

induced thermally and by an unsuitable geometrical configuration. Residual stresses can be generally determined by numerical methods [4,5] or experimentally. In this paper the numerical method will be presented, as this enables a full description of the residual stressing in the wheel.

2. Numerical Models

For the analyses of stresses in the worm wheel the FE-method was used. The determination of residual stresses as a result of the welding process was achieved by an uncoupled thermal and structural analysis in the MARC program. In the thermal analysis the electron beam advance along the welding path was simulated to calculate the temperature fields. Those were used as boundary conditions in the subsequent structural analysis. The electron beam was modelled as a moving heat source of a rectangular volume. While there is a vacuum in the welding chamber, only cooling due to convection was modelled after the welding process was finished. The models used five different material zones [1].

Due to the temperature dependence of all material properties, the analyses were highly non-linear. The maximum temperature change in the thermal analysis was set for 20°C, which resulted in many analysis increments and consequently in large result files. Fine temperature steps were necessary for the following structural analysis, in which a maximum allowed temperature change lay at 50°C so that two or three increments of the thermal result file were used at once. It turned out that with other settings of temperature steps more iterations and hence longer computational time were needed to reach sufficient accuracy. The structural models used updated Lagrange formulation [6].

In order to further reduce computational costs geometric and mesh optimization of the models was carried out. Initially a complete worm wheel was analyzed (*C66*), as the resulting strain of the part is in general non-symmetrical. Because the analysis took even with a coarse mesh extreme computational time, another analysis with a pie wedge model (*W66-o*) was performed (Figure 2). It used simplified boundary conditions of a constrained displacement at the radial cuts. This induced an unreal

assumption that the radial boundary surfaces remain planar. However, in regions far

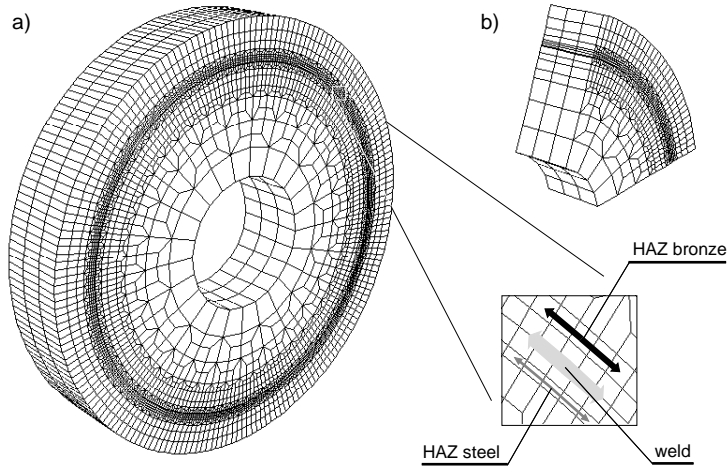


Figure 2. Coarse FE-meshes of a complete worm wheel with a detail of the weld (*C66*, a) and of a pie wedge model (*W66*, b)

enough from those surfaces results from the pie wedge model produced absolutely the same values as with the complete model (Figure 3). When using pie wedge models residual stresses agreed at a point far removed from the beginning of the weld as well as at a point of the weld overlap. With the geometrically reduced model a mesh optimisation was performed in order to make results independent of mesh density at a reasonable computational time. The degree of freedom (DOF) ranged from 8955 with the coarse model to 39207 with a fine meshed model. In the following analyses the medium fine mesh with 22485 DOF was used. One analysis parallel on two SGI R10000 computers took about 64 hours to finish.

3. Residual Stresses after Welding

In order to investigate residual stresses due to the welding process analyses with the pie wedge model in three variations of the weld depth were conducted using the following configurations:

- up to 66% of the wheel width welded model,
 - model out of the weld overlap (*W66-o*),
 - model at the weld overlap (*W66-a*),
- up to 80% of the wheel width welded model at the weld overlap (*W80-a*),
- up to 100% of the wheel width welded model at the weld overlap (*W100-a*).

The configuration with the weld overlap was mainly observed, as this region is critical for operation reliability.

As a result a full residual stress field at the weld overlap can be presented. In

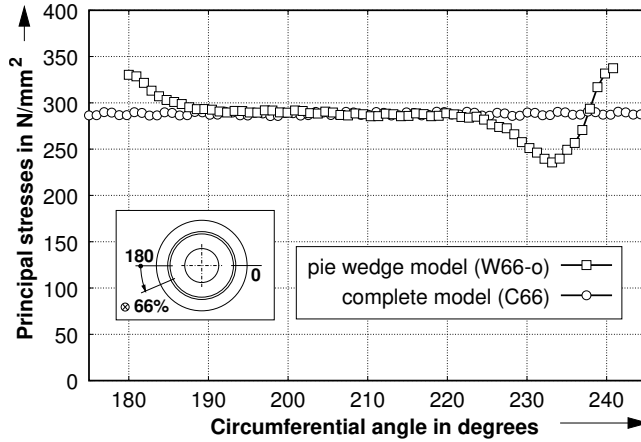


Figure 3. Maximum principal stress in the middle of the weld metal. Comparison of a complete model (*C66*) and a pie wedge model (*W66*).

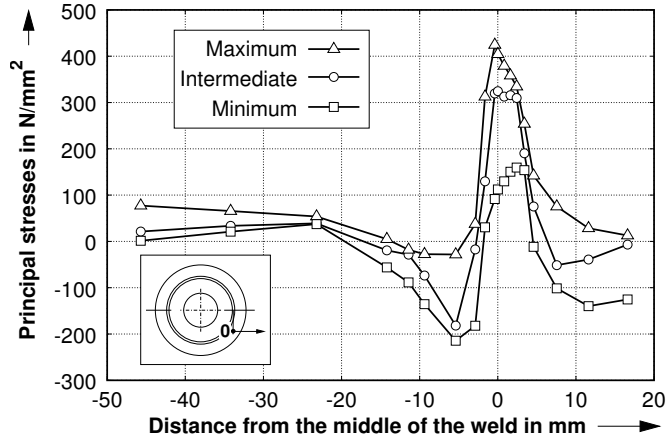


Figure 4. Principal residual stresses in the weld overlap along a radial path passing through the middle of the weld depth. Model *W66-a*

the middle of the weld (in radial direction) the maximum principal stress coincides mainly with the tangential direction. Similarly, the intermediate principal stress takes a predominantly axial direction and the minimum principal stress a radial direction. All principal stresses in the weld are positive. Shear stresses are almost zero in the whole wheel. In conclusion, the weld acts as a pre-stressed hoop. The equilibrium can only be established through negative stresses in the adjacent regions of the steel hub and the bronze rim, as can be seen in Figure 4. The course of principal stresses along the weld overlap shows an enormous fluctuation (Figure 5). This can be explained on the grounds of the time development of the maximum principal stress (Figure 6).

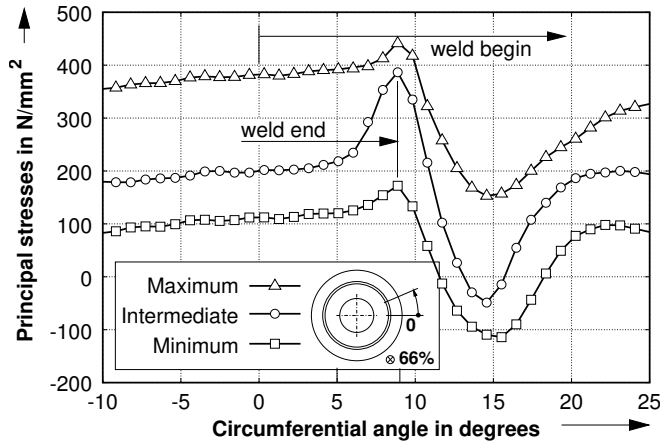


Figure 5. Principal residual stresses in the weld overlap along a tangential path lying in the middle of the weld depth. Model *W66-a*

After the first pass of the weld beam the stress rises with a high gradient. After the weld beam has passed along the whole wheel's circumference, the compressive stresses approach the tensile stresses of the already solidified weld seam and the ultimate stress difference reaches its maximum. With further advance of the weld beam reduction of the original tensile stresses takes place. This is caused by the frontal heat which leads initially to local annealing and subsequently to a full melting of the weld seam. After switching off, the weld beam goes forth for some more time, although it develops only little heat output. Therefore, the temperature field at the weld end does not spread uniformly during the final solidification process. Whereas during the welding process the generated heat is conducted mainly in radial directions from the weld seam, at the weld end the heat flux takes place in all directions. The end point cools down more quickly than the other regions and develops a local maximum of residual stresses. The stresses in front of the weld end are 'annealed' and do not recover any more to the high values. From a comparison of residual stress distribution for the considered models it can be concluded that the maximum stress levels virtually do not depend on the weld depth (Figure 7). The same conclusion can be drawn for the other primary stresses. Furthermore, residual stresses do not open the notch that exists in wheels with reduced weld depths. The deformed meshes show small mutual penetration of the elements at the crack faces, which implies crack closure due to compression forces. Therefore, unlike the original assumption about the mechanism of crack growth due to radial strain, the crack initiation and growth must depend on tangential strain. The crack initiation takes place probably at the weld end and approximately in the middle of the wheel width, where the principal stresses reach their highest values. This region is damaged by a large crack, which extends over the whole weld depth and crosses the weld root with up to 66% and 80% welded wheels. Along with this, the crack grows only in the middle of the weld thickness and propagates in the cylindrical plane

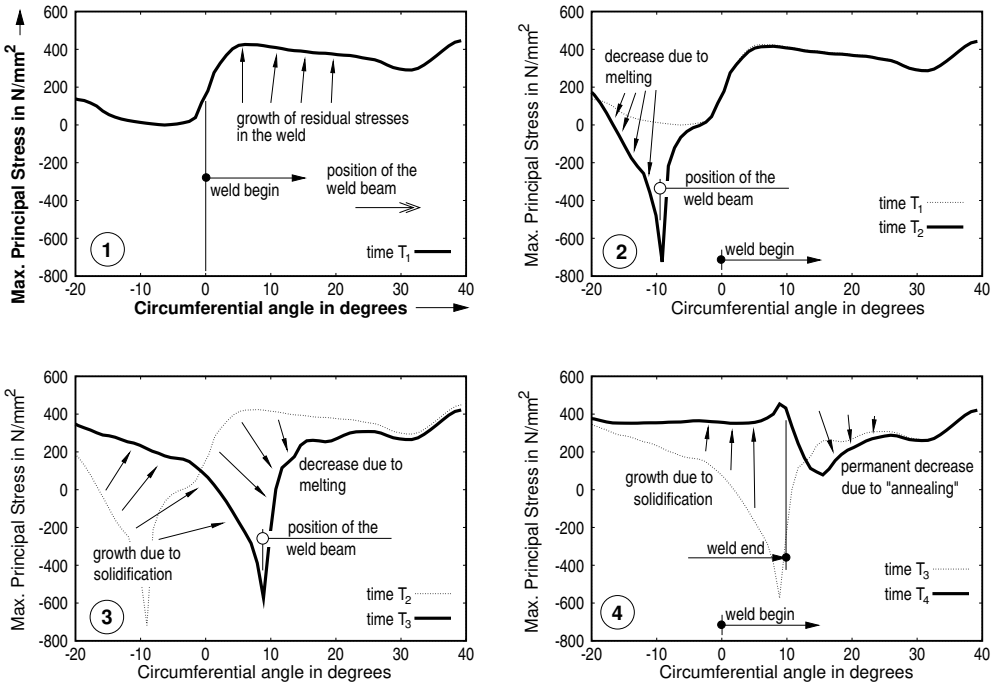


Figure 6. Time development of the maximum principal residual stress along a tangential path lying in the middle of the weld depth. Model *W66-a*

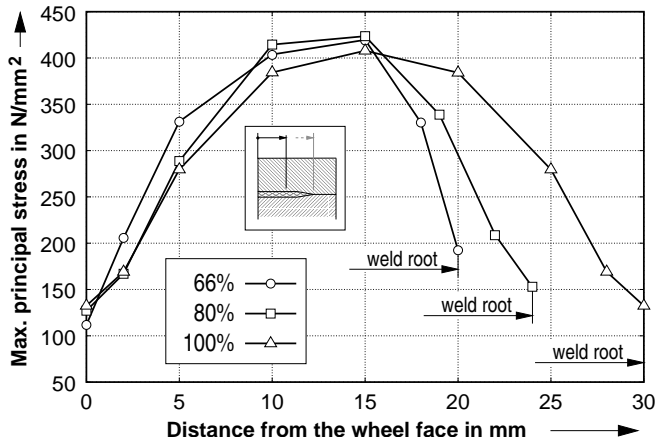


Figure 7. Maximum principal stress along an axial path lying in the middle of the weld depth. Models *W66-a*, *W80-a* and *W100-a*

coinciding with the weld. Whereas the stresses at the weld overlap are high in general and cause the crack to propagate through the whole wheel width, the stresses at other points of the weld cause only crack propagation in the middle of the wheel width and without any breaking through the weld root into the unwelded region. The stress peak along the weld depth stays in the middle of the wheel width, because the bronze rim thickness reaches its minimum there. Some preliminary numerical analyses have shown that with initiation of a small crack the maximum primary stress (as a hoop stress) has the effect of shear stress, i.e. the cracks grow due to Mode II and Mode III mechanisms. Since both heat affected zones show higher hardness, the crack is forced to remain fully within the weld material.

4. Teeth milling impact

After teeth milling the residual stress field changes. A simulation of this technological process was performed with the following models:

- up to 66% welded model at a point out of the weld overlap (*W66-om*),
- up to 66% welded model at a point of the weld overlap,
 - weld end under a tooth (*W66-amt*),
 - weld end under a tooth gap (*W66-amg*),
- up to 100% welded model at a point of the weld overlap (*W100-am*)

To analyze the stress distribution due to material ablation, the FE-meshes were built up with latent teeth. The geometry of tooth flanks was modelled only approximately. The simulation of the milling process was achieved by a gradual deactivation of elements within the tooth gaps. To keep the required accuracy only four analysis increments were needed. The analyses were performed with models cooled to 20°C. Residual stress fields were retrieved using the MARC restart files. The same numerical parameters were used during the analysis as previously. The results showed reduction of residual stresses in general. With the *W66-om* model the maximum principal stress reduces by approx. 50 N/mm^2 (Figure 8). The course of the stress along the welding path is sine shaped, with higher values under the tooth gaps. The course of the redistributed minimum principal stress has a similar shape. However, the stress peaks lie under the teeth and exhibit no decrease against the stress level before milling. The *W66-amt* and *W66-amg* models at the weld overlap proved little stress reduction at the weld end. This was particularly significant with the maximum principal stress. The stresses tended to acquire a similar sine course as above. The *W100-am* model showed only slightly higher stress levels than the *W66-amt* model. The intermediate principal stress reduced with all models by approx. 30 N/mm^2 and, unlike the other principal stresses, it showed very little fluctuation.

5. Operation load impact

After the simulation of teeth milling the external loading was applied to examine its influence on stress changes in the weld. Except for *W66-amg*, the same models as for the previous analysis were used. The related nominal loading of 825 Nm was

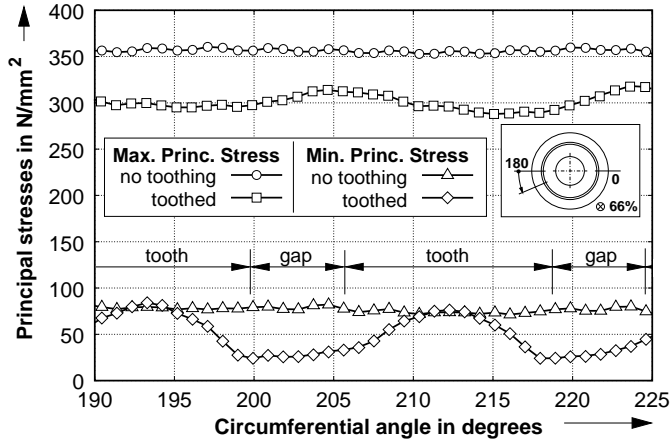


Figure 8. Teeth milling: redistribution of maximum and minimum principal stresses along a tangential path lying in the middle of the weld depth. Model *W66-om*

modelled by a distributed force on one tooth flank only. Although these conditions were rather exaggerated, there were only minor changes in the final stress in the weld. An example of the *W66-amt* model shows that the maximum and minimum principal stresses change by about 30 N/mm² at most (Figure 9). Because of tooth bending the

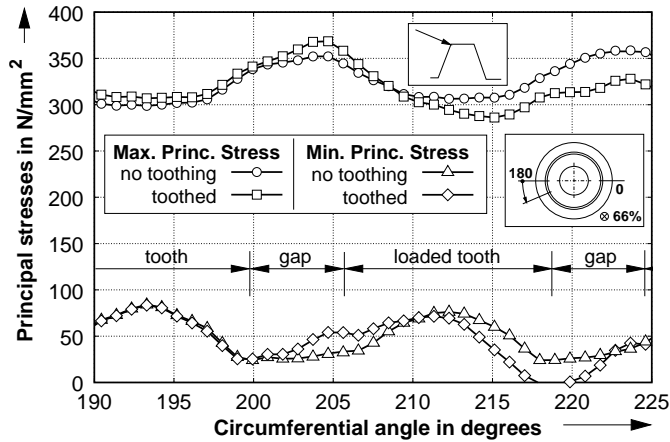


Figure 9. External loading: redistribution of maximum and minimum principal stresses along a tangential path lying in the middle of the weld depth. Model *W66-amt*

stresses decrease at the point under the loaded tooth flank and they get slightly higher at the point under the other flank of the loaded tooth. The elevated stresses do not

reach the values before the milling process in any way. The other models exhibited similar stress changes and there was almost no difference between the *W66-amt* and *W100-am* models. The intermediate principal stress did not change at all with any model. The results correspond well to the investigations made by Schmidt [2], where a stress change of maximum 25 N/mm^2 was determined using fine meshed models without residual stresses.

The important conclusion is that the stress levels in the weld reduce considerably and that they change little under the external loading. This means that the cracks in the weld, which are arrested right after the welding, become definitely stable after the milling process and also remain stable under the external loading. However, some ultrasonic tests have shown that the crack fronts are nonetheless strained up to the measure, which exceeds the threshold value necessary for a fatigue crack growth: the wheels after the operation exhibited larger cracks than before.

6. Improved welding technology

In general, welded components are often pre-heated before welding to prevent unwanted shrinking and high residual stresses which can also be eliminated by a subsequent stress-relief annealing. Worm wheels consisting of bronze can be pre-heated only up to limited temperatures. Referring to the ternary phase diagram Cu-Sn-Ni, the first phase change for the composition CuSn12Ni lies at 351°C [7]. Pre-heating beyond this temperature results in intensive hardening of the material, which is an unwanted feature for the weld as well as for the fatigue toughness of the teeth. Also some advantageous wear features would be irretrievably lost. Special stress-relief annealing could be introduced after the welding, but this would in no way dispose of the already existing cracks. Based on the numerical simulations, pre-heating of only 200°C is suggested so that the phase change temperature would not be exceeded in the whole rim during the welding process. Time development of the maximum principal stress in the weld of a pie wedge model out of the weld overlap shows that even a relatively small amount of pre-heating leads to some decrease of stress immediately after solidification (Figure 10). Due to natural cooling in the atmosphere after removal from the welding chamber, the maximum principal stress grows by about 70 N/mm^2 . In this model the stresses in the weld capillary were not set to zero [8]. In results of test calculations the highly negative stresses return to the real values after about 1.2 seconds behind the weld beam. As can be seen, the residual stresses develop immediately after the weld solidification. This is caused by a highly concentrated electron beam heat source, which means steep temperature gradients and fast cooling of the weld by the bordering material regions (Figure 11). Thus, the intention is to slow down the cooling in the weld behind the welding beam. However, in an electron beam welding chamber this is a complicated objective, which can only be achieved by approximating the desired temperature course through applying several electron beams with gradually reducing power successively. In an optimum case this would result in keeping the residual stresses always at zero values. A splitting of an electron beam into several beams is possible without high additional costs. The trade-off for higher energy costs would be a safe worm wheel without any cracks at all.

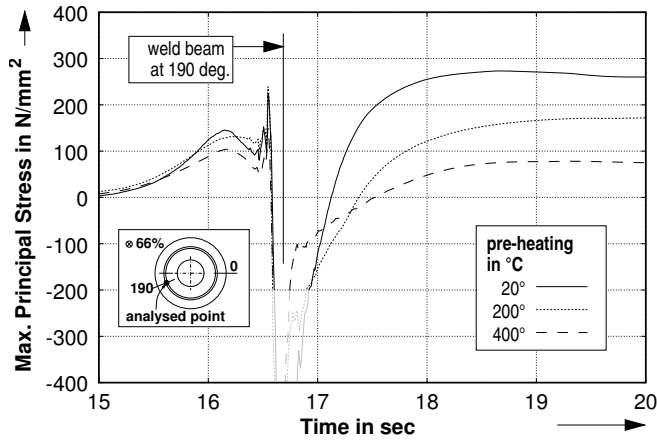


Figure 10. Time development of the maximum principal stress in the *W66-o* model under various pre-heating levels

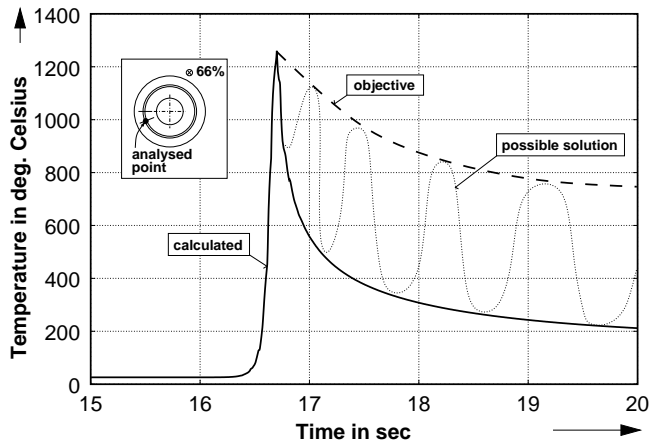


Figure 11. Time development of temperature in the *W66-o* model and desired improvements

To prove the benefits of the suggested welding technology, comprehensive numerical simulations were done with the *W66-o* pie wedge model while varying

- the number of electron beams (two, three or four),
- their intensity (100 to 30%), and
- the distance between them (3 to 15 mm).

To take advantage of pre-heating all models were considered at ambient temperature of 200°C. According to the above concept, the criterion for the optimized combination of the intensity and distance between the beams was that before the pass of the last

beam the maximum primary stress should never exceed its zero value. In order to find the optimum values for each number of beams, 16 simulations were done in a similar manner as above. It proved clearly that several concentrated electron beams following straight after each other with a 5 mm distance have a positive influence on residual stresses in the weld and in the neighboring regions. Directly after the solidification the maximum principal stress can be reduced by 220 N/mm^2 to 50 N/mm^2 when using four beams (Figure 12). This means that with a suitable subsequent cooling procedure the stresses would remain low and would not cause initiation of large cracks. To reach values of residual stresses near zero, many electron beams and therefore longer welding times would be necessary. However, this would be an inapplicable solution in terms of production costs. By welding with three or four beams the energy costs may rise considerably. However, with a perfect weld the wheel can be welded only up to 66%

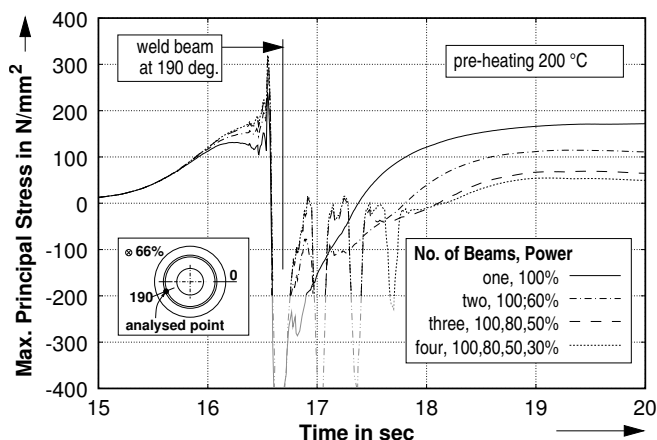


Figure 12. Time development of maximum principal stress in the *W66-o* model. Welding with one, two, three or four electron beams successively

while taking advantage of safe operation and reduced bronze rim thickness.

7. Conclusion

In this paper theoretical work was done in order to explain stress distribution in an electron beam welded worm wheel in different states. Extensive numerical 3D analyses produced full residual stress field in an uncracked worm wheel. The calculated stress fields give a good explanation for the loci of most probable crack initiation. The important result is that crack growth depends predominantly on tangential stresses and not on the radial stresses as was originally assumed. Through the analysis of time development of residual stresses during the welding process an improved welding procedure was proposed to reduce residual stresses considerably or to prevent them completely. This is achieved by additional warming up the weld with more electron

beams following directly after the welding beam. This technology implies higher energy costs but as a compensation offers a perfectly welded worm wheel. Currently, experimental tests are being conducted to verify the numerical results and prove the new welding technology.

In further research some numerical analyses are planned to evaluate stability of cracks in the weld under external loading. For this purpose experimental work is also necessary to determine the threshold value for fatigue crack growth.

References

1. VOREL, M. and LEIDICH, E.: *Impact of residual stresses on crack distribution in an electron beam welded worm wheel*. In Maschinenbau und Nanotechnik, 47. Internationales Wissenschaftliches Kolloquium, Ilmenau, 2002.
2. SCHMIDT, G.: *Untersuchungen zur Tragfähigkeit elektronenstrahlgeschweisster Schneckenräder*. Berichte aus dem Maschinenbau. Shaker Verlag, 1999, Aachen.
3. SCHULTZ, H.: *Elektronenstrahlschweißen*. Fachbuchreihe Schweißtechnik. DVS Verlag, 2000, Düsseldorf.
4. RADAJ, D.: *Schweißprozesssimulation: Grundlagen und Anwendungen*. Fachbuchreihe Schweißtechnik. Verlag für Schweißen und Verwandte Verfahren; 1999, DVS Verlag, Düsseldorf.
5. VOSS, O.: *Untersuchung relevanter Einflußgrößen auf die numerische Schweißsimulation*. Forschungsberichte des Instituts für Schweißtechnik. Shaker Verlag, 2001, Aachen.
6. ZIENKIEWICZ, O.C. and TAYLOR, R.L.: *The finite element method: Solid mechanics*, Volume 2. Butterworth-Heinemann, 2000, Oxford.
7. GUERTLER, W.: *Konstitution der ternären metallischen Systeme*. Kompendium, Heft 12., 1961, TU Berlin.
8. LENZ, B. and RICK, F.: *Lösungsansätze zur Simulation des Laserstrahlschweißens*. In Applications of Lasers and Electoptics, 1999, San Diego.

USE OF DISCONTINUITY FUNCTIONS TO OBTAIN THE FREQUENCY EQUATION

ISTVÁN ECSEDI AND KORNÉL DLUHI
Department of Mechanics, University of Miskolc
3515 Miskolc–Egyetemváros, Hungary
mechecs@uni-miskolc.hu, mechdk@uni-miskolc.hu

Dedicated to Professor József FARKAS on the occasion of his seventy-fifth birthday

[Received: January 26, 2004]

Abstract. An integration technique based on the use of discontinuous functions has been applied to obtain the natural frequencies of free flexural vibrations in beams. The two examples presented show the logical basis of the method in a detailed form.

Mathematical Subject Classification: 74K10

Keywords: light beam, flexural vibration, discontinuity functions, frequency equation

1. Introduction

In this paper discontinuity functions are applied to derive the frequency equation for the flexural vibration of light beams. The designations and the definitions of the discontinuity functions are borrowed from the textbook by Gere, J. M. and Timoshenko, S. P. [1]. We will use mainly Table 7-2 of the aforementioned textbook. Two examples illustrate how to derive the frequency equation in the form of a determinant. The sign rules we applied are shown in Figure 1. In the state of free flexural vibration all quantities vary with time in the following form

$$\tilde{X} = X \sin \omega t \quad X = v, \varphi, V, M, R, \dots \quad (1.1)$$

The factor independent of time in equation (1.1) is referred to as the amplitude of the quantity X .

2. Examples

2.1. The first problem is that of a light beam with uniform cross-section. The beam is clamped at its two ends. A mass m is attached to point B and a torsional spring is fixed to point C . In the present problem the Young modulus E of the beam is constant.

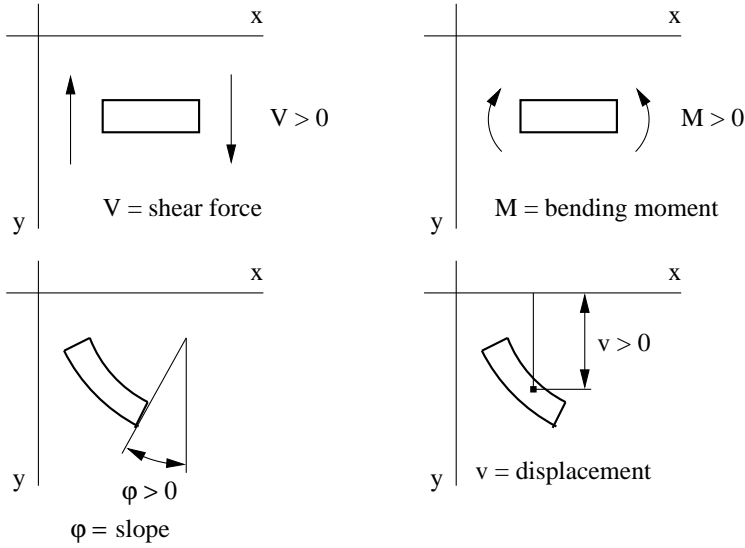


Figure 1. Sign rules for shear, bending, shape and deflection

The light beam with mass and spring is shown in Figure 2, and the free-body diagram of the beam segment AD is given in Figure 3.

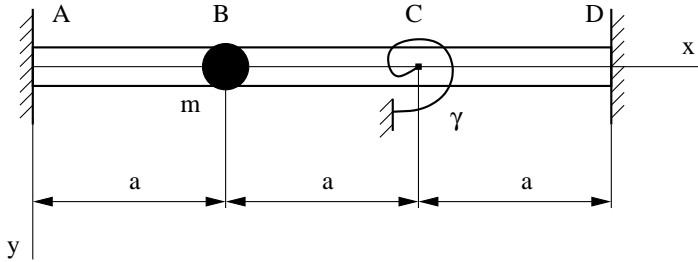


Figure 2. Fixed beam

We shall apply the following designations:

R_A, R_B	amplitudes of the reactions,
M_A, M_B	amplitudes of reaction couples,
$T_B = mv_B\omega^2$	amplitude of the inertia force,
v	displacement amplitude,
ω	eigenfrequency of the free vibrations,
$Q_C = -\varphi_C/\gamma$	amplitude of couple at the torsional spring,
γ_C	amplitude of slope,
γ	spring constant.

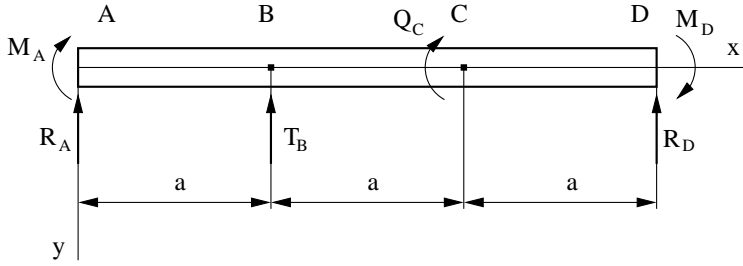


Figure 3. Free-body diagram of the beam segment AD

By using the method of **Clebsch-Macaulay** we obtain the exact expressions for the shear force V and the bending moment M :

$$V = R_A + M_A \langle x \rangle^{-1} + T_B \langle x - a \rangle^0 + Q_C \langle x - 2a \rangle^{-1} \quad , \quad (2.1)$$

$$M = R_A x + M_A + T_B \langle x - a \rangle^1 + Q_C \langle x - 2a \rangle^0 \quad . \quad (2.2)$$

It is well-known [1] that the bending moment satisfies the equation

$$IEv'' = -M \quad . \quad (2.3)$$

Here prime denotes the derivation with respect to x , i.e., $v'' = \frac{d^2v}{dx^2}$.

Combination of equation (2.2) with equation (2.3) yields the slope $\varphi = v'$ and the deflection v :

$$IE\varphi = - \left(R_A \frac{x^2}{2} + M_A x + T_B \frac{\langle x - a \rangle^2}{2} + Q_C \langle x - 2a \rangle^1 \right) + C \quad , \quad (2.4a)$$

$$IEv = - \left(R_A \frac{x^3}{6} + M_A \frac{x^2}{2} + T_B \frac{\langle x - a \rangle^3}{6} + Q_C \frac{\langle x - 2a \rangle^2}{2} \right) + Cx + D \quad . \quad (2.4b)$$

where C and D are constants of integration. From the boundary conditions

$$v(0) = 0, \quad v'(0) = 0, \quad (2.5a,b)$$

we get

$$C = 0, \quad D = 0. \quad (2.6a,b)$$

The boundary conditions $v(3a) = 0$ and $v'(3a) = 0$ at point D lead to the following equations:

$$4.5a^2 R_A + 3a M_A + 2a^2 T_B + Q_C a = 0 \quad , \quad (2.7a)$$

$$4.5a^3 R_A + 4.5a^2 M_A + 1.3333a^3 T_B + 0.5a^2 Q_C = 0 \quad . \quad (2.7b)$$

In the state of free vibration the relationship between the amplitude of inertia force and the amplitude of displacement at point B is

$$v_B = \frac{T_B}{m\omega^2} \quad . \quad (2.8)$$

From the definition of spring constant γ it follows that

$$\gamma_C = v' = -Q_C\gamma \quad . \quad (2.9)$$

By applying the expressions for the slope and deflection – these are given by equations (2.4a,b) – we can eliminate both v_B and γ_C from equations (2.8), (2.9). These eliminations give

$$0.16666a^3R_A + 0.5a^2M_A + \frac{IE}{m\omega^2}T_B = 0 \quad , \quad (2.10a)$$

$$2a^2R_A + 2aM_A + 0.5a^2T_B - IE\gamma Q_C = 0 \quad . \quad (2.10b)$$

We have four equations for the four unknown quantities R_A, M_A, T_B, Q_C . Equations (2.7a,b) and (2.10a,b) form a system of linear equations for the unknown amplitudes R_A, M_A, T_B, Q_C . There exists a non-trivial solution for the system of equations (2.7a,b) and (2.10a,b) if the frequency determinant vanishes:

$$\begin{vmatrix} 4.5a^2 & 3a & 2a^2 & a \\ 4.5a^3 & 4.5a^2 & 1.3333a^3 & 0.5a^2 \\ 0.16666a^2 & 0.5a^2 & IE/m\omega^2 & 0 \\ 2a^2 & 2a & 0.5a^2 & -IE\gamma \end{vmatrix} = 0 \quad . \quad (2.11)$$

2.2. The second example is that of a simply supported beam with non-uniform cross-section. In this case the material of the beam is also homogeneous, that is the Young modulus E is constant. The beam with a rigid disc and springs is shown in Figure 4. The spring constants are c and γ and the mass of the disc is m . The second moment of the disc with respect to centroidal axis b is J . The main centroidal axis b passes through point B and is perpendicular to the plane xy .

If the beam vibrates freely, it is loaded by a force and a couple at point B . This force-couple system arises from the inertia effects and the action of springs. The amplitude of the resultant force at point B is

$$T_B = \left(m\omega^2 - \frac{1}{C} \right) v_B \quad . \quad (2.12a)$$

The amplitude of the resultant couple at the same point is

$$Q_B = \left(J\omega^2 - \frac{1}{\gamma} \right) \varphi_B \quad . \quad (2.12b)$$

The free-body diagram of the beam AD is shown in Figure 5.

The shear force V and the bending moment M are given by the following formulae:

$$V = R_A + T_B\langle x - a \rangle^0 + Q_B\langle x - a \rangle^{-1} \quad , \quad (2.13)$$

$$M = R_Ax + T_B\langle x - a \rangle^1 + Q_B\langle x - a \rangle^0 \quad . \quad (2.14)$$

The boundary condition for the bending moment M at point D yields

$$M(4a) = 4aR_A + 3aT_B + Q_B = 0 \quad . \quad (2.15)$$

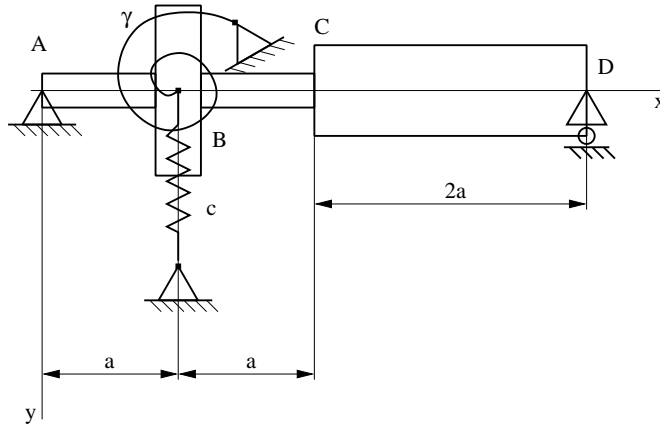


Figure 4. Simply supported beam of non-uniform cross-section

The flexural rigidity is given by the equations

$$EI = EI_0, \quad 0 \leq x < 2a, \quad (2.16a)$$

$$EI = 2EI_0, \quad 2a < x \leq 4a, \quad (2.16b)$$

where E and I_0 are constants.

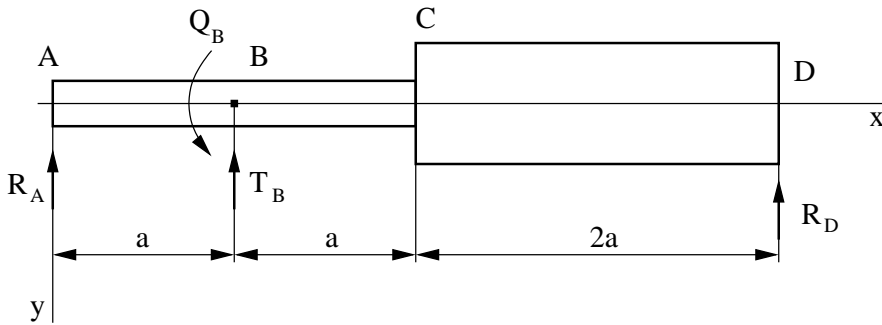


Figure 5. Free-body diagram for the non-uniform beam segment AD

Integrating equation (2.3) we obtain

$$-I_0 E v' = R_A \frac{x^2}{2} + T_B \frac{\langle x - a \rangle^2}{2} + Q_B \langle x - a \rangle^1 + C_1 \quad 0 \leq x < 2a, \quad (2.17a)$$

$$-2I_0 E v' = R_A \frac{x^2}{2} + T_B \frac{\langle x - a \rangle^2}{2} + Q_B \langle x - a \rangle^1 + C_2 \quad 2a < x \leq 4a. \quad (2.17b)$$

After a new integration we arrive at the deflection:

$$-I_0Ev = R_A \frac{x^3}{6} + T_B \frac{\langle x - a \rangle^3}{6} + Q_B \frac{\langle x - a \rangle^2}{2} + C_1x + D_1 \quad 0 \leq x < 2a, \quad (2.18a)$$

$$-2I_0Ev = R_A \frac{x^3}{6} + T_B \frac{\langle x - a \rangle^3}{6} + Q_B \frac{\langle x - a \rangle^3}{6} + C_2x + D_2 \quad 0 \leq x < 2a. \quad (2.18b)$$

By using the displacement boundary condition $v(0) = 0$ we get

$$D_1 = 0 \quad . \quad (2.19)$$

In the present case we have six unknowns, namely $R_A, T_B, Q_B, C_1, C_2, D_2$. The equations which we have to use to determine the above mentioned quantities are as follows:

$$M(4a) = 0 \quad , \quad v(4a) = 0 \quad , \quad (2.20a,b)$$

$$v'(2a - \varepsilon) = v'(2a + \varepsilon) \quad \varepsilon \rightarrow 0 \quad , \quad (2.20c)$$

$$v(2a - \varepsilon) = v(2a + \varepsilon) \quad \varepsilon \rightarrow 0 \quad , \quad (2.20d)$$

$$v(a) = \frac{T_B}{m\omega^2 - \frac{1}{c}} \quad , \quad v'(a) = \frac{Q_B}{J\omega^2 - \frac{1}{\gamma}} \quad . \quad (2.20e,f)$$

Equations (2.20c,d) are the joint conditions for the solutions which determine the deflection and the slope in the intervals $0 \leq x < 2a$ and $2a < x < 4a$. These solutions can be obtained from the formulae (2.17a,b) and (2.18a,b). The preceding equations form a system of linear equations for the six unknowns $R_A, T_B, Q_B, C_1, C_2, D_2$. From the condition of the existence of a nontrivial solution we get the frequency equation in the form of a determinant:

$$\begin{vmatrix} 4a^2 & 3a & 1 & 0 & 0 & 0 \\ 0.5a^2 & 0 & I_0E/(J\omega^2 - \frac{1}{\gamma}) & 1 & 0 & 0 \\ 0.16666a^3 & I_0E/(m\omega^2 - \frac{1}{c}) & 0 & a & 0 & 0 \\ 10.666a^3 & 4.5a^3 & 4.5a^2 & 0 & 4a & 1 \\ 2a^2 & 0.5a^2 & a & 2 & -1 & 0 \\ 1.3333a^3 & 0.16666a^3 & 0.5a^2 & 2a & -a & 1 \end{vmatrix} = 0 \quad . \quad (2.21)$$

3. Conclusion

An integration technique for the discontinuous expressions has been applied to obtain the frequency equation of the vibrations in beams. The two examples presented show the logical basis of the method and illustrate well the scheme to be followed in order to get the frequency equation for flexural vibrations. It is shown that this method can also be used if discontinuities arise in the expression of the flexural rigidity EI. The use of **Macaulay's** brackets in an analysis of the beam problems results in a unified method which has a pedagogical value in teaching the elementary theory of beams. As regards the **Macaulay-Clebsch** method, a number of applications can be found in Wittrick's paper [2].

More advanced mathematical methods based on the distribution theory of Schwarz are applied to solve the static bending problems of beams with material, geometric and loading discontinuities in the papers by Reddy, Yavari, Sarkani [3, 4, 5].

References

1. GERE, J. M. AND TIMOSHENKO, S. P.: *Mechanics of Materials*, PWS Eng. Boston. 351–361; 399–405. 1985.
2. WITTRICK, W. H.: *Generalization of Macaulay's method with applications in structural mechanics*, AIAA Journal. Vol. 3. No. 2. 326–330. 1965.
3. YAVARI, A. AND SARKANI, S.: *On applications of generalized functions to the analysis of Euler–Bernoulli beam-columns with jump discontinuities*, Int. Journ. Mechanical Sciences **43**, 1543–1562, 2001.
4. YAVARI, A., SARKANI, S. AND REDDY, J. N.: *On non-uniform Euler–Bernoulli and Timoshenko beams with jump discontinuities: applications of distribution theory*, Int. Journ. Solids and Structures **38**, 8389–8406. 2001.
5. YAVARI, A., SARKANI, S. AND REDDY, J. N.: *Generalized solutions of beams with jump discontinuities on elastic foundations*, Archives of Applied Mechanics **70**, 625–639. 2001.

Notes for Contributors

to the Journal of Computational and Applied Mechanics

Aims and scope. The aim of the journal is to publish research papers on theoretical and applied mechanics. Special emphasis is given to articles on computational mechanics, continuum mechanics (mechanics of solid bodies, fluid mechanics, heat and mass transfer) and dynamics. Review papers on a research field and materials effective for teaching can also be accepted and are published as review papers or classroom notes. Papers devoted to mathematical problems relevant to mechanics will also be considered.

Frequency of the journal. Two issues a year (approximately 80 pages per issue).

Submission of Manuscripts. Submission of a manuscript implies that the paper has not been published, nor is being considered for publication elsewhere. Papers should be written in standard grammatical English. Two copies of the manuscript should be submitted on pages of A4 size. The text is to be 130 mm wide and 190 mm long and the main text should be typeset in 10pt CMR fonts. Though the length of a paper is not prescribed, authors are encouraged to write concisely. However, short communications or discussions on papers published in the journal must not be longer than 2 pages. Each manuscript should be provided with an English Abstract of about 50–70 words, reporting concisely on the objective and results of the paper. The Abstract is followed by the Mathematical Subject Classification – in case the author (or authors) give the classification codes – then the keywords (no more than five). References should be grouped at the end of the paper in numerical order of appearance. Author's name(s) and initials, paper titles, journal name, volume, issue, year and page numbers should be given for all journals referenced.

The journal prefers the submission of manuscripts in \LaTeX . Authors should prefer the $\mathcal{A}\mathcal{M}\mathcal{S}\text{-}\text{\LaTeX}$ article class and are not recommended to define their own \LaTeX commands. Visit our home page for further details concerning the issue how to edit your paper.

For the purpose of refereeing, two copies of the manuscripts should initially be submitted in hardcopy to an editor of the journal. The eventual supply of an accepted-for-publication paper in its final camera-ready form (together with the corresponding files on an MS-DOS diskette) will ensure more rapid publication. Format requirements are provided by the home page of the journal from which sample \LaTeX files can be downloaded:

<http://www.uni-miskolc.hu/home/web/pumns/mechanics>

These sample files can also be obtained directly (via e-mail) from a member of the Editorial Board, Gy. Szeidl (Gyorgy.SZEIDL@uni-miskolc.hu), upon request.

Twenty offprints of each paper will be provided free of charge and mailed to the correspondent author.

The Journal of Computational and Applied Mechanics is abstracted in Zentralblatt für Mathematik and in the Russian Referativnij Zhurnal.

Responsible for publication: Rector of the Miskolc University

Published by the Miskolc University Press under the leadership of Dr. József PÉTER

Responsible for duplication: works manager Mária KOVÁCS

Number of copies printed: 200

Put to the Press on May 28, 2004

Number of permission: TU 2004-560-ME

HU ISSN 1586–2070

A Short History of the Publications of the University of Miskolc

The University of Miskolc (Hungary) is an important center of research in Central Europe. Its parent university was founded by the Empress Maria Teresia in Selmecebánya (today Banská Štiavnica, Slovakia) in 1735. After the first World War the legal predecessor of the University of Miskolc moved to Sopron (Hungary) where, in 1929, it started the series of university publications with the title *Publications of the Mining and Metallurgical Division of the Hungarian Academy of Mining and Forestry Engineering* (Volumes I.-VI.). From 1934 to 1947 the Institution had the name Faculty of Mining, Metallurgical and Forestry Engineering of the József Nádor University of Technology and Economic Sciences at Sopron. Accordingly, the publications were given the title *Publications of the Mining and Metallurgical Engineering Division* (Volumes VII.-XVI.). For the last volume before 1950 – due to a further change in the name of the Institution – *Technical University, Faculties of Mining, Metallurgical and Forestry Engineering, Publications of the Mining and Metallurgical Divisions* was the title.

For some years after 1950 the Publications were temporarily suspended.

After the foundation of the Mechanical Engineering Faculty in Miskolc in 1949 and the movement of the Sopron Mining and Metallurgical Faculties to Miskolc, the Publications restarted with the general title *Publications of the Technical University of Heavy Industry* in 1955. Four new series - Series A (Mining), Series B (Metallurgy), Series C (Machinery) and Series D (Natural Sciences) - were founded in 1976. These came out both in foreign languages (English, German and Russian) and in Hungarian.

In 1990, right after the foundation of some new faculties, the university was renamed to University of Miskolc. At the same time the structure of the Publications was reorganized so that it could follow the faculty structure. Accordingly three new series were established: Series E (Legal Sciences), Series F (Economic Sciences) and Series G (Humanities and Social Sciences). The latest series, i.e., the series H (European Integration Studies) was founded in 2001. The eight series are formed by some periodicals and such publications which come out with various frequencies.

Papers on computational and applied mechanics were published in the

Publications of the University of Miskolc, Series D, Natural Sciences.

This series was given the name Natural Sciences, Mathematics in 1995. The name change reflects the fact that most of the papers published in the journal are of mathematical nature though papers on mechanics also come out.

The series

Publications of the University of Miskolc, Series C, Fundamental Engineering Sciences

founded in 1995 also published papers on mechanical issues. The present journal, which is published with the support of the Faculty of Mechanical Engineering as a member of the Series C (Machinery), is the legal successor of the above journal.



Contents

Preface	3–5
Contributed Papers	
Ji Huan HE: Variational theory for 2-dimensional free surface flow: Why are G.L. Liu's variational principles incorrect?	7–19
R. KANDASAMY, Anjali DEVI: Effects of chemical reaction, heat and mass transfer on non linear laminar boundary - layer flow over a wedge with suction or injection	21–31
László ÉCSI and Pál ÉLESZTŐS: Finite element analysis of structures on the base of heterogeneous models	33–48
Béla KOVÁCS: Transverse shear and normal deformation theory for vibration analysis of curved bands	49–64
Flórián KOVÁCS: Mobility and stress analysis of highly symmetric generalized bar-and-joint structures	65–78
György KOVÁCS: Optimal design of a composite multicellular plate structure	79–88
Witold M. PACZKOWSKI, Adrian SILICKI and Stefan JENDO: Quasi-evolutionary polyoptimization of spatial trusses	89–102
Péter PÁLFI: Locally orthotropic femur model	103–115
Vanda POMEZÁNSZKI: Changing the connections of structural elements during an optimization process	117–127
Yarema H. SAVULA, Nestor Ya. SAVULA and Valentine SHCHUKIN: Finite element analysis of structures on the base of heterogeneous models	129–140
Valentine SHCHUKIN and Imre TÍMÁR: Calculation of stresses in isotropic plates with two circular holes	141–150
József UJ: A finite element model of delamination in cross-ply laminates	151–155
József VERHÁS: Onsager's reciprocal relations and some basic laws	157–163
Zoltán VIRÁG: Optimum design of stiffened plates for different loads and shapes of ribs	165–179
Michal VOREL and Erhard LEIDICH: Numerical analysis of the stress distribution in a welded worm wheel	181–192
Classroom Note	
István ECSEDI and Kornél DLUHI: The use of discontinuity functions to obtain the frequency equation	193–199